232
3·23

2081

A Study of $\pi^- p \to \pi^+ \pi^- n$, $K^+ K^- n$ at 15 GeV/c

and a Comparison with Absorptive One-Pion-Exchange

Hugh H. Williams

STANFORD LINEAR ACCELERATOR CENTER
Stanford University · Stanford, California

DISCLAIMER

DISCLAIMER

Portions of this document may be illegible in electronic image products. Images are produced from the best available original document.

SLAC-142
UC-34
(EXP)

A STUDY OF $\pi^- p \to \pi^+ \pi^- n$, $K^+ K^- n$ AT 15 GeV/c

AND A COMPARISON WITH ABSORPTIVE ONE-PION-EXCHANGE*

HUGH H. WILLIAMS

STANFORD LINEAR ACCELERATOR CENTER

STANFORD UNIVERSITY

Stanford, California 94305

ABSTRACT

Results are reported from a wire spark chamber experiment performed at the Stanford Linear Accelerator Center to study the production of $\pi^+\pi^-n$ final states in 15 GeV/c π^-p interactions. Approximately 10,000 $\pi^+\pi^-n$ events were detected with a $\pi\pi$ mass less than 1.0 GeV and a momentum transfer to the nucleon less than .3 $(GeV/c)^2$. The differential cross section and density matrix elements of the dipion system were determined as a function of momentum transfer for events with a $\pi\pi$ mass in the interval .665 - .865 GeV.

Many of the density matrix elements in the helicity frame are observed to exhibit structure for momentum transfers less than m_π^2. In particular, there is a pronounced dip in the value of $\rho_{00}-\rho_{11}$ which has not been previously observed. The interference terms, $Re\rho_{0s}$ and $Re\rho_{1s}$, exhibit similar shape and change sign at momentum transfers equal to m_π^2. The longitudinal and total differential cross sections also decrease rapidly in the forward direction, while the cross section for transversely polarized rho mesons exhibits a sharp rise analogous to that observed in single-pion photoproduction. Each of the qualitative features is correctly predicted by OPEA, and a five-parameter fit of the model to the data quantitatively reproduces all of the observed structure. We therefore conclude that the model provides a rather good explanation of this reaction at small momentum transfers.

In addition to the $\pi^+\pi^-n$ events, K^+K^-n and $\bar{p}pn$ states were also detected and identified by a Čerenkov counter. The production of ϕn events which subsequently decay into K^+K^-n is observed to proceed with a cross section of 65 ± 26 μb.

No sharp structure is observed in the $p\bar{p}$ mass spectrum, but this final state is produced with a relatively large cross section; the ratio of $\bar{p}pn$ to K^+K^-n final states is approximately 1:1.

ACKNOWLEDGEMENTS

In putting this experiment together, a great many people at all levels - riggers, technicians, engineers, and programmers, to name but a few - have made contributions far beyond their normal responsibilities. Thanks is due to each of these people.

I mention here those individuals with whom I have had the opportunity to work most closely. There are many others who have contributed an equal amount.

I have enjoyed very much working with the other physicists in the group - Fatin Bulos, Bob Carnegie, Gerry Fischer, Eike Kluge, Harvey Lynch, Blair Ratcliff, Steve Williams, and Professors Burton Richter and David Leith - and have learned much from each of them. In particular, I would like to thank David Leith, my thesis advisor, who has been a continual source of enthusiasm and encouragement during my research at SLAC.

Much credit is due to Mike Beniston, of IBM, who also collaborated on the experiment. The track-finding and event-reconstruction program is largely the result of his efforts.

Throughout the course of the experiment and particularly during the construction of the Čerenkov counter, I have worked closely with Al Kilert and Bill Walsh. I thank them not only for their tremendous help, but also for the many enjoyable times we have had working together. Don McShurley and Bob Friday were invaluable in the design and construction of various parts of the electronics.

Considerable effort has also gone into preparation of the manuscript. I thank Betty Pennington for typing the many rough drafts.

Many thanks are due to Martha Zipf who has been an unfailing source of help and information on practically all matters.

TABLE OF CONTENTS

LIST OF TABLES

LIST OF FIGURES

CHAPTER 1

INTRODUCTION

Some of the most direct evidence for the important role of the pion

in high energy interactions came initially from studies of single-pion

production in π^-p interactions. For incident pion energies above ≈ 2 GeV,

it was observed that there was a strong tendency for both pions to come

forward in the center-of-mass system while the nucleon was generally

observed in the backward direction.[1] The peripheral nature of this process,

taken together with the concept that the nucleon is surrounded by a cloud of

virtual pions, led to the suggestion that the reaction proceeds via a $\pi\pi$ collision

in which a virtual π is knocked out of the nucleon's field. Interest in the

reactions $\pi N \rightarrow \pi\pi N$ and $KN \rightarrow K\pi N$ was greatly spurred by the ensuing proposal

of Goebel,[2] and Chew and Low[3] that one might be able to extract from these

reactions the scattering amplitude for $\pi\pi$ and $K\pi$ interactions. Knowledge of

these scattering amplitudes is of great interest both because of the fundamental

nature of the interaction and also because of the inherent simplicity in the

scattering of two spinless particles. Further development of this theoretical

trend led to formulation of the one-pion-exchange model.[4] It was suggested

that many peripheral reactions might proceed primarily by the exchange of a

single pion, when permitted by the relative quantum numbers of the initial

and final states. The success of this model and the modifications to it since

its proposal are discussed below in some detail.

For small momentum transfers (t) to the nucleon, the reaction $\pi N \rightarrow \pi\pi N$

may be expected to be dominated by the exchange of a single pion as

represented by the diagram in Fig. 1. Since this amplitude is proportional
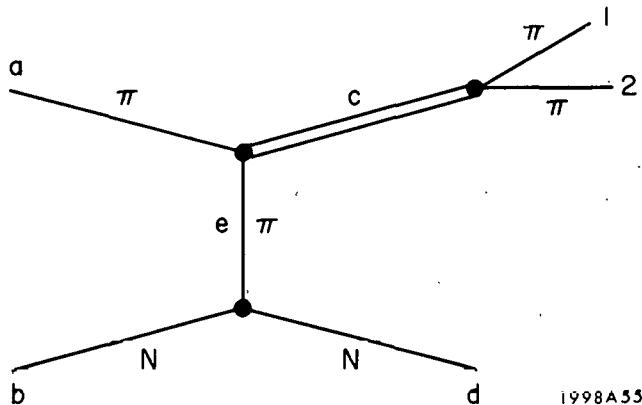
FIG. 1--One-pion-exchange
diagram

to $1/(t-m_\pi^2)$, the physical scattering which occurs for small negative values of

t (e.g., $0 > t > -.2$) is close to the "pion pole" at $t=m_\pi^2$. The one-pion-

exchange (OPE) amplitude should then dominate over the exchange of heavier

particles, such as the A_2, for which the amplitude is proportional to

$1/(t-m_{A_2}^2)$.

The OPE amplitude may be written in the form

$$A(\pi^- p \to \pi^+ \pi^- n) = \frac{G}{4\pi} A_{\pi\pi} (m_{\pi\pi}^2, t', t) \frac{\bar{u}(p_d)\, \gamma_5 \, u(p_b)}{t-m_\pi^2} \quad (1.1)$$

where G is the pion-nucleon coupling constant $(G^2/4\pi = 14.6)$, $t' = (p_1 - p_a)^2$

is related to the $\pi\pi$ scattering angle in the $\pi\pi$ rest frame, and t is the mass-

squared of the exchanged particle (= the momentum transfer to the nucleon).

For $t=m_\pi^2$, $A_{\pi\pi}(m_{\pi\pi}^2, t', m_\pi^2)$ is the amplitude for real $\pi\pi$ scattering and is

referred to as the "on-shell amplitude". The "off-shell amplitude"

$A_{\pi\pi}(m_{\pi\pi}^2, t', t \neq m_\pi^2)$ is the amplitude for scattering of a real pion by a

virtual π of mass $\sqrt{t}$. The suggestion of Goebel, and Chew and Low was that

if the OPE amplitude is dominant for small momentum transfers in the

physical region, one may extrapolate $A_{\pi\pi}^{OFF}(m_{\pi\pi}^2, t', t)$ into the

non-physical region to determine $A_{\pi\pi}^{ON}(m_{\pi\pi}^2, t', m_\pi^2)$. For this reason, and also to try to understand the production dynamics of particle interactions, a great deal of effort, both theoretical and experimental, has been spent studying the extent to which reactions such as $\pi N \to \pi\pi N$, $KN \to K\pi N$, $NN \to N\pi N$ and $\bar{N}N \to \bar{N}\pi N$ are explained at low momentum transfers by pion exchange.

A comparison of experimental measurements with the calculated OPE differential cross section for a variety of quasi-two-body interactions, and over a range of incident energies, indicated that the model, in its simplest form, failed rather badly.[5] For example, the predicted cross section for $\pi^+ p \to \rho^+ p$ at 2.75 GeV was too large, even at small t, and failed to fall off with increasing momentum transfer as fast as the data. Similar discrepancies were observed when the model was compared with measurements of $NN \to NN^*$ and $KN \to K^*N^*$. The fact that the experimental differential cross section falls off more steeply than predicted by the model, is a statement that the contribution of low partial waves in the model is too large. A partial wave expansion of the OPE amplitude confirms this; in fact, the contribution of simple OPE for low partial waves is so large as to violate unitarity.

Two primary kinds of modifications to OPE have been introduced without changing the basic model: one is to introduce form factors at the vertices[5-8] (and perhaps also in the propagator), and the other is to take into account the effects of absorption.[9-13] Since any particular reaction channel, e.g., $\pi^- p \to \pi^+ \pi^- n$, is a small part of the total cross section of the initial particles, a proper treatment of that channel must take into account all the other channels open to the initial state. A complete solution to this coupled-channel problem is at the moment not possible, but an approximate calculation may be made by assuming that the only influence of the competing channels on

the reaction of interest is to absorb part of the initial wave function.[†] The

effect of this absorption is to substantially reduce the contribution of the

low partial waves to the reaction of interest, thus reducing the overall cross

section and collimating significantly the production angular distribution.

Reasonably good agreement of this absorptive one-pion-exchange model

(OPEA) with experiment has been obtained.[9-17]

A number of prescriptions have been suggested for introducing t-

dependence in the vertex functions. Of these, the form factors introduced

by Dürr and Pilkuhn[6] (DP) and an "improved" set introduced by Benecke and

Dürr[7] (BD) have enjoyed the greatest success. In particular, Wolf[8] has

demonstrated that OPE with Benecke-Dürr form factors provides a rather

good description of the measured differential cross sections for the reactions

$$\bar{p}p \to \overline{\Delta^{++}}\Delta^{++}$$
$$pp \to \Delta^{++}n$$
$$\pi^+ p \to \rho^0 \Delta^{++}$$
$$\pi^- p \to \rho^0 n$$

(1.2)
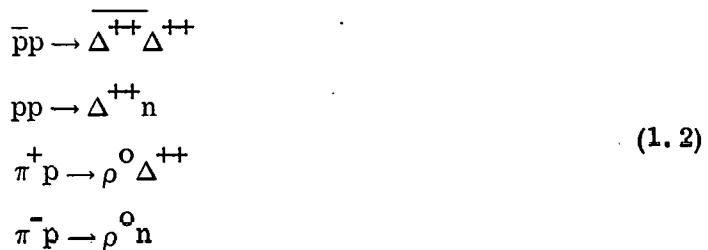
for momentum transfers < 1 $(GeV/c)^2$ and for an energy range of 1.6 - 16 GeV.

He also points out that for small momentum transfers the DP and BD form

factors are equivalent.

Further evidence in support of the premise that the one-pion-exchange

amplitude is dominant for small momentum transfers is provided by a

---

[†]A similar absorption results from interaction of the final state particles.

- 4 -

comparison of the proton induced reactions

$$pp \rightarrow \Delta^{++}(p\pi^-) \tag{1.3a}$$

$$\Delta^{++}(n\pi^-\pi^+) \tag{1.3b}$$

$$\Delta^{++}(p\pi^-\pi^0) \tag{1.3c}$$

$$\Delta^{++} + \text{(all neutrals)} \tag{1.3d}$$

with the pion induced reactions

$$\pi^- p \rightarrow \pi^- p \tag{1.3e}$$

$$\pi^- p \rightarrow n\pi^-\pi^+ \tag{1.3f}$$

$$\pi^- p \rightarrow p\pi^-\pi^0 \tag{1.3g}$$

$$\pi^- p \rightarrow \text{all neutrals} \tag{1.3h}$$

According to OPE, each of the reactions (a) - (d) is proportional to the amplitude for the scattering of the initial proton and a virtual pion (from the dissociation $p \rightarrow \Delta^{++}\pi^-$) to the inelastic states in parentheses. That is, each of reactions (a) - (d) is proportional to the off-shell amplitude for reactions (e) - (h). Colton et al.[18] have studied reactions (a) - (d) at 6.6 GeV and have compared them to the known on-shell reactions by plotting the relative cross sections

$$\frac{\sigma(\Delta^{++}, \text{neutrals})}{\sigma(\Delta^{++}, \pi^- p)}, \quad \frac{\sigma(\Delta^{++}, p\pi^-\pi^0)}{\sigma(\Delta^{++}, p\pi^-)}, \quad \frac{\sigma(\Delta^{++}, n\pi^-\pi^+)}{\sigma(\Delta^{++}, p\pi^-)}$$

as a function of the effective mass of the non-Δ^{++} final state, and for momentum transfers to the $\Delta^{++} < .2$ (GeV/c)^2. Their results agree reasonably well with the same ratios for reactions (e) - (h). Ellis et al.[19] have determined similar ratios for their 28.5 GeV pp data and find rather impressive agreement with the analogous ratios for the on-shell data.

Colton et al.[20] have also studied the angular distribution of off-mass-shell $\pi^- p$ elastic scattering in the reaction $pp \rightarrow \Delta^{++}p\pi^-$. A comparison,

at small momentum transfers, of the Legendre coefficients for their data with the well established coefficients for $\pi^- p$ elastic scattering yields good agreement.

Each of the above comparisons was made in the physical region. Z. Ming Ma et al.[21] have used OPE with DP form factors to extrapolate the off-shell $\pi^+ p$ elastic cross section, as determined from $pp \to p\pi^+ n$, to the pion pole. Their results agree well with on-shell $\pi^+ p$ elastic scattering.[22]

Finally, the presence of one-pion-exchange, independent of whether it can be considered to be the dominant contribution or not, is strongly indicated by the existence of narrow structure in the differential cross sections of reactions such as np charge-exchange[23] and single-pion photo-production.[24] For each of these reactions, a sharp rise is observed in the differential cross section for momentum transfers less than m_π^2.

Despite the impressive amount of evidence mentioned above which supports the validity of OPE, several qualifications should be noted. Although Wolf's OPE-BD fits reproduce beautifully the available data on the differential cross sections and energy dependence of the four reactions mentioned above, some caution is warranted in drawing conclusions. In particular, it has been pointed out that it is difficult to identify the type of particle exchanged solely on the basis of the energy dependence and differential cross section (if relatively featureless) of the reaction.[25] Some reactions, e.g., $\gamma p \to \pi^0 p$, have a $1/p_{inc}^2$ energy dependence even though π-exchange is not allowed; and, because of their highly peripheral nature, many reactions have similar differential cross sections irrespective of the particle exchanged. In addition, the decay angular correlations predicted by form-factor-modified OPE (OPEF) for quasi-two-body processes are those of the unadorned OPE

model, and are therefore incorrect for several reactions.

The absorption model reproduces reasonably well the available data on the angular correlations in $\pi^- p \to \pi^+ \pi^- n$ for $\pi\pi$ effective masses in the rho region.[14-17] However, a close examination of the data indicates that the sharp forward dip in $\rho_{00} - \rho_{11}$ which is expected from OPEA has not been observed either at 4 GeV,[15] or at 8 GeV.[16] In addition, the expected turnover in the differential cross section at low momentum transfers has not been established. There is an indication of it at 11 GeV,[17] but a study of the 8 GeV data[26] at small momentum transfers reveals no sign of any structure.

Another feature of importance is the following: both elementary OPE and OPEF predict that the differential cross section for transversely polarized ρ mesons in $\pi^- p \to \rho^0 n$ should vanish at t=0. If absorption effects are included, however, this is expected not to be the case; on the contrary, a sharp rise in the transverse rho cross section, $2\rho_{11} \frac{d\sigma}{dt}$, is predicted for momentum transfers less than m_π^2. The vector dominance model[27] also predicts a peak in this cross section analogous to that observed in single-pion photoproduction. Whether or not $2\rho_{11} \frac{d\sigma}{dt}$ vanishes as $t \to 0$ is therefore of interest in testing the vector dominance model, and in establishing whether or not factorization is rigorously observed, since it is this facet of OPEF that requires the cross section to vanish. It is an important question for Chew-Low extrapolations as well since most extrapolations to date have required that $\frac{d\sigma}{dt}$ vanish at t=0.

In conclusion, we note that although there is a large body of evidence supporting the premise that OPE is the dominant production mechanism of $\pi^- p \to \pi^+ \pi^- n$ and many other reactions at small momentum transfers, the

detailed behavior of $\pi^- p \to \pi^+ \pi^- n$ at high energies and particularly at low

momentum transfers is not known. The absorptive one-pion-exchange

model makes definite predictions about the behavior of the differential

cross section and the density matrix elements for this reaction, [11,13,28-31]

and it is to a measurement of these quantities that this experiment addresses

itself. [32]

In addition to the rather specific studies of the $\pi^+ \pi^- n$ system that were

discussed in the preceding section, the experiment also investigated

$\pi^- p \to K^+ K^- n$ and $p \bar{p} n$. These studies were of a more general nature since

relatively little information is available on these reactions. Because of the

low cross sections and the difficulty in unambiguously identifying the kaon

or proton, the reactions have proven difficult to study in bubble chambers,

particularly at high energies. It has been anticipated, however, that

information on these reactions should prove very fruitful in terms of furthering

the understanding of particle resonances, including their quantum numbers,

decay modes, and production mechanisms. [33]

Structure that is known to exist in the $(K\bar{K})^0$ system and to be produced

in $\pi^- p$ interactions includes the ϕ meson, the f^0 and A_2^0, the f' (1514) and the

S* (1070), which has been alternatively explained as a resonance or in terms

of a complex scattering length. With the exception of the ϕ, most of the

evidence for the $K\bar{K}$ states comes from study of the $K_1^0 K_1^0$ system. [34-37]

Previous studies of the $K^+ K^- n$ system include the bubble chamber experiments

of Dahl et al. [38] and Boyd et al. [39] at energies below 4 GeV and the spark

chamber experiment of Hyams et al. [40] at 11 GeV. The only structure that is

unambiguously observed in these experiments is the ϕ meson, which is found

to be produced with a rather small cross section. The measurements are

statistically limited, and since there is only the one measurement above 4 GeV, the energy dependence is relatively unknown. It is therefore interesting to measure ϕ production at a still higher energy.

There has been considerable activity studying possible $p\bar{p}$ resonances, particularly since the observation by Abrams et al.[41] of structure in the I=0 and I=1 total $\bar{p}p$ cross section, coupled with the missing mass experiment of Chikovani et al.[42] which reported the existence of resonances at 1929, 2195, and 2382 MeV (the S, T, and U mesons). The structure observed by Abrams et al. may be explained by the existence of resonances at 2190, 2345, and 2380 MeV; two of the masses therefore correspond to the masses observed by Chikovani et al.; however, the widths required to explain the $\bar{p}p$ data are much broader than those reported in the missing mass experiment. Further evidence of possible structure in the $p\bar{p}$ system is provided by $\bar{p}p$ backward elastic scattering[43] and $\bar{p}p$ annihilation into the various decay channels such as $\pi^+\pi^-$, K^+K^- and $\rho^0\rho^0\pi^0$.[44] The CERN Boson Spectrometer has also reported missing mass resonances near 2600 and 2800 MeV.[45]

If such structure does couple significantly to the $p\bar{p}$ system, then one of the most direct ways of observing it should be in a reaction such as $\pi^-p\rightarrow\bar{p}pn$ where high mass states that are produced can decay into $p\bar{p}$. Several runs in this experiment, therefore, concentrate on this channel, with the hope of elucidating any structure in the $p\bar{p}$ system that might exist, and of determining the strength of the coupling.

The experiment that is described in the ensuing chapters used a wire spark chamber spectrometer to study 15 GeV/c π^-p interactions and was performed at the Stanford Linear Accelerator Center during 1970. Although the primary objective of the initial data runs was a measurement of the low

momentum transfer behavior of $\pi^- p \to \pi^+ \pi^- n$, the trigger condition included all events in which two charged particles were detected by the spectrometer. Consequently, data was also obtained on other reactions such as $\pi^- p \to \pi^+ \pi^- \Delta^0$, $\pi^- p \to K^0(\Lambda, \Sigma)$, $\pi^- p \to K^*(\Lambda, \Sigma)$ and $\pi^- p \to K^+ K^- n$. A large, multicell Čerenkov counter enabled separation of the $\pi\pi$, πK, and $K\bar{K}$ ($p\bar{p}$) final states. During a second set of runs in late 1970 the pressure of the Čerenkov counter was increased so that $p\bar{p}$ states could be separated from the others.

This thesis describes in detail the measurement and analysis of the $\pi^+ \pi^- n$ state, for $\pi\pi$ effective masses in the rho region, and its interpretation in terms of absorptive one-pion-exchange. In addition, the current results of the $K^+ K^-$ and $p\bar{p}$ data are presented, although the analysis of these channels is still in progress.

A description of the apparatus is presented in Chapter 2, with the exception of the Čerenkov counter which is discussed in detail in Chapter 3. Its combination of hodoscopic properties and pulse height information provide it with a versatility that is very powerful in identifying multibody final states. Event reconstruction and data processing are discussed in Chapter 4, along with results on the spectrometer performance. Chapter 5 presents the dipion density matrix elements and differential cross section and discusses the raw data distributions and analysis from which they were determined. Derivation of the differential cross section for transversely and longitudinally polarized rhos is presented in Chapter 6, together with a comparison of our results with OPEA. Finally, Chapter 7 presents the observed data on $K^+ K^- n$ and $p\bar{p}n$.

CHAPTER 2

EXPERIMENTAL APPARATUS

A. General Description

The design of the apparatus was largely dictated by the various objectives of the experiment, the primary one being an accurate measurement of the small momentum transfer behavior of $\pi^- p \rightarrow \pi^+ \pi^- n$. In particular, the desired combination of high statistics, good t resolution, and the ability to unambiguously identify $\pi^+ \pi^-$ states--all at high energy--required that a spark chamber spectrometer or similar apparatus be used, rather than a bubble chamber. Because of their high data rate capability, good spatial resolution, and relatively simple readout, wire spark chambers with magnetostrictive readout were employed as the primary detectors. Other features of the apparatus were also motivated by the above requirements: an accurate measurement of the momentum transfer demanded that the direction of the incident pion as well as that of the decay pions be well determined; the separation, on the basis of missing-mass resolution, of $\pi^+ \pi^- n$ states from those in which additional particles were produced entailed an accurate knowledge of the incident pion momentum; and the separation of $\pi^+ \pi^-$ states from those consisting of $K\bar{K}$, $p\bar{p}$, or πK required a large-aperture Čerenkov counter.

A schematic diagram of the apparatus is shown in Fig. 2. The pion beam, which was incident on a 1 m long liquid-hydrogen target, was defined just upstream of the target by a 2.54×2.54 cm counter hodoscope. In addition, three scintillation counter hodoscopes in the beam line measured the momentum of the incident π^- and determined its horizontal and vertical projected angles. The target was surrounded on four sides by scintillator-Pb sandwich counters which detected particles that escaped the rest of the spectrometer.
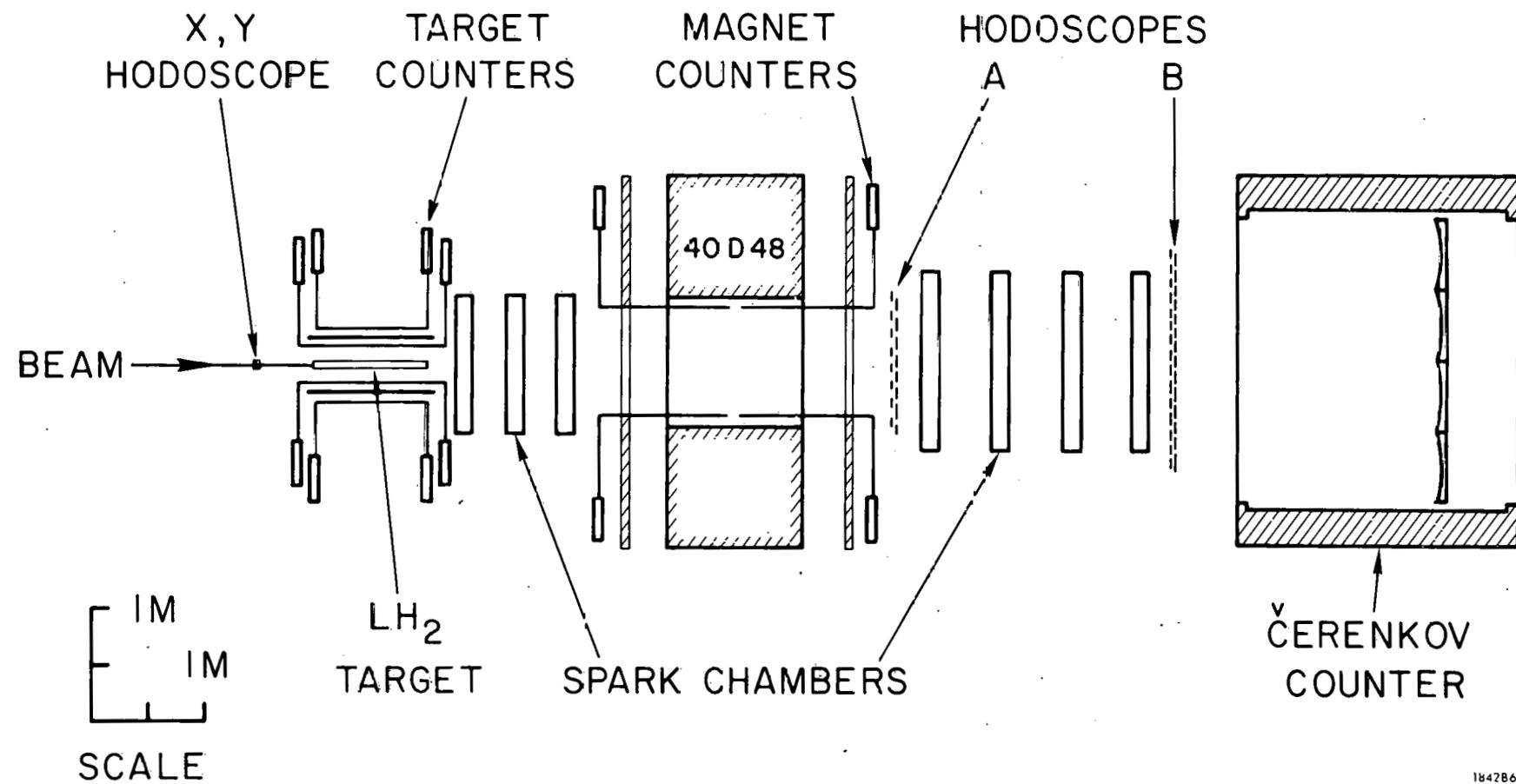
FIG. 2--Schematic diagram of the experimental apparatus.

Immediately downstream, three wire spark chambers measured the production angles of the forward-produced particles. Following these chambers, there was a momentum-analyzing magnet and a second group of four chambers to determine the momenta of the detected particles. The inner faces of the magnet gap were lined with scintillation counters to veto events in which a particle intersected the pole faces. Two "picket fence" type counter hodoscopes, one at each end of the downstream package of spark chambers, determined the number of charged particles which had been detected. Finally, a large, wide-aperture Čerenkov counter distinguished π mesons from heavier particles.

Because the pion beam passed through the main apparatus and because of the high instantaneous fluxes ($\approx 10\pi^-/1.6\ \mu s$), it was necessary to deaden a small region of the chambers by the installation of a polyurethane plug. The two trigger hodoscopes downstream of the magnet were also deadened in the region of the beam. This desensitized region of the apparatus prohibited the observation of very asymmetric events, i.e., events in which one of the particles comes forward at a very small angle with respect to the incident π^-, while the other particle is produced with a wide angle.[*] The exact nature of these dead spots and the extent to which they affected the experiment are discussed in the detailed descriptions of the spark chambers and hodoscopes, and in Chapter 5.

---

[*] It should be noted, however, that the size of the magnet aperture, and the fact that particles with momenta smaller than ≈ 1.5 GeV/c are swept out of the spectrometer system, also prohibit the observation of these decays. Hence, the detection efficiency is not substantially altered by the presence of the plugs.

The positions of the chambers, particularly the upstream ones, were determined by maximizing the efficiency of the apparatus for detecting the final state particles without sacrificing the required resolutions. The accuracy to which the production angles of the detected particles can be measured improves as the spacing of the front (upstream) chambers is increased; the momentum resolution of the apparatus is also improved by increasing the chamber spacing, both upstream and downstream of the magnet. On the other hand, the detection efficiency of the spectrometer is maximized by collapsing the apparatus so that the target and back chambers are as close to the magnet as possible.

The trigger condition required one incident beam particle (as defined by the small hodoscope upstream of the target), two or more charged particles downstream of the magnet, and no signal from the magnet veto counters. The magnet counters served a dual function: 1) they vetoed higher multiplicity events which would otherwise have dominated the trigger rate, and 2) they vetoed two-particle events which would have been distorted by interaction of one of the particles in the magnet iron.

Information from the counters surrounding the target was used only off-line; this allowed the simultaneous acquisition of data on other interesting channels, such as $\pi^+\pi^-\Delta^o$, and also prevented the following bias: For a substantial fraction of $\pi^+\pi^-n$ events ($\approx 25\%$), one of the target counters was fired by a delta ray produced in the target or by the recoiling neutron. Since the probability of this occurring may depend on the momentum transfer to the neutron and also on the decay angles of the π^+ and π^-, inclusion of the target counters in the trigger condition could bias the data sample. Use of the information offline avoided this problem by allowing greater flexibility in the

cuts which were used to separate $\pi^+\pi^-$n events from those in which additional particles were produced.

Information from the Čerenkov counter was also used only offline to permit greater flexibility in the cuts used to separate $\pi^+\pi^-$ and K^+K^- final states, and to allow a detailed study of the results of these cuts.

Data recording, monitoring of the apparatus, and online analysis were performed by an IBM model 1800 computer. A detailed description of each segment of the apparatus and a discussion of the monitoring and data recording is presented in the following sections.

B. Beam

The π mesons which comprised the secondary beam were produced by interaction of the SLAC primary electron beam, at an energy of 18-19 GeV, with a 1 radiation length beryllium target. Pions with a production angle of $\approx 1^\circ$ were focussed by quadrupoles 6Q1, 6Q2 (see Fig. 3) on to the point labelled F1 (the first focal point) where there was a collimator, and a Pb absorber to eliminate electrons. Only a rough momentum definition was achieved at this point because of the limited dispersion of the bending magnet 6D1. Quadrupoles 6Q3, 6Q4 refocussed the beam and the combination of the bending magnet 6D2 and a 6.3 mm wide collimator at F2, the second focal point, provided the primary momentum definition of the beam. This first part of the beam was achromatic and an rf-separator just upstream of F2 provided separated π^- and K^- beams.

At F2 the beam line split. A pulsed magnet, capable of operating at rates up to 180 pps, switched the beam on a pulse-by-pulse basis into either of two beam lines. When the magnet was OFF, the particles passed undeflected into the beam line used by the SLAC 82" bubble chamber. When the magnet was

- 15 -

BEAM DUMP

BEAM SWITCH YARD

END STATION "C"

TARGET

ELECTRON BEAM

e^-

π^- l°

6Q1,2 6D1

F1

K°

rf SEPARATOR

6Q3,4 6D2

CONTINUED

F2

BELOW

STREAMER CHAMBER

K_O

82" HBC

H_2 TARGET

MAGNET

BEAM
Č COUNTER

Č COUNTER

F2

IID3.5

IIS1

π, K

IID5.3

SPARK CH.

IID2,3

IIQ1 IIQ2

4° IIS2

IID4

IIQ3 IIQ4

IIC5 IIQ5 IIQ6

XY
HODOSCOPE

DATA AND
COMPUTER
BLDG

PULSE
MAGNET

P HODOSCOPE

θ,ϕ
HODOSCOPE

——— 100 ft. ———

Q QUADRUPOLE

D BENDING MAGNET

S SEXTUPOLE

COLLIMATOR

1998C5

FIG. 3--Diagram of the incident-pion beam. A description is presented in the text.

pulsed ON, the particles were deflected by an angle of .9° into septum magnets 11D2, 11D3 which deflected the particles by an additional 1.9^O into beam line 11. It was therefore possible to concurrently run a K$^-$ beam to the bubble chamber and a π^- beam to this experiment. Beam line 11 was independently achromatic, and used F2 as the source of particles. Two scintillation counters S1 and S2 monitored the flux at this point. Quadrupoles 11Q1, 11Q2 focussed the beam onto the counter hodoscope labelled P HODOSCOPE while 11D4 provided the dispersion necessary for a second, more accurate determination of the beam momentum. The calculated first-order dispersion in the beam at this point was 11.7 mm per $\frac{\Delta p}{p} = 1\%$, and the counters in this hodoscope determined the beam momentum to $\pm .3\%$. Quadrupoles 11Q3, 11Q4 reverse the sign of the dispersion from 11D4 so that the beam is achromatic after the final bending magnet, 11D5. The last set of quadrupoles 11Q5, 11Q6 focus the beam onto the target. Two small vertical steering magnets 11D3.5 and 11D5.3 corrected for the deflection introduced by the separator. The θ and φ hodoscopes, shown just downstream of 11Q6, together with the vertex of an event as determined by the spectrometer, measure the horizontal and vertical angles, respectively, of the π^- at the target to $\pm .5$ mr. The construction of the θ, φ, and P hodoscopes is described in section C.1.

The momentum and angular spectra of the beam, as measured by the P, θ, and φ hodoscopes, are shown in Fig. 4. Although the beam nominally had a momentum passband of $\pm 2.5\%$ and an angular passband of ± 2.5 mr horizontally and ± 3.5 mr vertically, the FWHM of the distributions were substantially smaller than these values, as is evident from the figure. The power of the primary electron beam was limited to 35 kW at the π production target for reasons of radiation safety; it was therefore necessary that such

MCMENTUM
DISTRIBUTION

ANGULAR
DISTRIBUTION
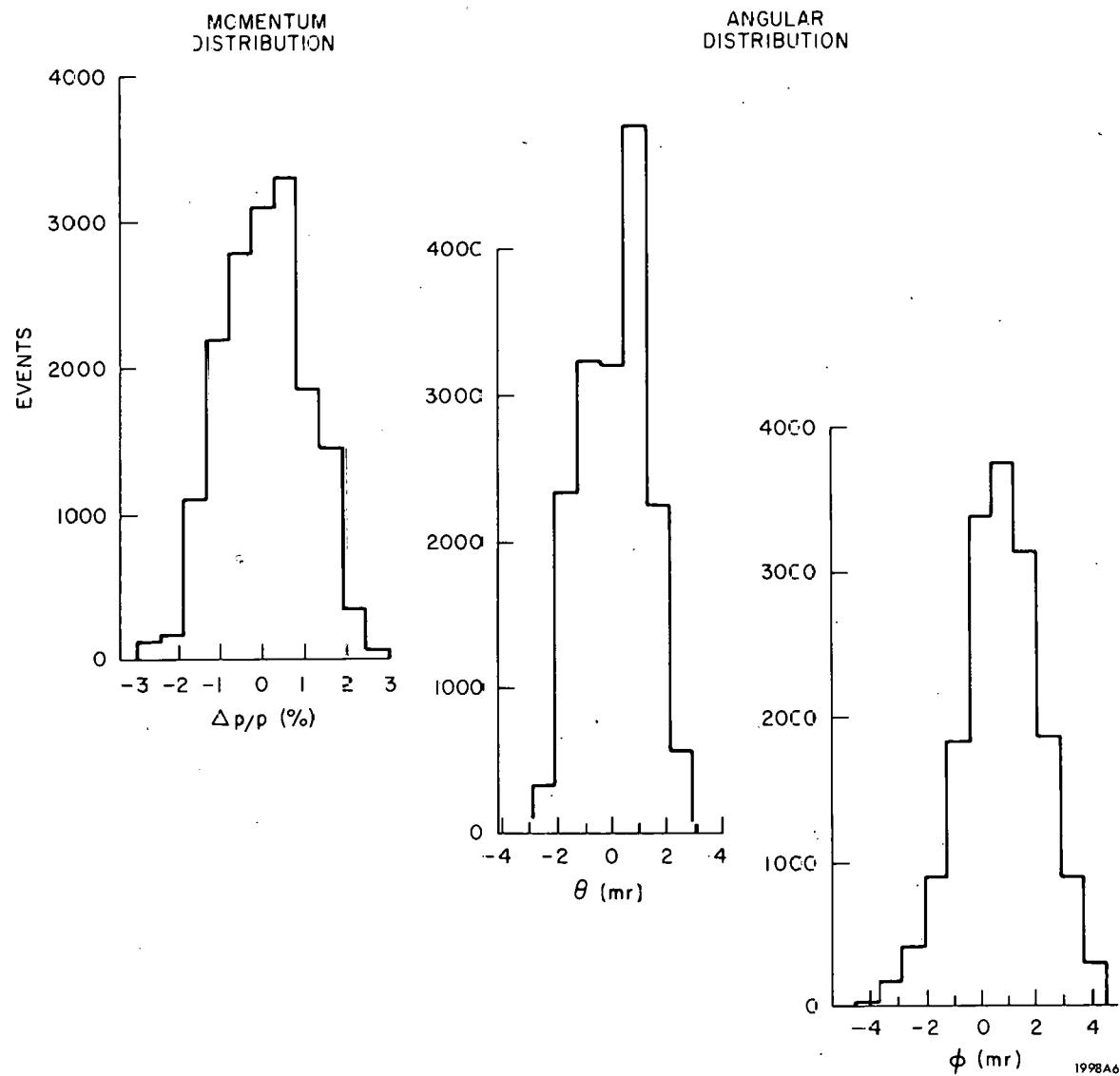
FIG. 4--Momentum and angular distributions of the incident π^-, as measured by the beam hodoscopes.

a large phase space be accepted in order to obtain sufficiently intense particle fluxes. This resulted in significant second order effects. Two sextupoles, 11S1 and 11S2, corrected for the largest of these effects in order to reduce the size of the beam at the target.[46]

The contamination of electrons in the beam was measured, by means of a shower counter, to be less than .2% at 15 GeV/c when a 1.27 cm lead absorber was installed at F1; this was the normal running condition. The μ-contamination of the beam was measured by a μ-telescope just downstream of the spectrometer. It was found to be 5 ± .5% at this point; when corrected for the π decay between the target and the point of measurement, this implied a contamination at the target of 3.9 ± .4%. The percentage of K^- and $\bar{p}$ in the beam was determined with a Čerenkov counter to be < .3%.

C. Counters and Hodoscopes

1. Beam Hodoscopes

. Each of the three beam hodoscopes was constructed in a similar fashion. Parallel strips of scintillator measured the position of the incident particle in either the x or y direction;* each counter overlapped one third of the adjacent counter on either side (see Fig. 5). By decoding the information on which counters fired, it was therefore possible to divide the position measurement into 2n-1 bins, even though only n counters were employed. This technique decreased the required number of phototubes and associated

---

*The coordinate system with respect to which the spectrometer is described is a right-handed system, with the z-axis anti-parallel to the incident beam and the y-axis vertical; the origin is taken to be the center of the magnet.

MOMENTUM HODOSCOPE

I 2 3 4 5 6

BEAM

SIDE VIEW

BEAM

2
3
4
5
6

COUNTERS

1
2
3
4
5
6
7
8
9
10
11

6.3mm

$$\frac{\Delta p}{p} = .54\%$$

MOMENTUM
BINS

TOP VIEW

THETA HODOSCOPE

I 2 3 4

BEAM

SIDE VIEW

BEAM

1
2
3
4

COUNTERS

1
2
3
4
5
6
7

12.7mm

$\Delta\theta = .88$mr

ANGULAR
BINS-θ

TOP VIEW

PHI HODOSCOPE

I 2 3 4 5 6

BEAM

TOP VIEW

BEAM

1
2
3
4
5
6

COUNTERS

1
2
3
4
5
6
7
8
9
10
11

12.7mm

$\Delta\phi = .88$mr

ANGULAR
BINS-ϕ

SIDE VIEW
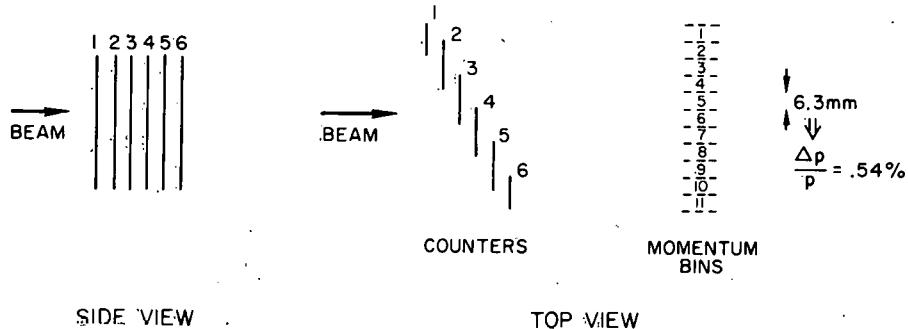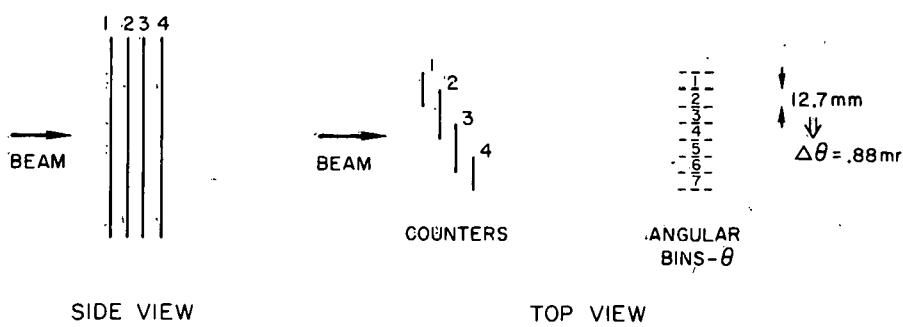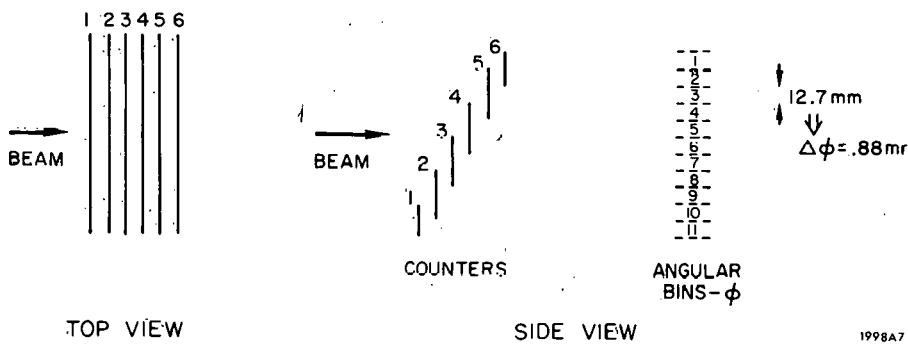
1998A7

FIG. 5--Illustrative diagram of the P, θ, and φ hodoscopes. The dashed
lines indicate the momentum and angular bins of the hodoscopes,
while the solid lines show the layout of the individual counters.

electronics while, at the same time, eliminating the problem of cracks between counters which is present if the counters are butted edge to edge.

The P hodoscope consisted of six counters, the central four of which were $19 \times 51 \times 3.2$ mm; the counters on each edge were $12.7 \times 51 \times 3.2$ mm. The effective bin width was therefore ≈ 6.3 mm. Since the calculated momentum dispersion of the beam was 11.7 mm per $\frac{\Delta p}{p} = 1\%$ at this point, the P hodoscope was theoretically capable of resolving the beam momentum to $\pm .27\%$. This agrees well with the observed momentum resolution of $\approx .3\%$.

The θ and φ hodoscopes consisted of four and six counters respectively, the θ hodoscope measuring the horizontal position of the particle and the φ hodoscope measuring the vertical position. The central counters were $38 \times 152 \times 3.2$ mm; the the edge counters $25.4 \times 152 \times 3.2$ mm so that the bin width was uniformly 12.7 mm. This ± 6.3 mm uncertainty in the position measurement at the θ, φ hodoscopes together with the 15 m spacing between the hodoscopes and the hydrogen target imply an angular resolution of $\pm .5$ mr (including multiple scattering). The error in the x-y vertex position of a reconstructed event was negligible compared to the ± 6.3 mm uncertainty at the hodoscope.

2. Target Counters

The scintillator – Pb sandwich counter array surrounding the target was constructed in the shape of a four-sided box encircling the target, with the upstream and downstream sides open. Each side was approximately 1 m long and consisted of three layers: 9.5 mm scintillator – 12.7 mm Pb – 9.5 mm scintillator. Both the inner and outer scintillators were viewed by two phototubes, one at each end (upstream and downstream). It was therefore possible to tell for a given event not only whether or not one of the target counters fired, but also whether it was an inner counter, an outer counter, or both. This information was useful from the point of view of understanding what kinds of particles were counting (e.g., delta rays, photons, neutrons, or charged particles). The counter array was not designed in such a manner as to detect with high efficiency all the particles which escaped the spectrometer; however, it detected a sufficiently large number of those particles to allow a clean separation of $\pi^+\pi^-$n events. This is illustrated by Fig. 33 which is discussed in detail in Chapter 5.

3. Trigger Hodoscopes

The hodoscope of counters just upstream of the target, which we refer to as the XY hodoscope, consisted of four 12.7 × 12.7 mm pieces of scintillator arranged two by two so that they formed a square 25.4 mm on a side (see Fig. 6). Each was viewed by a separate phototube. This square was surrounded by a larger piece of scintillator ≈ 12 cm in diameter, which is referred to as the RING counter. It was viewed by two phototubes. The counter array not only geometrically selected particles which lay within the central 25.4 × 25.4 mm area of the beam image, it also served to reject events in which two beam
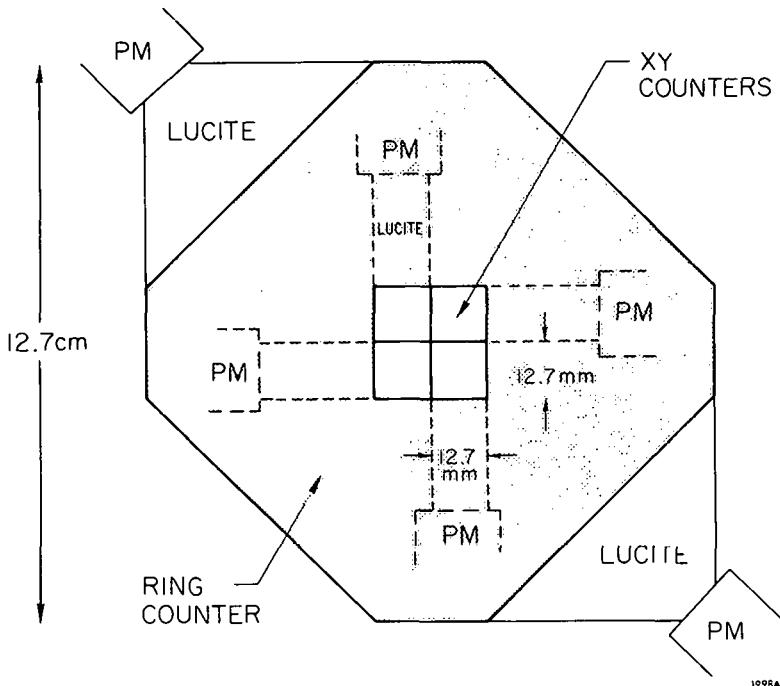
FIG. 6--Diagram of the XY and RING counters

particles were incident simultaneously (i.e., within ≈ 16 ns. For the average incident rate, this occurred ≈ 8% of the time).

The presence of more than one beam particle within the resolving time of the main strobe produced an ambiguous signature in each of the beam hodoscopes, thereby rendering it impossible to determine the correct momentum and angle of the π^- which interacted. Those events in which two particles were incident were readily vetoed if the particles traversed different quadrants of the XY hodoscope or if one particle intersected the RING counter. If they intersected the same XY quadrant, the event could be rejected only if the particles were separated by > 11 ns; this subject is discussed in further detail in Section F.1 which describes the trigger electronics.

Downstream of the magnet, there were two "picket fence" hodoscopes, one in front of, and one behind, the group of chambers. Both hodoscopes consisted of vertical strips of scintillator, 6.3 mm thick and 5.7 cm wide, placed edge to edge. Each counter was viewed by a separate phototube. The A (upstream)

hodoscope contained 20 counters which were 50.8 cm long, while the B (down-stream) hodoscope contained 34 counters, each of which was 81.3 cm long. A section of the A hodoscope 5.7 × 6.4 cm and a section of the B hodoscope 5.7 × 9.1 cm were deadened by replacing the scintillator with lucite so that beam particles would not be counted.

After the initial data taking runs, it was determined that a substantial number of triggers were produced by interactions of beam particles in the lucite plug of hodoscope A. During subsequent runs, therefore, this section was removed entirely, and two separate counters installed above and below the resulting hole.

4. Magnet and Magnet Veto Counters

The gap of the momentum analyzing magnet was 1.0 m wide, 38 cm high and 1.22 m long. The $\int Bdl$ along a trajectory parallel to the z-axis was approximately 26 kGm and was quite uniform as a function of the x-y coordinates of the trajectory.

A three-dimensional mapping of the field allowed detailed studies of the momentum computation. Other than the slight variations in $\int Bdl$, which were explicitly calculated for each particle trajectory, the magnet was well approximated by a dipole field with thin-lens focussing.

The field was monitored to an accuracy of a few parts in 10^4 during the course of the run by a Hall probe, and was quite stable; only occasional trimming was required. The precise value of the magnetic field was adjusted initially so that the deflected beam passed through the center of the dead spaces in the downstream chambers and hodoscopes. When running at lower energies (e.g., 8 GeV), the field was adjusted accordingly to maintain this condition.

As mentioned above, the inner faces of the gap were lined with scintillation counters. Each of the side faces was covered by two counters 35.6 × 61 cm while the upper and lower faces of the gap, were each covered with four counters 48.3 × 61 cm. The thickness of the counters was .95 cm.

D. Spark Chambers

During the design and construction of the spark chambers in this experiment, two of the most important considerations were that the chambers be able to operate at high repetition rates (in excess of 100 cps) and with high multiple spark efficiency. Several of the most important developments towards achieving these objectives are discussed here along with a general description of the chambers. For a detailed description of the construction and electronics, the reader is referred to the articles of F. Bulos and H. Lynch.[47]

Each of the wire spark chambers (WSC) contained two gaps, each gap consisting of two parallel planes of wires, one at high voltage and the other at ground potential. The width of the gap was .95 cm. "Wire Cloth", consisting of parallel aluminum wires with cross-woven polyester fibers, was stretched to form the planes. In one gap the wires had the conventional x-y orientation, i.e., one plane of horizontal wires and one plane of vertical wires. The angles of the wires in the second gap were ± 30° with respect to the vertical. The wire spacing was 1.05 wires/mm.

An important feature of the chambers, which was necessary for achieving high multiple spark efficiencies, was that connection to the high voltage and ground planes was made, not with a low-resistance buss bar, but with a thin wire having the same resistivity as the wires in the planes. As is evident from Fig. 7, if a buss bar is used, the total resistive path is different for sparks
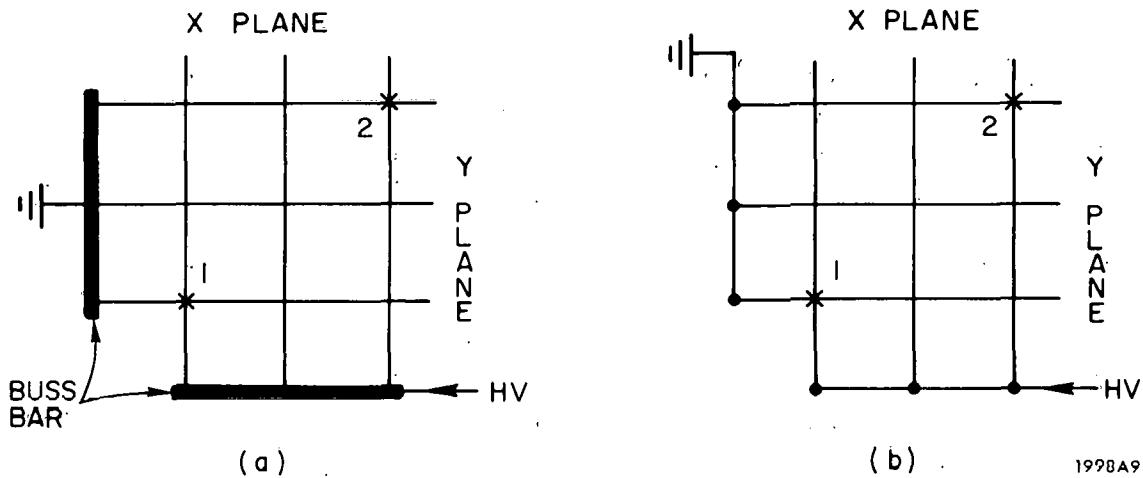
FIG. 7-- Illustration of the paths of unequal resistance for different spark
locations. (a) Connection to the high-voltage and ground planes
is made via a buss bar, resulting in different resistive paths for
sparks occurring at location (1) or (2). (b) Connection to the planes
is made with a wire possessing the same resistivity as the wires in
each plane. The total resistive path is independent of the spark
location.

occurring in different locations of the chamber. This leads to a lower spark

efficiency for some regions of the chamber than for others, and overall to a

low multiple-spark efficiency. When connection to the planes is made with a

wire of equal resistance, the resistive path is the same for all sparks, and

a high multiple spark efficiency may be obtained.

The high voltage on the spark chambers was supplied by thyratron pulsers,

capable of delivering a square 6 kV 225 ns pulse at rates in excess of 200 cps.

The chambers themselves were also rather thoroughly tested at rates in excess

of 100 cps, although the average data taking rate was ≈ 10 cps. A pulsed

clearing field was used to clear away "old" ions in order to prevent the reigni-

tion of previous sparks. This was particularly important at high repetition

rates. The clearing field consisted of a 50 volt dc component upon which

was super-imposed a 250 V pulse, 3 ms long and occurring after each beam

pulse.

A helium-neon gas mixture (90% neon, 10% helium) was used in the chambers; no quenching agents were necessary. The gas was recirculated and purified using a commercial system. It was observed that after the chambers had been run at high data rates for several days, their efficiency began to decrease. This was attributed to the fact that the purification system was not quite sufficient to keep the gas pure over long periods of time. Consequently, occasional purgings of the gas system were required to maintain a high chamber efficiency. Other than this, the chambers operated smoothly and reliably throughout the duration of the run.

Each plane of the chambers was read out with a magnetostrictive wand[48] and the spark location digitized by means of a 20 megacycle scaler. A brief discussion of this digitization is given in Section F.3.

The active area of the upstream chambers was 100 × 60 cm, that of the downstream chambers 150 × 100 cm. A small polyurethane plug was installed in each chamber to prevent sparking in the region of the beam. The diameters of the plugs were 3.6, 3.8, 3.8, 7.6, 8.1, 8.6, and 9.1 cm, progressively increasing for the chambers further downstream. The spatial resolutions of the chambers were for each plane, ± 1/3 mm for the smaller chambers and ± 1/2 mm for the larger. These figures are for experimental conditions and consequently include particles incident at all angles that are detected by the apparatus. Fig. 8 shows characteristic distributions of the deviations of the spark coordinates from the fitted track position. The chambers had a gap efficiency greater tha 98% for up to five sparks, as is shown in Fig. 9.

E. Čerenkov Counter

The Čerenkov counter was a large, wide-aperture detector which could be used either as a hodoscope of eight optically-independent Čerenkov cells or as

- 27 -
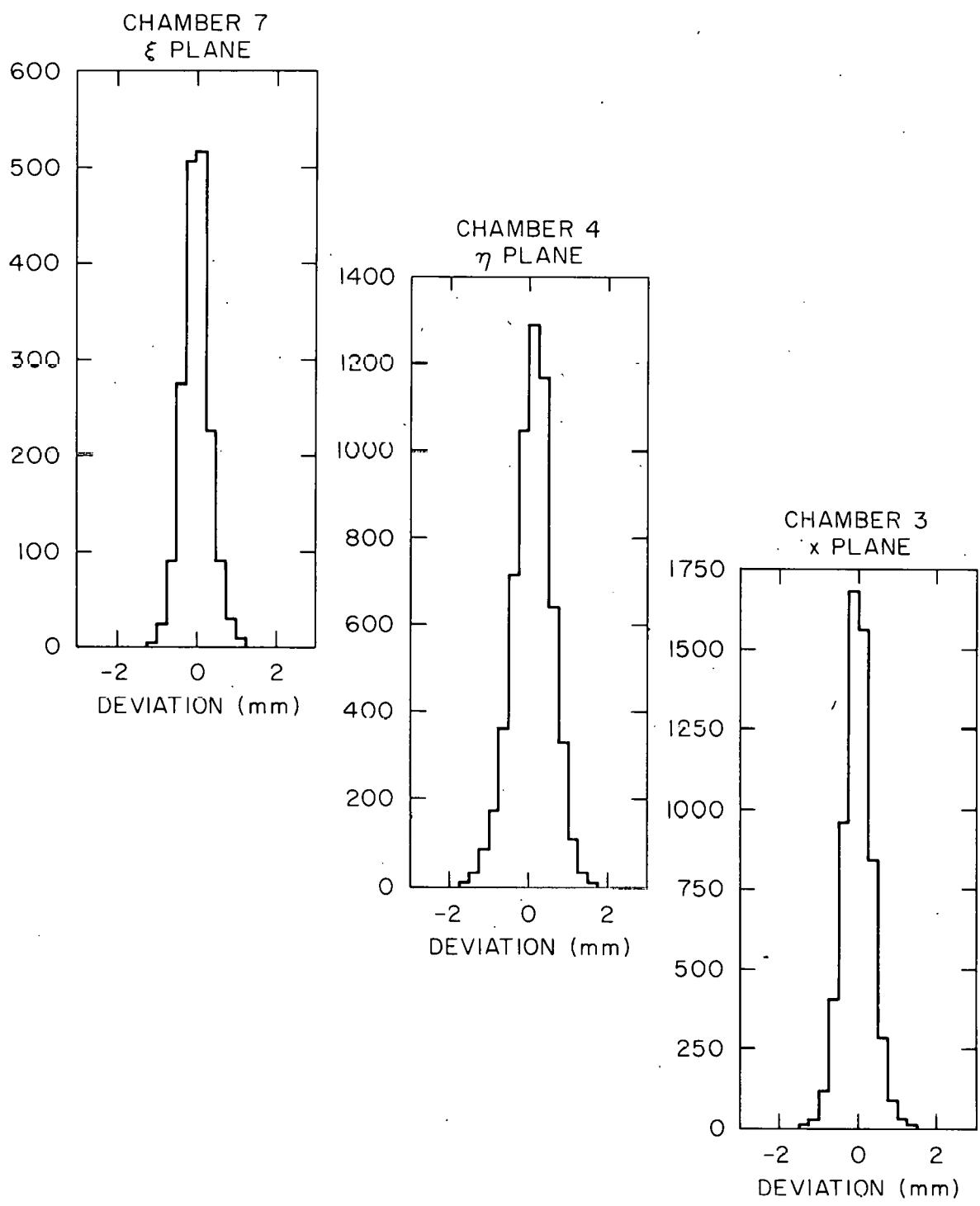
FIG. 8--Distributions of the deviation of the raw spark coordinates from the fitted tracks for several characteristic planes.

- 28 -
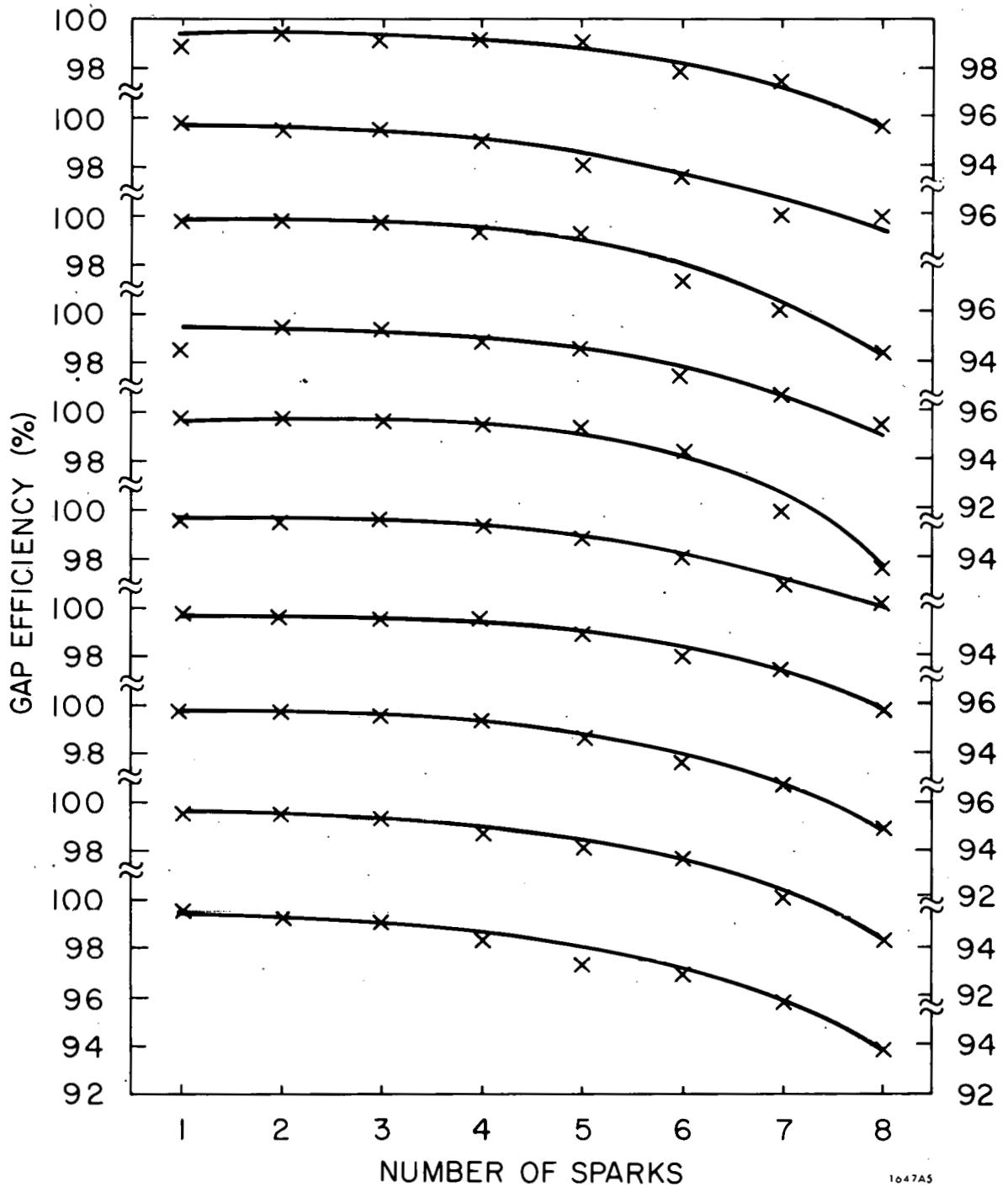
FIG. 9--Gap efficiency of the spark chambers as a function of the number of sparks per gap.

a single, uniformly efficient counter. Its construction, testing, and performance are discussed in detail in Chapter 3. For the purpose of selecting $\pi^+\pi^-$ events, it was used simply as a threshold counter; the output of each of the phototubes was summed by a high-input-impedance adder and the resulting signal (referred to as the "hardware sum") discriminated by a threshold discriminator. The $\pi^+\pi^-$ events were selected by requiring a signal from this discriminator.

The radiator was freon 12, chosen for its relatively high index of refraction and transmission of ultraviolet light. The operating pressure, during this experiment, was 1.25 atm; this provided a detection efficiency > 99% for pions above 4 GeV/c while K mesons did not become very efficient until their momenta reached 11 GeV/c (the threshold momentum for K's was 9.2 GeV/c).

The individual pulse heights for each of the eight phototubes were also recorded, thus providing offline the total pulse height from the counter for each event (ref. Section F.5, which describes the Čerenkov counter electronics). The distribution of this pulse height is shown in Fig. 10a for those events which could be interpreted as $\pi^+\pi^-$n, with .665 < $m_{\pi\pi}$ < .865 GeV, save for the Čerenkov test. Each event was required to have at least one particle into the counter with a momentum > 3.5 GeV/c. It is evident that there is a rather clean separation between the $\pi^+\pi^-$ events and the $K\overline{K}$ or $p\overline{p}$ events which fall in
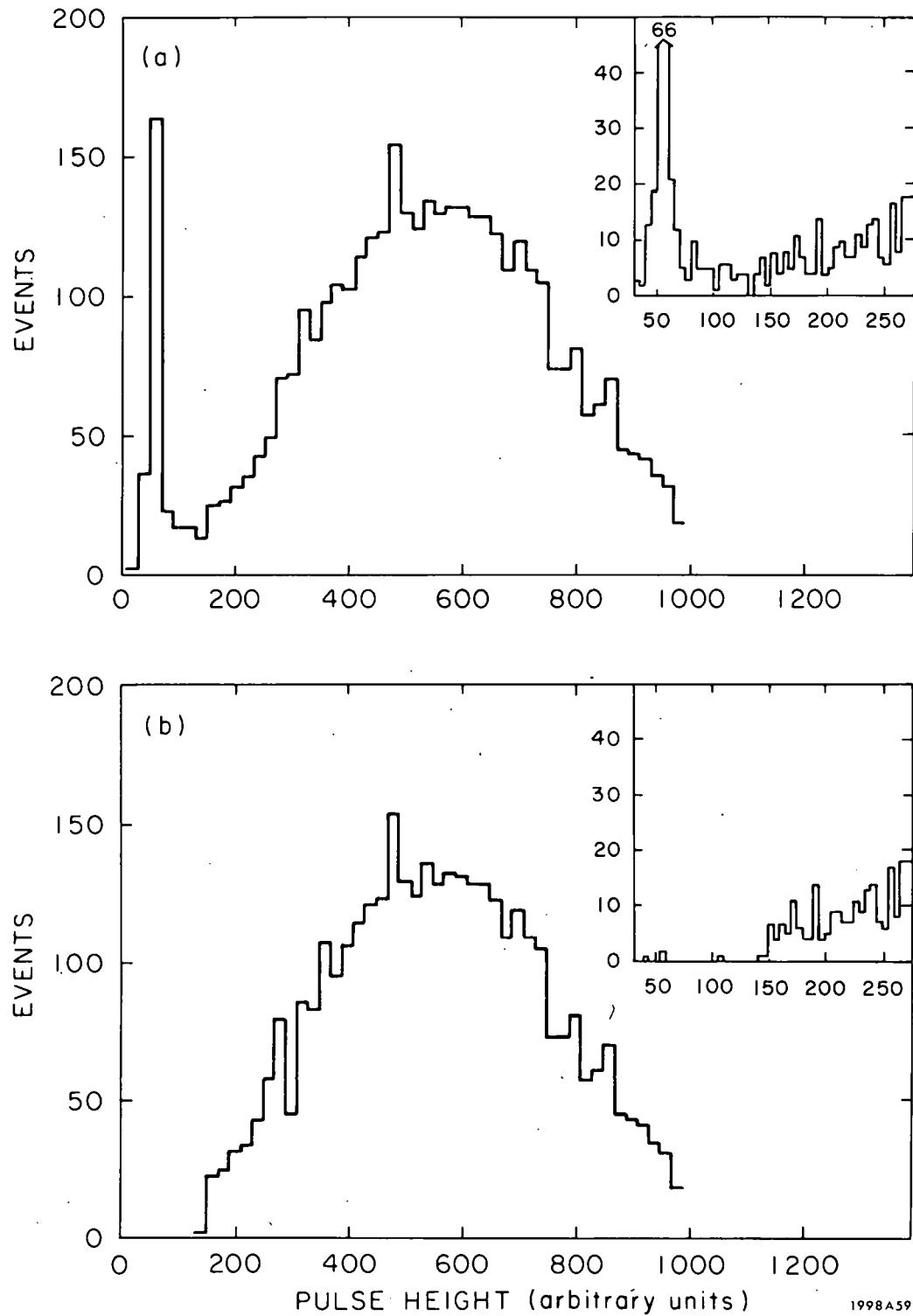
FIG. 10--Total pulse height distribution from the Čerenkov counter for events that could be interpreted as $\pi^+\pi^-n$ with $.665 < m_{\pi\pi} < .865$ GeV, save for the Čerenkov test. a) All events; b) events selected as $\pi^+\pi^-n$. The inserts show the same spectra on an expanded scale. Part (a) illustrates the clear separation of $\pi^+\pi^-$ and K^+K^- ($p\bar{p}$) events.

the sharp spike corresponding to zero pulse height.[*] Shown in Part (b) of

Fig. 10 is the same pulse-height spectrum for the events selected as $\pi^+\pi^-$.

F. Electronics

The primary functions of the electronics for the experiment were: a) to generate a master trigger for the apparatus when a potentially good event had occurred, b) to monitor the incident beam flux, and c) to record the relevant data from the spark chambers and counters. The electronics is most easily discussed in terms of the following sub-divisions:

1. fast trigger logic
2. gating system
3. WSC readout
4. strobed buffers for counter readout
5. Čerenkov counter electronics

1. Fast Trigger Logic

The function of the fast trigger logic was to decide, in the shortest time possible, whether or not an interesting event had occurred, and if so, to generate a master trigger for the rest of the apparatus. It was important that this decision be made quickly since a long delay before application of the high voltage to the spark chambers would allow substantial ion drift and therefore

---

[*] The reason the events which produced no Čerenkov light fall at channel number 50, rather than at 0, is that the stretcher amplifier for the signal from each phototube was set to have a slightly positive pedestal. This pedestal varied from unit to unit but the average value corresponded to channel number 6 or 7, thus resulting in a pedestal of ≈ 50 for the sum of all eight mirrors. The slight instability of the individual pedestals (variations in channel number of 2-3 units) produced a small but finite width of the zero-pulse-height spike.

lower the efficiency of the spark chambers. In addition, information as to which counters fired for a given event was obtained by forming a coincidence between the master trigger and the signals from each of the individual counters. A long delay in generating the master trigger necessitated delaying the signals from each of the counters. This additional delay (which is usually accomplished by increasing the length of the cable from the counter to the coincidence unit) broadens the width of the pulse and decreases the amplitude. When the delay is extensive, the effect can decrease the efficiency of the counters and increase the accidental rate. This consideration was particularly important for the signals from the Čerenkov counter, since the phototube pulses went directly to a gated (by the master trigger) stretcher amplifier unit. For the other counters, the length of the delay was less important, since the phototube signals went first to a discriminator, and the major delay was installed after the discriminator. The rack of fast electronics was placed close to the apparatus so that the cable length from the trigger counters to their respective discriminators was minimized.

The trigger was chosen to be:

1) one and only one good beam particle

2) no signal from the magnet veto counters

3) (≥ 1 counter fired in hodoscope A and ≥ 2 counters in hodoscope B) or

   (≥ 2 counters fired in hodoscope A and ≥ 1 counter in hodoscope B).

The motivations for 1) and 2) have already been discussed. Condition 3) was chosen for the following reasons: First, it was decided that the trigger condition would be two or more charged secondary particles to allow simultaneous acquisition of data on three-body final states. Second, for certain regions of $\pi\pi$ effective mass and angular distribution, the magnet focuses the

particles so that they pass through the same hodoscope counter. This is true for both hodoscopes A and B depending on the value of the $\pi\pi$ mass and the strength of the magnetic field. Implementation of a ≥ 2 requirement for both hodoscopes would therefore exclude certain kinematical regions of the final state; such biases can complicate considerably the interpretation of the data.

The trigger condition may be logically represented by (BEAM) $\cap \left((HA1 \cap HB2) \cup (HA2 \cap HB1) \right) \cap \overline{MAG}$ where BEAM, $\overline{MAG}$, and $\left((HA1 \cap HB2) \cup (HA2 \cap HB1) \right)$ represent conditions 1), 2), and 3) respectively. This logical coincidence was formed in several stages.

The BEAM logic, a schematic of which is shown in Fig. 11, generated the coincidence $(XY \geq 1) \cap \overline{((XY \geq 2) \cup RING)}$. The signals from each of the four XY quadrants were discriminated and the 6.5 ns* discriminator outputs added by a mixer. The output of the mixer was then discriminated by two different units; the threshold level of one was set at 1 or more XY pulses, the other at 2 or more XY pulses. In this way the signals $XY \geq 1$ and $XY \geq 2$ were obtained. The signals from the two halves of the RING counter were added directly and the sum discriminated.

The veto signal $((XY \geq 2) \cup RING)$ was generated by a majority coincidence unit with $XY \geq 1$ (7 ns width), $XY \geq 1$ delayed by 9 ns, $XY \geq 2$ (8 ns), and RING (16 ns) as inputs. If two or more inputs occurred simultaneously a veto was generated. Therefore, the event was vetoed under the following conditions:

    a) a signal occurred in the RING counter within ± 16 ns of a signal in XY

    b) two different XY quadrants were triggered within ± 16 ns: if the pulses occurred within ± 6 ns of one another, the event was vetoed

---

* All the pulse widths quoted are full-width-at-half-maximum unless specified otherwise.
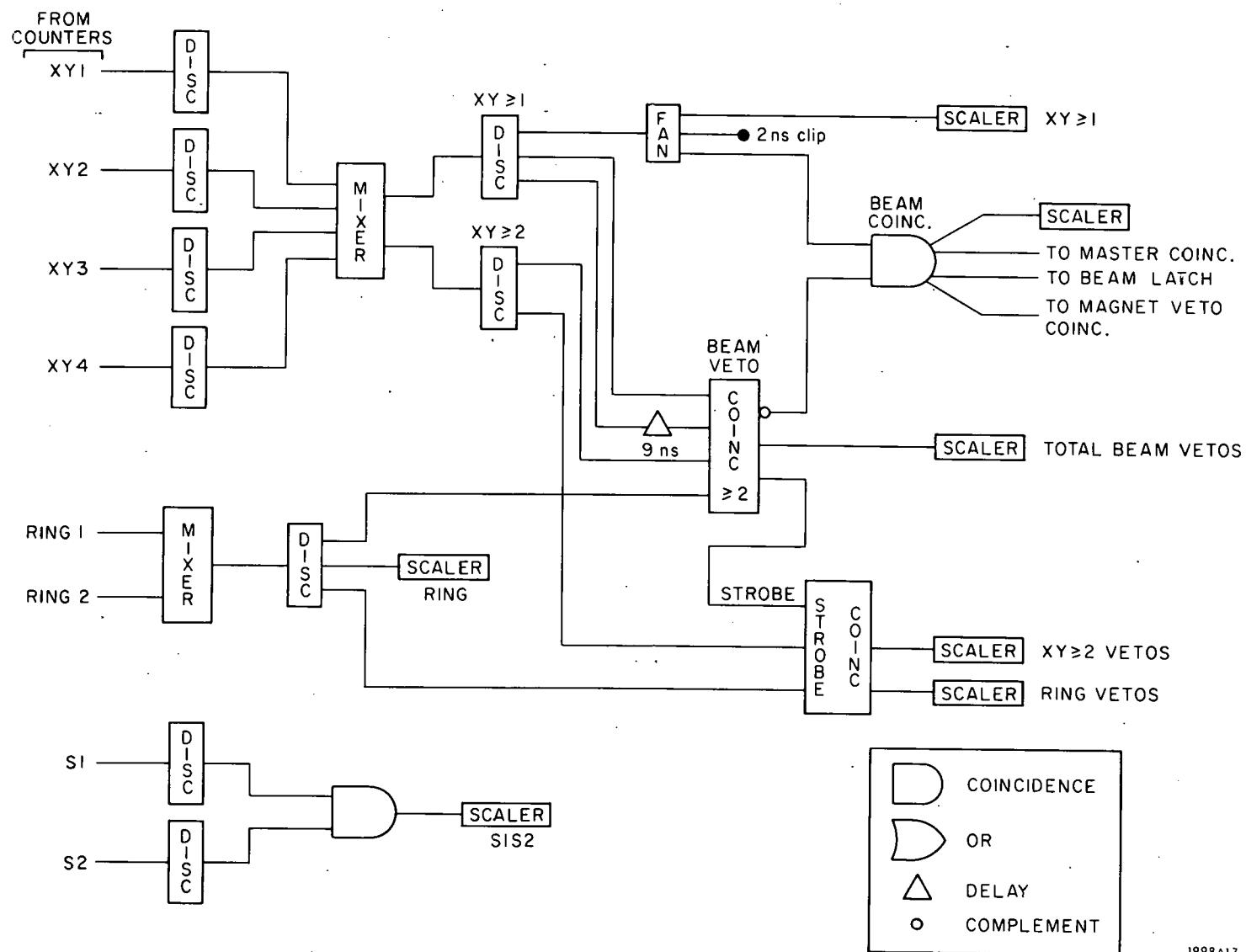
FIG. 11--Fast Electronics: generation of the BEAM COINCIDENCE. The rest of the Fast Electronics is shown in Fig. 12.

by XY $\geq$ 2. If the pulses were separated by 5–16 ns, the 7 ns output of the XY $\geq$ 1 discriminator was lengthened to the duration of the two input pulses, and was therefore in coincidence with itself when delayed by 9 ns

c) two particles occurred in the same XY quadrant, but were separated by 11–16 ns.

Only if two beam particles occurred in the same XY quadrant within 11 ns was the logic unable to veto the event. The overall veto efficiency for two beam particles occurring in XY within ±16 ns is therefore ≈83%. If the two particles were separated by more than ± 16 ns, there was no problem since one of the particles was completely out of coincidence with the rest of the electronics.

The BEAM signal was then obtained by forming a coincidence between XY $\geq$ 1, clipped to 4 ns, and the 27 ns complement from the majority logic unit.

The signals from each of the twenty counters in hodoscope A were discriminated and the 12 ns discriminator outputs added by mixers. The sum of the twenty counters was then discriminated by two different units; one unit (HA1) triggered if one or more counters fired, the other (HA2) triggered for two or more counters. An identical procedure was used for hodoscope B (see Fig. 12). Coincidences between the 10 ns outputs of HA1 and HB2, and also HA2 and HB1 were obtained; the logical OR of these two coincidences was the desired combination, (HA1 $\cap$ HB2) $\cup$ (HA2 $\cap$ HB1) $\equiv$ HODO.

The magnet veto counters were treated in a similar fashion: signals from the twelve counters were discriminated and added and a 26 ns complement signal $\overline{\text{MAG}}$ generated if one or more of the counters fired.
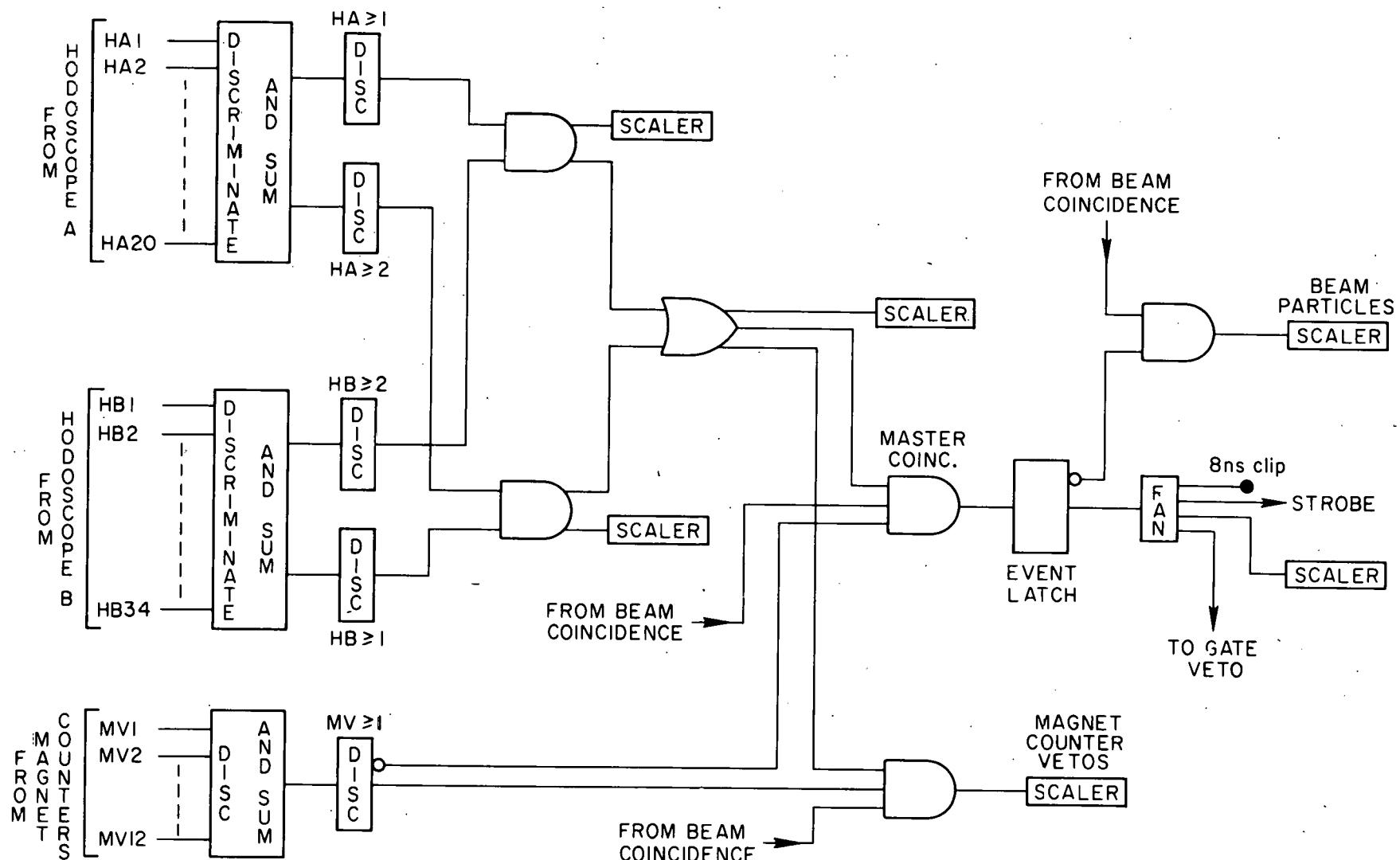
FIG. 12--Fast Electronics: generation of the MASTER COINCIDENCE and STROBE. The logic that produces the BEAM COINCIDENCE, and the Legend, are shown in Fig. 11.

1998A16

The master trigger was then obtained by a three-fold coincidence between BEAM and HODO (both 10 ns wide) and $\overline{\text{MAG}}$. The relative timing was adjusted so that both the BEAM and HODO pulses were enveloped by $\overline{\text{MAG}}$, and so that the leading edge of BEAM was delayed ≈ 2 ns with respect to the leading edge of HODO. The timing of the master trigger is then determined by BEAM. This is important since the jitter in $\overline{\text{MAG}}$ (≈ 5-6 ns) and HODO (≈ 2-3 ns) is significantly larger than the jitter in BEAM (≈ 1 ns).

The EVENT LATCH was a single-shot pulse triggered by the master trigger. This LATCH, because it could not be retriggered until its output pulse had returned to zero, introduced a dead time into the system so that no more than one trigger could be generated per beam burst. The width of the pulse was variable, depending on the desired dead time. It was normally set to 50 μs, the important criterion being simply that the width be longer than the duration of the beam burst, i.e., > 1.6 μs. The LATCH signal was fanned out and one of the outputs clipped to 16 ns. This MASTER STROBE was also fanned out and was used to trigger the spark chambers, strobe the buffer storage for the counters, gate the Čerenkov counter electronics, and begin the event read-out by the computer. One of the other LATCH outputs was used as a fast veto for the scalers; this is discussed in some detail in the following section.

For scaling the number of beam particles, a coincidence was formed between BEAM and the complement of LATCH, so that particles incident after an event had occurred were ignored. To obtain the proper cross section normalization, the incident flux must reflect only those particles which are capable of producing an event.

2. Gating System

The primary function of the gating system was to prevent pickup of spurious signals, either by the fast electronics or by the scalers. These spurious signals could be generated by phototube noise, background radiation produced by other beams in the experimental area, or by the electromagnetic radiation produced by discharge of the spark chambers. The gating system was also used to suspend data taking if there was a major failure in the spark chamber system or to temporarily block the generation of a new master trigger if the computer had not finished recording the previous event.

The trigger for the gating system was the "trigger pattern" for our beam and was received from accelerator control. It consisted of 1 μs pulses occurring at the same repetition rate as our primary electron beam, and timed such that they reached the experimental apparatus 2.5 μs prior to the beam particles. A gate generator, driven by this pattern, produced the 8 μs pulse which gated ON the scalers and fast electronics: The GATE outputs were used for gating the scalers; for the fast electronics, a LOGIC signal was used to drive two separate gate generators which reiterated the 8 μs pulse and applied it to the two racks of electronics.

The output of the main gate-generator was vetoed by signals indicating any of the following conditions:

1) an event had occurred and a LATCH signal had been generated

2) the computer had not finished recording the previous event

3) the high voltage system for the spark chambers had failed

4) the clearing field for the chambers was not being properly applied.

In this way the LATCH signal inhibited any additional triggers within a beam burst and prevented scaler pickup when the spark chambers were fired. Shutoff of the scaler gate began ≈100 ns prior to the chamber breakdown.

It was only occasionally when triggers occurred on successive pulses that condition 2) was necessary. The normal time for recording an event was 3.5 ms, substantially less than the 5.6 ms delay between beam pulses. During tape writing, however, this time occasionally increased to 5-6 ms, in which case it was not possible to receive triggers on successive pulses.

Conditions 3) and 4) not only prevented the recording of meaningless data, but also protected the chambers since a continuous breakdown of the clearing field could produce serious damage.

3. Spark Chamber Readout

The digitization of the signals from each of the spark chamber wands was accomplished by means of eight scalers per wand and a 20 megacycle clock. Upon receipt of the first pulse (the start fiducial) from a given wand, all eight scalers began counting at the 20 megacycle rate. As successive pulses were received, successive scalers were stopped, thereby digitizing the time from receipt of the fiducial to receival of the pulse corresponding to a particular spark. A second fiducial pulse was received from the opposite end of the wand. Given the velocity of propagation of the pulses along the wand, the scaler readings were then a digitization of the spark positions with respect to the fiducials. The two fiducials were used not only to calibrate the position and propogation velocity of the wand; by observing the magnitude and sign of the fiducial pulses, the magnetization of the wand could also be monitored.

When the number of sparks per plane was less than seven, which was usually the case, the scalers which were not stopped by a pulse from the wand ceased counting automatically upon overflow.

In the event that more than eight sparks per plane had occurred, coordinates from some of the sparks, as well as the second fiducial, were missing. The occasional absence of the second fiducial produced no ill effects since the velocity of propagation of the magnetostrictive wire was rather constant as a function of time. It was important that the spark overflow be minimized, however, since it could result in a preferential loss of coordinates from one side of the chamber (the side opposite the wand readout) and therefore in a corresponding bias in measured angular distributions. For this reason, the beam intensity was always maintained at a level such that spark overflow was not significant, and the number of scalers per plane was increased from four to eight between the December and January runs* to allow higher incident fluxes.

4. Strobed Buffers

The determination of which counters had fired in coincidence with the master trigger, and the storage of this information until readout by the computer, was accomplished by the STROBED BUFFER modules. Each of these units had eight signal inputs plus a STROBE input. If a logic pulse was received at one of the signal inputs in coincidence with a pulse at the STROBE input, a logical 1 was stored in the corresponding memory location. The strobe input was the 16 ns MASTER STROBE generated by the FAST LOGIC. The signal inputs were $\approx$12 ns output pulses from the respective discriminators for each of

---

*A brief description of the data collection is given in the last section (H) of this chapter.

the counters in the experiment. Only the information from the S1, S2 and RING counters was not recorded. The buffers were interrogated by the computer and reset to zero after each event.

5. Čerenkov Counter Electronics

The electronics for the Čerenkov counter was designed not only to record which of the eight phototubes had fired, but to record the individual pulse heights as well. Each of the anode signals from the phototubes, which were $\approx.05-1$ volts and 10 ns wide were stretched and amplified so that the output pulse was $\approx.1-2$ volts and 1-2 μs in width. The peak of the output pulse was proportional to the total charge of the phototube pulse, and hence to the total amount of light detected by the phototube. The stretcher amplifier modules were gated by the MASTER STROBE; only that part of the input signal which was coincident with the STROBE was integrated. It was particularly important that the phototube signals be narrow and that this coincidence be clean for the following reason: since the main pion beam passed through the Čerenkov counter, two of the phototubes counted at a rate of ≈ 10 per 1.6 μs. If the phototube pulses were fairly wide or had long tails, the accidental coincidences with the MASTER STROBE would be significant. Since the signature for a $K\bar{K}$ event is no signal in the Čerenkov counter, only a small overlap of the STROBE with a phototube pulse is sufficient to "lose" a $K\bar{K}$ event. This possibility was strongly diminished by the BEAM logic which vetoed an event if a second beam particle occurred within $\pm$ 16 ns.

The peak of the stretched pulse was determined by modules which charged up to the maximum voltage of the input and held that voltage until reset to zero. The outputs of the "peak-hold" units then passed through a multiplexer so that

each of the channels could be successively selected by the analog-to-digital converter (A/D).

The dynode signals from the phototubes were also recorded, though only in the usual hard-logic fashion. Each output was discriminated and recorded in the STROBED BUFFERS. This additional logic for each of the phototubes was employed partly for redundancy and partly for ease in monitoring.

Finally, a signal proportional to the sum of the anode signals was obtained with a high-input-impedance adder. This signal was split, one half being digitized by the pulse-height electronics and the other half being discriminated and recorded by the strobed buffers. These two signals were used for selection of the $\pi^+ \pi^-$ events and for testing and monitoring purposes.

G. Data Recording and Online Monitoring

During the data-taking runs, there were two primary tasks to be performed:

1) a transfer of the information from the temporary storage buffers to magnet tape

2) Online monitoring of the apparatus.

The first task consisted of interrogating the strobed buffers, WSC scalers, and A/D converter on an event-by-event basis and of reading out the scalers and multi-channel digital voltmeter (DVM) at regular intervals. This operation was handled by communication between the IBM model 1800 computer and the interface electronics for the storage buffers. The DVM readings and scalers were read at 10 min intervals as well as at the end of each run, and the information recorded on tape as separate non-event records. Each run constituted one full tape of $\approx 35,000$ events and lasted $1-1\frac{1}{2}$ hrs depending upon the incident beam intensity and accelerator performance. Two tape drives were used to minimize dead time due to tape changeover.

The second task, that of monitoring the apparatus, relied heavily on the 1800 as well as on the experimenters and electronic interlocks. It included checking the following conditions:

1) Beam line: magnet currents, distributions in P, θ, φ, and XY hodoscopes, incident flux

2) Spark chambers: high voltage, clearing field, and gas flow

3) Spark chambers: efficiencies, average spark-multiplicities and overflows

4) magnetic field of analyzing magnet

5) Čerenkov counter: high voltage, temperature and pressure, pulse-height distributions

6) Scintillation counters: high voltage and efficiencies

7) Hydrogen target: pressure and temperature

8) Trigger and "good event" rates.

The power supplies for the beam magnets, as well as the clearing field and high voltage supplies for the spark chambers, were equipped with alarms which sounded if the currents or voltages strayed from within certain limits. In addition, the magnet currents, and the temperature and pressure of the Čerenkov counter, were monitored by the 1800 via the DVM. At 10 minute intervals the values of these parameters were read by the 1800 and printed out; the computer had no direct control over the currents, however.

Signals from each of the counters in the beam hodoscopes (P, θ, φ, XY) were scaled so that the average distribution of particles in these hodoscopes could be readily watched. Count-rate meters for the XY hodoscope and for the four central counters of the P hodoscope enabled a rapid and accurate determination of whether the beam was properly centered at a particular

- 44 -

instant. In addition, at the end of each run, and upon request during a run, the 1800 printed a histogram showing the integrated number of counts, for that run, for each of the counters in the experiment (except for S1, S2 and RING). This histogram was compared run to run to check that none of the counters was inefficient or multiple-counting. A comparison of the particle distributions in hodoscopes A and B from run to run checked that these hodoscopes were properly positioned and that the beam was properly steered through the dead spaces; if either of the hodoscopes was off center in the horizontal direction, or if the beam was slightly mis-steered, a dramatic increase in the counting rate of the hodoscope counters resulted.

As a background task, the computer calculated the spark chamber efficiencies and also the average spark multiplicities and number of overflows for each of the wire planes. This was one of the more important monitoring tasks since the spark chamber performance was rather sensitive to such factors as the gas purity and the average spark multiplicity. A decrease in efficiency correlated with an overall increase in spark multiplicities and overflows was indicative of too high an incident beam flux. An abnormally low spark multiplicity for one plane coupled with a decreasing efficiency for that chamber implied problems with the wand magnetization or preamplifier threshold. On the other hand, sagging efficiencies for all the chambers without any apparent cause was a strong indication that the gas system had been "poisoned". These spark chamber statistics were printed out at regular intervals so that they could be carefully watched.

The computer also produced a histogram of the total pulse-height distribution of the Čerenkov counter. This was extremely useful, during test runs, for checking that the stretcher amplifier, peak-hold, and A/D electronics

were working properly and also for measuring the efficiency of the counter. During the data-taking runs, the histogram was of limited use, since it was compiled for all events: the complete sample of events contained particles incident with a continuum of angles and momenta, including some which were marginally above threshold or which missed the counter altogether. The resulting spectrum was therefore somewhat meaningless. For the latter runs to detect $p\bar{p}$, pulse-height distributions were collected for each mirror separately, subject to position and momentum cuts which ensured that a particle above threshold was directly incident upon the mirror. These distributions sensitively monitored the efficiency of each optical cell throughout the course of the run.

The WSC high voltages, clearing field and gas flow were checked every few hours, as were the temperature and pressure of the hydrogen target which were continuously monitored by chart recorders. The magnetic field of the analyzing magnet was monitored by a Hall probe placed on the center of the bottom face of the gap, and was maintained constant to a few parts in 10^4. Phototube high voltages, for the scintillation counters and for the Čerenkov counter, were checked manually.

Important coincidences from the fast logic, such as MASTER STROBE, $(HA1 \cap HA2) \cup (H\bar{A}2 \cap \bar{HB}1)$, and the number of magnet counter, $XY \geq 2$ and RING vetos, as well as $S1 \cap S2$, XY, and RING counts, were scaled for easy reference and monitoring. Several ratios of these quantities, which were sensitive indicators of whether the apparatus was working consistently and correctly were determined hourly and checked against previous runs. For example, XY/RING and (XY + RING)/S1S2, the transmission of the beam line from F2 on, monitored whether the beam was properly tuned and centered on XY. The trigger rate, MASTER STROBE/S1S2, was closely related to the

- 46 -

cross section and the trigger efficiency, and was therefore expected to be relatively constant as a function of time. The percentage of MASTER STROBES which were vetoed by $XY \geq 2$ or RING was also closely watched. Characteristic values of the trigger rate and several other ratios are shown in Table 1.

Besides the data recording and specific monitoring tasks, the computer reconstructed $\approx 25\%$ of the events and calculated the dipion invariant mass and momentum transfer to the nucleon for these events. This event reconstruction was neither sophisticated enough nor complete enough to produce accurate kinematic distributions; however, it was possible to determine the approximate number of ρn events detected per run. The integrated number of ρn events detected, plotted as a function of time, was particularly useful for determining the rate at which these events were being accumulated, and also for extrapolating this number to some point in the future. It was therefore possible after only a few days running, to determine whether the desired number of events would be obtained by the end of the run, and to determine the sensitivity of the ρn rate to such factors as beam intensity and spark chamber efficiency.

Although the tasks performed by the 1800 were adequate for monitoring most features of the apparatus and for determining the approximate number of ρn events detected, sophisticated checks of the apparatus and a detailed knowledge of the kinematic distributions were desired. This was possible on an essentially online basis through use of the SLAC IBM 360/91. At the end of each run, the output tape was taken to the computer center and analyzed. A relatively sophisticated geometric and kinematic reconstruction of the data was therefore available within a few hours of its recording.

TABLE 1

Characteristic Trigger Rates and Monitoring Ratios

Quantity	Symbol	Value
Average number of incident π^- per pulse	$\dfrac{XY + RING}{PULSE}$	8-10
Ratio of counts in XY and RING counters	XY/RING	10-11
Transmission of beam line from F2 to XY hodoscope (see Fig. 3)	$\dfrac{XY + RING}{S1S2}$	.56
Fraction of XY counts vetoed by EVENT LATCH or by a second incident particle within 16 ns	$\dfrac{XY - \pi}{XY}$	.14
Trigger rate: number of master coincidences per incident π	$\dfrac{MC}{\pi}$	.0083
Trigger rate: average number of triggers per second	—	10

PULSE   denotes accelerator pulses

π denotes the number of XY ≥ 1 counts that are not vetoed by a second beam particle occurring within 16 ns or by the EVENT LATCH

MC   denotes "master coincidence" which is defined in the text and in Fig. 12

XY   denotes XY ≥ 1 which, along with RING and S1S2, is defined in the text or in Fig. 11

H. Data Collection

The data for this experiment was taken at the Stanford Linear Accelerator Center, in two separate runs, during December 1969 and January 1970. Although the two runs were almost identical, some slight improvements in the apparatus were made during the two-week "off" period between the runs. Hence, the two cycles are occasionally referred to separately in the text simply as January or December. The total number of 15 GeV/c incident π^- was 8.58×10^8 resulting in approximately 10^7 triggers. Some data was also taken at 8 GeV/c, but it will not be discussed here.

The data-taking was preceded by several months of checkout including detailed tests of the beam line, spark chambers, and Čerenkov counter.

During October and November 1970, two more data runs were made, the primary motivation being a study of $p\bar{p}$ final states. The pressure of the Čerenkov counter was increased accordingly, so that it separated π and K mesons from protons (and antiprotons). The beam energy was again 15 GeV/c, and most of the running was with incident π^-, although some data was taken with incident π^+. The target counters were removed and the spark chambers and target collapsed towards the magnet to improve the acceptance. Except for these changes and some minor improvements, the apparatus was almost identical with the earlier runs. These cycles are collectively referred to in the text as "E67".

CHAPTER 3

ČERENKOV COUNTER

A. Introduction

Although the phenomenon of Čerenkov radiation has been widely utilized

by a variety of counters and detectors in particle physics, its application

to the study of particle interactions at high energies has been limited primarily

to two kinds of devices: differential counters and threshold counters. Because

differential counters require that the angular dispersion of the incident particles

be rather small, their usage has been largely confined to identifying incident

beam particles, or secondary particles when the angular phase space is quite

small.

Threshold counters can be, and have been, built with quite large solid-

angle acceptances. By the nature of their operation, however, they have been

used primarily in relatively simple applications in which they determine either

that no particles were above threshold or that at least 1 particle was above

threshold. In addition, when used in the simple "Yes-No" mode, the range

of momentum over which they can distinguish between two particles of different

masses is limited to momenta between the respective thresholds of the particles.

As there is now considerable interest in studying multibody states at

reasonably high energies, e. g., > 10 GeV, there is a need for large-aperture

detectors which can identify each of the particles in many-body final states.

States such as $K\overline{K}$ or $p\overline{p}$ may be identified simply by threshold counter tech-

niques, but a clean separation of more complicated states such as $K\pi$, $\pi\pi K$,

$K\overline{K}\pi$ or $p\overline{p}\pi$ requires separate identification of several, if not all of the particles.

In general, it is necessary not only to correctly distinguish the final states,

but in addition to identify each of the individual particles; otherwise the

kinematic correlations that are characteristic of a particular final state may be obscured by particle mis-identification.

Although the Čerenkov chamber that is described here is basically a threshold-type counter, the optical system is designed such that each of the eight mirrors reflects the Čerenkov light into a corresponding light horn and phototube (see Figs. 13 and 14). Hence the counter may be used as a hodoscope of eight optically independent Čerenkov cells. The different optical units are not physically separated, but if the Čerenkov cone of a particle intersects only one mirror, it will be detected only by the opposing phototube. For multibody states in which several particles are incident upon different areas of the counter, independent information is therefore available on the identity of each particle.

The chamber may also be used as a single, large, uniformly efficient counter by summing the outputs of each of the phototubes.

The other feature (of operation more than design) that distinguishes it from simple "Yes-No" threshold counters is that the individual pulse heights from the phototubes are recorded. Thus, identification may be made, in some cases, on the basis of how much light was emitted. This extends the useful range of the counter to momenta somewhat above the threshold of the heavier particle, and may aid in identification when more than one particle enters a single mirror. The detailed design of the counter, and the extent to which it is successful in obtaining these objectives, is discussed below.

B. Construction and Optical Design

The main frame of the counter was a large, rectangular, steel box designed to withstand pressures between 0 and 3 atm (Figs. 13-14); its size was determined primarily by the desire to match its solid-angle acceptance to that of
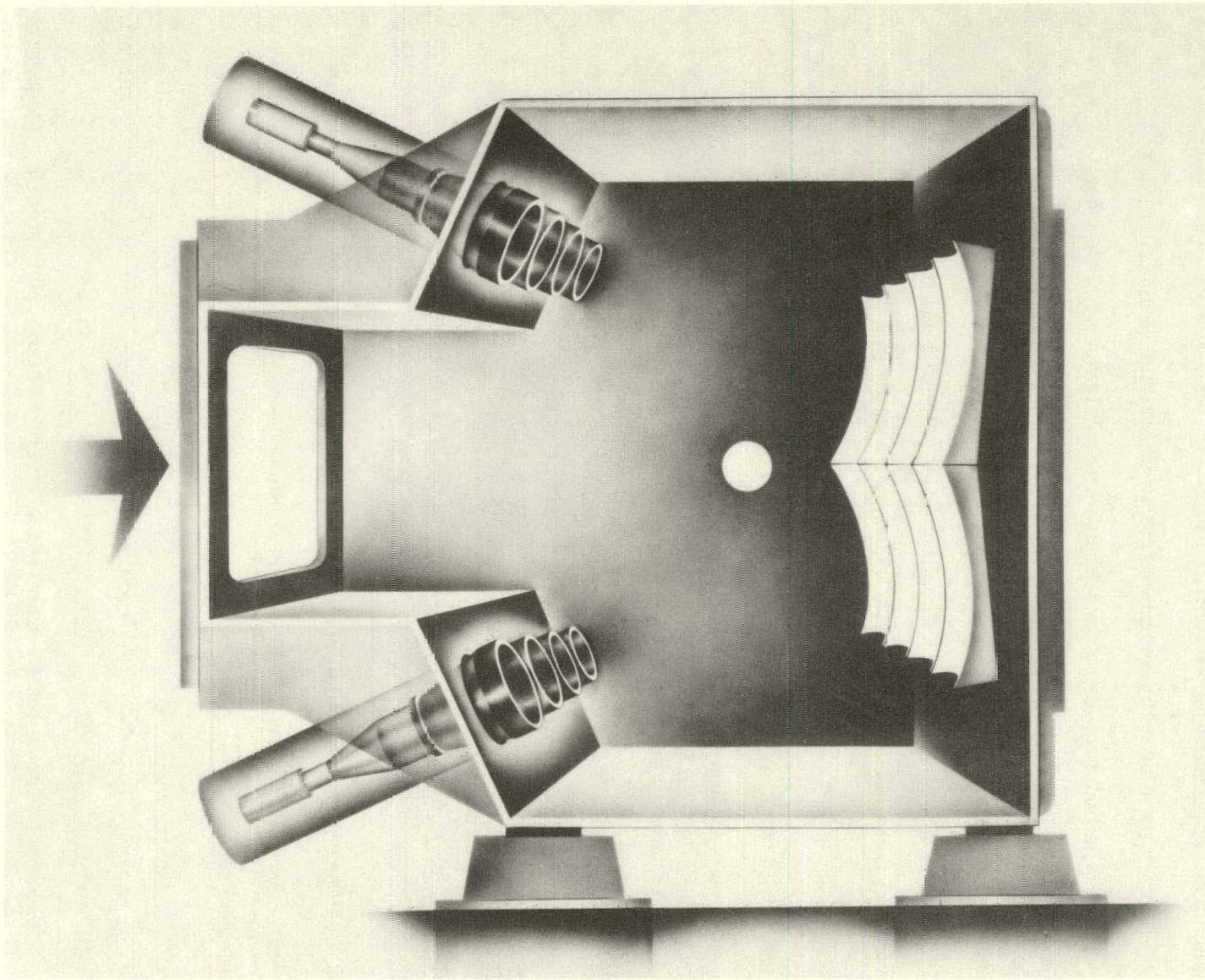
FIG. 13--Artist's conception of the Čerenkov counter showing, in particular,
the mirrors, light horns and phototubes.

1621A7

20
CM 10
0
0   10   20
CM
SCALE
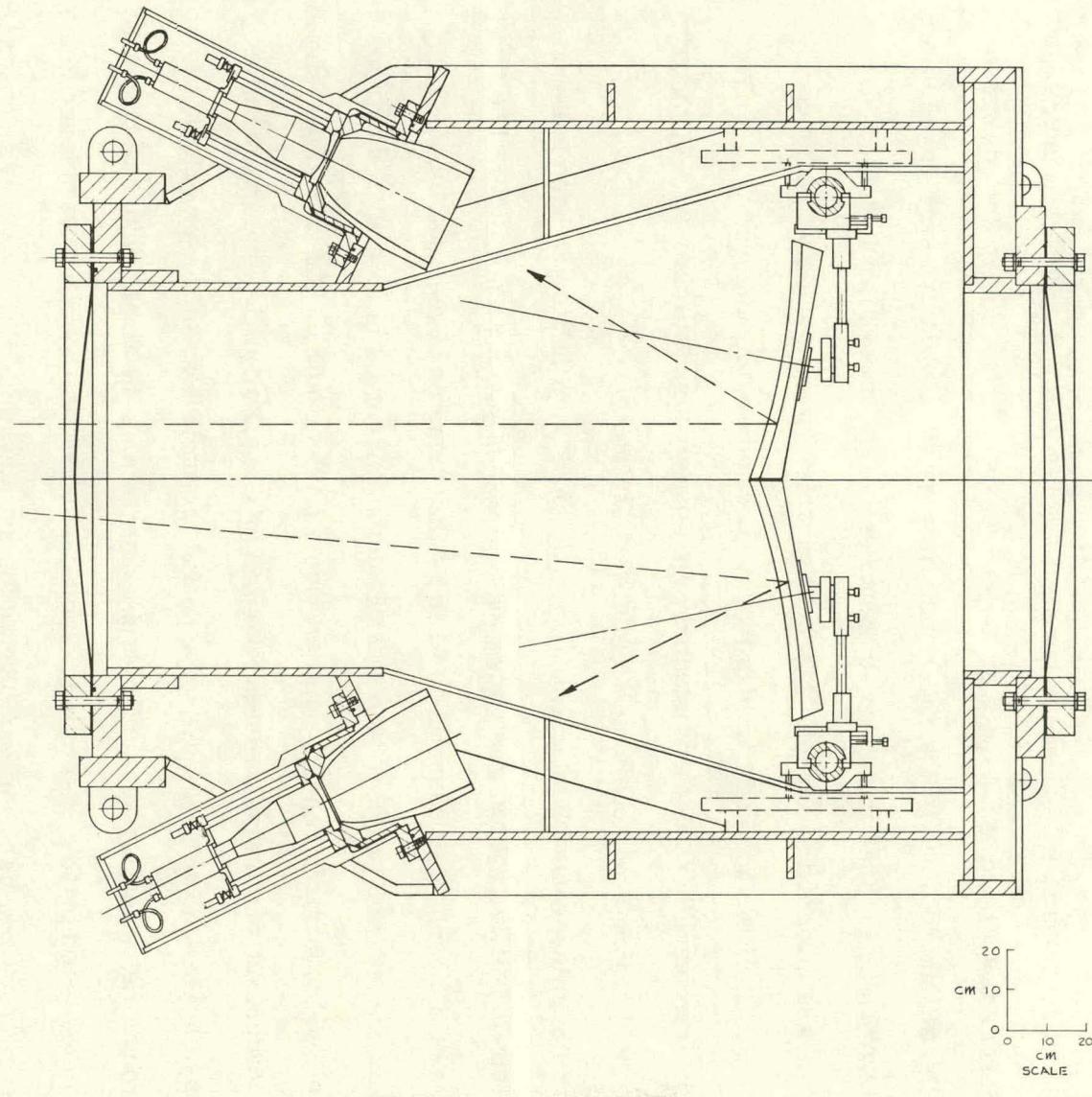
FIG. 14--Side view of the Čerenkov counter.

the momentum analyzing magnet and the rest of the spectrometer system. The entrance window, which is 2 mm thick Al, is 2.5 m × 1 m and the minimum path length of radiatior is 1.75 m. At the back of the counter there is a plane of mirrors covering a total area of 2.5 m × 1.25 m and consisting of eight square sections of spherical mirrors set edge to edge. Each of the upper four mirrors is inclined at an angle of 10° with respect to the horizontal so that it reflects light into one of the upper four light horns; similarly, each of the lower mirrors was inclined to reflect light into one of the lower light horns. The horns are designed to accept all light rays which have an angle with respect to the axis of the horn that is less than a maximum cutoff angle of 25°.[49] The light from each horn is then detected by a single photomultiplier tube (Amperex 58 UVP) having a photocathode diameter of 110 mm.

The mirrors and light horns were machined from lucite and hand polished. A thin UV-reflecting aluminum coating was deposited by evaporation. The size of the horns was essentially fixed by the diameter of the phototubes, while the optimal radius of curvature for the mirrors was determined by conventional ray tracing and by detailed Monte Carlo studies. The latter consisted of simulating photon emission (at the proper Čerenkov angle) from each of the possible particle trajectories, calculating the trajectory of these photons through the optical system and thereby determining the final number of photons to be detected by the phototube (including loss due to imperfect reflectance of the mirrors and light horns). The radius of curvature, r=1.75 m, was chosen so as to optimize the uniformity of the optical efficiency for the various particle trajectories.

A particularly important feature of the optics was that it was designed to detect ultraviolet Čerenkov radiation for wavelengths as low as 2300 Å. Since

the photon spectrum from Čerenkov radiation is proportional to $1/\lambda$, the amount of light emitted between 2300 and 5000 Å is three times that emitted between 3500-5000 Å, the visible region normally detected when no effort is made to prevent absorption of the ultraviolet. For this reason phototubes with quartz windows were used, and the ports between the light horns and the phototubes were also constructed of quartz. The reflectance of the mirrors and horns was measured as a function of wavelength and was > 80% for wavelengths as short as 2300 Å. This comprised the primary quality control on the mirror production. Mirrors which did not achieve this reflectance were polished further and re-coated. The radiator was chosed to be freon 12 (CCl_2F_2) because of its relatively high index of refraction (n-1=1.15 $\times 10^{-3}$) and good transmission of ultraviolet frequencies; the transmission is $\approx 100\%$ for $\lambda > 2300$ Å (although it falls rapidly to zero for shorter wavelengths).[50]

The photocathode response of the phototubes was studied using a flying spot scanner: light from the beam spot of an oscilloscope was focussed so that an identical image was produced on the photocathode (neutral density filters were used to reduce the intensity). As this spot scanned a series of horizontal lines on the photocathode, each displaced vertically ≈ 1 cm, the output of the phototube was displayed on a second oscilloscope driven by an identical raster. In this way, one could obtain a cross-sectional mapping of the photocathode response as shown in Fig. 15. The focussing electrodes of the phototube were then adjusted to maximize the uniformity of the response.

Although the mirror alignment was initially optimized by ray tracing and the Monte Carlo studies noted above, it was desired that the final alignment be performed in such a way that the uniformity of the optical efficiency for the various particle trajectories could be checked in a straightforward manner.
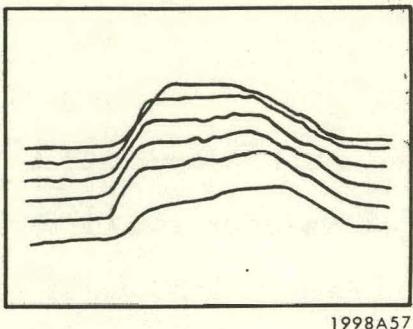
FIG. 15--Cross-sectional mapping of a
typical photocathode response.

1998A57

Consequently, a scanning technique was employed similar to that described above for the phototube adjustment.

A rectangular array of twenty-four 2 cm square mirrors was constructed and positioned such that it occupied the same location, relative to the Čerenkov counter, as the exit of the spectrometer magnet during the experiment (see Fig. 16). The mirrors were then aligned such that when a laser beam was horizontally scanned across the successive rows, the reflected rays from each mirror converged to the same point at the mirror plane in the Čerenkov counter.

The laser scan was accomplished by a three-sided rotating mirror; one of the three faces was vertical, while the other two were respectively tilted with respect to the vertical by $\approx \pm 40$ mrad. The mirror was driven by a variable speed dc motor and oriented such that an incident laser beam was successively vertically deflected and scanned across each of the three rows while the mirror underwent a single rotation.

The entire setup consisting of the laser, rotating mirror, and mirror array was pivoted so that it could be rotated horizontally or vertically. Hence, this converging set of light rays could be directed to any point on the plane of mirrors in the Čerenkov counter. This permitted an almost instantaneous check of the optics for Čerenkov light emitted (with zero Čerenkov angle)

ALL RAYS FOCUSSED TO A POINT
AT CERENKOV MIRROR PLANE

ROTATING
MIRROR

TRIGGER
MIRRORS

MOTOR

SILICON
PHOTODIODE

LEVEL STEPS
WITH EACH
TRIGGER

SILICON
PHOTODIODE

A
X 1000

75 Ω

DISC

EXT.
TRIG.

DISPLAY A+B

A

B

PHOTOTUBE

50 Ω

10 K

.0047 μfd

1998A50
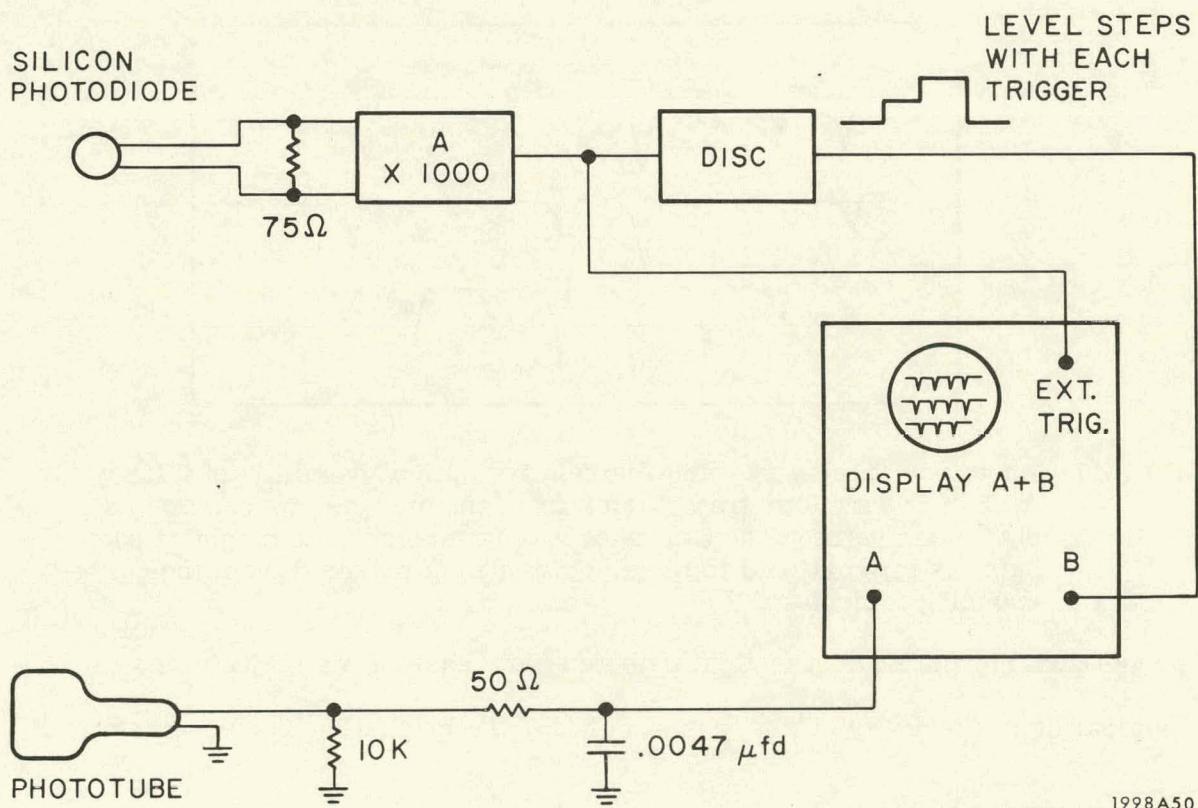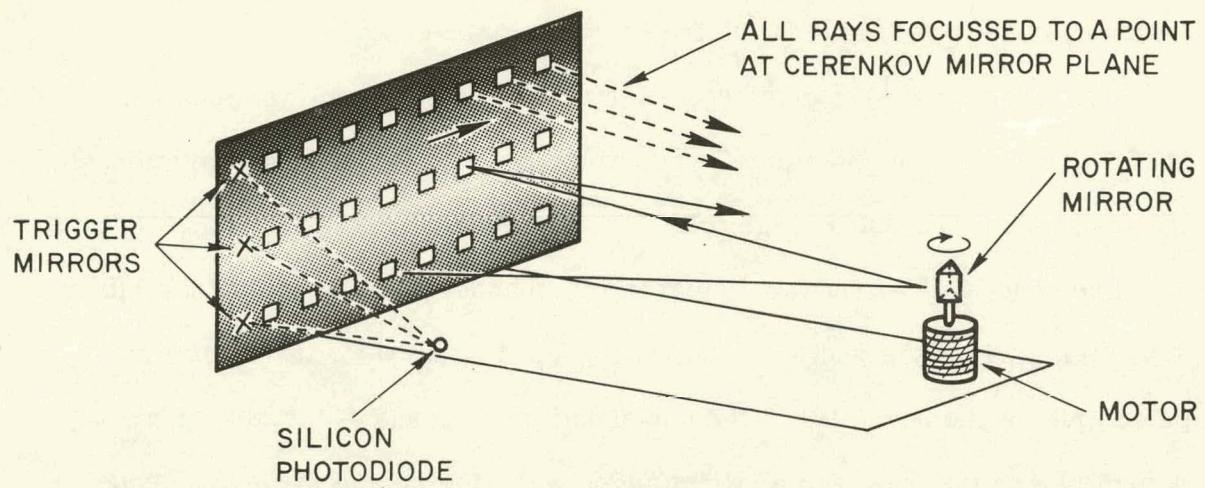
FIG. 16--Schematic diagram of the laser scanner and electronic display used for
the mirror alignment.

from any of the possible particle trajectories in the experiment. *

The laser rays were detected, after reflection by the mirror and light horn, directly by the phototube. Neutral density filters were used to attenuate the intensity to prevent damage to the photocathode.

The phototube output was displayed in a manner similar to that described above for study of the photocathode response. In this case, three mirrors placed just at the beginning of the horizontal laser scans of the mirror array, reflected the laser beam to a silicon photodiode; the signals from this diode triggered the horizontal scan of the oscilloscope and also incremented a dc level which displaced the trace vertically (see Fig. 16). An example of the resulting display is shown in Fig. 17. The individual pulses are respectively

1998A56
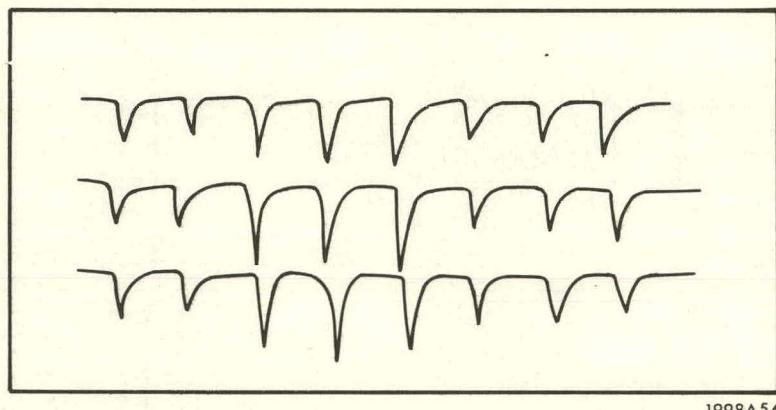
FIG. 17--Phototube display showing the relative optical detection efficiency for each of twenty-four trajectories from the "magnet aperture" to a particular point at the Čerenkov mirror plane. The height of each pulse is proportional to the amount of light detected from the corresponding trajectory.

proportional to the amount of light detected from each of the trajectories

originating at the array of mirrors simulating the magnet aperture. Variations

---

* The set of trajectories represented is in fact much larger than those actually present in the experiment since, for example, there is no requirement in this setup that the rays intersect the target when projected upstream.

in this pattern were studied as the bundle of rays was directed to different points on the mirrors in the Čerenkov counter.

Since the effects of a finite Čerenkov angle are not included in this "simulator", the displays obtained do not fully reproduce the relative optical efficiency for real particles. The scanner was, however, very useful in performing the optical alignment. In addition, these tests verified an important point that had been only partially realized, during the ray tracing studies: the interfacing of the phototube to the light horn is critical. Although all of the rays that enter the horn with an angle of less than 25° are reflected out the other end, many of these rays exit at rather acute angles (i.e., approaching 90° with respect to the axis of the horn). It is therefore essential that the photocathode be mounted as close to the end of the horn as possible.

C. Electronics

The pulse-height information from the counter was obtained by separately integrating the signals from each of the phototubes and converting the resulting signal to a dc voltage level. This voltage level was proportional to the amount of light detected by the phototube and was subsequently converted to digital information by an analog-to-digital converter. A detailed discussion of the electronics employed is given in Section F.5 of Chapter 2.

D. Testing and Performance

The counter was tested using a pion beam at 8 and 5 GeV/c which when undeflected passed through the center of the Čerenkov chamber. Two bending magnets 10 m and 6.35 m upstream from the counter were used to deflect the beam vertically and horizontally towards various points on the mirror plane. In this way, it was verified that the efficiency of the counter to detect a

particle was uniform for various particle trajectories. It was particularly important to check the regions at the edges of the mirrors where the Čerenkov light may be split two or even four ways and detected by separate phototubes. The uniformity was found to be very good. For example, Fig. 18 shows the pulse-height spectrum obtained for two different incident trajectories of the pion beam (5 GeV/c) with a gas pressure of 1.5 atm freon 12 in the counter. Note that although the Čerenkov light divides equally between two mirrors for the trajectory shown in parts (a) and (b), the pulse height spectrum obtained by summing the outputs of the two phototubes, Fig. 18c, is essentially undegraded. The pulse-height spectrum for the beam incident on the center of a mirror, shown in part (d), was fit with a Poisson distribution $P(k)=\frac{m^k}{k!}e^{-m}$ to estimate the average number of photoelectrons, m. The best fit value of m was 11 which, when corrected for the statistics of the dynode multiplication, implies an average of 12-13 photoelectrons.

An 8 GeV/c pion beam was used to measure the efficiency of the counter as a function of the gas pressure for a typical trajectory, as shown in Fig. 19. The efficiency was determined by comparing the fourfold coincidence counting rate between three scintillation counters (two upstream and one downstream of the chamber) and a threshold gas Čerenkov counter set to count on π's, with the fivefold rate which included the Čerenkov chamber. The inefficiency is plotted in Fig. 19. In addition, a series of measurements were made without the beam Čerenkov counter. These measurements, also shown in Fig. 19 illustrate that the chamber is capable of detecting a .1-.2% contamination of K^- mesons in the beam.

Although the maximum efficiency of the counter is indicated by Fig. 19 to be ≈99.85 ± .1%, a subsequent pressure curve at 7.2 GeV/c with higher
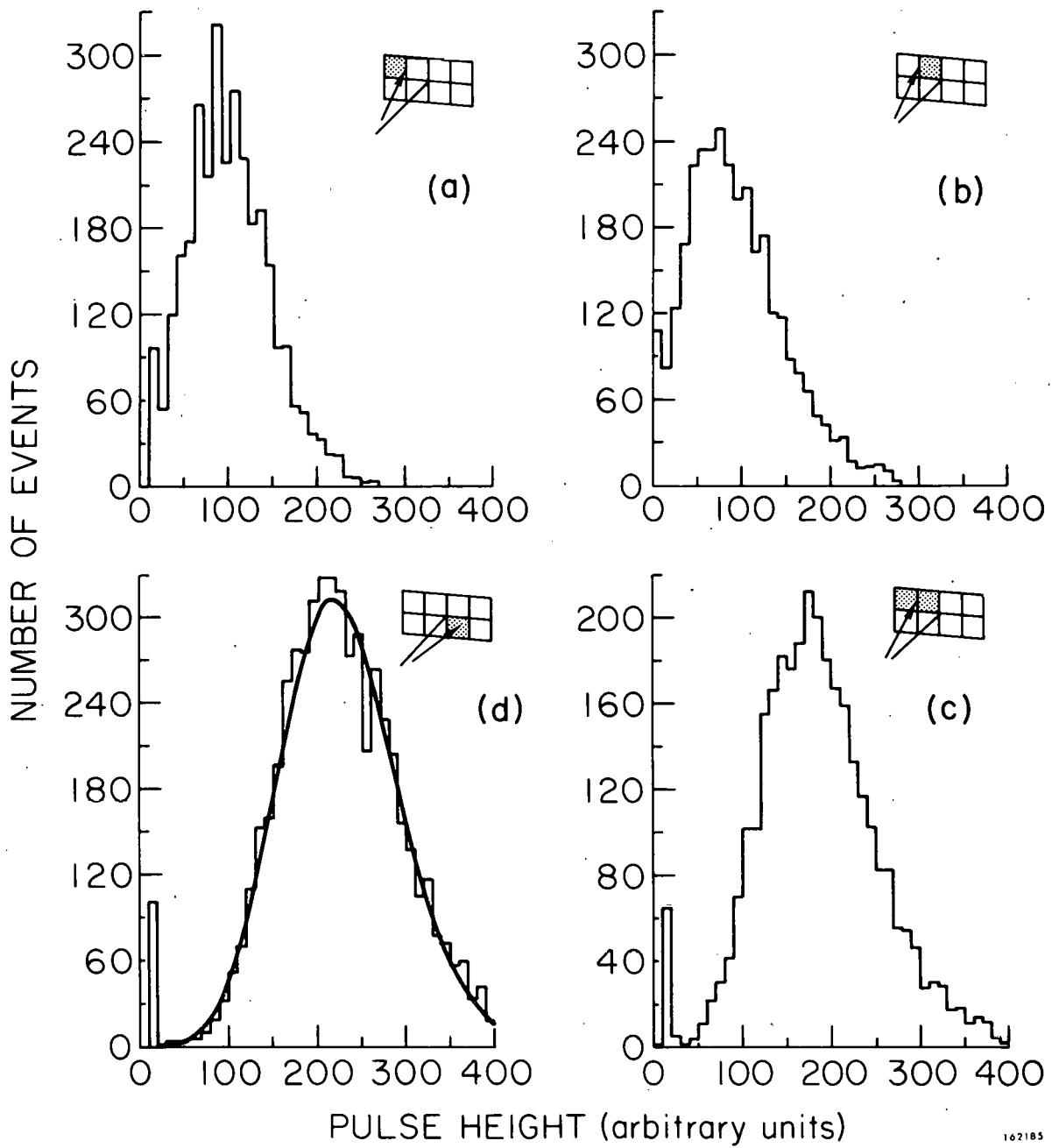
FIG. 18--The pulse height spectrum is shown for two different trajectories of a 5 GeV/c pion beam, as indicated by the inserts. The shaded region indicates for which mirror (phototube) the spectrum is plotted. Figures (a), (b), and (c) show for a trajectory which intersects the crack between two mirrors, the spectra of the two corresponding phototubes, both separately and summed together. The solid line in (d) is the best fit to a Poisson distribution. The small spike near the origin indicates the zero-pulse-height pedestal and consists largely of mistriggers.
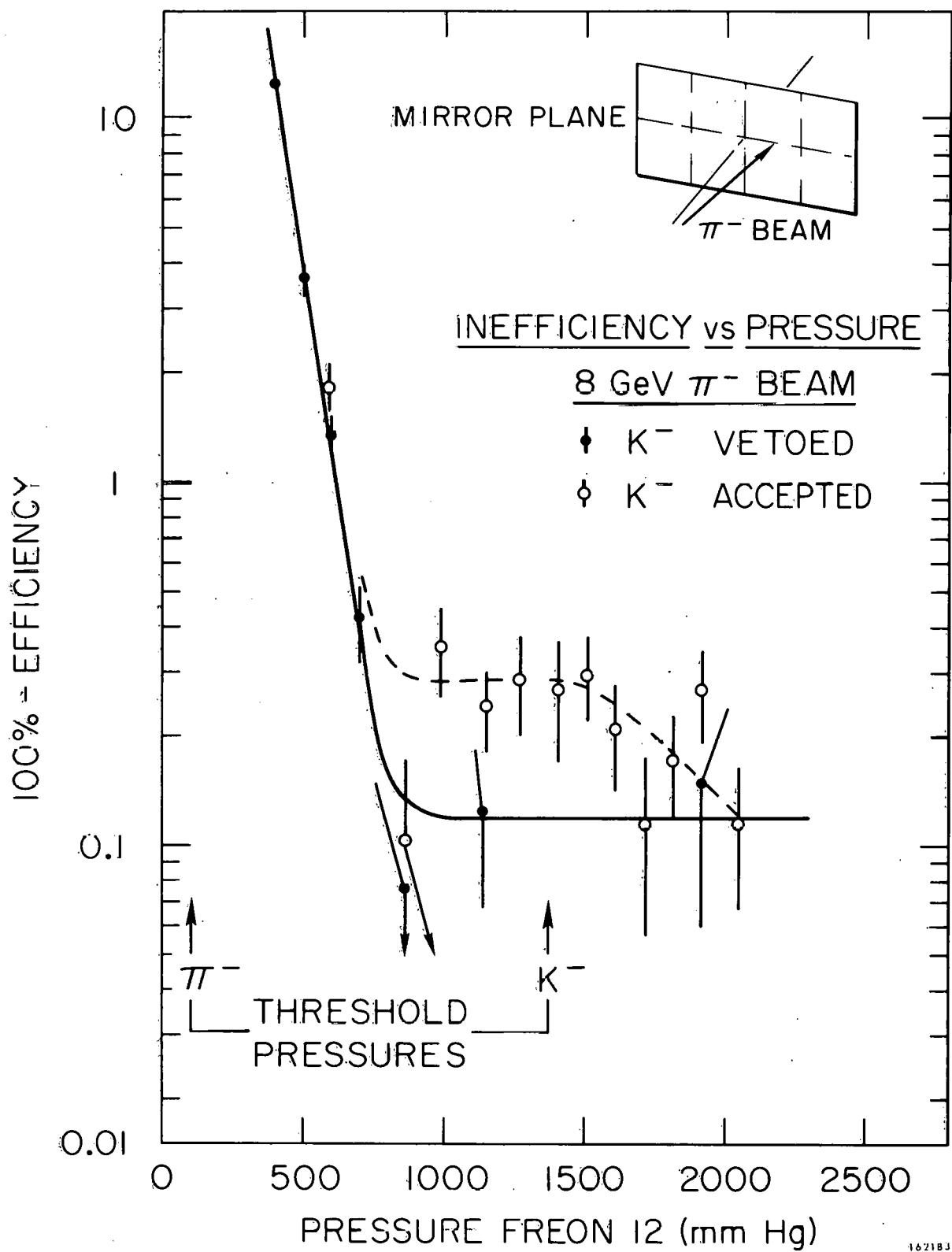
FIG. 19--Detection inefficiency of the Čerenkov counter for 8 GeV/c π⁻. For the solid points, a beam Čerenkov counter requiring the incident particle to be a π⁻ was included in the trigger. For the open points, this requirement was omitted. The difference between the two measurements indicates that the counter is capable of detecting a .2% contamination of K⁻ in the beam.

statistics and a better trigger resulted in a maximum efficiency of 99.986 ± .01%. The primary objective of this second set of measurements was to obtain an efficiency vs. pressure curve for K mesons; consequently the rf-separator was used and the beam consisted largely of K^- ($\approx$65%). Since the remaining 35% of the beam particles were pions, however, it was possible to repeat the π^- efficiency measurements by including the beam Čerenkov counter in the trigger. The counter is thus capable of discriminating between π and K mesons (or K and p at a higher momentum) with a rejection ratio in excess of 5000:1.

E. Results

The total-pulse-height spectrum for events in which at least one particle entered the counter has already been presented in Chapter 2 (Fig. 10). It was also noted there that selection of $\pi^+\pi^-$ events was made on the basis of a threshold discriminator applied to the hardware sum--i.e., in the standard threshold-counter fashion. The somewhat more sophisticated criteria used in selecting $K^+\pi^-$ and K^+K^- events are now discussed here.*

To study these events, it was required that both particles enter the Čerenkov counter, and that the momenta of each be sufficiently far above π-threshold that pions be rejected with > 99% efficiency; this corresponded to a lower momentum cutoff of $\approx$4 GeV/c, as will be demonstrated below. The

_____

*
For the rest of the figures (and analysis) in this chapter, the zero-pulse-height pedestal mentioned in Section 2, E was set to zero. Thus the "spike" in the pulse-height distribution corresponding to K^+K^- and $p\bar{p}$ events occurs approximately at channel number zero. The slight instability of the pedestal still remains, however, so that this zero-pulse-height spike has a small but finite width.

separate pulse heights for the positive and negative particles were then determined in the following manner: each track was projected to the mirror plane of the Čerenkov counter and it was determined which mirrors would have been intersected by the Čerenkov cone of the corresponding particle. The pulse heights for those mirrors were then summed. In the event that the light cones from the two particles intersected the same mirrors, it is necessary to resolve the identification on the basis of how much light was detected in each mirror. However, this occurred for less than 15% of the events.

A convenient display of the results obtained is shown in Fig. 20 which is a two-dimensional scatter plot of the pulse height for the positive particle (CERSMP) versus that for negative one (CERSMN). It is evident that there is quite a clean separation between the events in the horizontal and vertical bands along the edges, the events at the intersection of these two bands, and the events occupying the rest of the plot; these correspond, respectively, to $K^-\pi^+$, $K^+\pi^-$, K^+K^- and $\pi^+\pi^-$ final states.[*] Note in particular that there is almost no feedthrough from the $\pi^+\pi^-$ to the K^+K^- events; out of a total of $\approx 25,000$ events there are at most only a few $\pi^+\pi^-$ events that could be construed as K^+K^-.

Given the pulse heights of the individual particles, it is possible to estimate the efficiency of the counter under experimental conditions. One may select a sample of negative particles that consists largely of pions by requiring that the positive particle emit light in the counter; this selects primarily $\pi^+\pi^-$ events

---

[*] Since the pressure of the counter was set to separate π and K mesons, no information was available to distinguish kaons from protons (or muons and electrons from pions). Background from these particles will often not be explicitly referred to in the text, but the reader should bear in mind that they may exist.

since there is no strong production of $K^-\pi^+$ or $\bar{p}\pi^+$ final states. The converse selection may also be made but one does not obtain as clean a sample of π mesons since the K^* (890) $\to K^+\pi^-$ is quite strongly produced. The fraction of the negative particles, as a function of momentum, that yield a null signal in the counter is then an upper limit on the counter inefficiency. This is illustrated by Figs. 21 (a) and (b) which show respectively, the momentum spectrum of the negative particle for all events with CERSMP > 100 and for those events with CERSMP > 100 and CERSMN < 30.

The efficiency of the counter as a function of momentum, when calculated from these two figures, is shown in Fig. 22. This determination is only a lower limit on the efficiency, since not all of the particles are pions. On the contrary, the difference in the shapes of the two distributions in Fig. 21 for momenta greater than 6-7 GeV/c indicates that most of the particles producing a "null" signal are not pions. It is therefore evident from Fig. 22 that the efficiency of the counter is $\gtrsim 99\%$ for particles above 4 GeV/c and averaged over all trajectories in the experiment.

As an illustration of the effectiveness in identifying the positive and negative particles separately, Fig. 23 shows the mass spectrum for $K^+\pi^-$ events selected from Fig. 20. The selection criteria was CERSMP < 50 and CERSMN > 34. A strong K^* (890) signal is observed with relatively little background; the events in this spectrum were also subjected to a missing mass cut of 1.02 - 1.28 GeV and therefore were produced in the reactions $\pi^- p \to K^* (\Lambda, \Sigma)$. The corresponding missing mass distribution for events with $.84 < M_{K\pi} < .94$ GeV is shown in Fig. 24 for masses < 1.5 GeV; a strong peak is observed at the location of the Λ and Σ.
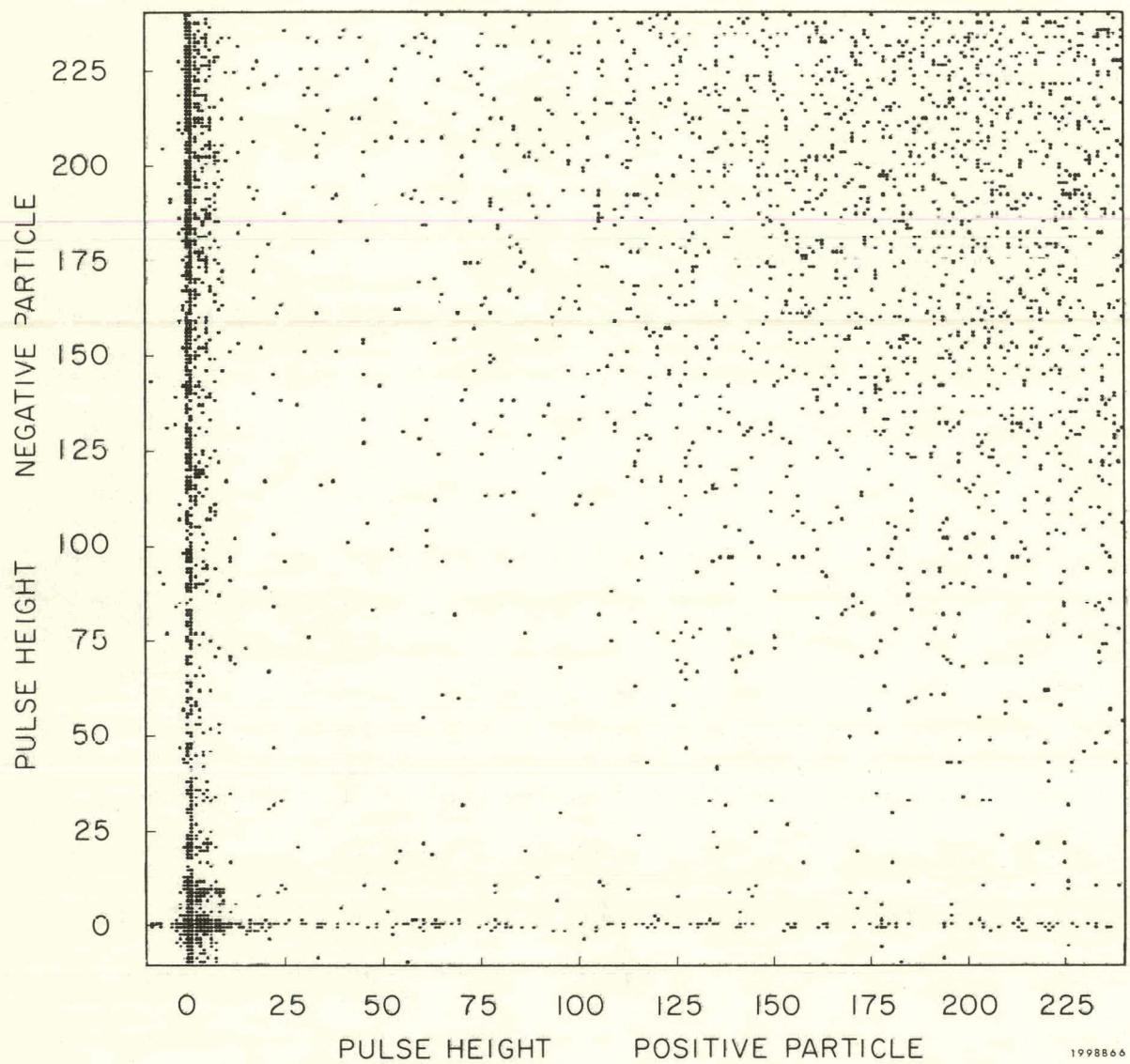
FIG. 20--Scatter plot of the pulse heights for the positive and negative particles. The horizontal and vertical bands, the intersection of the two bands, and the rest of the plot correspond to $K^-\pi^+$, $K^+\pi^-$, K^+K^-, and $\pi^+\pi^-$ events respectively. There are $\approx 20,000$ $\pi^+\pi^-$ events (including over-flow) and ≈ 2500 K^+K^- events in the plot.
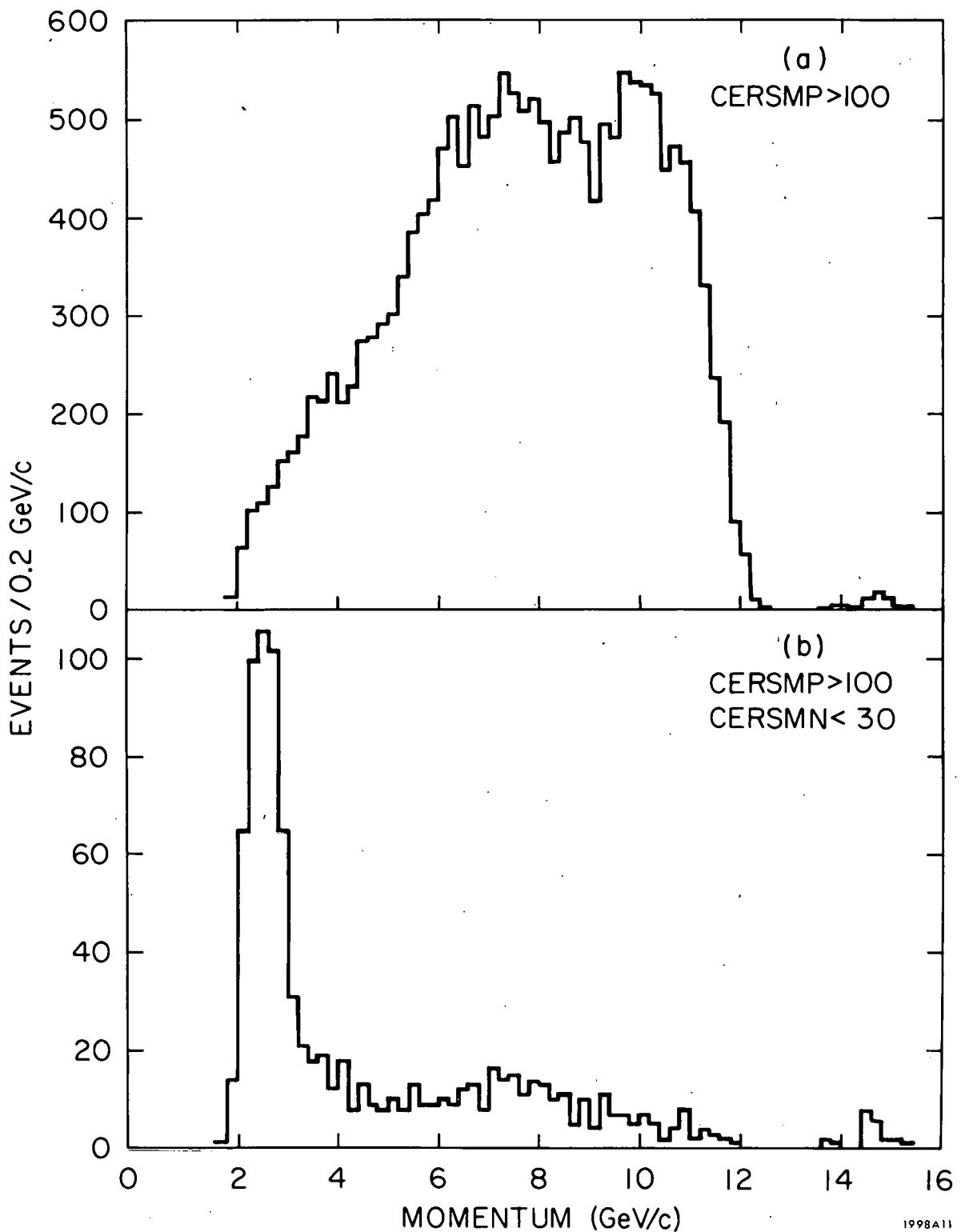
FIG. 21--Momentum spectra of the negative particle. (a) All events for which the positive particle is a pion (CERSMP > 100); (b) same as (a), but the negative particle emitted no light in the Čerenkov counter (CERSMN < 30).
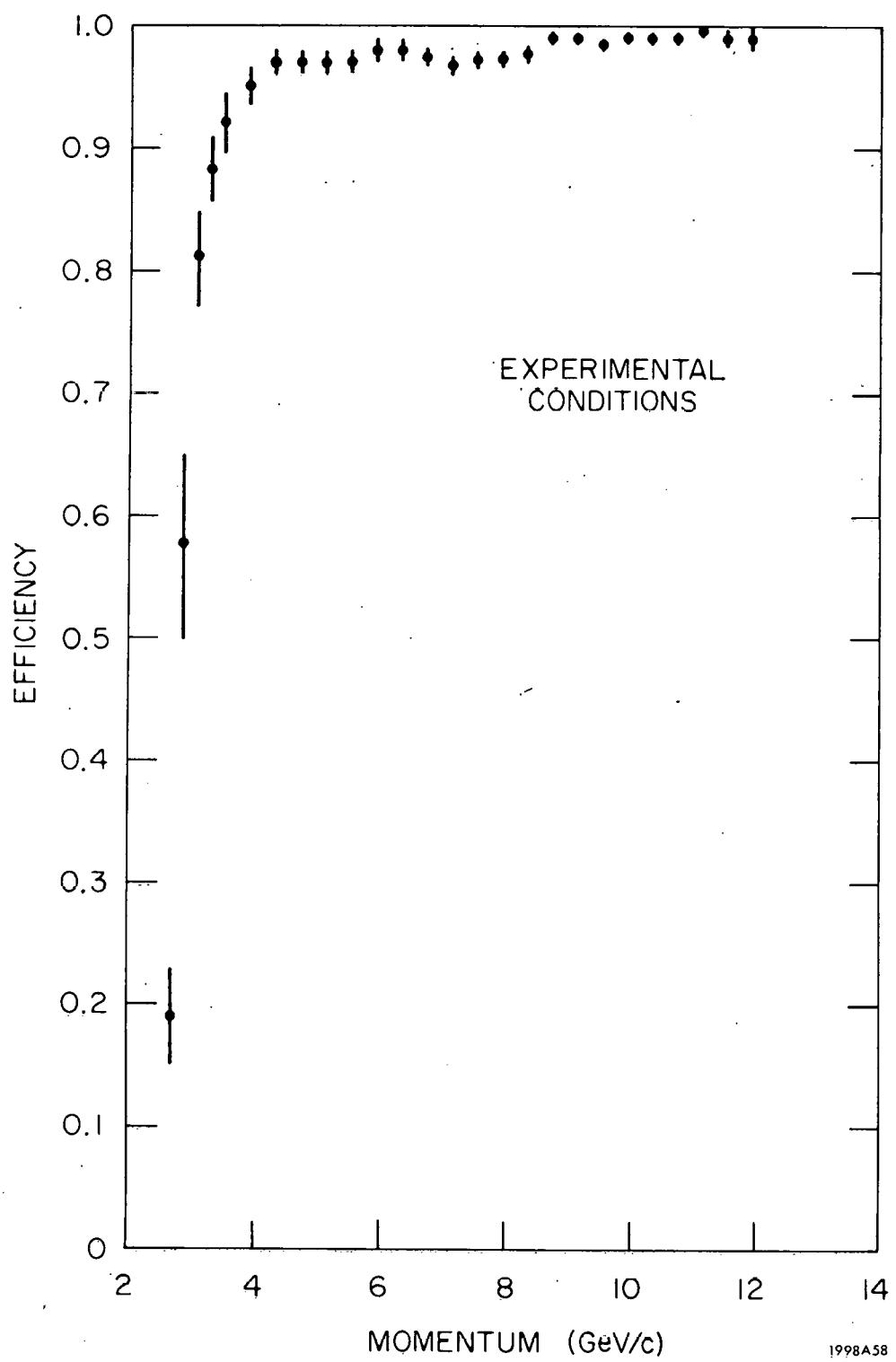
FIG. 22--<u>Lower limit</u> on efficiency of Čerenkov counter as caluclated from Fig. 21.
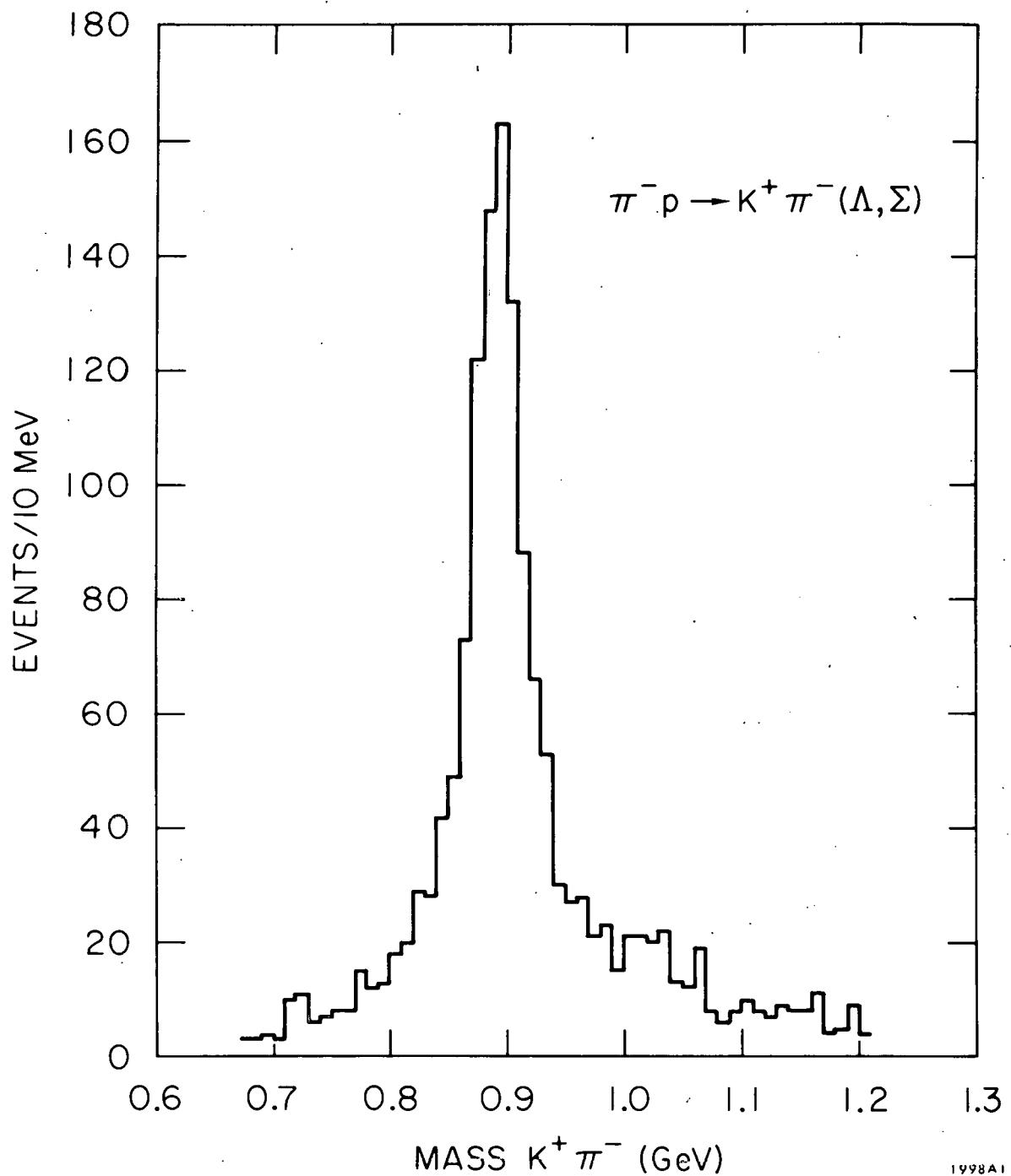
FIG. 23--$K^+\pi^-$ mass spectrum. The events are selected from the vertical band in Fig. 20, subject to the missing mass cut 1.02 - 1.28 GeV.
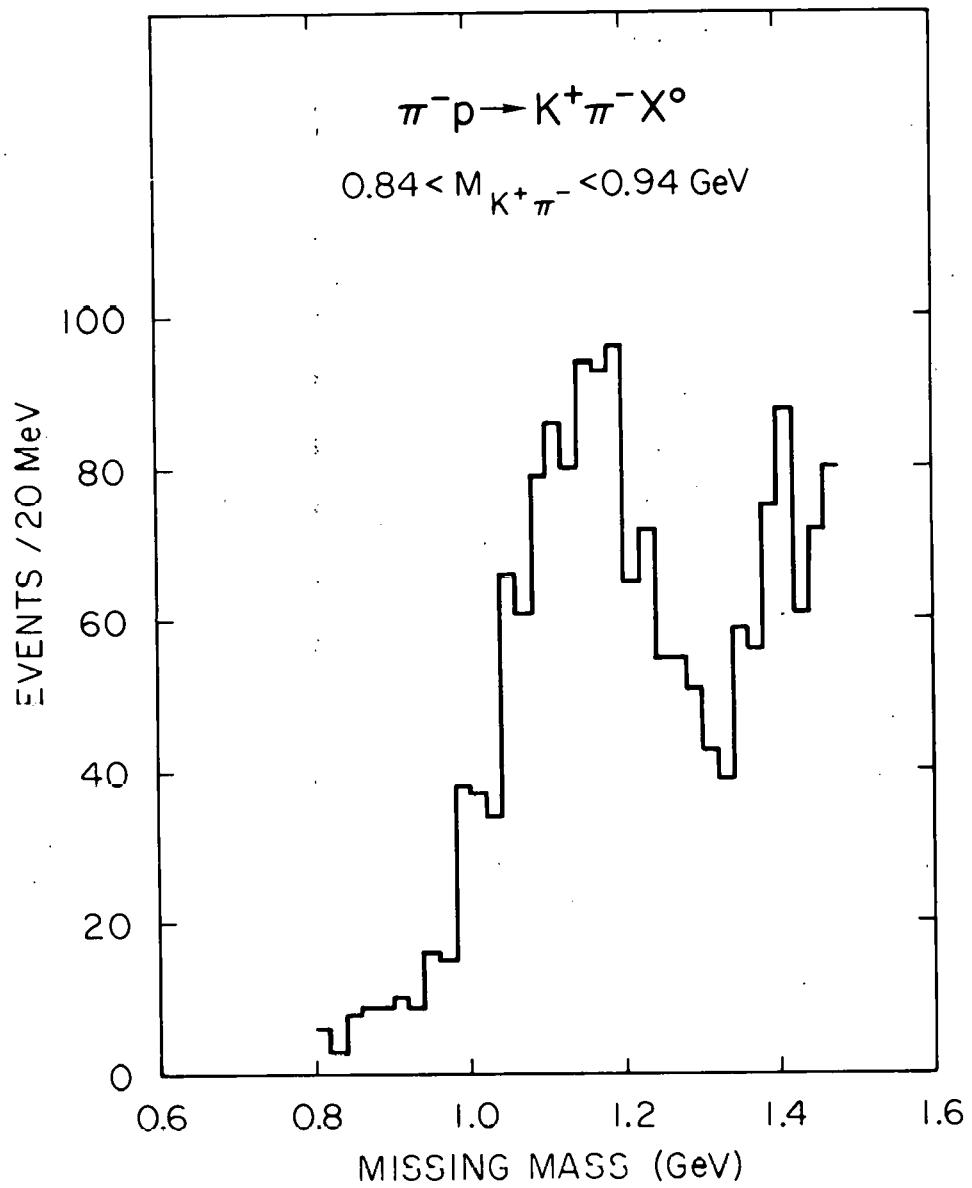
FIG. 24--Missing mass distribution for $K^+\pi^-$ events with $.84 < m_{K^+\pi^-} < .94$ GeV.

The selection of K^+K^- events was also made by cutting on the pulse heights of the two particles separately, rather than simply requiring that the total pulse height for the counter be less than a given cutoff. In addition, a different cutoff was used for particles with momenta below K-threshold than for those above. In Fig. 25 is shown the pulse height spectrum for the negative track, for momenta between 4-9.5 GeV/c (the K^- threshold is 9.2 GeV/c). It is seen that there is quite a clean separation between the particles that are above and below threshold. The same pulse-height spectrum for momenta in the range 9.5 - 11 GeV/c is shown in Fig. 26. Part (a) is subject to a cut requiring the positive particle to be a kaon (CERSMP < 30) and includes ≈50% K mesons, while part (b) is subject to a cut requiring the positive particle to be a pion (CERSMP > 100) and therefore consists largely of pions. It is evident from part (a) that a substantial number of K mesons produce pulse heights as large as ≈65. There are very few pions in this region, however, as is illustrated by part (b). Similar spectra for the positive particle are shown in Figs. 27(a), (b). In this case, parts (a) and (b) are respectively enriched in kaons or pions by selecting K* or non K*-type events (the negative particle is required to be a pion, CERSMN > 100, and the two-particle effective mass, interpreted as $K^+\pi^-$, is respectively required to fall inside or outside the range .84 < $M_{K\pi}$ < .94 GeV). As for the negative track, part (a) illustrates that there are a substantial number of events with pulse height in the range 0-80 while part (b) verifies that they cannot be pions.

By choosing cutoffs of 65 for the negative particle and 80 for the positive one, it is therefore possible to select kaons up to 2 GeV/c above threshold without sacrificing the π - K separation. A comparison of Figs. 25 and 26 indicates that it is not possible to do this with a single cutoff since the pulse
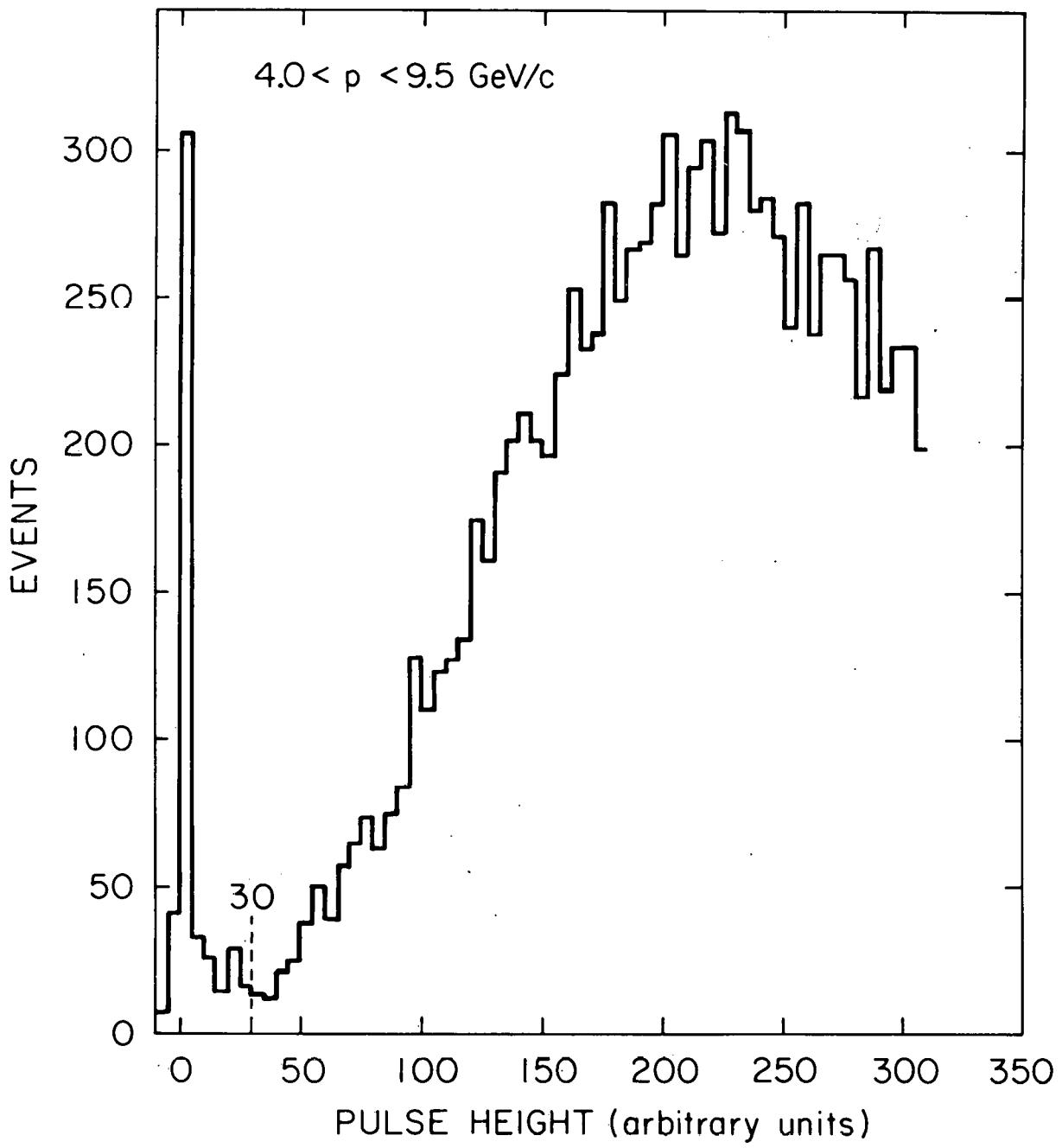
FIG. 25--Pulse height distribution for negative particle with
4.0 < p < 9.5 GeV/c.
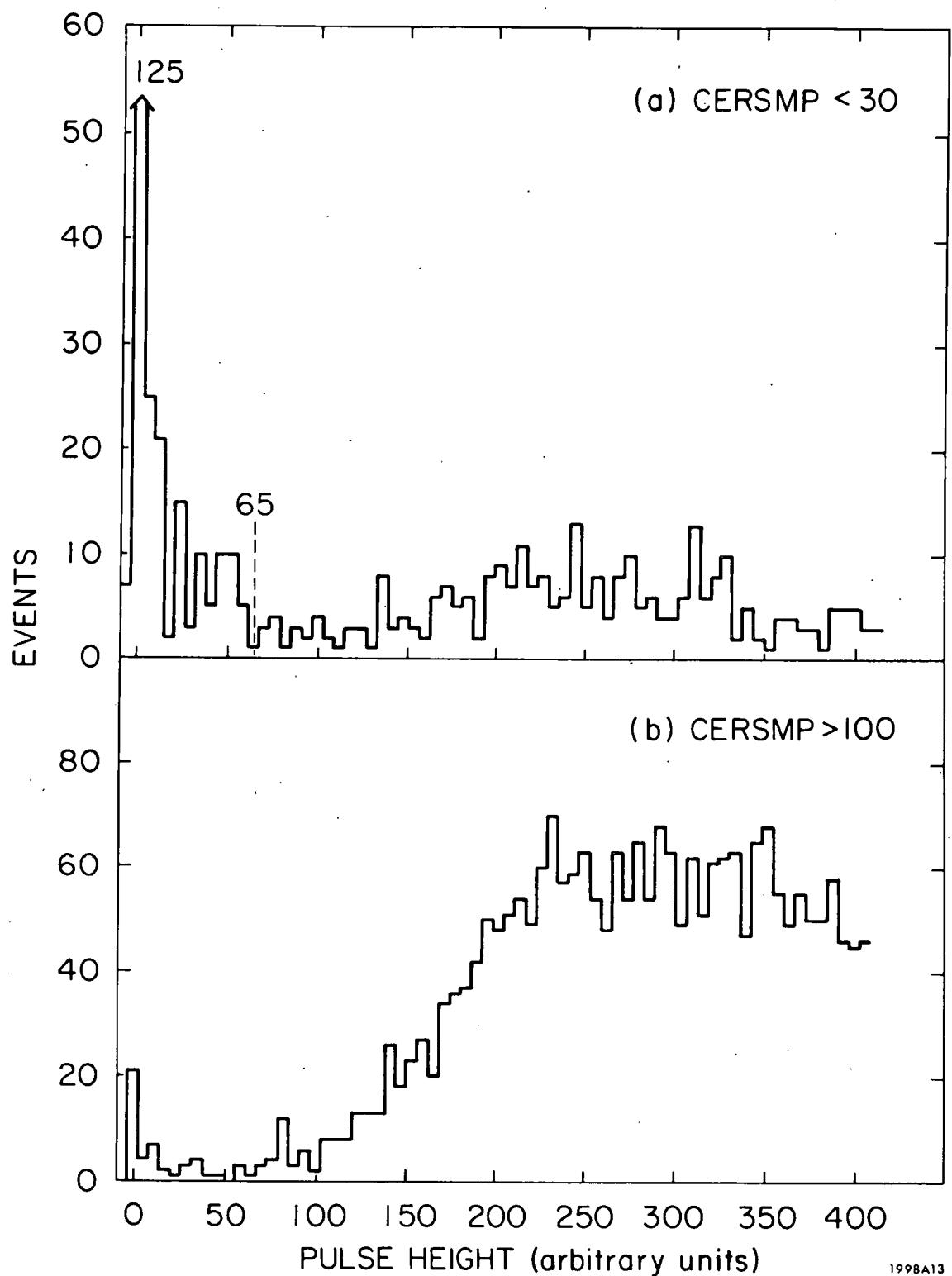
FIG. 26--Pulse height distribution for negative particle with
9.5 < p < 11.0 GeV/c. Part (a) is enriched in K⁻
while part (b) consists largely of π^-. See discus-
sion in text.
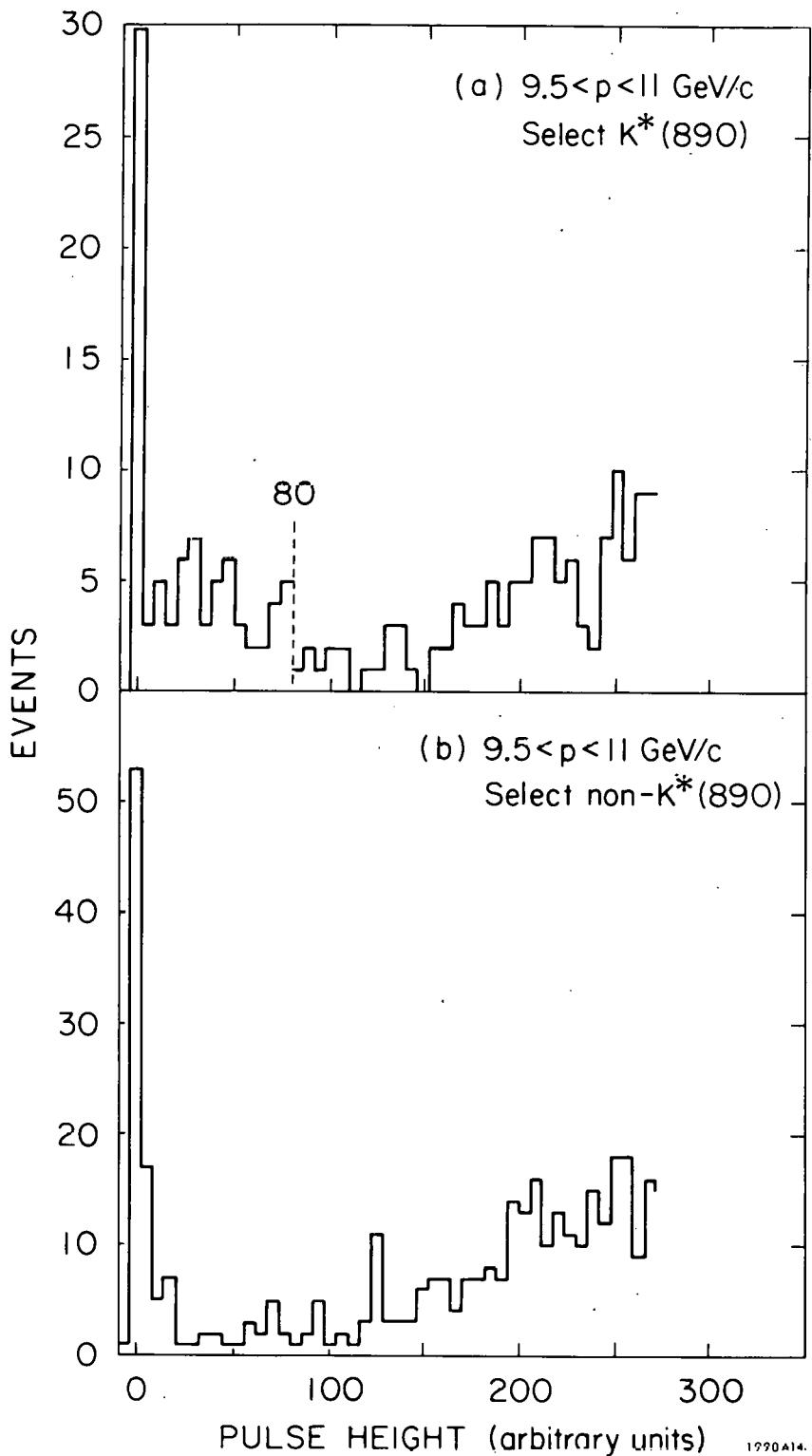
FIG. 27--Pulse height distribution for positive particle with
9.5 < p < 11.0 GeV/c. Part (a) is enriched in K^+
while part (b) consists largely of π^+. See discussion in text.

height spectrum for low momentum pions and high momentum kaons overlap. The effective mass and missing mass for the K^+K^- events selected in this manner are shown in Figs. 64 and 62 and are discussed in Chapter 7.

In conclusion, we have described a large, wide-aperture Čerenkov detector that is capable of extremely good single-particle separation when used as a threshold counter; for example, when operated at a pressure to select K mesons in the approximate momentum range 5 - 10 GeV/c, the π rejection ratio is in excess of 5000:1. In addition, the hodoscopic properties and pulse-height information of the counter have been shown to be very useful for identifying $K^+\pi^-$ and K^+K^- final states. Although the present counter has been demonstrated to be a valuable tool for particle identification, the performance could be further enhanced by increasing the number of optical units and the amount of light detected. Such a chamber would then be an extremely powerful instrument for identification of multibody final states.

CHAPTER 4

EVENT RECONSTRUCTION,

CALIBRATION OF SPECTROMETER, AND KINEMATICS

A. <u>Track Reconstruction</u>

1) Track Reconstruction Downstream

The algorithm for track reconstruction was chosen such that it be at the same time comprehensive, selective, and efficient. The definition of what constituted a legitimate track was made as stringent as possible, subject to the constraint that all real tracks be found with high efficiency. The speed of the reconstruction was an important factor due to the large number of events ($\approx 10^7$).

The raw data, consisting of the scaler readings from each of the wands, was readily converted to measurements of the x, y, η, and ξ positions of the sparks. (These coordinates were respectively determined by the chamber planes with wires at an angle of 0°, 90°, -30°, and $+30^\circ$ with respect to the vertical). Since the measurements of x and y (and of η and ξ) were independent, if more than one spark per chamber was present it was not possible to determine a priori the correct pairing of the coordinates, viz. which x belonged with which y (see Fig. 28). This ambiguity in the coordinate pairing was resolved by matching the x and y measurements with those of η and ξ using the relations

$$\eta = x - y/\sqrt{3}$$
$$\xi = x + y/\sqrt{3}$$

For each downstream chamber, all possible (x, y) pairs were formed and the coordinate lists for that chamber searched to determine whether there existed a
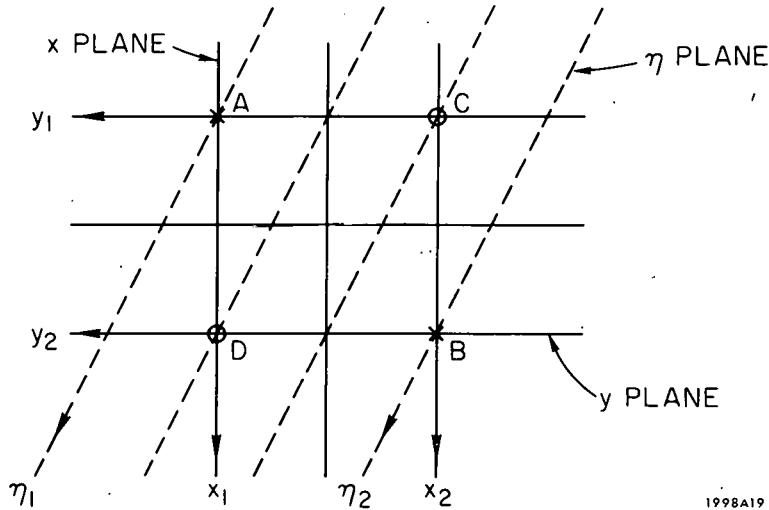
FIG. 28--Illustration of coordinate ambiguity. Suppose sparks occurred at
A and B. From the x, y information alone (x_1, x_2, y_1, y_2), it is
ambiguous whether the sparks occurred at A and B or at C and D.
The η coordinates (η_1, η_2) resolve the ambiguity.

measured η or ξ coordinate within a tolerance $\pm \Delta$ of the calculated η, ξ values.

The tolerance Δ was the distance between the x, y and η, ξ planes multiplied by

the maximum possible slopes, $\frac{d\eta}{dz}$, $\frac{d\xi}{dz}$ for a track detected by the apparatus.

Either an η or a ξ coordinate was sufficient to determine whether or not a

pairing was correct.

When all possible pairings of (x, y) had been exhausted, the procedure was

repeated for (η, ξ) pairs, either an x or a y coordinate determining the correct

combination. No coordinates were deleted during this process, so that a given

coordinate could in principle belong to several matched points.

Once all the matched points had been found for the downstream chambers,

a primary search for tracks was made. This was accomplished by constructing

the line determined by a pair of matched points from chambers 1 and 3, and

searching for a third matched point in chamber 2 or 4, lying within a given

tolerance of this line.[*] The procedure was repeated for matched points from chambers 2 and 4. Each time a third matched point was found, the following procedure was used to optimize the selection of spark coordinates belonging to that "track". All planes of the downstream chambers were searched to select any additional coordinates lying within a distance ALLCOTOL of the line, and a least-squares fit to the resulting set of coordinates was performed. The search was then repeated keeping, for each plane, only the closest coordinate that was within a distance BESCOTOL of the line. If the set of coordinates so selected was unchanged, it was considered that a good track had been found. If the set of coordinates had changed, a new least squares fit was performed and the search with BESCOTOL repeated.

This sequence of least-squares fit and selection with BESCOTOL was iterated either until the set of coordinates selected was stable or until five iterations had been performed. If there were fewer than six coordinates at any step of the selection process, the track was discarded. In addition a final, more stringent, test was imposed requiring that not more than one chamber have coordinates from fewer than three planes.

Each new track that was so found was compared with the existing tracks to see if it was a duplicate; because of the redundancy in the initial track searches, the reconstruction program often found two almost identical tracks where, in reality, there had existed only one. The two tracks were labelled as identical, however, only if they had exactly the same set of coordinates. To ensure that such duplicate tracks would converge to the same coordinates, the entire procedure above was repeated, for all tracks found, beginning with the search with ALLCOTOL as the tolerance.

---

[*] For reference purposes, the spark chambers are sequentially numbered 1-7, chamber 1 being the furthest downstream.

Because of the high spark chamber efficiency, the searching of all (x, y) and (η, ξ) coordinates for matched points was unnecessarily redundant; if the average number of sparks/plane was larger than three or four, it was also very time consuming. A FAST mode of reconstruction, in which only (x, y) pairs were considered for matched points, was instituted. Checks were made that reconstruction efficiency in the FAST mode was the same (within a few per cent) as in the SLOW mode, and the FAST option was therefore used for all the event reconstruction.

Because of the memory time of the spark chambers, tracks which had been produced in a previous interaction (in the same beam burst) were often found. In order to select only those tracks associated with the event producing the trigger, it was required that a signal be present in the hodoscope counters at each end of the track; this ensured that the track was in time with the trigger.

This requirement also permitted a substantial decrease in the reconstruction time. Since all tracks were required to lie in the solid angle subtended by the hodoscope counters which had fired, it was necessary to search only these regions for matched points. The combined effect of this together with the FAST mode of operation, reduced the average reconstruction time per event to ≈ 25 ms from the ≈ 55 ms which was obtained if the entire chambers were searched in the SLOW mode.

2)   Track Reconstruction Upstream

Once all the tracks downstream of the magnet had been reconstructed, the corresponding upstream tracks were found in the following manner: An estimate of the particle trajectory in the upstream chambers was obtained by extrapolating the downstream tracks through the magnet, and a search was

made for sparks in the vicinity of this trajectory. A sequence of extrapolations was implemented: In each case an (x, z) coordinate upstream of the magnet was used, together with the downstream track, to estimate the orbit in the horizontal plane (x-z); the vertical slope and position of the upstream trajectory were then estimated by extrapolating the slope of the downstream track along this orbit, correcting for vertical focussing at the entrance and exit of the magnet.

The first extrapolation was made using the (x, z) coordinates of the center of the target and the downstream track; a search was made for x, y, η, or ξ coordinates within the respective tolerances ALLCOTOLX, ALLCOTOLY, ALLCOTOLN, ALLCOTOLP. If fewer than six coordinates were found, the extrapolation was repeated using, one at a time, each of the x coordinates in chamber 5, the first chamber upstream of the magnet. If this failed to find a potential track, the procedure was again repeated for each of the x coordinates in chamber 6. Note that unlike the downstream track reconstruction, separate tolerances, (ALLCOTOLS) were used for each of the coordinate planes. This reflected the fact that the uncertainties in the extrapolated position and slope of the track were substantially different for x than for y.

When a potential track was found (i.e., more than six plane coordinates), the track was optimized using the same algorithm as for downstream tracks (successive least-square fits and selections with BESCOTOL, followed by the requirement that not more than one chamber be missing more than one coordinate). A check was made that the upstream and downstream tracks matched properly. Assuming a uniform magnetic field, the track, when linearly projected, should have intersected at an xy plane displaced an amount ϵ from the median plane of the magnet, where ϵ can be calculated from the angles of

the tracks. The horizontal distance between the upstream and downstream tracks at this plane was calculated and divided by the associated error. If the resulting deviation exceeded 5 (corresponding to five standard deviations if the errors were gaussian) the track was discarded. A similar test was made requiring that the vertical slopes of the two tracks match properly. For this purpose, a more accurate vertical focussing was employed: In addition to the usual thin-lens focussing effected by the B_z component of the fringe field, correction was made for the effect of the B_x field by two additional thin lenses located inside the magnet aperture. It was determined from a study of the field map that this contribution was of the same magnitude as the conventional fringe-field effect.

Whenever a potential upstream track was discarded because it failed to match properly, the search was continued by extrapolating to any x coordinates in chambers 5 or 6 that had not yet been considered.

B.   Alignment and Constants

The track reconstruction efficiency, as well as a correct determination of the momenta and angles of the tracks, depended sensitively on the alignment of the spark chambers; considerable care was therefore taken in this regard.

The groups of spark chambers before and after the magnet were premounted and aligned in the laboratory, and the resulting spark chamber packages surveyed into position when mounted in the experimental area. This constituted the physical alignment of the chambers.

A second more accurate alignment of the individual planes was accomplished using the particle tracks; in this case, it was the coordinate systems with respect to which the plane coordinates were measured that were shifted,

rather than the planes themselves. Prior to, and periodically during, the data-taking, several runs were made with the analyzing magnet OFF, and the target empty, so that beam particles passed undeflected through both sets of spark chambers; the front chambers were displaced in the x direction so that the deadened region was removed from the beam path.[*] The tracks were reconstructed and the deviations of the spark coordinates from the reconstructed line plotted for each plane. Whenever the average deviation for a plane was non-zero, the coordinate system for the plane was shifted accordingly; the shifts were $\approx .1 - .5$ mm. In this way, the entire set of spark chambers was aligned with respect to one another.

When similar test runs with the magnet ON were analyzed, it was found that the average deviations had shifted from zero, and that the shift occurred in opposite directions for tracks with positive and negative horizontal angles. This effect, which has been observed in optical-chamber experiments, was produced by the electron drift occurring prior to spark formation. During the ≈ 100 ns delay between the application of the high-voltage pulse and the beginning of spark formation, the electrons drifted towards the positive high-voltage plane. At the time of breakdown, the observed position (x, y, η, ξ) of the particle had shifted $\approx \frac{1}{4}$ mm from the true position, the exact shift depending on the angle of the tracks. (For tracks perpendicular to the planes, there is no shift.) This effect was corrected for by shifting the plane coordinate systems in a direction opposite to that of the electron drift, the displacement being $\approx \frac{1}{2}$ of a gap width. The observed x, y, η, and ξ positions of the track then corresponded correctly with this "effective" z position of the planes.

---

[*] The spark chamber mounting was designed such that it could be shifted 10 cm in the -x direction and then restored to its original position without affecting the alignment.

The set of constants for the chamber and plane positions were determined as discussed above for the December and January cycles separately. Only one set of constants was used for each cycle, however; no realignment or changing of constants was done on a run-to-run basis. A typical set of deviation distributions obtained during the data analysis has already been presented in Fig. 8 for several planes. The spatial resolution of each plane was 1/3 - 1/2 mm.

C. Reconstruction Efficiency

The efficiency of the track reconstruction, and the optimal tolerances to be used, were determined by hand-scanning of events. The x, y, η, and ξ coordinates for each chamber, together with a list of the tracks reconstructed by the program and the hodoscope counters which had fired, were printed out for several hundred events. These events were individually reconstructed by several physicists to determine the efficiency of the program for finding real tracks and the extent to which it created spurious ones. By repeating this process with different values of BESCOTOL, ALLCOTOL, ALLCOTOLX, etc., the efficiency and selectivity of the reconstruction were maximized. A list of the final tolerances used in the analysis is given in Table 2. The inefficiencies of the program in finding tracks downstream of the magnet, and in successfully crossing these tracks once found, were each determined to be $2 \pm 2\%$ for this set of constants.

D. Hodoscope and Spark Chamber Efficiencies

The efficiencies of the spark chambers and the A and B hodoscope counters could be determined from tracks collected during the data-taking itself and could therefore be calculated on a run-by-run basis throughout the experiment.

- 83 -

TABLE 2

The tolerances, in millimeters, that were used for track recon-
struction; each quantity is defined in the text. The letters in
parentheses indicate plane type.

ALLCOTOL	5	ALLCOTOLX	(x)	5
BESCOTOL	2	ALLCOTOLY	(y)	7.5
		ALLCOTOLN	(η)	5
		ALLCOTOLP	(ξ)	5

The efficiency for an individual plane (i) was given by the ratio of the number of tracks for which that plane coordinate was present divided by the total number of tracks, subject to the condition that each track would have been reconstructed whether the coordinate from plane (i) was present or not. The hodoscope counter efficiencies were calculated in a similar manner.

The overall spark-chamber efficiency for track reconstruction in the upstream and downstream chamber packages is presented in Table 3 for various blocks of runs throughout the experiment. Two numbers are presented, one corresponding to tracks which intersected the active area of all chambers in the respective group and one corresponding to tracks that missed the active area of one chamber. The individual gap efficiencies have already been presented in Fig. 9. The only significant variation from run-to-run was a gradual decrease in efficiency as the gas became slightly poisoned (ref. Section 2.D). When this occurred the chambers and gas system were purged, and the chamber efficiency returned to normal.

Studies were made of the efficiency as a function of position in the chambers, but no variation was observed. It should also be noted that the downstream section of the apparatus subtends a sufficiently small solid-angle that the decrease in efficiency that may be expected for very wide-angle tracks was not a problem.

The hodoscope efficiencies were also calculated for several blocks of runs and no significant variations were noted. The average efficiencies for all data runs are presented in Table 4.

E. Momentum Computation

Given a particle trajectory through a magnetic field, with the track measured upstream and downstream of the magnet, there are several

TABLE 3

Spark chamber efficiency for track reconstruction in the upstream and downstream groups of spark chambers, for blocks of runs throughout the experiment. Two numbers are presented in each case, one corresponding to tracks which intersected the active area of all chambers in the respective group, and one corresponding to tracks that missed the active area of one chamber.

Run Number	Downstream Track		Upstream Track	
	4 chambers	3 chambers	3 chambers	2 chambers
24 – 38	.919	.633	.976	.871
62 – 74	.971	.799	.988	.911
79 – 91	.975	.808	.989	.907
92 – 112	.979	.827	.981	.889
118 – 135	.983	.848	.876	.140
165 – 176	.987	.863	.987	.908
177 – 188	.979	.820	.988	.889
189 – 200	.978	.821	.986	.856
201 – 210	.969	.792	.984	.811
211 – 222	.993	.896	.994	.936
223 – 232	.996	.924	.993	.939
233 – 249	.994	.903	.989	.917
250 – 261	.993	.908	.988	.914
262 – 271	.994	.904	.990	.922
272 – 281	.993	.894	.990	.914
282 – 300	.990	.876	.991	.896
302 – 310	.988	.865	.990	.894
311 – 320	.994	.902	.994	.931

TABLE 4

Efficiencies for the Counters in Hodoscope A and Hodoscope B

HA1	.960	HB8	1.0
HA2	.955	HB9	.972
HA3	.966	HB10	..903
HA4	.970	HB11	.987
HA5	.986	HB12	.994
HA6	.983	HB13	.947
HA7	.990	HB14	.992
HA8	.980	HB15	.996
HA9	.990	HB16	.994
HA10	.989	HB17	.995
HA11	.986	HB18	.992
HA12	1.0	HB19	.950
HA13	.982	HB20	.979
HA14	.974	HB21	.932
HA15	.994	HB22	.966
HA16	.982	HB23	.994
HA17	.991	HB24	.964
HA18	.990	HB25	.996
HA19	.976	HB26	.973
HA20	.976	HB27	.997
HB1	.990	HB28	.962
HB2	1.0	HB29	.995
HB3	.994	HB30	..965
HB4	.996	HB31	.999
IIB5	.987	HB32	.960
HB6	.996	HB33	1.0
HB7	.982	HB34	.960

alternative methods of computing the momentum. One may calculate it using the angles of the track in front and back of the magnet without any knowledge of the track position. Alternatively, it may be calculated from a knowledge of the vector describing the trajectory on one side of the magnet, and any of the measured points on the other side. Either of these methods does not make full use of the information available, as would a least-squares fit.

The method which was used in this experiment may be called an "improved vector-point" calculation. The momentum was calculated using the reconstructed downstream track together with a single point on the upstream track. However, the z-coordinate of the upstream point was chosen by minimizing the variance of the calculated momentum. Specifically, one has

$$P = \frac{B}{a_1 - a_2}$$

where a_1 is the measured downstream slope in the x-z plane (which was perpendicular to the magnet field) and a_2 is the upstream slope as determined from the upstream point and the intercept of the downstream track at the center of the magnet. The constant B was separately determined for each track by analytically integrating a multipole expansion of the field map along the trajectory of the particle. The variance of P (assuming B to be constant) is then

$$V(P) = \left(\frac{P^2}{B}\right)^2 \left[V(a_1) + V(a_2) - 2C(a_1, a_2)\right]$$

where $V(a_1)$, $V(a_2)$ and $C(a_1, a_2)$ are respectively the variances and covariance of a_1 and a_2. By minimizing this expression with respect to the z-coordinate of the upstream point, one may optimize the vector-point calculation. It is

interesting to note that for tracks confined to the horizontal plane (and for other reasonable assumptions such as equal spatial resolutions in each of the chambers), this calculation gives exactly the same result as a least-squares fit to the upstream and downstream measurements. A three-dimensional least-squares fit was not attempted because it requires a precise knowledge of the vertical focussing if it is to substantially improve the calculation.

The accuracy to which the momentum can be determined depends on the uncertainty in B and the variances of a_1 and a_2. The variances of a_1 and a_2 vary according to the number of spark coordinates measured, but may be evaluated in a straightforward manner given this information. For tracks with all coordinates present (which was $\approx 60\%$ of the tracks), $\sigma(a_1) \approx .2$ mr and $\sigma(a_2) \approx .4$ mr. These uncertainties, by themselves, imply a momentum resolution varying from $\approx .15\%$ at 3 GeV/c to $\approx .8\%$ at 15 GeV/c. The uncertainty in B was determined by comparing the analytical integrations of the multipole expansion with a step-by-step numerical integration of the field for various particle trajectories. In all cases the error was found to be less than $\approx .15\%$. The momentum resolution was therefore limited at the higher momenta by the spatial resolution of the spark chambers. At the lower momenta, the uncertainly in B began to be important, but the dominating factor was multiple scattering in the A hodoscope which at 3 GeV/c was $\approx .6$ mr. The overall momentum resolution for tracks with all coordinates present therefore varied from $\approx 1/3\%$ at 3 GeV/c to $\approx .8\%$ at 15 GeV/c. For tracks with coordinates missing in one of the front chambers, the only difference is that the combined contribution of the variances $V(a_1)$, $V(a_2)$ to the momentum uncertainty was increased $\approx 50\%$.

F.   Calibrations and Resolutions

1)   Calibration of P, θ, φ Hodoscopes

Although the calculation of the dispersion and resolution of the P, θ, φ hodoscopes was fairly straightforward, these quantities were also determined directly with the spectrometer; the same set of test runs were used as for the alignment of the spark chambers; the target was empty and several runs were made with the analyzing magnet ON and OFF.

For the momentum calibration, cuts were made selecting only those beam particles which counted in a particular bin of the P hodoscope, and histograms were compiled of the corresponding momentum distribution as measured by the spectrometer. The central momentum value of the distributions was plotted as a function of bin number. The dispersion measured in this way was .55% per bin, in excellent agreement with the value of .54% calculated from the first-order optics of the beam. The resolution of each momentum bin, ΔP_{BIN}, which was calculated to be $\pm .27\%$, could not be determined from this data since the width of the distributions was dominated by the $\pm .8\%$ uncertainty (for 15 GeV/c particles) of the spectrometer measurement. An upper limit on ΔP_{BIN} could be obtained from the observed missing mass resolution, however, since the uncertainty in the incident beam momentum contributed to it substantially. The width of the observed missing mass distribution for $\pi^- p \rightarrow \pi^+ \pi^- \pi^- p$ events, where only the proton was missing, was ≈ 185 MeV. By unfolding the uncertainty in the missing mass contributed by the spectrometer, it was determined that ΔP_{BIN} was $\lesssim .3\%$.

The dispersion of the θ and φ hodoscopes was determined in the same manner as for the P hodoscope. The distribution of incident angles, as measured by the spectrometer, was compiled for beam particles counted

in each θ and φ bin. The measured dispersion and angular resolution for both hodoscopes was consistent with the expected values: respectively, .88 mr/bin and ±.5 mr, where the latter quantity includes multiple scattering in the XY hodoscope and target.

2) Mass Resolutions and Calibration of P_{inc} , $\int Bd\ell$

An accurate calibration of the incident beam momentum and of the field in analyzing magnet was possible by measuring the mass of the K^o and the nucleon. The missing mass and $\pi^+\pi^-$ mass resolutions could also be determined from the observed "width" of these particles.

A sufficiently large number of K^o's were detected (primarily from the reactions $\pi^-p \to K^o(\Lambda, \Sigma)$ that a measurement of the K^o mass could be made for blocks of 5-6 runs throughout the course of the experiment. The variations in these measured values were consistent with the small fluctuations in the field of the analyzing magnet that were recorded by the Hall probe; consequently no ad hoc changes in the magnetic field were made during the analysis on a run-to-run basis. In addition, the absolute value of the K^o mass, averaged over all runs, agrees with the presently accepted value[51] of 497.79 MeV to within .1%. This is quite good agreement since the measurements of the magnetic field were not made to an accuracy better than .1 - .2%.

Shown in Fig. 29 is the mass distribution for all K^o's decaying within the target and with a missing mass of .98 - 1.28 GeV. The curve shown is the fit to the mass spectrum that is obtained with a gaussian resolution function and a linear background. It yields a K^o mass of 497.4 MeV and a resolution, σ, of 6.5 MeV. A conservative estimate of the error in these quantities, including systematic effects, is ±1 MeV. This measured
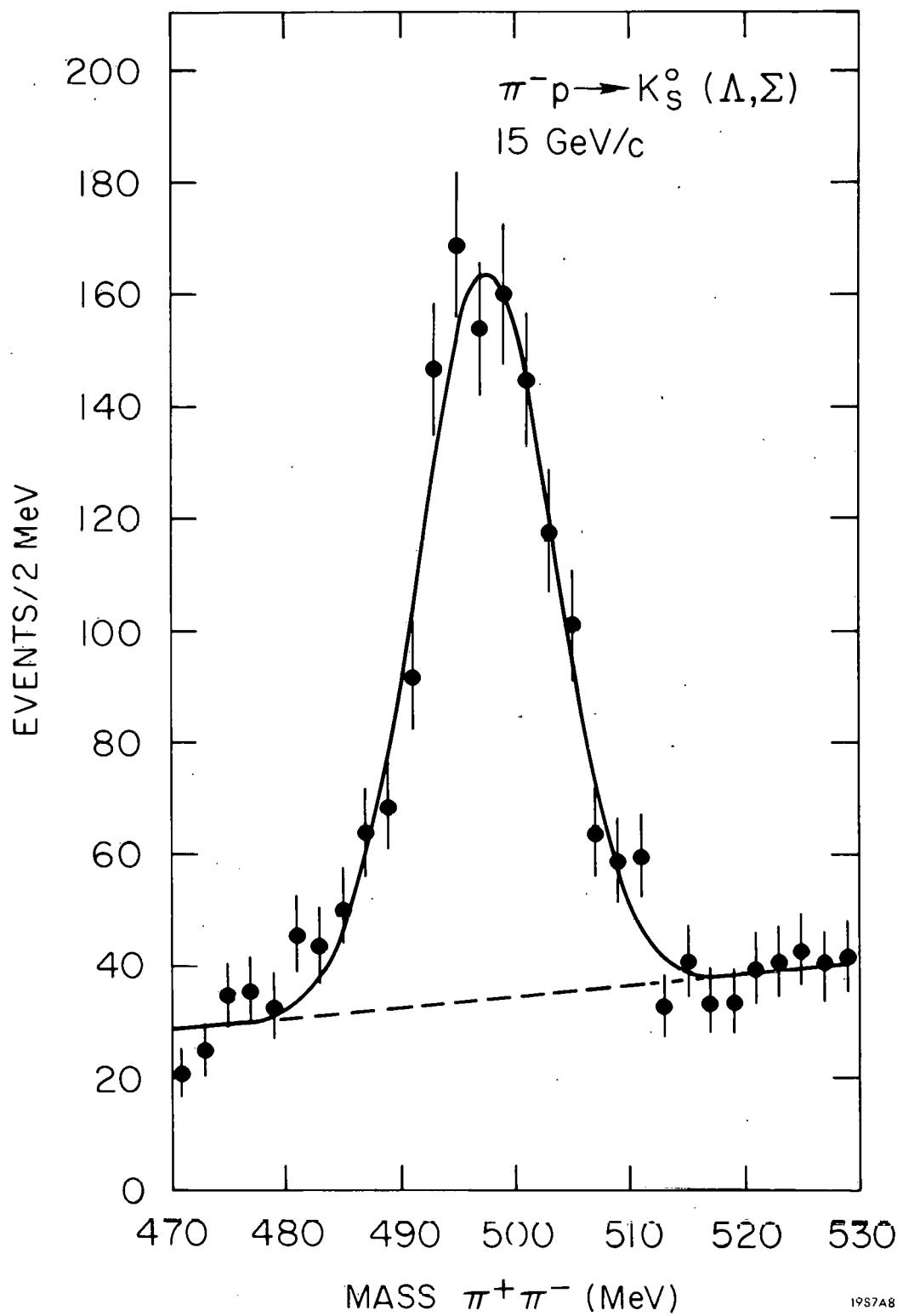
FIG. 29--Observed K^0 mass distribution. The spectrum includes all K^0's decaying within the target, subject to the missing mass cut .98 - 1.28 GeV. The curve is a fit to the data with a gaussian resolution function and a linear background. The parameters are given in the text.

resolution corresponds to ≈ 8 MeV at the rho mass, which is also the value

calculated from the known spark chamber and momentum resolutions.[*] The

calculations of the $\pi\pi$ mass resolution indicated that multiple scattering in

the target was a substantial contribution; this was verified by the fact that

the observed K^O mass distribution was approximately 3-4 MeV narrower

(FWHM of ≈ 11-12 MeV instead of 15 MeV) when only K^O's decaying down-

stream of the target were selected.

The absolute magnitude of the incident beam momentum was determined

in a similar fashion by observing the missing mass distribution for the

nucleon; systematic deviations of 10-25 MeV in the measured neutron "mass"

were observed. In most cases these deviations were correlated with recorded

variations in the beam magnets and the incident momentum was therefore

updated by centering the observed nucleon distribution at 938 MeV. These

calibrations were made to an accuracy of ≈ 10 MeV for blocks of five runs

each throughout the course of both data-taking cycles. The missing mass

resolution was measured to be ± 100 MeV at the nucleon mass for events in

which two particles were detected by the spectrometer; this agrees with the

calculated value to withing ≈ 5 MeV.[†] For $\pi^+ \pi^- \pi^- p$ events, where all three

pions were detected, the measured resolution was ± 90 MeV. The MM dis-

tribution for $\pi^+ \pi^- n$ events is shown in Figs. 32-33.

---

[*] The actual mass resolution for each event depends, of course, on the decay angles of the π^+ and π^- and also on just how many sparks were present for each track. The number, 8 MeV, is an estimated average over these various conditions.

[†] All resolutions quoted are half-width-at-half-maximum unless specified otherwise.

The momentum transfer resolution was calculated to be $\sigma \approx .03\sqrt{-t}$ $(GeV/c)^2$. Since the calculated errors for the $\pi\pi$ mass and missing mass agree well with the measured values, it is believed that this calculation should also be reasonably accurate. [*]

G. **Event Selection and Kinematic Reconstruction**

1) DST

After the events had been geometrically reconstructed and the momentum of each track determined, a data summary tape (DST) containing all the pertinent information for each event was created. The only selection criterion for the primary two-body DST was that each event should have two crossing tracks, no additional "hodoscope-agreeing" tracks downstream of the magnet, and a total charge of zero (i.e., one positive and one negative track). [†] The presence of additional hodoscope-agreeing tracks indicated that the event was not a three-body final state.

The contents of the tape included selected information from the scintillation counters and spark chambers, as well as the position and momentum vector of each track, and the kinematical quantities of interest. The vertex of each event was calculated; it was defined to be that point for which the sum

---

[*] Some of the resolutions quoted here differ slightly from those quoted in earlier publications. [32a] As noted above, each of the errors quoted, whether for momentum transfer, $\pi\pi$ mass, or missing mass may vary somewhat depending on exactly what distributions are considered. The values quoted here are perhaps somewhat more representative of the entire data sample than those presented earlier.

[†] The term "hodoscope-agreeing" is used to refer to those tracks which intersected at each end a hodoscope counter which had fired, indicating that the track occurred in time with the event.

of the distances-squared from the point to each of the tracks was a minimum. Note that the requirement that the two tracks have a common origin was not used as a constraint in the geometrical reconstruction because of the relatively large multiple scattering in the target.

2) Kinematics

The kinematic reconstruction was relatively straightforward. For events of the type $\pi^- p \rightarrow \pi^+ \pi^- X^o$, where the X^o is undetected, there were four unknowns, the mass and momentum of the X^o, and four constraints, the conservation of energy and momentum.[*] It was therefore possible to calculate the effective mass and momentum of X^o. Once this missing mass was determined, $\pi^+ \pi^- n$ events were selected by imposing a cut on the missing mass distribution. For this class of events, it was possible to perform a one-constraint kinematic fit. This was not attempted, primarily because the magnitude of the incident beam momentum, p_{inc} was determined with less confidence and precision than the momenta and angles of the secondary particles. Rather, the constraint was used to eliminate p_{inc} so that the momentum transfer t and other kinematic quantities were calculated solely from the angles of the beam particle and the momenta and angles of the outgoing π^+ and π^-.

It should also be noted that correction was made for the energy loss of the incident and final state particles in the target and spectrometer.

---

[*] Here and elsewhere in the text, general remarks concerning the reaction $\pi^- p \rightarrow \pi^+ \pi^- X^o$ apply equally well to $\pi^- p \rightarrow K^+ K^- X^o$, $p\bar{p}X^o$.

3)   Cuts and Selection Criteria

As noted above, the only requirement imposed when selecting events for the DST was that two and only two tracks were detected by the spectrometer. The motivation for this was the desire to be able to easily study the effect on the kinematic distributions of any additional cuts which might be made.

A number of non-kinematic cuts were employed in selecting "good" events for data distributions and further analysis. These included restrictions on the vertex of an event and a requirement that the signature in the P, θ, and φ hodoscopes be unique. For $\pi^+\pi^-$ events, a signal was required from the Čerenkov counter. Distributions of the x, y, and z coordinates of the vertex, for events with a $\pi\pi$ mass in the rho region and .65 < MM < 1.35 GeV, are shown in Fig. 30. The dashed lines indicate the standard cuts which were used for event selection. Also shown in the figure is the distribution of DIST, the sum of the squares of the distances from the vertex to each track. Distributions of the total pulse height from the Čerenkov counter, both before and after the cut selecting $\pi^+\pi^-$ events, were presented in Fig. 10 and discussed in Section 2.E.

All further analysis and data distributions to be presented are based on events subject to these cuts on the vertex, beam hodoscopes, and (for $\pi^+\pi^-$ events) Čerenkov counter.
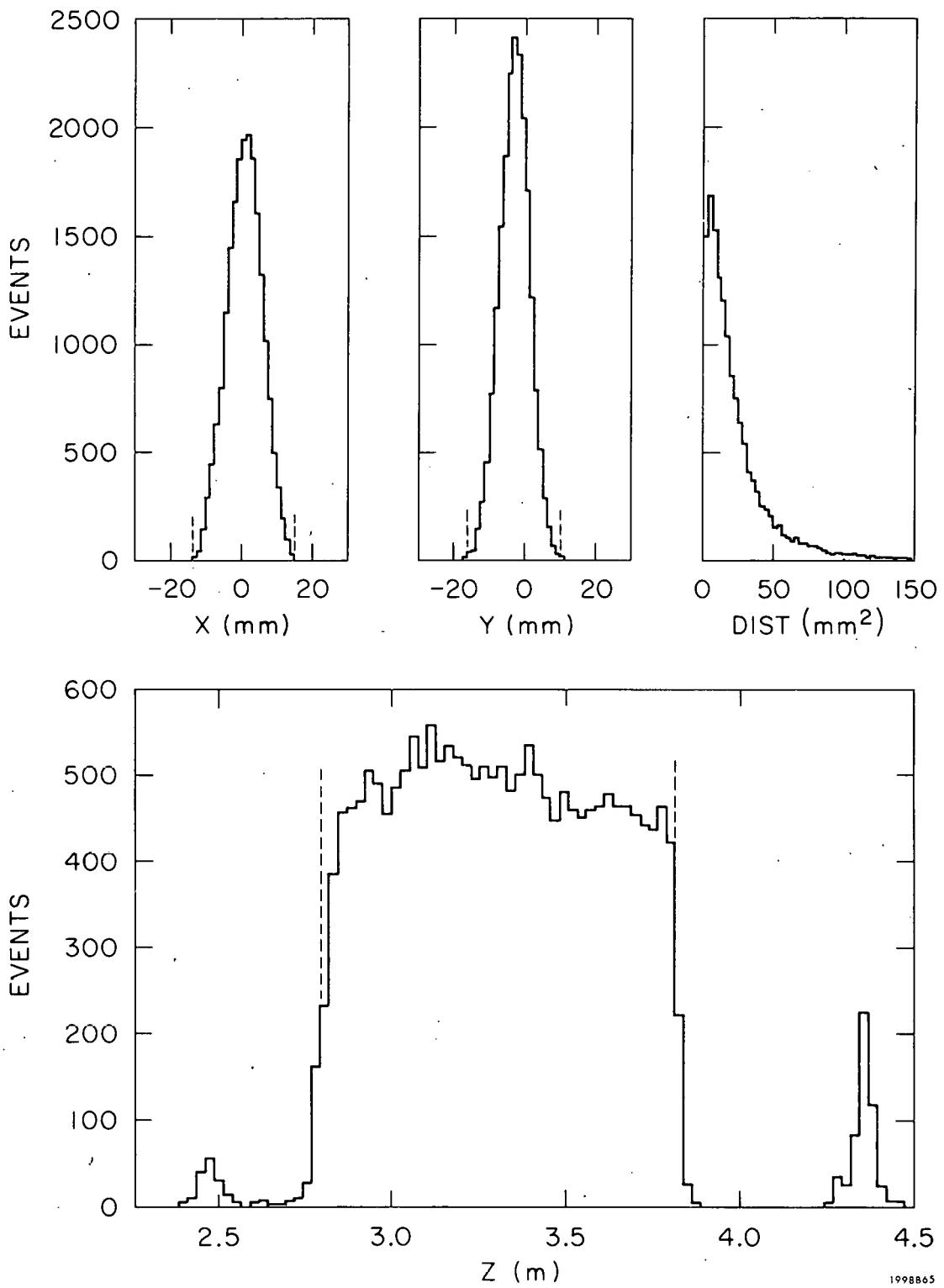
FIG. 30--Vertex distributions. x, y and z are the vertex coordinates for each event. DIST is defined in the text. The dashed lines indicate the cuts made. The clusters of events at 4.4 m and 2.5 m in the z-distribution correspond to events produced in the XY hodoscope and spark chamber number 7.

CHAPTER 5

KINEMATIC DISTRIBUTIONS AND ANALYSIS OF $\pi^+\pi^-$n EVENTS

It has characteristically been true that the detection efficiency of spark chamber spectrometers is non-uniform as a function of the kinematic variables of interest. One is not permitted the relative luxury of a bubble chamber or similar 4π detector: namely, that the observed data distributions closely resemble those produced in nature. Rather, it is important, even when observing qualitative effects that one understand the efficiency of the detector; only then may it be discerned which aspects of a data distribution are produced by nature and which are produced by the apparatus.

To obtain quantitative information on the angular distribution or differential cross section, it is necessary either to weight each event by the reciprocal of its detection probability or to fit the observed spectra to the expected theoretical distribution function modified by the detection efficiency of the apparatus. The major part of this chapter is concerned precisely with this task.

It is nonetheless very instructive to examine the raw data distributions in order to obtain a feeling for the data actually observed. Consequently, the observed $\pi\pi$ mass, missing mass, momentum transfer, and angular distributions are presented and briefly discussed below.

Qualitatively, the detection efficiency of the spectrometer in this experiment, as a function of the $\pi\pi$ effective mass, reaches a maximum in the vicinity of 500 MeV and falls smoothly and slowly as the mass increases. The detection efficiency also decreases slowly with increasing momentum transfer, but is quite independent of t for momentum transfers smaller than 1-2 m_π^2. The acceptance of the apparatus as a function of the dipion decay angles is discussed below.

A. Raw Data Distributions

The $\pi^+\pi^-$ effective mass distribution for all $\pi^+\pi^- X^0$ events, irrespective of the mass of the X^0, is shown in Fig. 31. It is apparent that a strong ρ^0 signal is detected even when no cut is made on the missing mass; a substantial K^0 signal is also observed. The shoulder at 1.2 GeV is indicative of the f^0 meson, but the mass spectrum in this region is suppressed because the acceptance of the apparatus falls off at higher $\pi\pi$ masses and for higher spin resonances.

The corresponding missing mass (MM) distribution for events in the rho region, i.e., $.665 < m_{\pi\pi} < .865$ GeV is shown in Figs. 32-33. Figure 32 shows the entire distribution and illustrates the preponderance of events with large missing masses. This reflects the fact that at 15 GeV the inelastic $\pi^- p$ cross section is dominated by higher multiplicity events than n=3. Figure 33 presents the MM spectrum up to 1.5 GeV for three different cuts on the information from the target counters. In the top spectrum, which includes all events, the n and Δ^0 (1236) bumps stand out clearly. The middle spectrum corresponds to the cut which was used for selecting neutron events, while the lowermost spectrum results if only those events are selected with no signal from the target counters. It is evident that the number of $\pi^+\pi^-\Delta^0$ events selected may be strongly varied by choosing different cuts on the target counter information. In particular, the background of $\pi^+\pi^-\Delta^0$ events under the neutron bump may be reduced by imposing a target counter cut. Note, however, that in the bottom MM spectrum a substantial number of $\pi^+\pi^- n$ events have been rejected; this is primarily caused by delta rays which are produced in the target and then fire the surrounding counters, though a certain fraction of the loss is produced
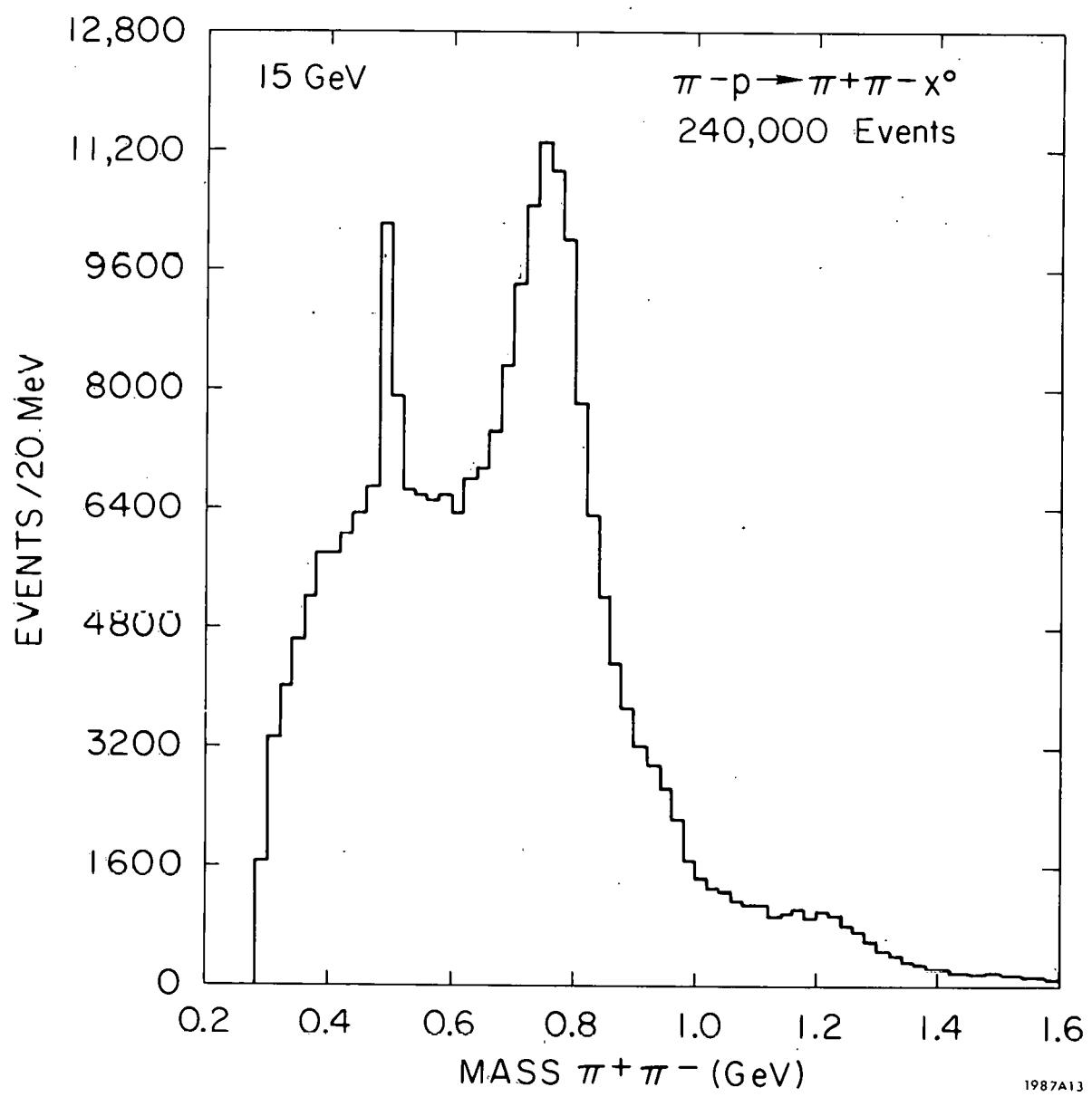
FIG. 31--$\pi^+\pi^-$ mass distribution for all events.
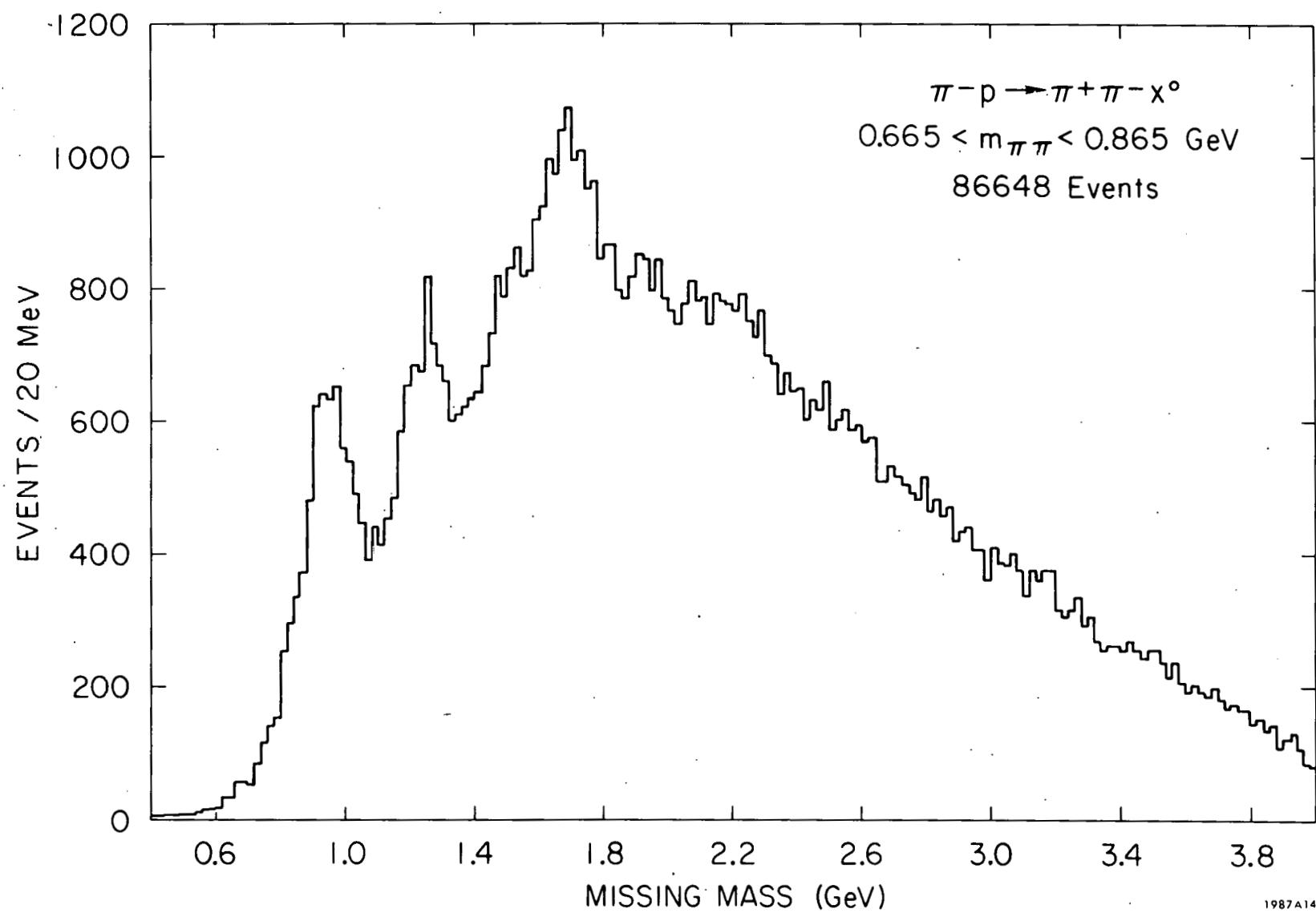
FIG. 32--Missing mass distribution for all $\pi^+\pi^-$ events with $.665 < m_{\pi\pi} < .865$ GeV.
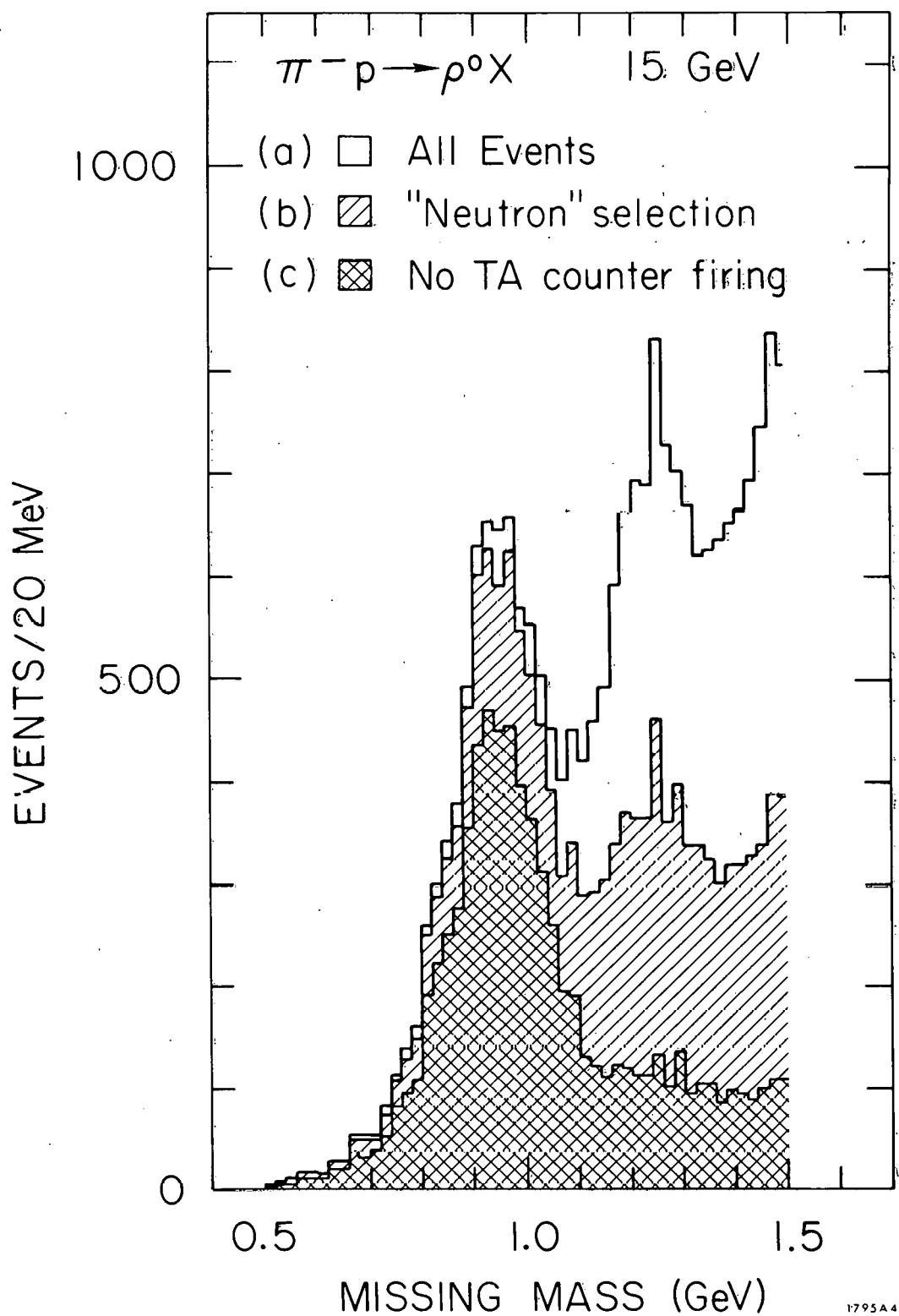
FIG. 33--Missing mass distribution for all $\pi^+\pi^-$ events with .665 < $m_{\pi\pi}$ < .865 GeV, subject to different cuts on the target-counter information. See discussion in text.

by the neutrons counting. The number of events lost will vary depending on the momentum transfer to the neutron, and also, perhaps, on the decay angles of the π^+ and π^-. It is for this reason that such a stringent cut was not employed. The cut which was employed rejected those events for which two or more counters fired, with at least one of the counters being an outer one. The following possibilities were therefore allowed for a $\pi^+\pi^- n$ event, without its being rejected:

(1) the neutron or delta ray counted in an outer counter

(2) any number of delta rays and/or the neutron counted in the inner counters.

It was unlikely that a neutron or a delta ray counted in both an inner and an outer counter.

Imposing this target counter cut and the missing mass selection $.80 < MM < 1.06$ GeV, one obtains the $m_{\pi\pi}$ spectrum shown in Fig. 34. It is similar to the spectrum in Fig. 31 for all missing masses, but there is less background and the rho stands out more clearly. The signal at the mass of the f^0 is also a bit more respectable, though it is still strongly suppressed.

Figures 35a-c present the same mass spectrum, cut on several different intervals of t; a substantial $\rho-\omega$ interference signal is observed at the larger momentum transfers. It is expected that such an interference, if it exists, should be most easily observed in this range since the ω differential cross section falls off significantly more slowly than that of the rho for increasing momentum transfer and decreases quite rapidly in the forward direction. There is, in fact, no observable effect at small momentum transfers and a study of the angular distribution as a function of mass for $-t < .1 (\text{GeV/c})^2$ also
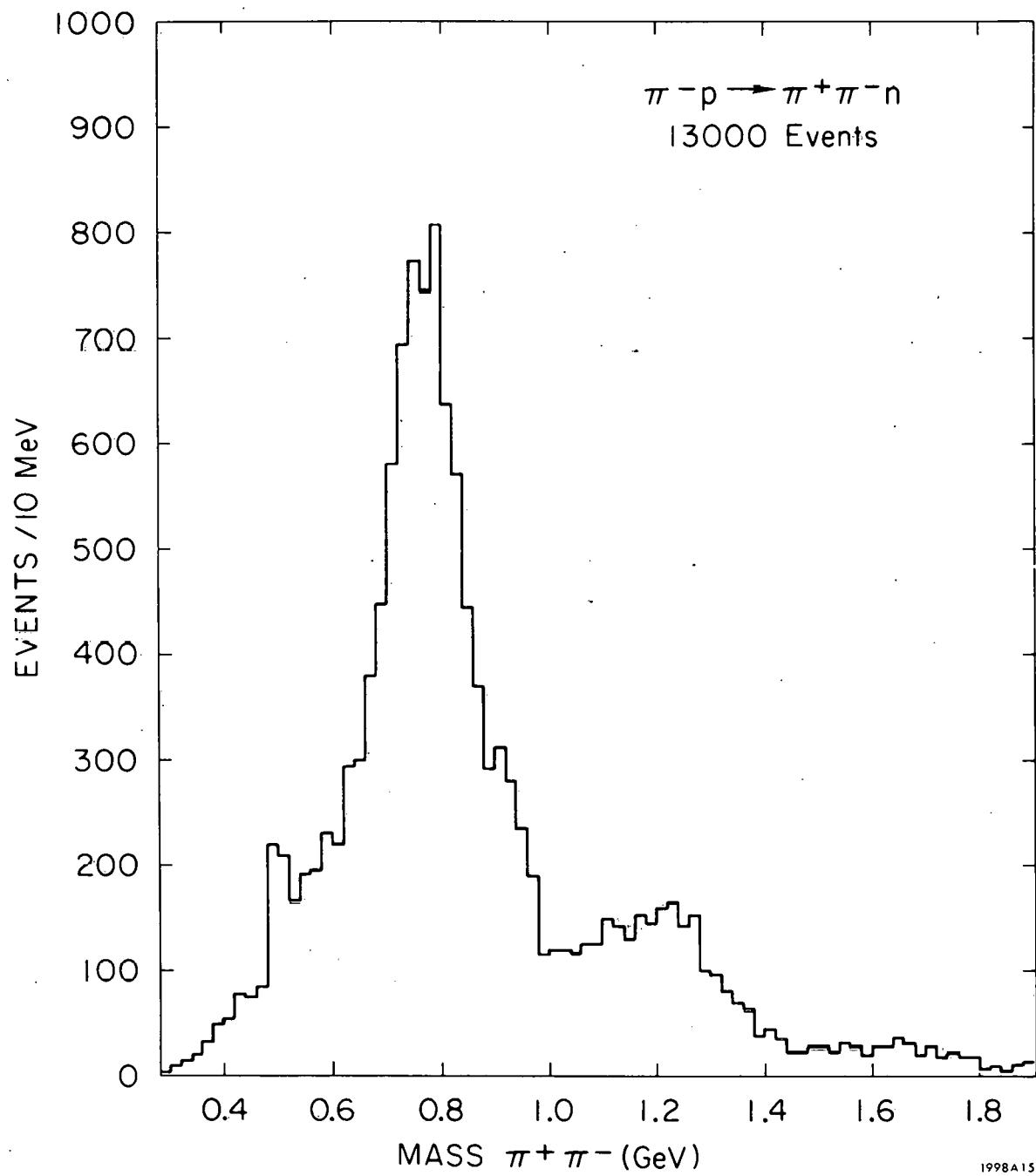
FIG. 34--Observed $\pi^+\pi^-$ mass distribution for $\pi^+\pi^-$n events.
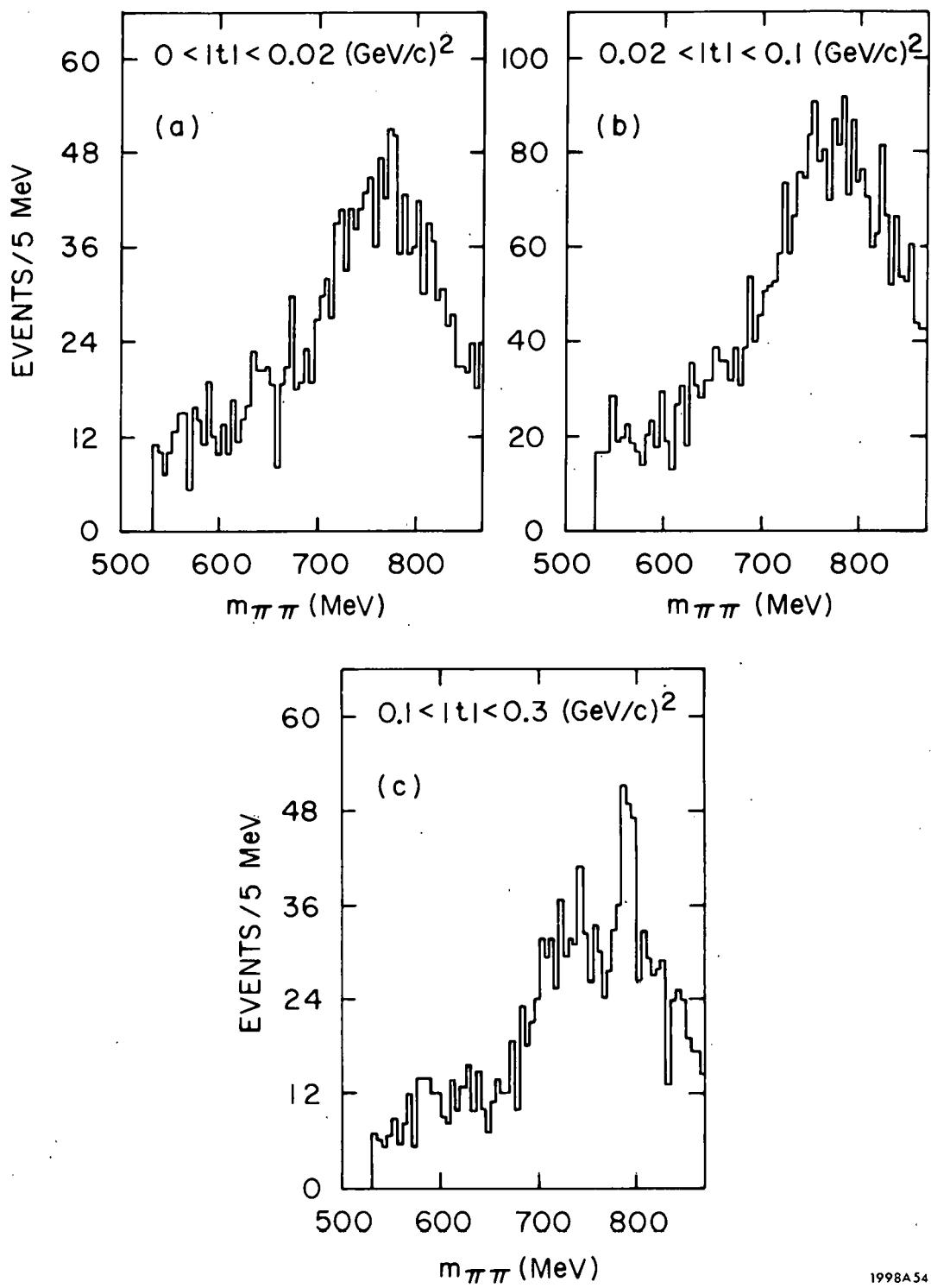
FIG. 35--Observed $\pi^+\pi^-$ mass distribution for $\pi^+\pi^-$n events, subject to cuts on the momentum transfer.

1998A54

yields no indication of any interference. A detailed study of the interference at the larger momentum transfers is presented elsewhere.[27b]

The observed dipion decay angular distribution for $\pi^+\pi^-n$ events with $.665 < m_{\pi\pi} < .865$ GeV is shown in Fig. 36, for momentum transfers to the nucleon in the region $.02 < -t < .06$ $(\text{GeV}/c)^2$. The distribution is plotted as a function of $\cos\theta_H$, where θ is the polar angle of the outgoing π^- in the helicity frame.[*] The dashed line indicates the approximate shape of the true angular distribution, as observed in bubble chamber experiments at lower energies and as reconstructed in this experiment when the detection efficiency of the apparatus is taken into account. It is evident that the shape of the angular distribution is substantially altered by the non-uniform acceptance, and that for $\cos\theta_H$ greater than $\approx .85$, no events are detected. (It should be noted, however, that in the Gottfried-Jackson frame, events are detected for $\cos\theta_{GJ}$ as large as $.95$.[†]) Nevertheless, it is a straightforward matter to determine the original angular distribution by fitting the expected theoretical function, modified by the detection efficiency, to the observed spectrum. This procedure, and its limitations, are discussed in detail in the next section.

The momentum transfer distribution for $\pi^+\pi^-n$ events in the same dipion mass interval is shown in Fig. 37, and exhibits a small turnover in the forward direction. In addition to this total differential cross section, the cross sections for transversely and longitudinally polarized rho mesons, $2\rho_{11}\dfrac{d\sigma}{dt}$

---

[*] The "helicity frame" is defined to be the right-handed coordinate system in the ρ rest frame which has the -z-axis along the direction of the neutron and the y-axis normal to the production plane.

[†] The Gottfried-Jackson frame is the coordinate system in the ρ rest-frame which has the z-axis along the direction of the incident π^- and the y-axis normal to the production plane.
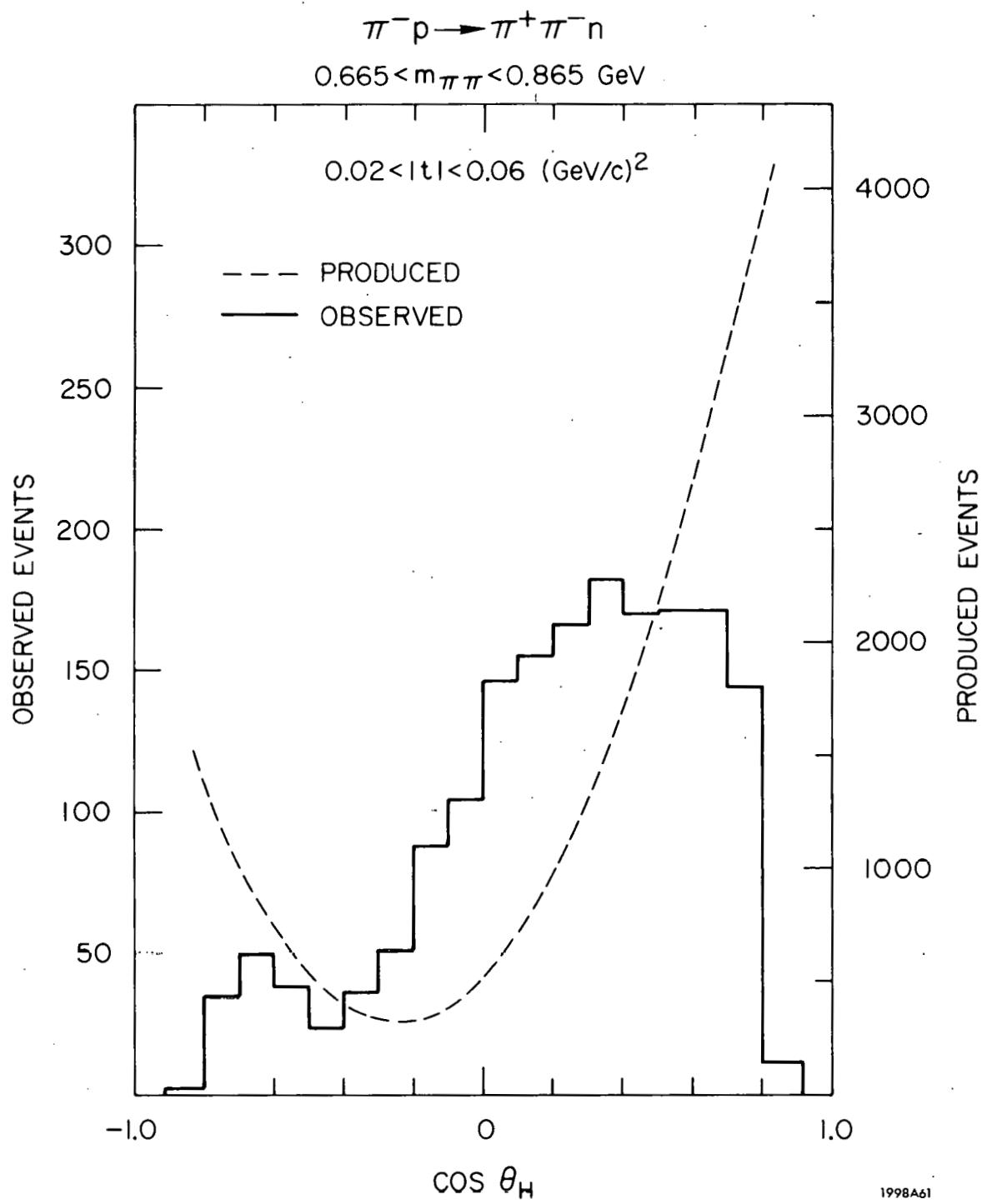
FIG. 36--Observed angular distribution of $\pi^+\pi^-$n events, where θ_H is the polar angle of the π^- in the helicity frame. The dashed line is the corrected distribution as determined from a fit to the data.

OBSERVED MOMENTUM TRANSFER DISTRIBUTION
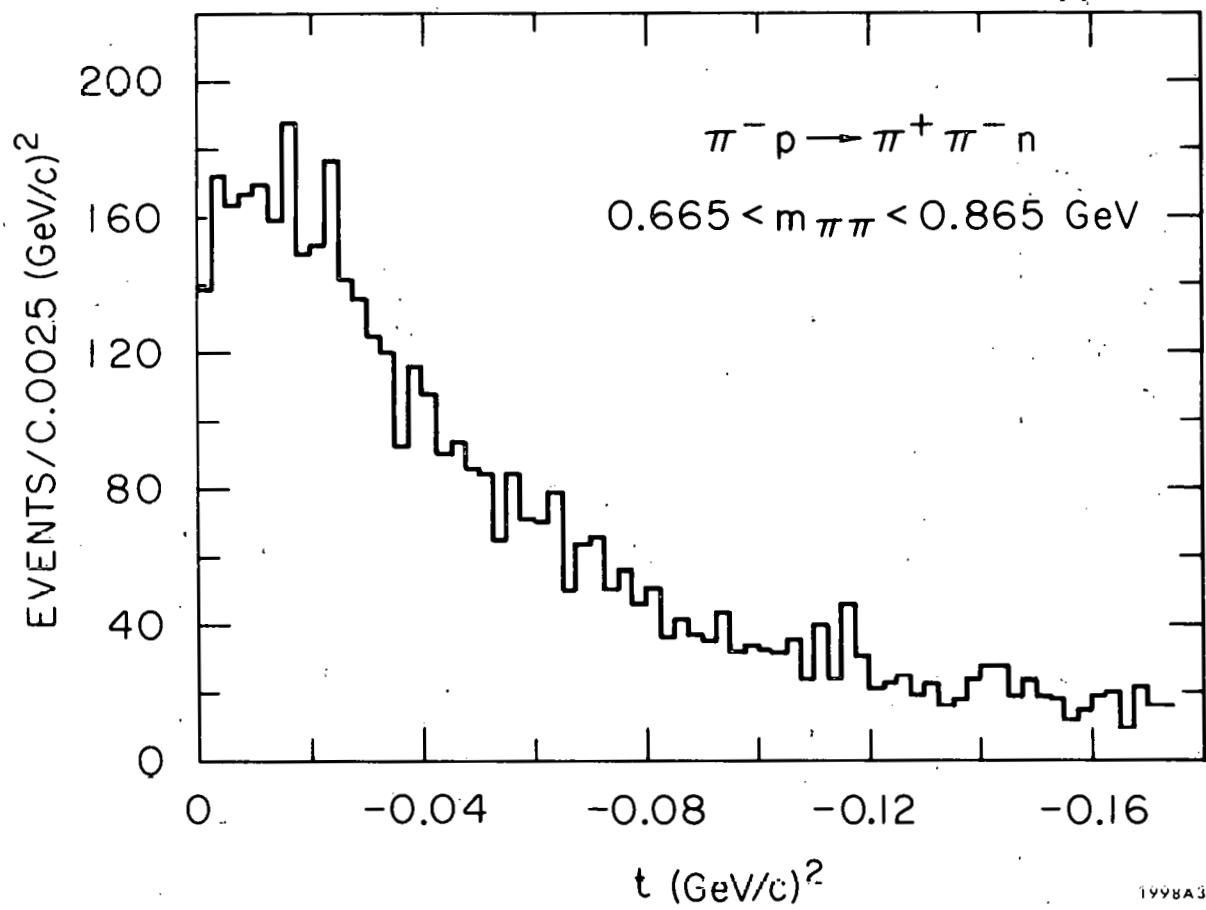
FIG. 37--Observed momentum transfer distribution for $\pi^+\pi^-$n events.

and $\rho_{00} \frac{d\sigma}{dt}$, are also interesting from the point of view of trying to understand the production dynamics of the reaction. Since the transversely polarized rhos decay with a $\sin^2\theta$ distribution, and the longitudinally polarized rhos with a $\cos^2\theta$ distribution, one can obtain an enriched sample of one polarization or the other by selecting events which decay with large or small $\cos\theta$. It should therefore be possible to observe qualitative differences in the transverse and longitudinal cross sections simply by making cuts in $\cos\theta$, i.e., without fitting the data and explicitly obtaining ρ_{11} and ρ_{00}. Figure 38 shows the differential cross section subject to the cuts $\left|\cos\theta_H\right| < .2$ and $.5 < \left|\cos\theta_H\right|$. It should be noted that although the acceptance is quite different for these two angular regions, it is very slowly varying as a function of t. A substantial difference is observed between the two different data samples: the large $\cos\theta$ sample, which is enriched with longitudinal rhos, falls off quite rapidly at small momentum transfers, whereas the sample enriched in transverse rhos exhibits no such structure. In order to quantitatively study these differential cross sections and the associated change in the angular distribution as a function of momentum transfer, however, it is necessary to determine the dipion density matrix elements.

B. <u>Determination of the Density Matrix Elements</u>

1) Formalism

For a reaction of the form $a + b \rightarrow c + d$

$ \llcorner\!\!\rightarrow e + f$

Observed Momentum Transfer Distribution
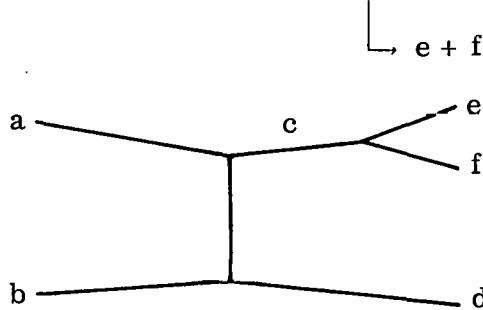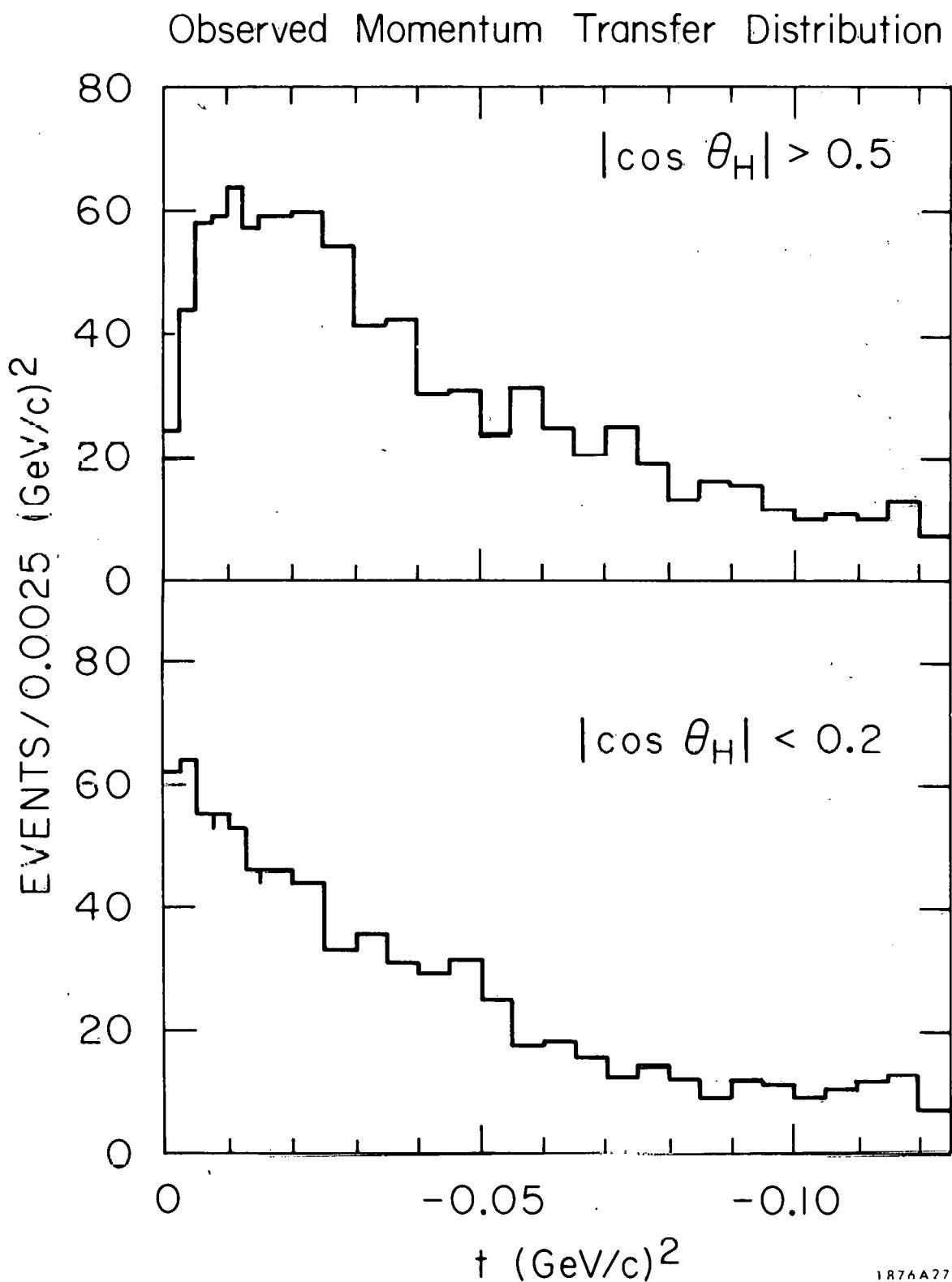
FIG. 38--Observed momentum transfer distribution for $\pi^+\pi^-n$ events with $.665 < m_{\pi\pi} < .865$ GeV, subject to different cuts on the decay angular distribution.

where a and b are unpolarized, the spin states of d are summed over, and e and f are spin zero particles, the angular distribution of particle e (or f) in the c rest frame is[52]

$$T(\theta,\varphi) = \frac{1}{4\pi} \left\{ 3\rho_{11}^{11}\sin^2\theta + 3\rho_{00}^{11}\cos^2\theta - 3\rho_{1-1}^{11}\sin^2\theta \cos2\varphi \right.$$

$$-3\sqrt{2}\ \mathrm{Re}\ \rho_{10}^{11}\sin2\theta\ \cos\varphi + \rho_{00}^{00} - 2\sqrt{6}\ \mathrm{Re}\ \rho_{10}^{10}\sin\theta\ \cos\varphi$$

$$+2\sqrt{3}\ \mathrm{Re}\ \rho_{00}^{10}\cos\theta \left.\right\} \qquad\qquad (5.1)$$

where θ, φ are the polar and azimuthal angles. This form of $T(\theta,\varphi)$ assumes that only s-and p-waves are present in the e-f final state. The $\rho_{\lambda_c\lambda_c'}^{JJ'}$ are the spin density matrix elements describing the production of particle c:

$$\rho_{\lambda_c\lambda_c'}^{JJ'}(s,m_c,t) = \frac{1}{(2S_a+1)}\ \frac{1}{(2S_b+1)}\ \sum_{\lambda_a,\lambda_b,\lambda_d}$$

$$f_{\lambda_c'\lambda_d;\lambda_a\lambda_b}^{J'}{}^*(s,m_c,t)\ f_{\lambda_c\lambda_d;\lambda_a\lambda_b}^{J}(s,m_c,t) \qquad (5.2)$$

where $f_{\lambda_c\lambda_d;\lambda_a\lambda_b}^{J}(s,m_c,t)$ is the amplitude for producing (c) with mass m_c, momentum transfer t, spin J, and helicity λ_c, given that λ_a,λ_b, and λ_d are the helicities of particles (a), (b) and (d) respectively.[53] The spins of the incident particles are given by S_a and S_b, and s is the total energy-squared in the center-of-mass system of particles (a) and (b). The expression for $T(\theta,\varphi)$ also assumes that parity is conserved in the reaction and that the coordinate system with respect to which the reaction is described is chosen with the y-axis normal to

the production plane.[†] For the moment it is assumed, as has generally been done in the past, that only s-and p-waves are present in the dipion state. Whether or not higher partial waves are in fact important is discussed in some detail below.

By using the normalization condition $\rho_{00}^{11} + 2\rho_{11}^{11} + \rho_{00}^{00} = 1$, ρ_{00}^{00} may be eliminated and $T(\theta,\varphi)$ written in the form:

$$T(\theta,\varphi) = \frac{1}{4\pi}\left\{ 1+(\rho_{00}-\rho_{11})(3\cos^2\theta-1)+2\sqrt{3}\mathrm{Re}(\rho_{0s})\cos\theta \right.$$ (5.3)

$$-3\sqrt{2}\mathrm{Re}(\rho_{10})\sin2\theta\,\cos\varphi-2\sqrt{6}\mathrm{Re}(\rho_{1s})\sin\theta\,\cos\varphi$$

$$\left. -3\rho_{1-1}\sin^2\theta\,\cos2\varphi\right\}$$

The less cumbersome notation of $\rho_{mm'}^{11} \equiv \rho_{mm'}$, $\mathrm{Re}\,\rho_{mm'}^{10} \equiv \rho_{ms}$, $\rho_{00}^{00} \equiv \rho_{ss}$ has been introduced, s being a mnemonic for the single s-wave amplitude. The fact that ρ_{ss} can be explicitly eliminated is representative of an inherent ambiguity: it is not possible to independently determine ρ_{00}, ρ_{11}, or ρ_{ss} solely from a knowledge of the angular distribution. This ambiguity occurs because an isotropic term in the angular distribution may be produced either by ρ_{ss} or by a combination of ρ_{00} $(\cos^2\theta)$ and ρ_{11} $(\sin^2\theta)$.

The observed angular distribution is then expected to be of the form

$$W(\theta,\varphi,m,t) = T(\theta,\varphi,m,t)\,E(\theta,\varphi,m,t)$$ (5.4)

where $E(\theta,\varphi,m,t)$ is the detection efficiency of the apparatus as a function of

---

[†]The derivation of Eq. (5.1) relies on the familiar relation $\rho_{-m-m'}=(1)^{m-m'}\rho_{mm'}$ which is itself valid only if the y-axis is normal to the production plane.

the kinematic variables. The values of $\rho_{mm'}(m,t)$ and hence the original angular distribution are obtained by fitting $W(\theta, \varphi, m, t)$ to the observed angular distribution as a function of m and t. In principle one could take sufficiently small intervals in m and t that the $\rho_{mm'}$ do not change appreciably over the width of the interval. In practice this is often not possible due to statistical limitations. Equation (5.4) is then replaced by

$$\int_{t_1}^{t_2} dt \int_{m_1}^{m_2} dm\, W(\theta,\varphi,m,t) = \int_{t_1}^{t_2} dt \int_{m_1}^{m_2} dm\, T(\theta,\varphi,m,t)\, E(\theta,\varphi,m,t) \qquad (5.5)$$

If one assumes that the t interval is chosen sufficiently small that neither $T(\theta,\varphi,m,t)$ or $E(\theta,\varphi,m,t)$ changes appreciably from t_1 to t_2 (an assumption which is valid for the fits discussed below) one obtains

$$\overline{W}(\theta,\varphi,m,t) = \frac{1}{4\pi}\left\{ 1 + \left[\overline{\rho_{00}}(m,t) - \overline{\rho_{11}}(m,t) \right] (3\cos^2\theta - 1) \right.$$

$$+ 2\sqrt{3}\,\mathrm{Re}\overline{\rho_{0s}}(m,t)\cos\theta - 3\sqrt{2}\,\mathrm{Re}\overline{\rho_{10}}(m,t)\sin2\theta\,\cos\varphi$$

$$\left. - 2\sqrt{6}\,\mathrm{Re}\overline{\rho_{1s}}(m,t)\,\sin\theta\,\cos\varphi - 3\overline{\rho_{1-1}}(m,t)\sin^2\theta\,\cos2\varphi \right\}$$

$$(5.6)$$

where $\overline{\rho_{mm'}}(m,t) = \int_{m_1}^{m_2} dm\, \rho_{mm'}(m,t)\, E(\theta,\varphi,m,t).$

The values of $\overline{\rho_{mm'}}(m,t)$ obtained then represent average values of the matrix elements over the particular mass interval. In this experiment, it was verified that the $\rho_{mm'}(m,t)$ did not vary appreciably within the mass cut .665 - .865 GeV by fitting the matrix elements as a function of mass for $.01 < -t < .1$ $(\mathrm{GeV/c})^2$. The fact that $E(\theta,\varphi,m,t)$ is not constant over this mass

range does have a slight effect on the normalization of the $\rho_{mm'}$. The detailed nature of the fit and the calculation of the detection efficiency are discussed below.

2. Maximum Likelihood Fit

The density matrix elements were obtained by fitting the right-hand side of Eq. (5.4) to the observed angular distribution using a maximum likelihood technique. The likelihood function was calculated by binning the data in $\cos\theta$ and φ (20 bins each) and forming the product of the probability distributions for each bin. The number of events in each bin was distributed according to a Poisson distirbution: i.e., the probability of obtaining k events in a bin if the expected number is m is

$$P(k, m) = \frac{(m)^k}{k!} e^{-m} \tag{5.7}$$

From Eq. (5.4), it is clear that the expected number of events in bin i, j is $m_{ij} = NT(\theta_i \varphi_j)E(\theta_i \varphi_i)\Delta(\cos\theta_i)\Delta\varphi_j$ where θ_i, φ_j are the values of θ and φ at the center bin*, and N is the total number of events produced for the particular $\pi\pi$ mass and momentum transfer intervals under consideration. The likelihood $\mathscr{L}$ of observing an event distribution such that in each bin i, j there are k_{ij} events is then

$$\mathscr{L} = \prod_{\substack{i=1,20 \\ j=1,20}} \frac{\left[NT(\theta_i\varphi_j)\,E(\theta_i\varphi_j)\,\Delta(\cos\theta)\,\Delta\varphi\right]^{k_{ij}}}{(k_{ij})!}\, e^{-NT(\theta_i\varphi_j)\,E(\theta_i\varphi_j)\Delta(\cos\theta)\Delta\varphi} \tag{5.8}$$

---

*It is assumed that the $\cos\theta$ and φ bins are chosen sufficiently small that any variation in $T(\theta,\varphi)E(\theta,\varphi)$ over the width of a bin is linear; then the average value of $T(\theta,\varphi)E(\theta,\varphi)$ within the bin is given by its value at the bin center.

and the log-likelihood is

$$\log \mathscr{L} = \sum_{ij} k_{ij} \log \left[NT(\theta_i \, \varphi_j) E(\theta_i \, \varphi_j) \Delta(\cos\theta) \Delta\varphi \right]$$

$$-N\sum_{ij} T(\theta_i \, \varphi_j) E(\theta_i \, \varphi_j) \Delta(\cos\theta) \Delta\varphi - \sum_{ij} \log (k_{ij})!$$

Note that the normalization of the likelihood function is, in a sense, automatically built in since the Poisson distribution is a properly normalized probability distribution independent of the value of $T(\theta,\varphi)E(\theta,\varphi)$.

3.   Detection Efficiency

The detection efficiency of the apparatus was calculated as a function of θ, φ by Monte Carlo techniques. For each value of θ_i and φ_j used in the fitting program, and for a grid of m and t values, fake events were produced with Monte Carlo'd vertex coordinates, XO, YO, ZO, incident beam angles θ_B, φ_B, and angle of rotation of the production plane about the incident particle direction, φ_{PR}. These fake events were tracked through the spectrometer system to determine what fraction of the events would have been observed. This fraction then represents the probability that a real event produced with these values of θ, φ, m, and t was detected, if the geometric variables (XO, YO, ZO, θ_B, φ_B, φ_{PR}) are summed over.

The x and y distributions of the beam, according to which XO and YO should be Monte Carlo'd were taken from the observed vertex distribution for all real events. The sum over a whole range of kinematic variables (m, t, θ, φ, MM, particle masses, etc.) which is implicit when all two-track events are included, eliminates any dependence of the detection efficiency on XO and YO and the observed x-y vertex distribution is equivalent to the beam

profile. The θ_B and φ_B distributions were taken from the angular divergence of the beam as observed during the calibration runs (see Section 4.F), although they could equally well have been obtained in the same manner as the XO and YO distributions. Both φ_{PR} and ZO were Monte Carlo'd according to uniform distributions; absorption of the incident particle in the target was explicitly included as is discussed below.

The features of the spectrometer which affected the detection efficiency may be divided into two classes: geometrical and statistical. The geometrical acceptance of the spectrometer was the predominant factor; it was determined by the active area of the spark chambers and trigger hodoscopes, and by the magnet aperture and magnetic field. Numerous checks were made to ensure that the apparatus was well understood and correctly represented by the efficiency program: as a check that the events were being tracked through the magnet properly, upstream tracks measured in the experiment were projected through the magnet and the resulting downstream tracks compared with the actual tracks observed. Events were Monte Carlo'd according to the reconstructed mass and momentum transfer distributions and according to the fitted density matrix elements, in order to compare the resulting track distributions near the edges of the plugs and magnet aperture with the observed track distributions. The agreement was very good. In addition, the angular distribution of the fake events that successfully passed through the apparatus was compared with the observed angular distribution to check for possible angular biases; none were observed. Finally, it should be noted that the events from which the density matrix elements were obtained were required to

pass through the geometrical tracking routine of the efficiency program so that the data sample and calculated efficiency reflected identical geometrical conditions.

The statistical loss of events included (1) absorption of the incident and outgoing tracks in the target, (2) inefficiency of the spark chambers and individual hodoscope counters, and (3) decay or interaction of the secondary particles before detection. The effect of (3) was sufficiently small that it was taken into account only in the overall normalization. The effects of (1) and (2), however, were explicitly included. The total $\pi^- p$ cross section was parameterized as a function of momentum and the path length of each track in the hydrogen calculated, to allow an accurate determination of the absorption probability. Tracks were discarded on a Monte Carlo basis according to this absorption probability. The individual hodoscope efficiencies presented in Table 4 were included in the program. For the spark chambers, the net efficiencies for the upstream and downstream groups of chambers were used, rather than the individual chamber efficiencies. Two different efficiencies were included: one for tracks which intersected the active area of each chamber in the group, and one for tracks which missed the active area of one chamber, either because they intersected the plug or because they missed the chamber altogether. No additional dependence of the spark chamber efficiency on the angle or position of a track was included, since none was observed when the chamber efficiencies were studied as a function of these variables.

One additional effect that was included in the program was the loss of events due to the missing-mass cut. Since the missing-mass resolution depends on the momenta and angles of the decay particles (variations of 10-15 MeV were observed), this loss is a function of the decay angles and can

introduce biases if ignored. It was included by explicitly calculating the MM resolution for each event and then discarding the event according to the corresponding probability that its "observed" MM fell outside the cut.

The average efficiency over any given range of m or t was calculated by numerically integrating the product of the efficiency matrix and the appropriate distribution function; in particular, the average acceptance for the interval $.665 < m_{\pi\pi} < .865$ GeV was obtained by weighting the efficiency matrix with the rho meson shape obtained from a fit to the $\pi\pi$ mass distribution (ref. Section E). The average acceptance for this interval is shown in Fig. 39 as a function of θ and φ for three different ranges of momentum transfer.

4. Presentation of Density Matrix Elements

Using the fitting procedure described above, the density matrix elements were determined as a function of momentum transfer for $\pi^+\pi^-n$ events in the interval $.665 < m_{\pi\pi} < .865$ GeV; there were 5000 such events remaining after all cuts had been made and for $0 < -t < .3$ $(GeV/c)^2$. The matrix elements were independently determined in both the helicity and Gottfried-Jackson frames, with the angles θ and φ chosen to refer to the direction of the π^-.

The results are shown in Figs. 40 and 41 and in Tables 5 and 6.[*] A number of qualitative features are evident: Many of the matrix elements exhibit structure in the forward direction, i.e., for momentum transfers less than m_π^2. In particular there is a pronounced dip in the value of $\rho_{00} - \rho_{11}$ in the helicity frame. This turnover occurs also in the Gottfried-Jackson frame, though to a lesser extent, and has long been predicted for this reaction

---

[*]The values of the matrix elements in the <u>Gottfried-Jackson</u> frame that were presented in an earlier publication,[32] SLAC-PUB-884, contained a slight error and were incorrect by 5-10%. The values presented here are the correct ones.
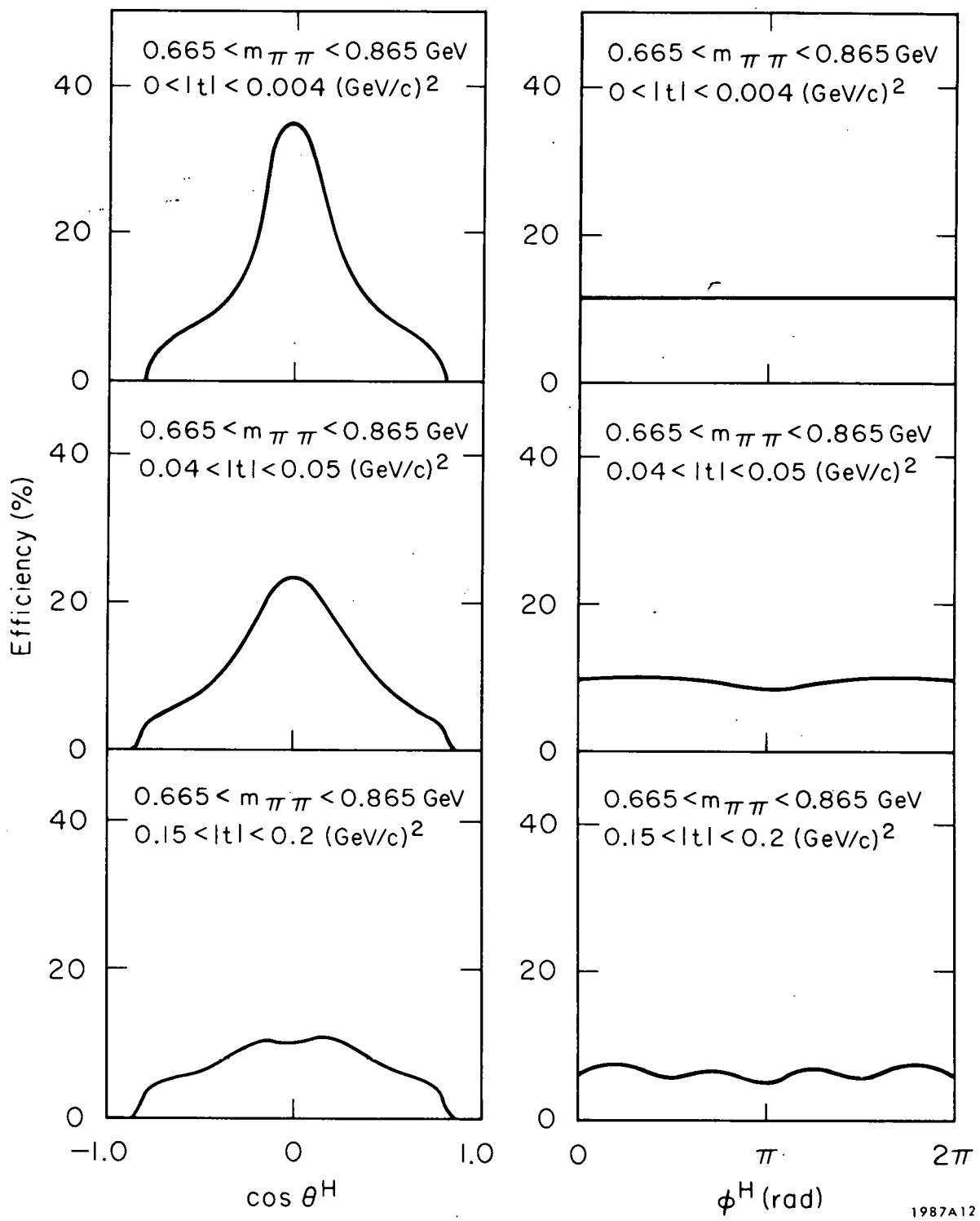
FIG. 39--Detection efficiency of the apparatus as a function of cos θ, φ in the helicity frame for several different regions of momentum transfer. The figures include loss due to target absorption, spark-chamber inefficiency, and the missing mass cut .80 - 1.06 GeV. See discussion in text.
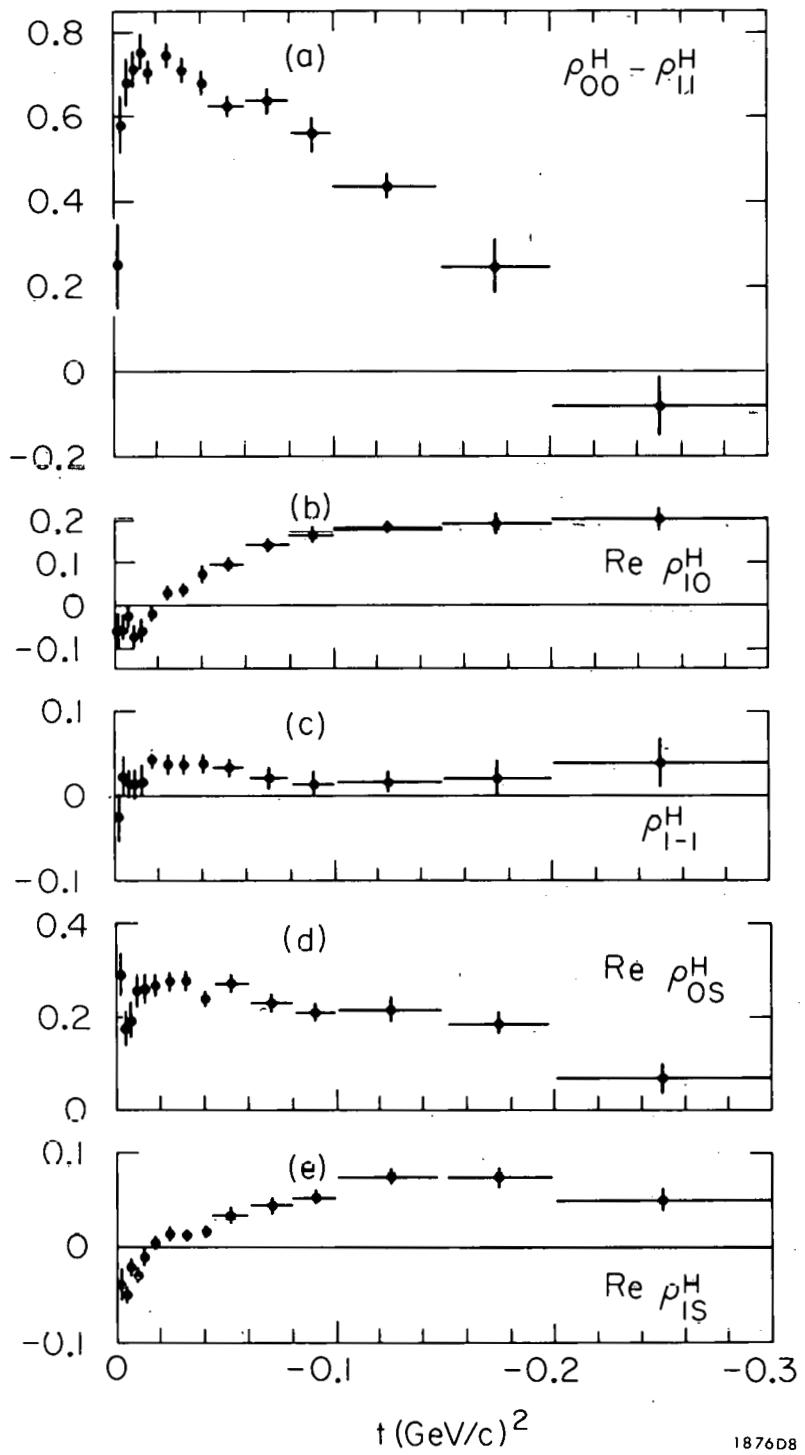
FIG. 40--The density matrix elements in the helicity frame.
The error bars indicate the statistical errors.

$\pi^- p \rightarrow \pi^+ \pi^- n$ $0.665 < m_{\pi\pi} < 0.865$ GeV

(a) $\rho_{00}^J - \rho_{11}^J$

(b) Re ρ_{10}^J

(c) ρ_{1-1}^J

(d) Re ρ_{0S}^J

(e) Re ρ_{1S}^J
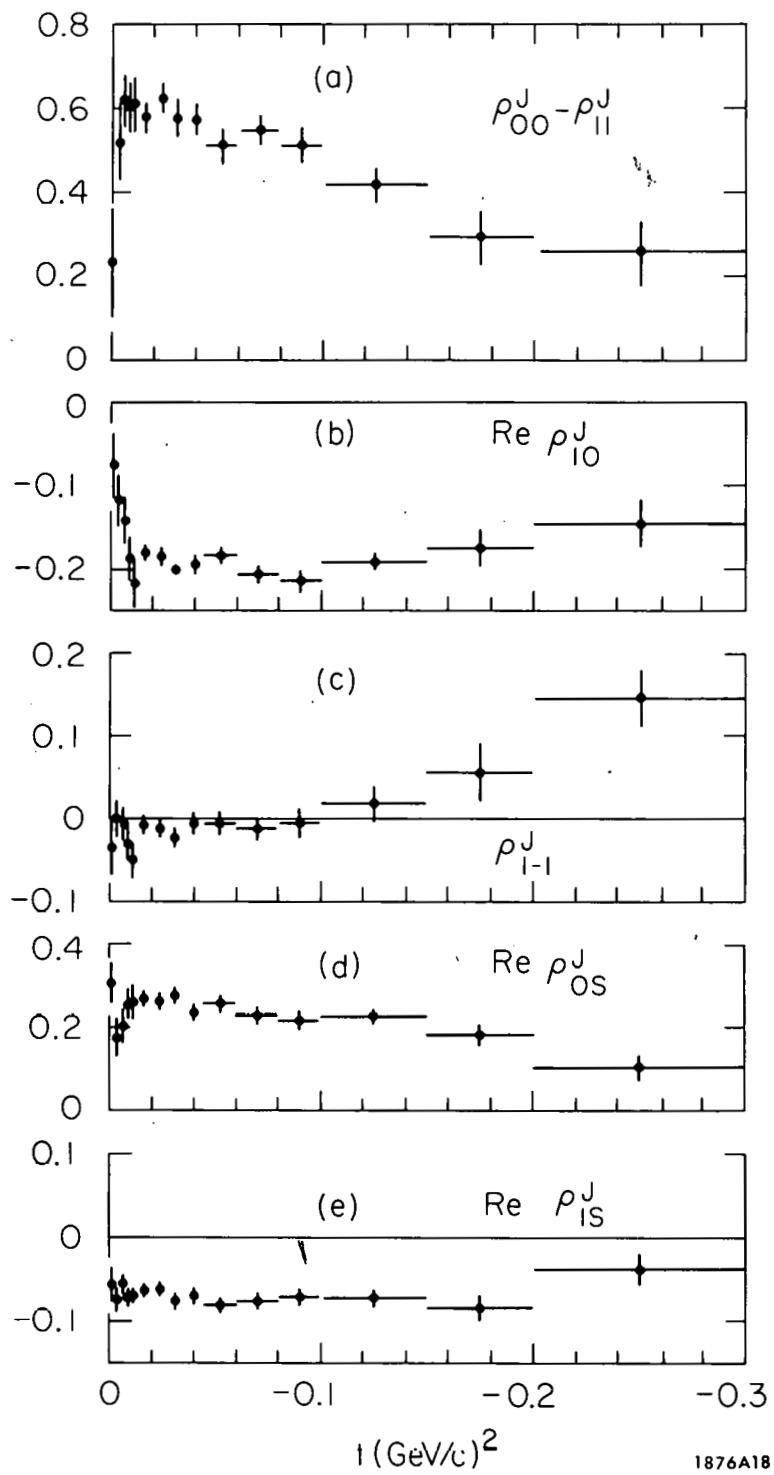
$t \, (\text{GeV/c})^2$

1876A18

FIG. 41--The density matrix elements evaluated in the
Gottfried-Jackson frame. The error bars
indicate the statistical errors.

TABLE 5

Density Matrix Elements Evaluated in the Helicity Frame for $\pi^- p \to \pi^+ \pi^- n$, $.665 < m_{\pi\pi} < .865$ GeV

$-t$ (GeV/c)^2	$\rho^H_{00} - \rho^H_{11}$	Re ρ^H_{10}	ρ^H_{1-1}	Re ρ^H_{0S}	Re ρ^H_{1S}	ρ^H_{11} *
t_{min} $-.0025$	$.248 \pm .127$	$-067 \pm .040$	$-.025 \pm .033$	$.296 \pm .048$	$-.038 \pm .021$	$.228 \pm .042$
$.0025 - .0050$	$595 \pm .080$	$-.053 \pm .031$	$.023 \pm .020$	$.180 \pm .045$	$-.048 \pm .012$	$.097 \pm .027$
$.0050 - .0075$	$699 \pm .061$	$-.034 \pm .030$	$.015 \pm .020$	$.202 \pm .042$	$-.022 \pm .011$	$.054 \pm .020$
$.0075 - .0100$	$734 \pm .054$	$-.079 \pm .028$	$.014 \pm .016$	$.257 \pm .037$	$-.029 \pm .010$	$.038 \pm .018$
$.0100 - .0125$	$.778 \pm .045$	$-.068 \pm .035$	$.015 \pm .016$	$.268 \pm .038$	$-.010 \pm .009$	$.024 \pm .015$
$.0125 - .0200$	$.722 = .033$	$-.020 \pm .010$	$.044 \pm .010$	$.280 \pm .020$	$.005 \pm .006$	$.038 \pm .011$
$.0200 - .0275$	$.760 = .028$	$.028 \pm .013$	$.038 \pm .010$	$.280 \pm .020$	$.017 \pm .005$	$.031 \pm .009$
$.0275 - .0350$	$.734 \pm .036$	$.037 \pm .015$	$.039 \pm .011$	$.283 \pm .023$	$.012 \pm .007$	$.034 \pm .012$
$.035 - .045$	$.705 \pm .035$	$.078 \pm .016$	$.040 \pm .012$	$.247 \pm .023$	$.022 \pm .007$	$.040 \pm .012$
$.045 - .060$	$.644 \pm .034$	$.098 \pm .014$	$.035 \pm .012$	$.274 \pm .021$	$.037 \pm .007$	$.057 \pm .011$
$.060 - .080$	$.656 \pm .033$	$.145 \pm .013$	$.023 \pm .011$	$.240 \pm .020$	$.045 \pm .006$	$.061 \pm .011$
$.080 - .100$	$.580 \pm .047$	$.174 \pm 017$	$.017 \pm .018$	$.219 \pm .026$	$.057 \pm .009$	$.079 \pm .016$
$.100 - .150$	$.454 \pm .039$	$.186 \pm 012$	$.019 \pm .016$	$.225 \pm .020$	$.077 \pm .008$	$.123 \pm .013$
$.150 - .200$	$.250 \pm .073$	$.203 \pm 020$	$.024 \pm .027$	$.194 \pm .012$	$.077 \pm .012$	$.197 \pm .024$
$.200 - .300$	$-.086 \pm .099$	$.211 \pm .022$	$.041 \pm .034$	$077 \pm .033$	$.053 \pm .016$	$.306 \pm .033$

*Note: The values of ρ^H_{11} are not directly measured and depend on certain assumptions concerning the s-wave. See discussion in text.

TABLE 6

Density Matrix Elements Evaluated in the Gottfried-Jackson Frame for $\pi^- p \to \pi^+ \pi^- n$, $.665 < m_{\pi\pi} < .865$ GeV

$-t(\text{GeV/c})^2$	$\rho^J_{00} - \rho^J_{11}$	Reρ^J_{10}	ρ^J_{1-1}	Reρ^J_{0S}	Reρ^J_{1S}	ρ^J_{11}*
t_{min} - .0025	.231 ± .131	-.073 ± .042	-.032 ± .034	.299 ± .050	-.055 ± .021	.232 ± .044
.0025- .005	.518 ± .091	-.114 ± .030	.001 ± .022	.167 ± .046	-.070 ± .015	.124 ± .030
.005 - .0075	.621 ± .057	-.134 ± .029	-.007 ± .019	.186 ± .039	-.052 ± .010	.082 ± .019
.0075- .010	.601 ± .061	-.185 ± .027	-.029 ± .018	.243 ± .037	-.070 ± .012	.084 ± .020
.010 - .0125	.603 ± .066	-.211 ± .033	-.047 ± .021	.263 ± .038	-.068 ± .009	.083 ± .022
.0125- .020	.575 ± .034	-.178 ± .011	-.006 ± .011	.268 ± .015	-.061 ± .005	.088 ± .011
.020 - .0275	.618 ± .032	-.184 ± .016	-.011 ± .011	.258 ± .028	-.059 ± .007	.079 ± .011
.0275- .035	.574 ± .042	-.195 ± .013	-.016 ± .013	.267 ± .022	-.078 ± .009	.088 ± .014
.035 - .045	.576 ± .034	-.196 ± .016	-.007 ± .015	.228 ± .019	-.069 ± .008	.085 ± .011
.045 - .060	.505 ± .038	-.184 ± .013	-.009 ± .012	.257 ± .020	-.079 ± .008	.104 ± .013
.060 - .080	.546 ± .035	-.207 ± .013	-.014 ± .015	.222 ± .020	-.073 ± .008	.097 ± .012
.080 - .100	.508 ± .044	-.214 ± .012	-.008 ± .018	.208 ± .023	-.067 ± .009	.103 ± .015
.100 - .150	.416 ± .038	-.194 ± .007	.015 ± .016	.232 ± .021	-.072 ± .008	.137 ± .013
.150 - .200	.293 ± .063	-.178 ± .022	.056 ± .035	.182 ± .026	-.081 ± .016	.182 ± .021
.200 - .300	.247 ± .079	-.144 ± .029	.145 ± .031	.102 ± .031	-.035 ± .020	.195 ± .026

*Note: The values of ρ^{GJ}_{11} are not directly measured and are dependent on certain assumptions concerning the s-wave. See discussion in text.

by OPEA. It is also interesting to note that $\text{Re}\rho_{10}^{H}$ and $\text{Re}\rho_{1s}^{H}$ exhibit similar shape and cross zero at $-t \approx m_{\pi}^{2}$. This crossover point is, in fact, explicitly predicted by OPEA and is discussed in Chapter 6. Finally, we note that the interference terms between the s-and p-wave are reasonably large, indicating a significant s-wave contribution.

As mentioned above, it is not possible to separately determine either ρ_{00}, ρ_{11}, or ρ_{ss} from a knowledge of the angular distribution alone; additional information of some kind is needed. Since these quantities are related by the trace condition $\rho_{00} + 2\rho_{11} + \rho_{ss} = 1$ and by the measured values of $\rho_{00} - \rho_{11}$, the ambiguity may be resolved either by independent information on one of these matrix elements or by an additional constraint between them. It is also possible to establish limits on these quantities since the interference terms $\text{Re}\rho_{0s}$ and $\text{Re}\rho_{1s}$ are non-zero. A discussion of these limits and a determination of ρ_{00} and ρ_{11} based on independent information which is available on the s-wave cross section (ρ_{ss}) is presented in Chapter 6; the transverse and longitudinal differential cross sections, $2\rho_{11}\frac{d\sigma}{dt}$ and $\rho_{00}\frac{d\sigma}{dt}$ are also presented in that chapter.

Before proceeding further to discuss the differential cross section or to make quantitative comparisons of the measured ρ_{ij} with models, it is important to discuss possible backgrounds in the $\pi^{+}\pi^{-}n$ event sample and also the errors on the ρ_{ij} which have been obtained.

C. Errors and Systematic Effects

1. Errors

The error bars shown in Figs. 40 and 41 are statistical only; the error in each parameter is defined to be that change in the parameter which results in

a net increase in $-\log \mathscr{L}$ of .5, when the other parameters are adjusted to reminimize the function. For a parabolic likelihood function, this corresponds to a one-standard-deviation error.

Systematic errors which could result from small, unknown biases in the detection or track reconstruction efficiency are estimated to be less than the statistical errors. As a check that the ρ_{ij} obtained were not sensitive to the geometry of the apparatus, the density matrix elements were also obtained from more restrictive data samples, selected by imposing more stringent geometrical cutoffs than those actually presented by the apparatus. For example, Fig. 42 shows the density matrix elements obtained when only those events are selected in which both tracks intersect the active area of all three front chambers. This requirement eliminates most of the events with tracks close to the plugs. The agreement with the matrix elements presented above is quite good, and in all cases is within a standard deviation. The comparison is presented for the three smallest bins in momentum transfer since one might expect this region to be the most sensitive.

A similar, but considerably more stringent cut, was made for the density matrix elements shown in Fig. 43. In this case, all those events were excluded which occupied regions of the decay angular distribution where the detection efficiency was less than 10%. This removes events in the vicinity of the plugs or the edges of the magnet aperture, and represents a cut on the polar decay angle of $\cos\theta \simeq .5$. The agreement with the matrix elements presented above, which are also shown in Fig. 43, is again seen to be quite good.

Finally, it was established that the matrix elements obtained in the Gottfried-Jackson and helicity frames were consistent with one another by rotating from one frame to the other.

$\pi^- p \longrightarrow \pi^+ \pi^- n$

$0.665 < m_{\pi\pi} < 0.865$ GeV

o 3 CHAMBERS
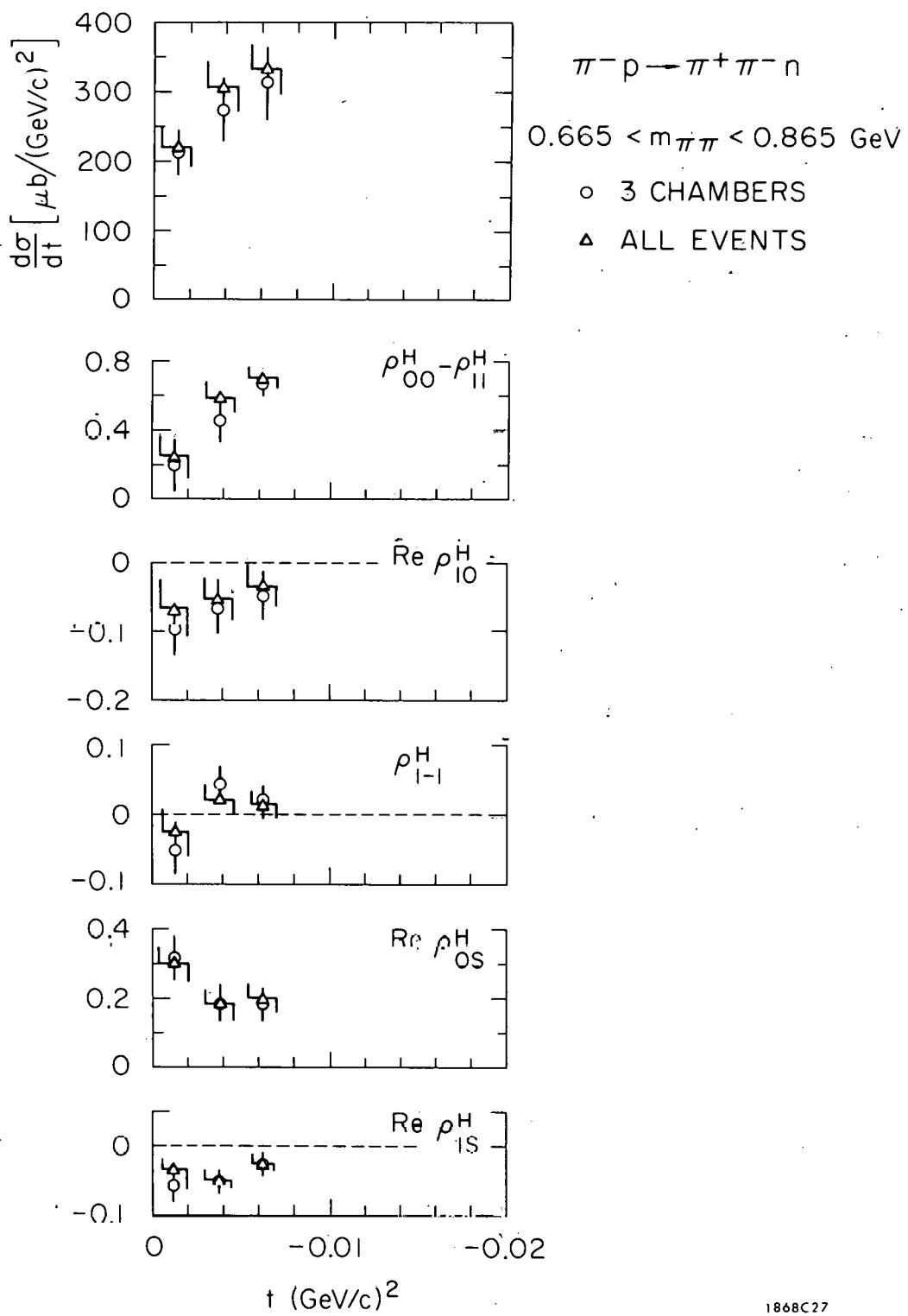
Δ ALL EVENTS

FIG. 42--Comparison of the density matrix elements obtained from all events, with those obtained from only those events that pass through the active area of all three front spark chambers.
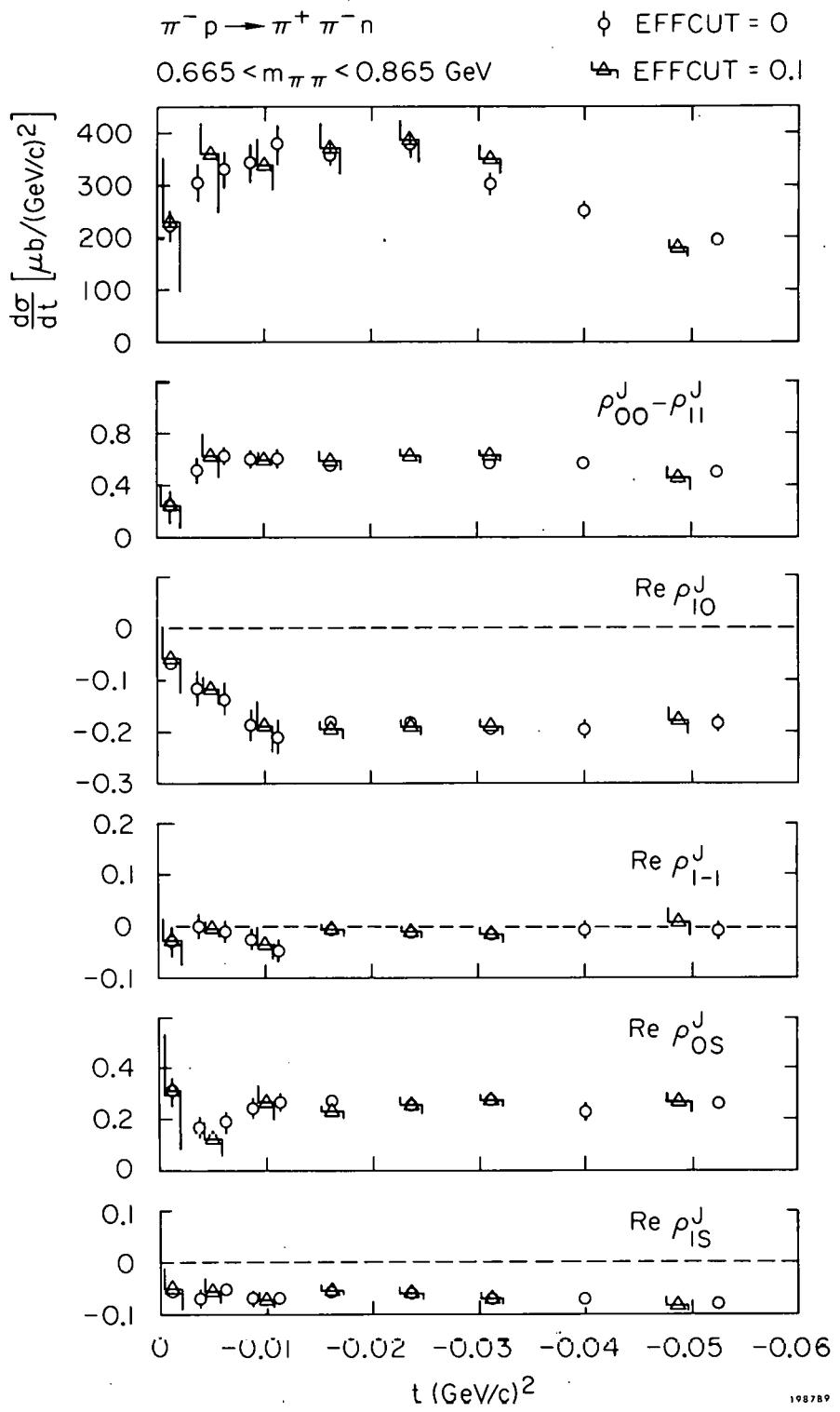
FIG. 43--Comparison of the density matrix elements obtained from all
events (EFFCUT = 0), with those obtained from only those
events for which the detection efficiency was greater than
10% (EFFCUT = .1).

2. Background from Higher Missing Mass Events

The fact that a certain fraction of the "$\pi^+\pi^-n$" event sample consisted of events with additional missing particles besides a nucleon is evident from Fig. 33; even with the relatively good resolution of ± 100 MeV, some higher missing mass events fall in the cut $.80 <$ MM < 1.06 GeV. A substantial number, but not all of these, are $\pi^+\pi^-\Delta^0$ events.

As mentioned above and illustrated in Fig. 33, the number of Δ^0 events selected could be varied by choosing different cuts on the target counter information. It was therefore possible to extrapolate to zero background in the $\pi^+\pi^-n$ sample in the following manner: Six different cuts were chosen, each of which reduced the number of events with MM in the region $1.1 - 1.2$ GeV by approximately equal amounts.[*] The number of events with MM in the region $.8 - 1.06$ GeV was then plotted as a function of the number of events with $1.1 <$ MM < 1.2 GeV, as the target counter cuts were successively imposed. The cuts were chosen in a somewhat arbitrary fashion, except that they were ordered such that the cuts most apt to affect $\pi^+\pi^-n$ events were the last applied.

The results are shown in Fig. 44 for several regions of momentum transfer. It is seen that for approximately the first four cuts, the number of events rejected from the neutron region is linearly proportional to the number of events rejected from the Δ^0 region. It is only when the last one or two cuts are applied that the number of events lost deviates from the linear slope; these last two cuts include respectively rejecting events in which two inner counters fired and in which a single outer counter fired. As already pointed out, it may

---

[*] It should be noted that each of these cuts was independent. For example, since there are four sides to the target counter array, four independent and equal cuts could be made by rejecting events in the upper, lower, right or left sides of the counter array, respectively.
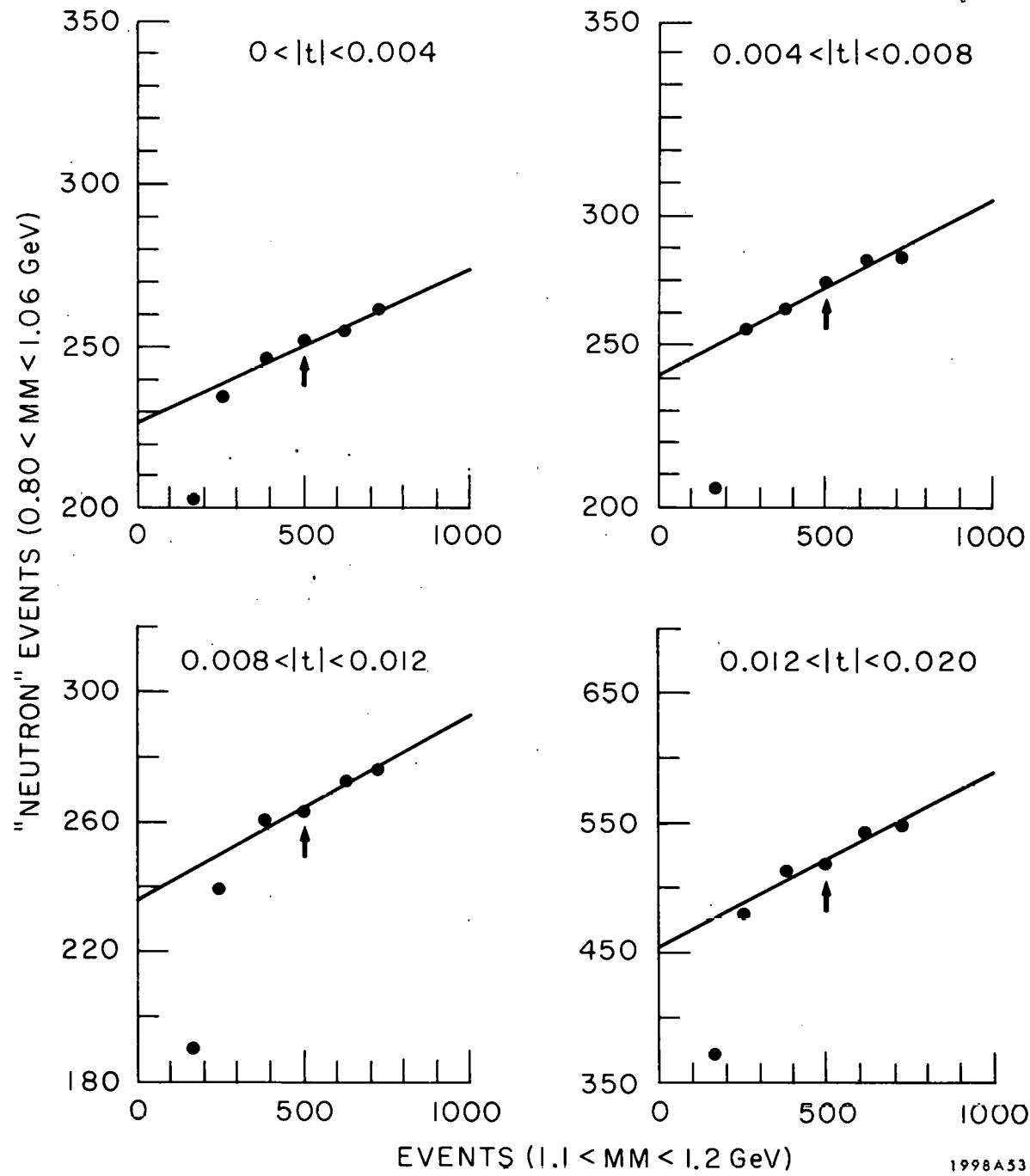
FIG. 44--Examples of the extrapolation to zero higher-missing-mass background in the cut .80 - 1.06 GeV. The extrapolation procedure is described in the text.

- 129 -

be expected that some $\pi^+\pi^-n$ events will be rejected if these cuts are employed. The fact that the first four cuts did not affect $\pi^+\pi^-n$ events was verified by studying the lower half of the neutron, i.e., events with MM < .94 GeV; less than $\approx 1\%$ of the events were rejected when these cuts were applied. The arrow in Fig. 44 indicates the target cut which was used to select the $\pi^+\pi^-n$ sample. The remaining background of higher MM events was estimated by linearly extrapolating to zero background as illustrated by the lines. The results of these extrapolations, which were performed as a function of momentum transfer are shown in Fig. 45. Within the statistical and systematic errors of this procedure, the background is consistent with being independent of momentum transfer; therefore the average value of 12% was taken to be an overall normalization correction.

An independent and relatively accurate estimate of exactly how much of this background could be attributed to $\pi^+\pi^-\Delta^0$ events was obtained from the data on $\pi^+p \rightarrow \pi^+\pi^-\Delta^{++}$. Since there are no $\pi^+\pi^-n$ events in this reaction, the low mass tail of the Δ^{++} could be readily examined, as is evident from the missing mass distribution shown in Fig. 46. Scaling the number of events in the region .8 - 1.06 GeV by the relative $\pi^-p \rightarrow \pi^+\pi^-\Delta^0/\pi^+p \rightarrow \pi^+\pi^-\Delta^{++}$ cross sections and taking into account the number of events rejected by the target counter cut, one predicts a background of $\approx 6\%$ $\pi^+\pi^-\Delta^0$ events in the "$\pi^+\pi^-n$" sample. This is an upper limit since the MM resolution during the π^+ run was slightly larger than during the π^- run ($\approx \pm 105$ MeV compared with $\approx \pm 100$ MeV). Approximately 2-4% of the remaining background was due to $K\pi$ and πp final states which were not rejected by the Čerenkov cut used.

The extent to which this 12% background affected the angular distribution and therefore the density matrix elements was estimated by determining the
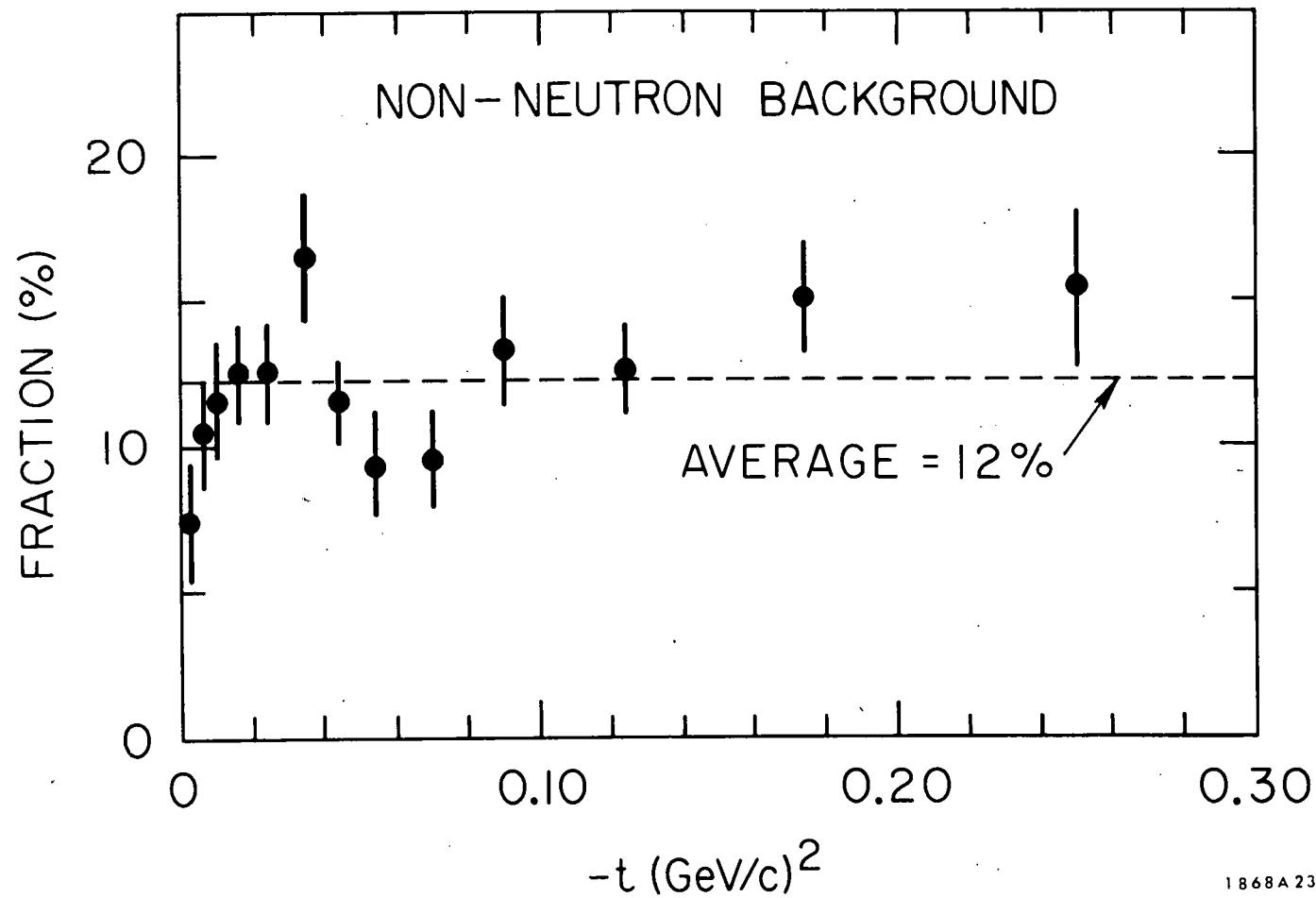
FIG. 45--Fraction of "non-neutron" background in the $\pi^+\pi^-$ event
sample as determined from the extrapolations illustrated
in Fig. 44.
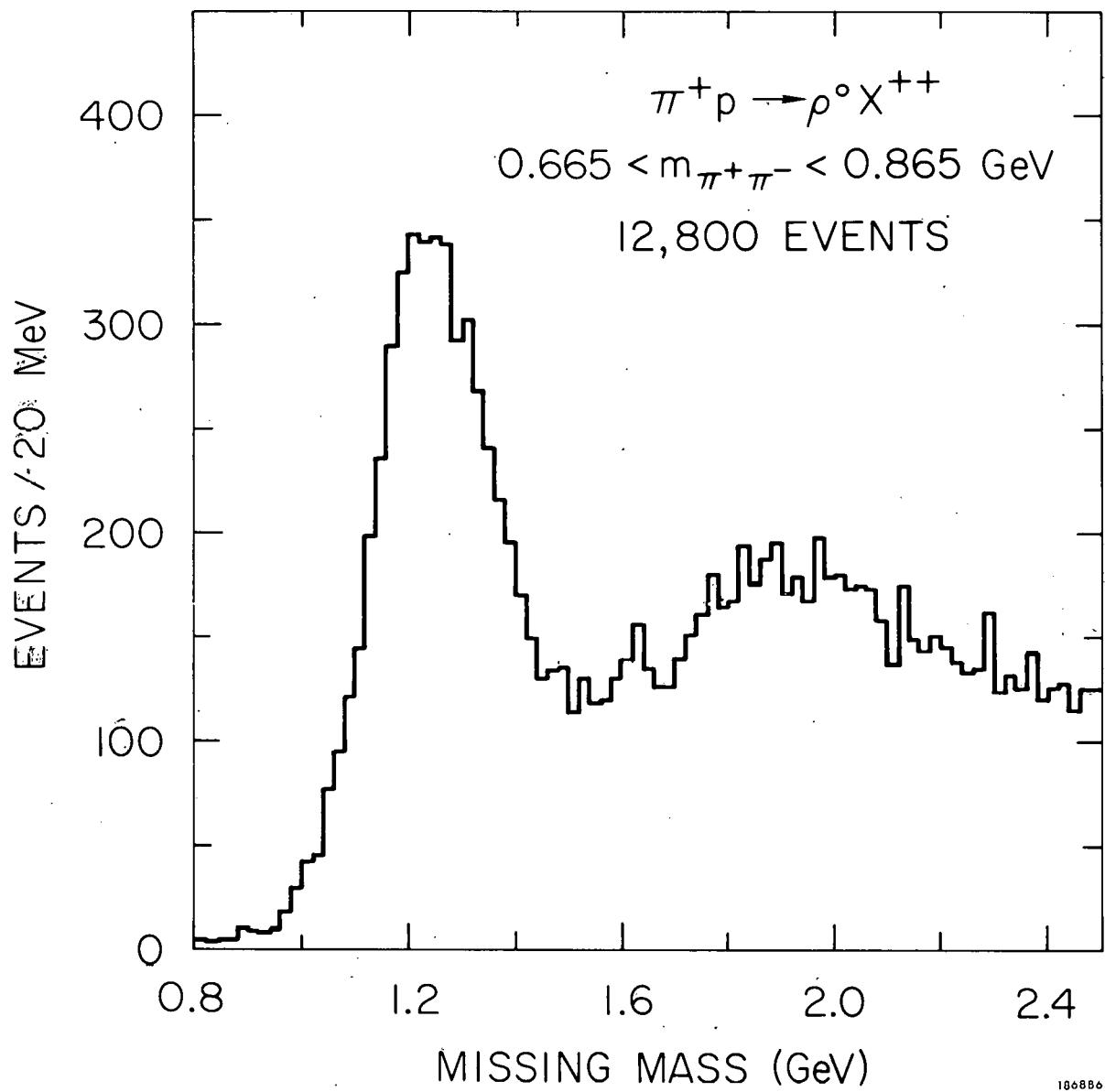
FIG. 46--Missing mass distribution for $\pi^+p \to \pi^+\pi^-X^{++}$.

ρ_{ij} for more restrictive missing-mass cuts; the results obtained agreed with the values presented above to within the statistical errors. For example, Fig. 47 compares the matrix elements obtained for the two MM cuts .8 – 1.0 GeV and .8 – 1.06 GeV.

3. Higher Partial Waves

It has commonly been assumed in previous analyses of this reaction, often for reasons of simplicity and lack of statistics, that higher partial waves than $\ell=1$ in the $\pi\pi$ system are negligible for $M_{\pi\pi} < 1$ GeV. The experimental evidence for and against this assumption is somewhat mixed. In particular, Oh et al.[54] observe an angular distribution at 7 GeV which is inconsistent with only s-and p-waves. They suggest that this may be produced by inter-ference from the channel $\pi p \rightarrow \pi N^*$. Biswas et al.[55] have also suggested that higher partial waves than $\ell=1$ may contribute in the ρ region of $\pi\pi$ mass: they find that their 4 GeV data are inconsistent with the relation $<\cos 2\,\varphi> = -\frac{3}{4}\rho_{1-1}$ $\sin^2\theta$ which is valid if only s-and p-waves are present, and they also find ρ_{1-1} to be mass dependent. They suggest that these effects may be indicative of contributions from $\ell \geq 2$. On the other hand, Schlein et al.[22,56] in a moment analysis of their data, have shown that moments arising from $\ell \geq 2$ are small compared to $\ell=0$ and 1, for the mass region $<.9$ GeV.

We find no evidence in our data that higher partial waves contribute in the ρ region. In checking for the discrepancies cited by Biswas et al., $<\cos 2\varphi>$ is found to be consistent with $-\frac{3}{4}\rho_{1-1}\sin^2\theta$ ($\chi^2 = 16.5$ for 18 degrees of freedom) and ρ_{1-1} is consistent with zero mass dependence ($\chi^2 = 10.6$ for 10 degrees of freedom). Note that at 15 GeV the final states ρn and πN^* are kinematically separated so that there can be no interferences between these
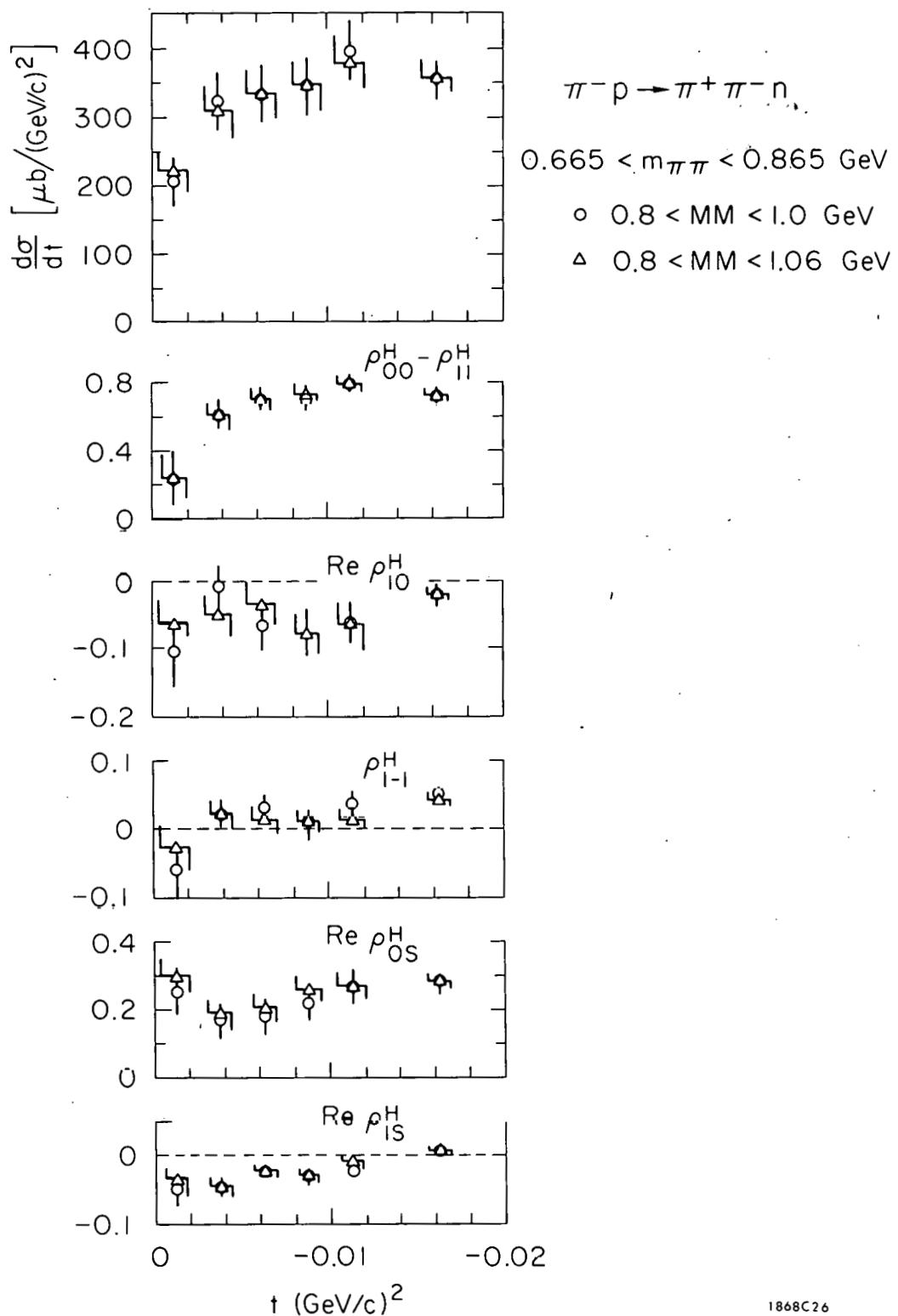
FIG. 47--Comparison of density matrix elements obtained from event
samples subject to different missing mass cuts.

two states (see Fig. 48). We have fit the angular distribution as a function of
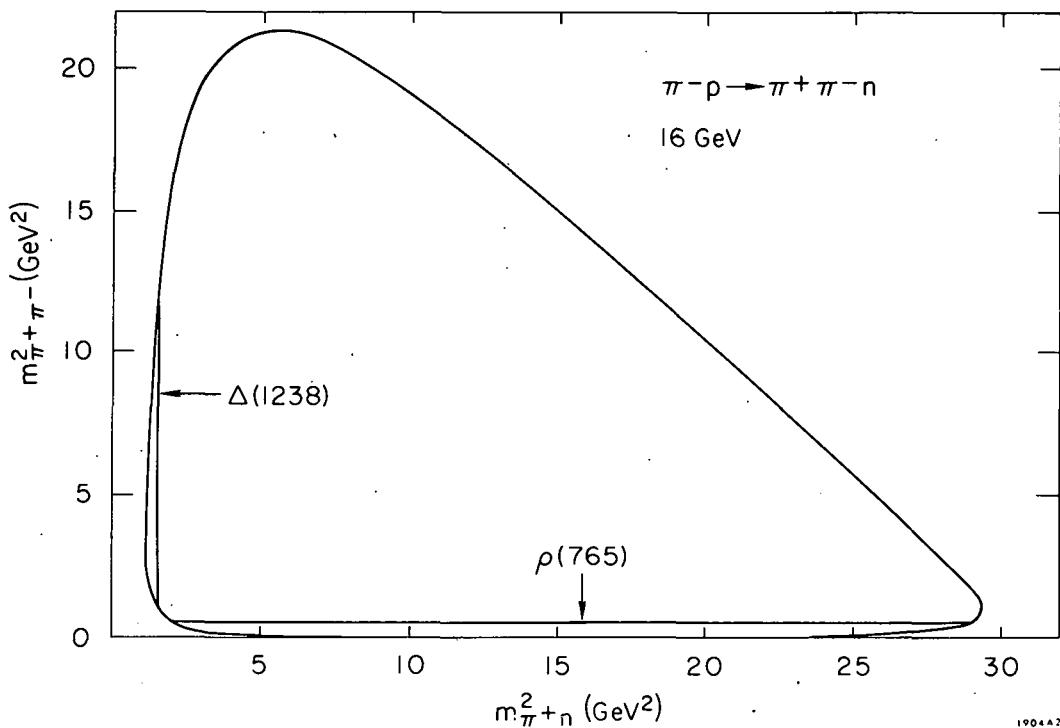
FIG. 48--Dalitz plot for $\pi^- p \rightarrow \pi^+ \pi^- n$ at 16 GeV.

$\pi\pi$ mass, adding $Y_4^0(\theta \, \varphi)$ and $Y_3^0(\theta \, \varphi)$ terms to Eq. 5.3. The fitted coefficients

of these terms are consistent with zero for $m_{\pi\pi} < .9$ GeV. In addition, we have

checked that there is no systematic deviation of the fit from the data in any

particular region of $\cos\theta$, φ ; this was performed by summing the χ^2/bin

over $\varphi \, (\theta)$ and plotting the sum as a function of $\theta \, (\varphi)$.

We therefore conclude that at the statistical level of this experiment,

partial waves with $\ell \geq 2$ are not required to describe the data.

D. Differential Cross Section and Normalization

Once the dipion angular distribution is known, it is a simple matter to

correct for the number of events not observed by the apparatus, and hence to

determine the total $\pi\pi$ differential cross section, $\frac{d\sigma}{dt}$. The number of

events, N, of Eq. 5.8, which was determined directly from the fit to the angular distribution, includes the corrections for event loss due to the geometrical acceptance of the apparatus, absorption in the target, the missing mass cut, and, to a certain extent, for the spark chamber and counter inefficiency. The following additional corrections were made to the number of events, N, and to the incident π^- flux to determine the differential cross section; the Correction Factor shown is the amount by which the "raw" cross section is multiplied to take into account each effect.

Event Loss (or Gain)			Correction Factor
a)	fraction of good events lost by the vertex cuts (ref., Section 4.G.3 and Fig. 30)	.018 ± .002	1.018
b)	estimated background of non $\pi^+\pi^-$n events (ref., Section C.2)	.122 ± .02	.878
c)	fraction of events lost due to decay of the produced π^+ or π^-	.022 ± .01	1.022
d)	event loss due to magnet veto counters being fired by delta rays produced in the target	.012 ± .005	1.012
e)	fraction of events produced in empty target runs	.008 ± .001	.992
f)	fraction of events lost during track and event reconstruction	.02 ± .01	1.02
g)	as noted in Section 4.G.1, an event was rejected if it had more than two hodoscope-agreeing tracks. Since occasionally the reconstruction program found two almost	.028 ± .002	1.029

identical tracks, where in reality only

one had existed, a fraction of good events

were lost to this selection criteria.

h)   events lost due to absorption in the   .042 ± .014   1.04

spectrometer material

i)   correction for spark chamber inefficiency*   0.08 ± .045   1.08

Corrections of Measured Incident Flux

j)   contamination of muons in the beam   .039 ± .004   1.04

k)   fraction of incident π's which produced a   .088 ± .011   1.096

non-unique signature in the P, θ, or φ

hodoscopes

The overall correction factor incorporating the above effects was 1.240

with an error of ± 0.66, if the individual errors are added in quadrature. This

does not yet include uncertainties in the absorption and missing mass correc-

tions in the Monte Carlo program, nor systematic uncertainties in the geomet-

rical detection efficiency; these are respectively estimated to be 3%, 2% and 2%.

Inclusion of these errors yields a correction factor of 1.240 ± 0.84. This, to-

gether with the average hydrogen density (.0694 gm/cm^3) and the measured

number of incident π^- (8.58 × 10^8) resulted in the following correspondence

between the number of events, N, and the cross section: .34± .023 μb/1000 events.

---

*Although the calculation of event loss due to spark chamber inefficiency should
be reasonably accurate when the chambers are working well, it becomes increas-
ingly difficult to extrapolate from the individual plane and gap efficiencies meas-
ured to an overall "event" efficiency when the chambers are working at less than
their peak capability. The decreases in event yield (per incident π^-) which
occurred during periods of lower chamber efficiency (ref. Section 2.D) were
partially, but not fully, accounted for by the calculated spark chamber efficiency.
An empirical correction has therefore been made based on a comparison of the
average yield for the entire run with the yield which was obtained when the
chambers were operating optimally.

The resulting $\pi\pi$ differential cross section for the interval $.665 < m_{\pi\pi} < .865$ GeV is presented in Fig. 49 and in Table 7. The most notable feature is the distinct turnover in the forward direction, i.e., for momentum transfers $-t < m_{\pi}^2$. Note also the rather steep slope of the cross section for larger momentum transfers; a comparison of this falloff with the exponential form e^{At} yields a slope of $A \approx 14$ $(\text{GeV}/c)^{-2}$.

The error bars indicate the statistical errors, which were determined in the same manner as for the density matrix elements. The systematic uncertainty in the absolute normalization results from the uncertainties in the above correction factors and is $\pm 6.7\%$ if the errors are added in quadrature. Some of the estimated uncertainties certainly do not add in quadrature, how- ever, so that this error may be too small. An estimated upper limit on the systematic uncertainty may be obtained by adding the absolute magnitudes of each of the above errors. This yields an uncertainty of 19%. The most plausible estimate lies somewhere in between, probably on the order of 10%.

As a check on the absolute normalization, the elastic scattering differential cross section $\frac{d\sigma}{dt}$ $(\pi^- p \to \pi^- p)$ was measured with the same apparatus.[57] The results agree well with those of Foley et al.[58] as shown in Fig. 50.

E. Fitted Mass Spectra and Normalization for $\pi^- p \to \rho^0 n$

It is evident from Fig. 34 that there is a non-negligible amount of back- ground in the $\pi^+\pi^-$ mass spectrum in the region of the ρ; this has been observed at other energies as well. A determination of either the total or the differential cross section for the $\rho^0 n$ final state therefore requires a rather detailed knowledge of the rho line-shape or of the background. Although the rho shape is in fact not well understood, even less is known about the background. In

TABLE 7

Differential Cross Sections for $\pi^- p \to \pi^+ \pi^- n$

$-t$ $(GeV/c)^2$	$\frac{d\sigma}{dt}(\pi\pi)$ $\mu b/(GeV/c)^2$	$\rho_{11}^H \frac{d\sigma}{dt}(\pi\pi)$* $\mu b/(GeV/c)^2$	$\rho_{11}^{GJ} \frac{d\sigma}{dt}(\pi\pi)$* $\mu b/(GeV/c)^2$	$\frac{d\sigma}{dt}(\rho)$* $\mu b/(GeV/c)^2$
t_{min} - .0025	221 ± 29	50.5 ± 11.4	51.2 ± 12.1	368 ± 51
.0025 - .005	307 ± 36	29.9 ± 8.9	37.9 ± 10.5	487 ± 65
.005 - .0075	332 ± 36	17.9 ± 7.0	27.3 ± 7.2	511 ± 65
.0075 - .010	344 ± 36	13.0 ± 6.3	28.9 ± 7.8	521 ± 64
.010 - .0125	377 ± 38	9.2 ± 5.8	31.3 ± 9.0	574 ± 68
.0125 - .020	355 ± 17	13.6 ± 4.0	31.2 ± 4.5	531 ± 30
.020 - .0275	375 ± 23	11.7 ± 3.5	29.6 ± 4.4	572 ± 41
.0275 - .035	301 ± 21	10.1 ± 3.7	26.5 ± 4.7	448 ± 38
.035 - .045	250 ± 17	10.0 ± 3.0	21.3 ± 3.3	368 ± 30
.045 - .060	195 ± 12	11.2 ± 2.3	20.3 ± 2.8	284 ± 22
.060 - .080	168 ± 10	10.2 ± 1.9	16.3 ± 2.2	252 ± 18
.080 - .100	111 ± 8.5	8.7 ± 1.8	11.4 ± 1.8	162 ± 15
.100 - .150	74.1 ± 3.9	9.1 ± 1.1	10.2 ± 1.1	109 ± 7.0
.150 - .200	44.7 ± 3.5	8.8 ± 1.3	8.1 ± 1.1	67.0 ± 6.3
.200 - .300	20.5 ± 1.7	6.3 ± 0.8	4.0 ± 0.6	30.5 ± 3.0

$$\frac{d\sigma}{dt}(\pi\pi) \equiv \frac{d\sigma}{dt}(\pi^- p \to \pi^+ \pi^- n), \quad .665 < m_{\pi\pi} < .865 \text{ GeV}$$

$$\frac{d\sigma}{dt}(\rho) = \frac{d\sigma}{dt}(\pi^- p \to \rho^0 n)$$

---

*Note: The values of $\rho_{11}^H \frac{d\sigma}{dt}$, $\rho_{11}^{GJ} \frac{d\sigma}{dt}$, and $\frac{d\sigma}{dt}(\rho)$ are not directly measured and depend on certain assumptions concerning the s-wave. See discussion in text.
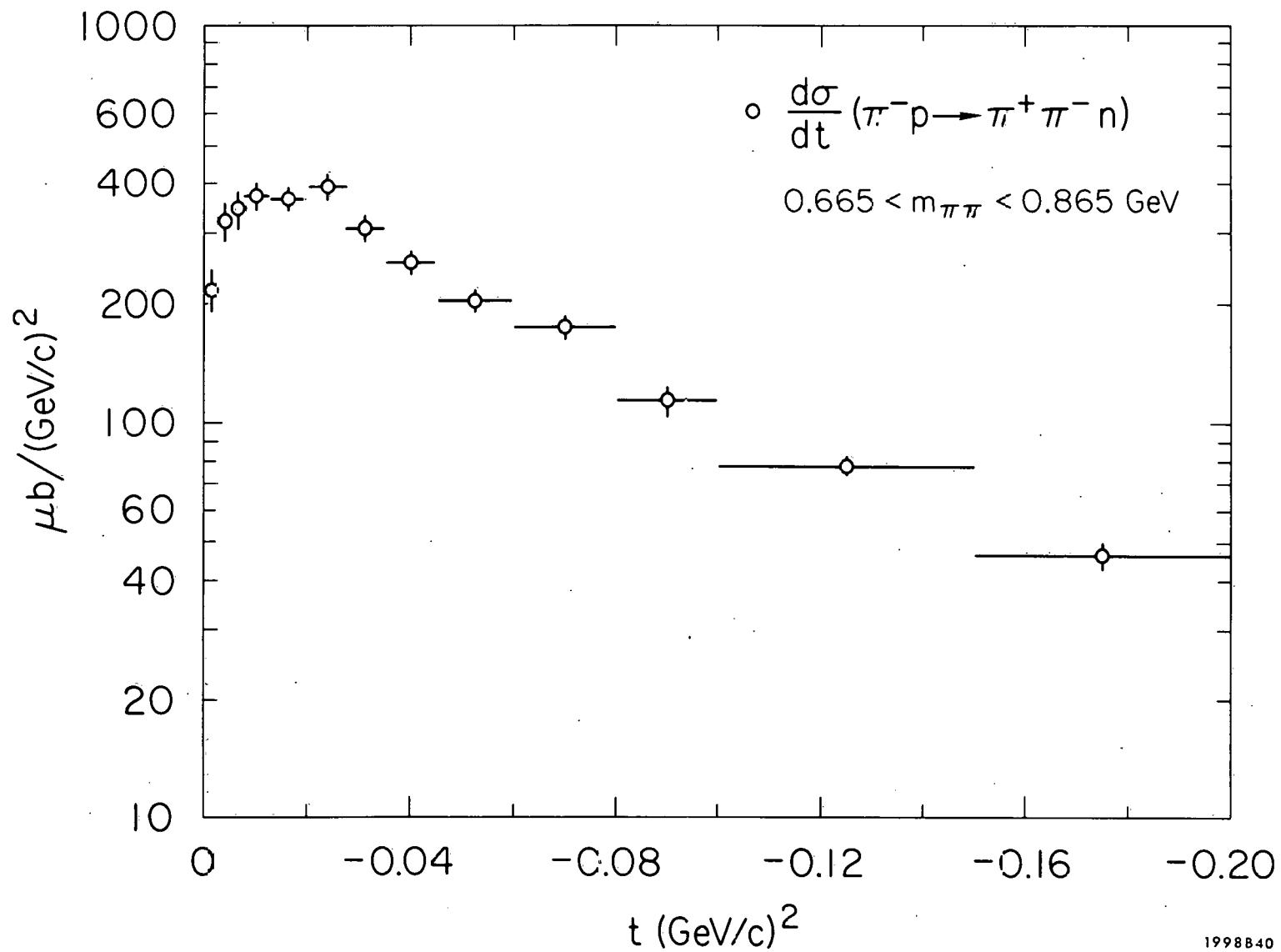
FIG. 49--Total $\pi\pi$ differential cross section as a function of momentum transfer.

1998B40
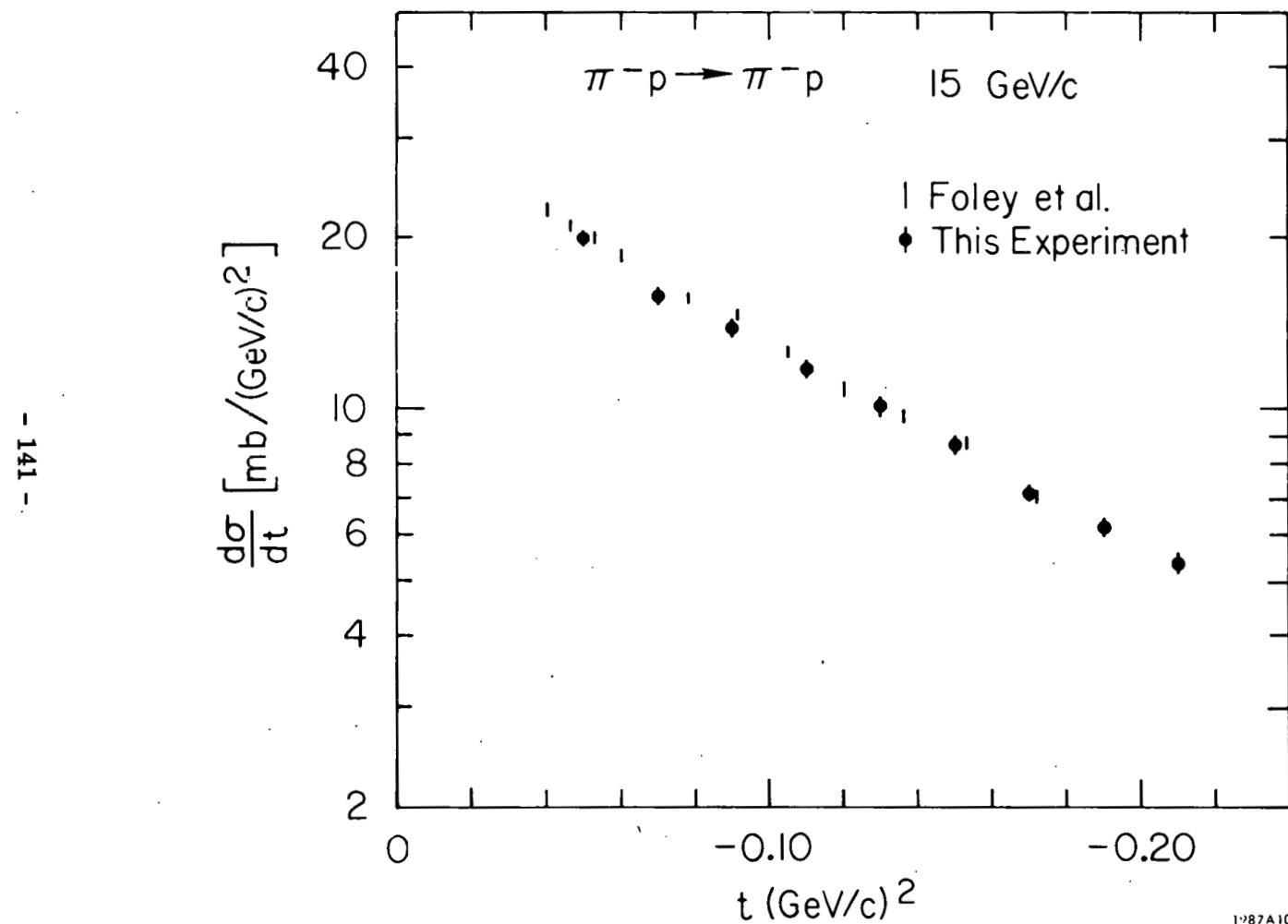
FIG. 50--Elastic-scattering differential cross section.

this experiment it was also necessary to determine the fraction of rho mesons produced outside the interval .665 - .865 GeV in order to calculate the ρ^0 differential cross section, $\frac{d\sigma}{dt} (\pi^- p \to \rho^0 n)$, from the $\pi\pi$ differential cross section presented above. (The differential and total cross section for $\pi^- p \to \rho^0 n$ are presented in Chapter 6.)

To determine this fraction, and also the amount of background under the ρ^0, the $\pi\pi$ mass spectrum for $-t < .02$ $(GeV/c)^2$ was fitted for $.4 < m_{\pi\pi} < .9$ GeV; the cut on small momentum transfers was made so that $\rho - \omega$ interference effects would be negligible.

It was assumed that only a p-wave resonance and an s-wave background contributed. The p-wave was parameterized by a Breit-Wigner form which has been used by Pisut and Roos[59] to fit both ρ^- and ρ^0 mass distributions at lower energies:

$$\frac{d\sigma}{dm} \propto \frac{1}{q} \frac{m^2 m_0^2 \Gamma_\ell^2(m)}{(m_0^2-m^2)^2+m_0^2 \Gamma_\ell^2(m)} \int_{t_{min}(m)}^{T} e^{At} dt$$

where $\quad \Gamma_\ell(m) = \Gamma_0 \left(\frac{q}{q_0}\right)^{2\ell+1} \frac{m_0}{m} \frac{1+R^2 q_0^2}{1+R^2 q^2}$,

ℓ = the dipion relative angular momentum

$$q = \left(\frac{m^2}{4} - m_\pi^2\right)^{\frac{1}{2}}$$

$$q_0 = \left(\frac{m_0^2}{4} - m_\pi^2\right)^{\frac{1}{2}}$$

m_0, Γ_0 = mass and width of resonance

A is the slope of $\frac{d\sigma}{dt}$ $(\pi^- p \to \rho^0 n)$

$t_{min}(m)$ is the kinematical lower limit of t

T is the upper limit of -t for the event sample,

and R is a parameter which corresponds to the range of the interaction.

The s-wave contribution was parameterized by the same form with R=0 and an assumed mass and width of .7 GeV and .4 GeV respectively; this is consistent with the shape of the $\pi^0 \pi^0$ mass distribution which has been studied in $\pi^- p \to \pi^0 \pi^0 n$.[60,61] Since, as is discussed in Chapter 6, this final state may be used to estimate the $\pi^+ \pi^-$ s-wave differential cross section, it was interesting to check whether the background in the $\pi^+ \pi^-$ mass spectrum was consistent with the $\pi^0 \pi^0$ mass distribution.

The resulting fit to the data is shown in Fig. 51 together with the $\pi^+ \pi^-$ mass distribution; it yields a rho mass and width of $m_\rho = .771 \pm .004$ GeV, $\Gamma_\rho = .160 \pm .014$ GeV, and $R^2 = 4.8 \pm 3.2$ $(GeV/c)^{-2}$. The amount of s-wave required (in the interval $.665 < m_{\pi\pi} < .865$ GeV and $0 < -t < .02$ $(GeV/c)^2$) is $11 \pm 2\%$, in accord with the figure of 12% which is obtained by scaling the $\pi^0 \pi^0$ cross section for the same interval to 15 GeV/c. A fit to the mass distribution for $-t < .3$ $(GeV/c)^2$ with a similar form, results in ρ parameters of $m_\rho = .764 \pm .003$ GeV and $\Gamma_\rho = .157 \pm .008$ GeV.

It should be emphasized that other acceptable fits to the mass spectrum may be obtained by changing R or the background, or by choosing different Breit-Wigner functions, such as the standard p-wave form discussed by Jackson.[52] There exist at least several Breit-Wigner forms which are indistinguishable within the interval .4 - .9 GeV and yet which have high mass behaviors resulting in normalizations differing by $\pm 20\%$. The $\pi\pi$ mass region
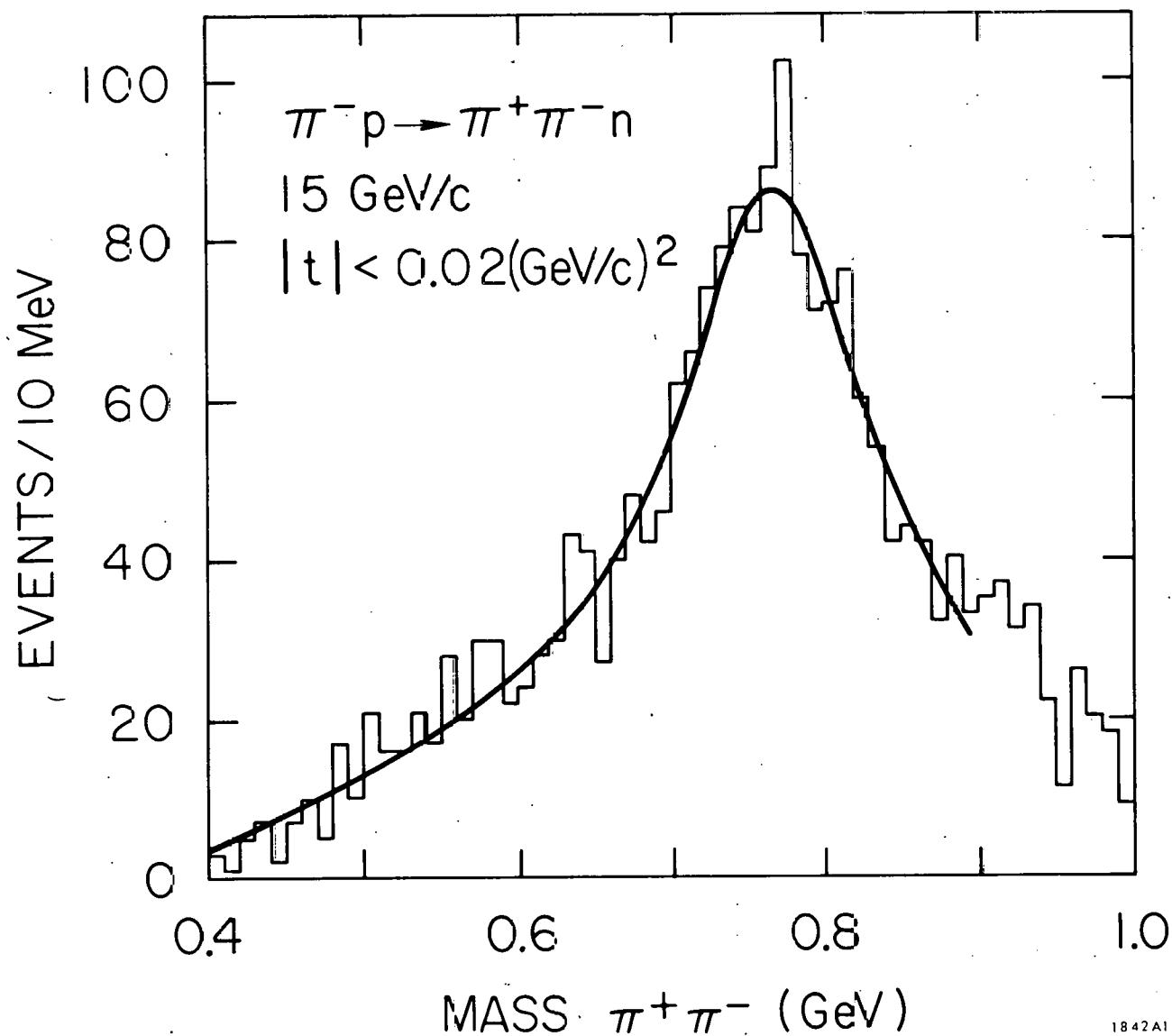
FIG. 51--The observed $\pi^+\pi^-$ mass spectrum for $|t| < .02$ $(GeV/c)^2$. The curve represents the fit described in the text.

above $\approx .9$ GeV is complicated by the presence of other resonances, as well as by the now reasonably well established anomaly occurring in the vicinity of the $K\bar{K}$ threshold.[62] Until these other effects are better understood, it is difficult to distinguish between the various forms for the rho line shape by extending the fit to higher masses.

CHAPTER 6

DETERMINATION OF THE TRANSVERSE AND LONGITUDINAL

DIFFERENTIAL CROSS SECTIONS AND DISCUSSION OF RESULTS

A. <u>Determination of</u> $\rho_{11}-\rho_{00}$ <u>and the Transverse and Longitudinal</u> $d\sigma/dt$

In the preceding chapter, the total $\pi\pi$ differential cross section and the measured density matrix elements were presented. These quantities by themselves -- that is, without a separation of ρ_{00} and ρ_{11} -- make convincing statements about the nature of the production process, as is discussed both qualitatively and quantitatively in Section B of this chapter. Here it is simply noted that the relatively large value of $\rho_{00}-\rho_{11}$, the consistency of ρ_{1-1}^{GJ} with zero, and the structure present in the matrix elements and differential cross section for $-t \stackrel{\sim}{<} m_\pi^2$ are indicative of one-pion-exchange; the fact that $\rho_{00}^{GJ}-\rho_{11}^{GJ} \neq 1$ and that ρ_{1-1}^{H} is positive rather than negative indicates that absorption (or some similar mechanism) is also present.

It is, in addition, of considerable interest to extract the transverse cross section, $2\rho_{11} \frac{d\sigma}{dt}$, since its behavior is expected to be markedly different depending on whether or not absorption is present. The existence of the sharp $\frac{1}{(t-\mu^2)^2}$ rise in the forward direction that is expected from OPEA would, of itself, be strong confirmation of the importance of one-pion-exchange.[*] In addition, whether or not a peak is observed is important from the point of view of the vector dominance model, as was noted in Chapter 1.

In determining ρ_{11} or ρ_{00} from the directly measured matrix elements, there are several approaches which may be followed. One of the most

_____

[*]Both μ and m_π are alternatively used in this chapter to refer to the mass of the pion.

straightforward procedures is to use a model, such as the one discussed in the next section (and which, in fact, describes the data very well). It is desirable, however, to determine these quantities in a model-independent fashion and to use only experimental information where possible. Consequently, three separate determinations of ρ_{11} (and therefore ρ_{00} and ρ_{ss}) are presented: The first establishes only upper and lower limits on these quantities but has the advantage that it depends only on the measurements of this experiment; the second method also relies largely on experimental measurements, but assumes that the s-wave $\pi\pi$ interaction is the same in $\pi^- p \rightarrow \pi^0 \pi^0 n$ as in $\pi^- p \rightarrow \pi^+ \pi^- n$; the third method is a model-dependent determination based on the measured ρ_{ij} presented above.

1. Limits on ρ_{00}, ρ_{11}, and ρ_{ss}

The fact that the interference terms between the s-and p-waves, and between the different p-wave amplitudes, are non-zero places significant restrictions on the values of ρ_{00}, ρ_{11}, and ρ_{ss}. In addition to the obvious constraints that are imposed by the normalization condition ($0 < \rho_{11} < .5$, $0 < \rho_{00} < 1$, $0 < \rho_{ss} < 1$), inequalities amongst the density matrix elements may be obtained by applying the Schwartz inequalities to the helicity amplitudes: The matrix element Re ρ_{10} is, by definition:[*]

$$\text{Re } \rho_{10} = \frac{1}{(2S_b+1)} \sum_{\lambda_b \lambda_d} f_{1\lambda_d ; \lambda_b} f^*_{0\lambda_d ; \lambda_b}$$

---

[*] Since the incident π^- is spin zero, the index λ_a on the helicity amplitude $f_{\lambda_c \lambda_d ; \lambda_a \lambda_b}$ has been suppressed.

which is an inner product (A_1, A_0) of the two vectors

$$A_1 = (f_{1\ \frac{1}{2};\frac{1}{2}},\ f_{1\ \frac{1}{2};-\frac{1}{2}},\ f_{1-\frac{1}{2};\frac{1}{2}},\ f_{1-\frac{1}{2};-\frac{1}{2}})\quad \text{and}$$

$$A_0 = \left(f_{0\ \frac{1}{2};\frac{1}{2}},\ f_{0\ \frac{1}{2};-\frac{1}{2}},\ f_{0\ -\frac{1}{2};\frac{1}{2}},\ f_{0\ -\frac{1}{2};-\frac{1}{2}}\right).$$

The inequality $(A_1,\ A_0) \leq |A_1|\ |A_0|$ then implies that

$$\text{Re } \rho_{10} \leq \left(\sum_{\lambda_b \lambda_d} \left|f_{1\lambda_d;\lambda_b}\right|^2\right)^{\frac{1}{2}} \left(\sum_{\lambda_b \lambda_d} \left|f_{0\lambda_d;\lambda_b}\right|^2\right)^{\frac{1}{2}} \frac{1}{(2S_b+1)}$$

$$\text{Re } \rho_{10} \leq \left(\rho_{11}\rho_{00}\right)^{\frac{1}{2}}$$

Similarly, one obtains in the same manner

$$\text{Re } \rho_{1s} \leq \left(\rho_{11}\,\rho_{ss}\right)^{\frac{1}{2}}$$

$$\text{Re } \rho_{0s} \leq \left(\rho_{00}\,\rho_{ss}\right)^{\frac{1}{2}}$$

$$\left|\rho_{1-1}\right| \leq \rho_{11}$$

The fact that the density matrix must be positive definite also requires that certain inequalities be satisfied. These are:

$$\rho_{00}\left(\rho_{11}-\rho_{1-1}\right) \geq 2\left(\text{Re } \rho_{10}\right)^2$$

$$\rho_{ss}\left(\rho_{11}-\rho_{1-1}\right) \geq 2\left(\text{Re } \rho_{1s}\right)^2$$

$$\rho_{00} \, \rho_{11} \, \rho_{ss} + 2\Big(\mathrm{Re}\, \rho_{1s}\Big) \Big(\mathrm{Re}\, \rho_{0s}\Big) \Big(\mathrm{Re}\, \rho_{10}\Big) \geq \rho_{11} \Big(\mathrm{Re}\, \rho_{0s}\Big)^2$$

$$+ \rho_{ss}\Big(\mathrm{Re}\, \rho_{10}\Big)^2 + \rho_{00}\Big(\mathrm{Re}\, \rho_{1s}\Big)^2$$

$$\rho_{00} \, \rho_{ss} \Big(\rho_{11} - \rho_{1-1}\Big) + 4\Big(\mathrm{Re}\, \rho_{1s}\Big) \Big(\mathrm{Re}\, \rho_{0s}\Big) \Big(\mathrm{Re}\, \rho_{10}\Big)$$

$$\geq \Big(\rho_{11} - \rho_{1-1}\Big) \Big(\mathrm{Re}\, \rho_{0s}\Big)^2 + 2\rho_{ss}\Big(\mathrm{Re}\, \rho_{10}\Big)^2$$

$$+ 2\rho_{00}\Big(\mathrm{Re}\, \rho_{1s}\Big)^2$$

Application of these inequalities to the measured matrix elements yields the limits on ρ_{11}^H shown in Fig. 52.
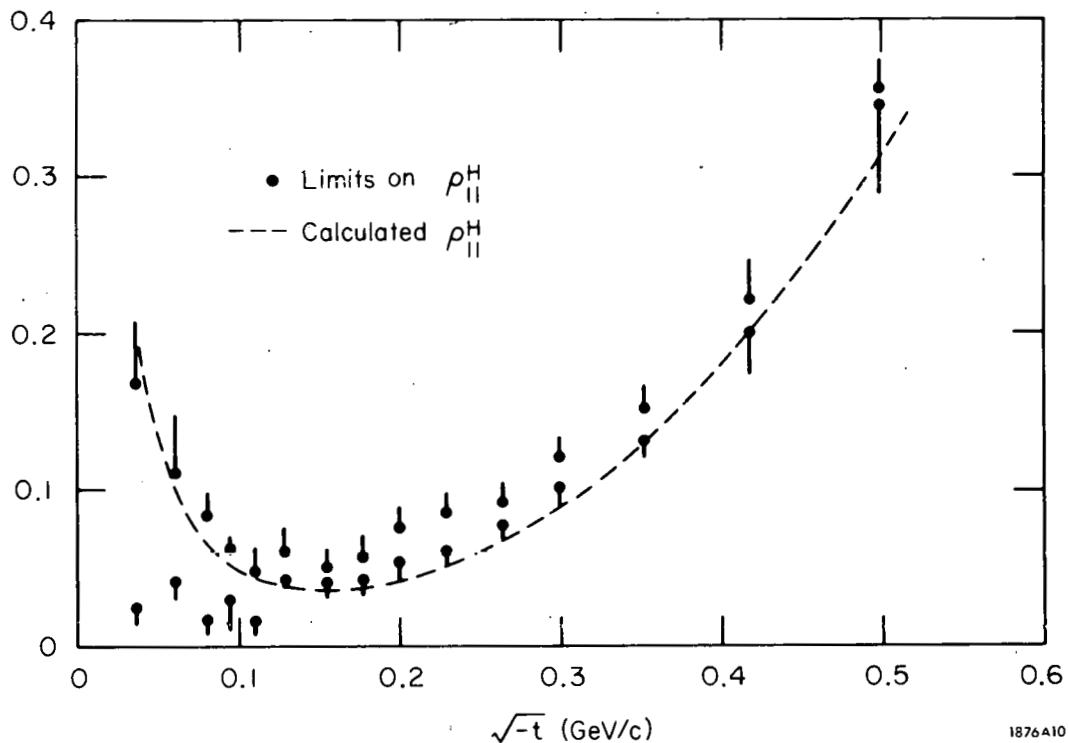
FIG. 52--The upper and lower limits on ρ_{11}^H which are determined from the Schwartz inequalities on the helicity amplitudes and the requirement that the density matrix be positive definite. The errors on the limits result from the propagation of the errors on the density matrix elements. The curve is the calculated value of ρ_{11}^H obtained when the amount of s-wave is estimated from the $\pi^- p \rightarrow \pi^0 \pi^0 n$ data.

- 149 -

The points represent the upper and lower limits while the error bars indicate

the errors on these limits resulting from propagation of the errors on the

measured ρ_{ij}. It is interesting to note that the values of ρ_{11} are, in fact,

rather well determined for momentum transfers $> m_\pi^2/2$. The corresponding

upper and lower limits on ρ_{ss}, for the same range, are approximately 18 and

12% and are quite independent of t. For smaller momentum transfers, the

behavior of ρ_{11} as well as that of ρ_{00} and ρ_{ss}, is undetermined since the limits

are not very restrictive in this region. To proceed further it is necessary to

obtain information on the t-dependence of one of these quantities -- for example,

on ρ_{ss}.

2. S-wave and Determination of ρ_{11}

The fact that there exists an s-wave $\pi\pi$ interaction in the mass region of

the rho meson has been established for some time. The first experimental

evidence was the observation of the forward-backward asymmetry,

$A = \dfrac{F-B}{F+B} = \sqrt{3} \, \mathrm{Re} \, \rho_{0s}$, of the decay angular distribution in the $\pi\pi$ rest frame.

The properties of this s-wave interaction, for example, its "mass" and "width",

its behavior as a function of momentum transfer, and whether or not it is a

resonance, have not been well established. Some phase shift analyses [63] have

favored a narrow resonant s-wave, whereas other phase shift analyses and

experiments studying $\pi^- p \rightarrow \pi^0 \pi^0 n$, [60, 61, 64] have favored a broad mass spectrum

that is non-resonant.

Until recently, experimental information about the t-dependence of the s-wave

has been particularly lacking. Theoretically, the cross section has been expected

to largely vanish in the forward direction (except for very low energies)

because it is anticipated that the reaction is dominated by OPE at small

momentum transfers. According to elementary OPE, the cross section vanishes

exactly at t=0. If absorption effects are significant, as is generally thought to be the case, the contribution to the s-wave from the nucleon-helicity-non-flip amplitude need not vanish, whereas the contribution from the helicity-flip amplitude <u>must</u> vanish at $t=t_{min}$ by angular momentum conservation.[*] The prediction that the s-wave largely vanishes in the presence of absorption then follows from the OPE prediction that the non-flip amplitude is smaller than the flip amplitude by $\approx 1/s$ (where $\sqrt{s}$ is the total energy in the c.m. system). It should be noted that the statement that the helicity-flip amplitude must vanish at $t=t_{min}$ is general, and holds regardless of the details of the inter-action.

One can obtain an experimental estimate of the s-wave differential cross section from data on $\pi^- p \rightarrow \pi^o \pi^o n$. Reasonably good measurements of the differential cross section for this reaction have recently been made by Shibata, Frisch, and Wahlig[61] at MIT and by Sonderegger and Bonamy at Saclay.[60] Since the $\pi^o \pi^o$ state in the rho mass region appears to be predominantly I=0, ℓ=0, one can obtain from these measurements an estimate of the differential cross section for the corresponding I=0, ℓ=0, $\pi^+ \pi^-$ state. The measure-ments of $d\sigma/dt$ $(\pi^- p \rightarrow \pi^o \pi^o n)$ are shown in Fig. 53; both groups observe a turn-over in the cross section for momentum transfers $< \frac{1}{2} m_\pi^2$. The data is well represented for momentum transfers $> \frac{1}{4} m_\pi^2$ by the function $\frac{|t|}{(t-\mu^2)^2} e^{At}$ (A=7(GeV/c)$^{-2}$) which is the form expected from OPE. For smaller momentum transfers the data are clearly not sufficient to determine the behavior.

---

[*] Here and elsewhere in this chapter, statements concerning flip or non-flip of the nucleon helicity refer to the center-of-mass frame of the interaction.

The figure shows two stacked plots. The top plot has y-axis "$\frac{dN}{dt}$ EVENTS/0.01 (GeV/c)^2" with values 100, 50, 10, 5 marked, and text:

Shibata, Frisch & Wahlig
MIT (1970)
$0.27 < m_{\pi^\circ \pi^\circ} < 1.0$ GeV
10 GeV/c

To the right:

$\pi^- p \rightarrow \pi^\circ \pi^\circ n$

Differential Cross Section

$$\frac{d\sigma}{dt} \propto \frac{|t|}{(t-\mu^2)^2} e^{7t}$$

The bottom plot has y-axis "$\frac{d\sigma}{dt} \left[\mu b / (GeV/c)^2 \right]$" with values 100, 50, 10, 5 marked, and text:

Sonderegger, Bonamy
SACLAY (1970)
$0.270 < m_{\pi^\circ \pi^\circ} < 0.570$ GeV
"5" GeV/c

x-axis: 0, -0.1, -0.2, -0.3, t (GeV/c)^2

1875C1

FIG. 53--Differential cross section, $d\sigma/dt$, for $\pi^- p \rightarrow \pi^0 \pi^0 n$.

Assuming, then, that $\dfrac{|t|}{(t-\mu^2)^2}\, e^{7t}$ is the form of the s-wave cross

section in this experiment, and extrapolating the normalization of Sonderegger

and Bonamy to 15 GeV, one obtains the values of ρ_{11} shown by the dashed lines

in Fig. 52.[*] The agreement with the limits, which have been determined in a

completely independent fashion is quite good. One of the most notable features

is the sharp rise in the calculated value of ρ_{11} for the momentum transfers less

than m_π^2. The existence of this peak does not depend sensitively on the behavior

of the s-wave cross section: for example, if $d\sigma/dt$ (s-wave) decreases from

$t=-m_\pi^2$ to $t=t_{min}$ by only 25%, as is actually observed in the $\pi^o\pi^o$ data, rather

than vanishing at $t=0$ as is assumed in the above form, the peak in ρ_{11} is

decreased by only 20-25%. If, however, the s-wave cross section in reality

continues rising exponentially as $t\to t_{min}$, then the peak would be largely

eliminated.

The same calculation of ρ_{11} in the Gottfried-Jackson frame yields a

similar peak, though not as pronounced. It is shown, together with the

corresponding limits, in Fig. 54. (The values of ρ_{11}^{H} and ρ_{11}^{GJ} are also pre-

sented in Tables 5 and 6).

It will be seen below that this rise in ρ_{11}^{GJ} simply reflects the turnover in

the total differential cross section since the transverse cross section,

$2\rho_{11}^{GJ}\, \dfrac{d\sigma}{dt}$ exhibits no significant structure in the forward direction.

---

[*] The $\pi^o\pi^o$n data were scaled according to p^{-2} where p is the incident beam
momentum. Sonderegger and Bonamy have shown that this scaling works well
over a range of 3-18 GeV/c. As indicated in the text, it was assumed that the
$\pi^o\pi^o$ state is entirely I=0.
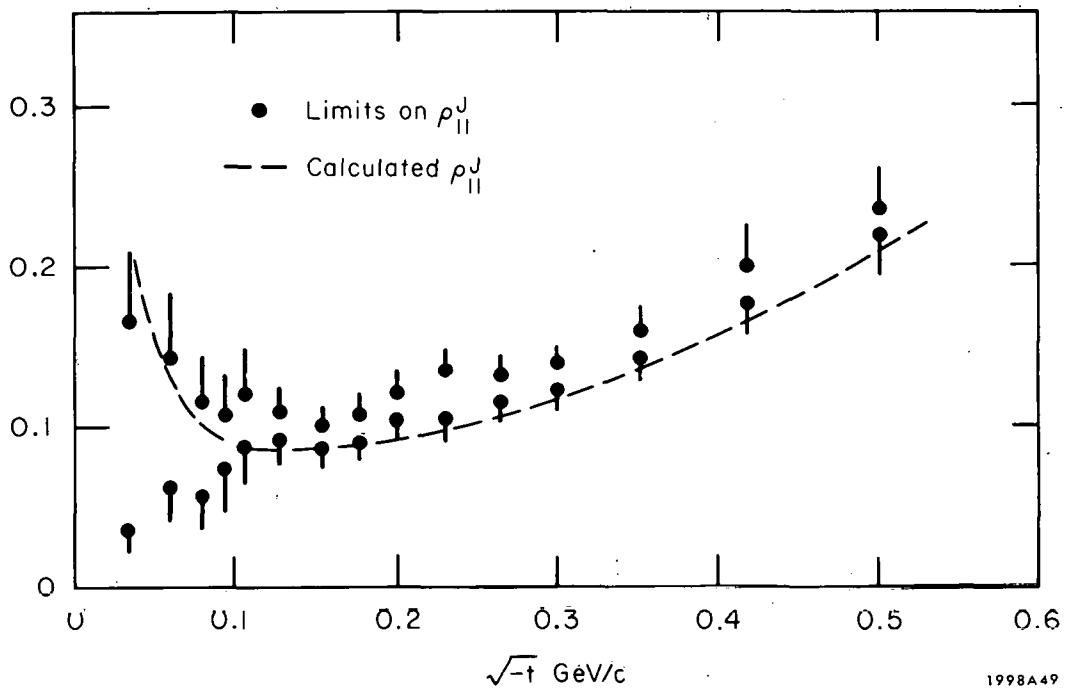
FIG. 54--The upper and lower limits on ρ_{11}^{GJ} which are determined from the Schwartz inequalities on the helicity amplitudes and the requirement that the density matrix be positive definite. The errors on the limits result from the propagation of the errors on the density matrix elements. The curve is the calculated value of ρ_{11}^{GJ} obtained when the amount of s-wave is estimated from the $\pi^- p \to \pi^0 \pi^0 n$ data.

3. Transverse and Longitudinal Differential Cross Section

Since the values of ρ_{11} obtained by estimating the $\pi^+ \pi^-$ s-wave from the $\pi^0 \pi^0$ data agree rather well with the limits presented above, this procedure has been used in calculating the transverse and longitudinal differential cross sections. This determination of ρ_{11} also agrees well with that which is obtained from fits of OPEA to the directly measured matrix elements.

- 154 -

In summary the following comparison can be made: The percentage of the total $\pi\pi$ cross section that is s-wave, when integrated from $t=t_{min} \rightarrow t=-m_{\pi}^2$ is:

$\approx 12\%$	when estimated from the $\pi^{o}\pi^{o}$ data
$\approx 10\%$	when taken from fits to OPEA
$\approx 11 \pm 2\%$	if the form is assumed to be $\dfrac{|t|}{(t-\mu^2)^2} e^{7t}$ and the magnitude is taken from the limits
$\approx 11\%$	when taken from the fits to the mass spectrum

The determination from the mass fit is largely a consistency check since it is sensitive to the mass shapes assumed for the p-and s-wave. Each of the other determinations have systematic uncertainties of $\approx 2\%$, and they are not completely independent. However, they present a consistent picture that the amount of s-wave in this region is 10-12%.

The transverse and longitudinal differential cross sections in the helicity frame, $2\rho_{11}^{H}\, d\sigma/dt$ and $\rho_{00}^{H}\, d\sigma/dt$, are presented in Fig. 55: the fact that in the forward direction there is a sharp falloff in the number of longitudinally polarized rhos produced, and a rapid rise in the number of transversely polarized rhos is evident. It is interesting to note that although the structure begins at $-t \approx m_{\pi}^2$, it does not become really significant until the momentum transfer is $\gtrsim 1/2\, m_{\pi}^2$.

The turnover in $\rho_{00}^{H}\, d\sigma/dt$ is predicted by OPE, whether it be elementary, form-factor-modified, or absorptive. The rise in $2\rho_{11}^{H} d\sigma/dt$, however, is expected only if absorption is present; elementary and form-factor-modified OPE require the transverse cross section to vanish at $t=0$ since they assume complete factorization of the upper and lower vertices.
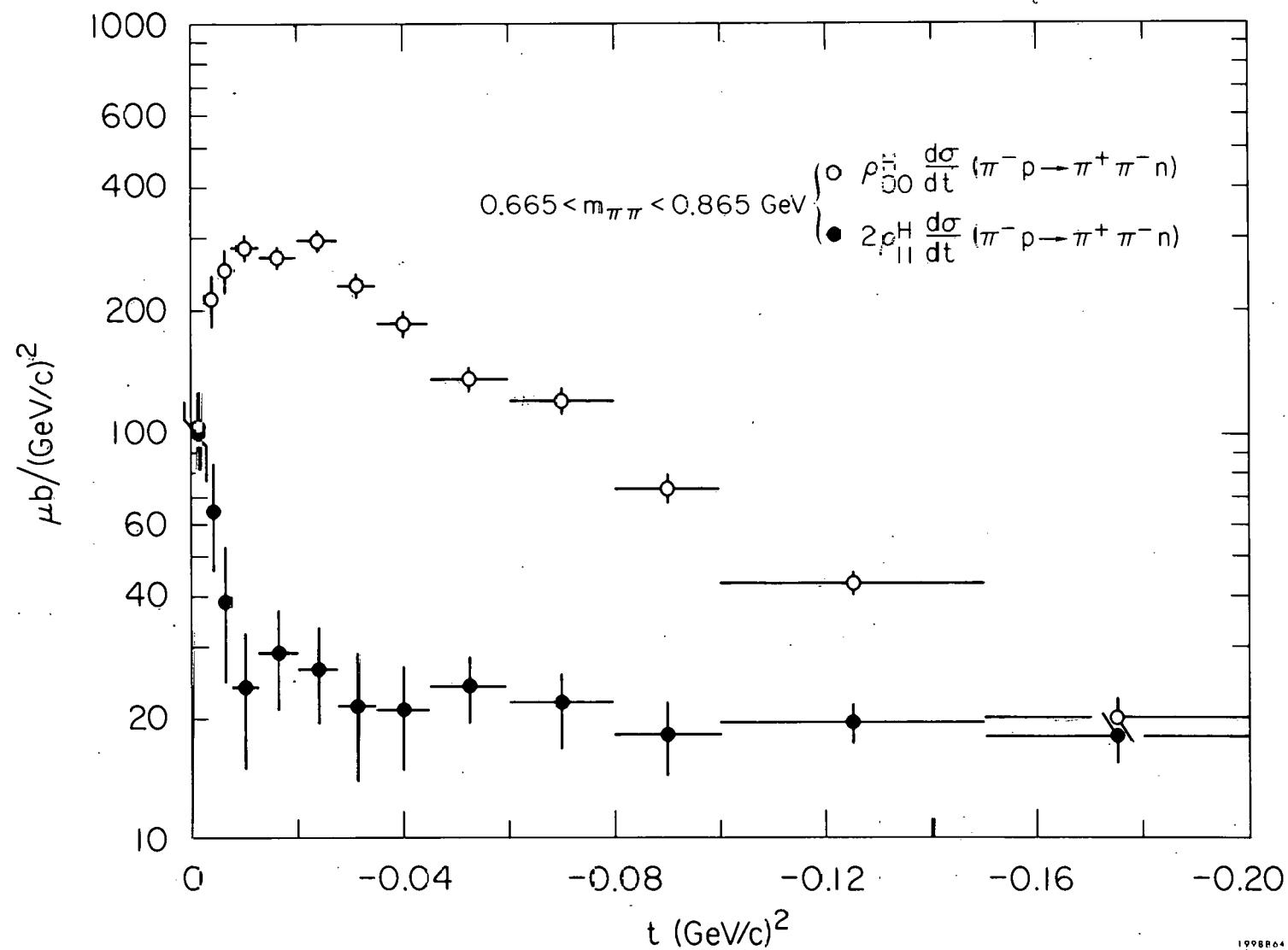
FIG. 55--The differential cross sections for transverse and longitudinally polarized rho mesons in the helicity frame. The error bars indicate the statistical errors.

Specifically, the nucleon helicity-flip at the lower vertex and the production of a transversely polarized rho meson at the upper vertex respectively require the amplitudes at these two vertices to be proportional to $(t_{min}-t)^{1/2}$, (plus some additional t-dependence that is slowly varying). Since the upper and lower vertices are assumed to be independent, the net production amplitude is proportional to $|t|/(t-\mu^2)$ (ignoring t_{min}); introduction of additional t-dependence either in the propagator or at the vertices, as is done in form-factor models, does not alter the fact that the amplitude must vanish as $t \to 0$.

From the point of view of absorption, it is convenient to consider the amplitude in terms of partial waves in the overall center-of-mass frame. Then the amplitude may be rewritten in the form

$$\frac{t}{(t-\mu^2)} = 1 + \frac{\mu^2}{t-\mu^2}$$

The first term is an anomalously large, unitarity violating contribution from one of the low partial waves; when it is strongly absorbed (for example, entirely), the remaining amplitude is proportional to $\dfrac{1}{(t-\mu^2)}$ and therefore peaks in the forward direction. The existence of the large low-partial-wave term and the motivation for its strong absorption is discussed in more detail in the next section.[11, 65, 66]

The existence of the forward rise in $2\rho_{11}$ dσ/dt may be interpreted as a strong qualitative confirmation of the vector dominance model. In addition, comparison of the unnatural-parity-exchange contributions to this cross section and to single-pion photoproduction yields quantitative agreement for $-t < 2m_\pi^2$. For a detailed comparison of the two reactions via VDM, the reader is referred to an earlier publication[27a] and to the thesis of B. Ratcliff.[27b]

In the Gottfried-Jackson frame, the longitudinal cross section also exhibits a dip as shown in Fig. 56; the transverse cross section, however, is consistent with no structure. Whereas in the helicity frame contributions to $2\rho_{11}$ $d\sigma/dt$ may arise both from pion exchange and from absorption and other mechanisms, in the Gottfried-Jackson frame pion exchange <u>cannot</u> contribute to non-zero helicity states. The transverse cross section is therefore expected not to have any structure on a scale as small as the pion mass. For more rigorous theoretical arguments on this point the reader is referred to the literature.[67] The values of $\rho_{11}^{H} \frac{d\sigma}{dt}$ and $\rho_{11}^{GJ} \frac{d\sigma}{dt}$ are listed in Table 7.

4.   Density Matrix Elements and $d\sigma/dt$ for $\pi^{-}p \rightarrow \rho^{0}n$

Having estimated the amount and the t-dependence of the s-wave background, it is possible to determine the density matrix elements and the total differential cross section for ρ^{0} production. The ρ_{ij} were obtained from the corresponding $\pi\pi$ matrix elements by imposing the normalization condition $2\rho_{11} + \rho_{00} = 1$, while $d\sigma/dt$ $(\pi^{-}p \rightarrow \rho^{0}n)$ was obtained from the total $\pi\pi$ differential cross section by subtracting the s-wave and correcting for the fraction of the rho mass spectrum outside the cut .665 - .865 GeV. The behavior of each of these quantities is shown in Figs. 57-58 and is qualitatively the same as the corresponding quantities for the $\pi\pi$ system as a whole. The values of $\frac{d\sigma}{dt}$ are listed in Table 7.

The normalization uncertainty in the differential cross section is ± 25%, the dominant contribution arising from the uncertainty in the rho line shape (ref. Section 5 . E). A calculation of the total rho cross section,
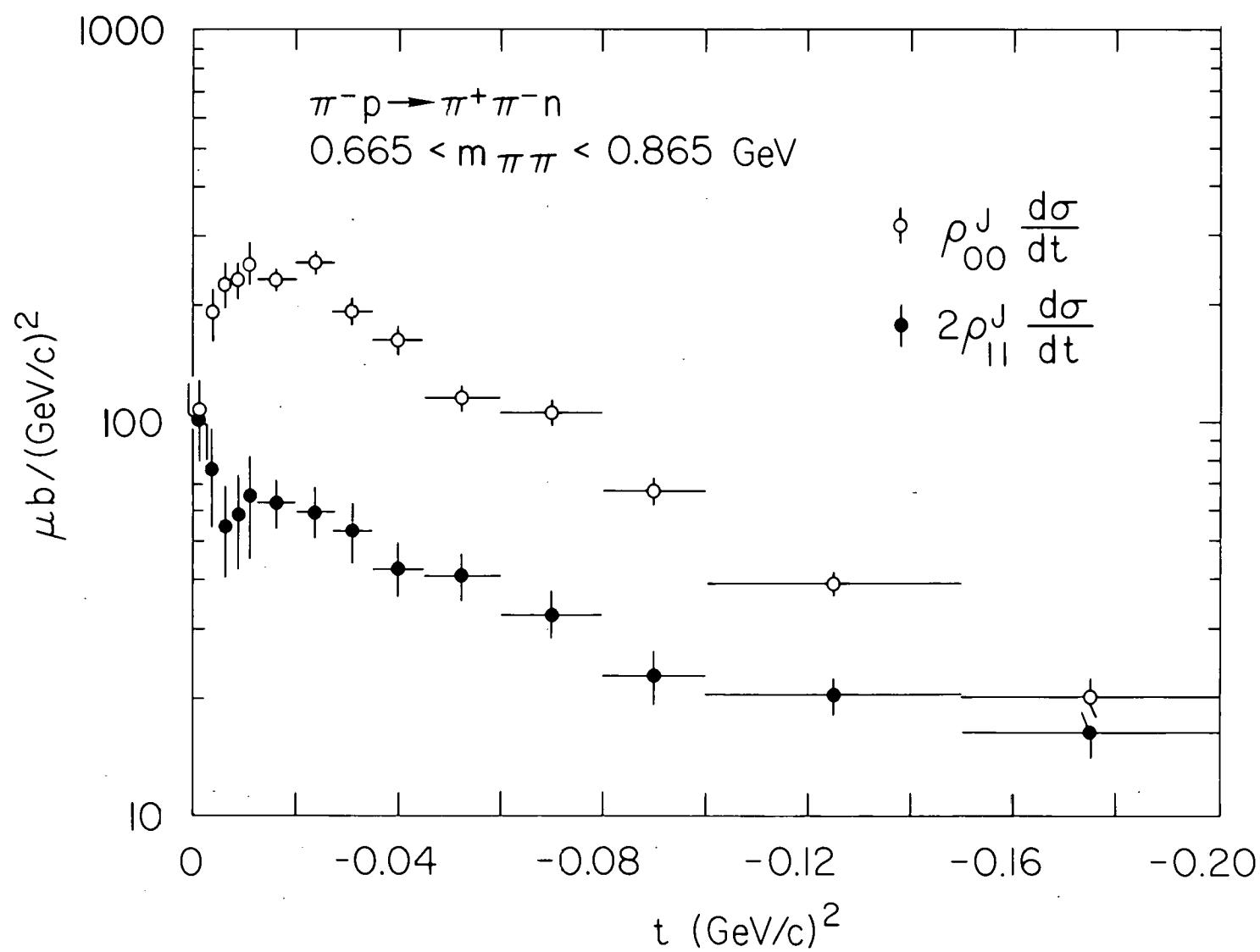
FIG. 56--The differential cross sections for transverse and longitudinally polarized rho mesons in the Gottfried-Jackson frame. The error bars indicate the statistical errors.
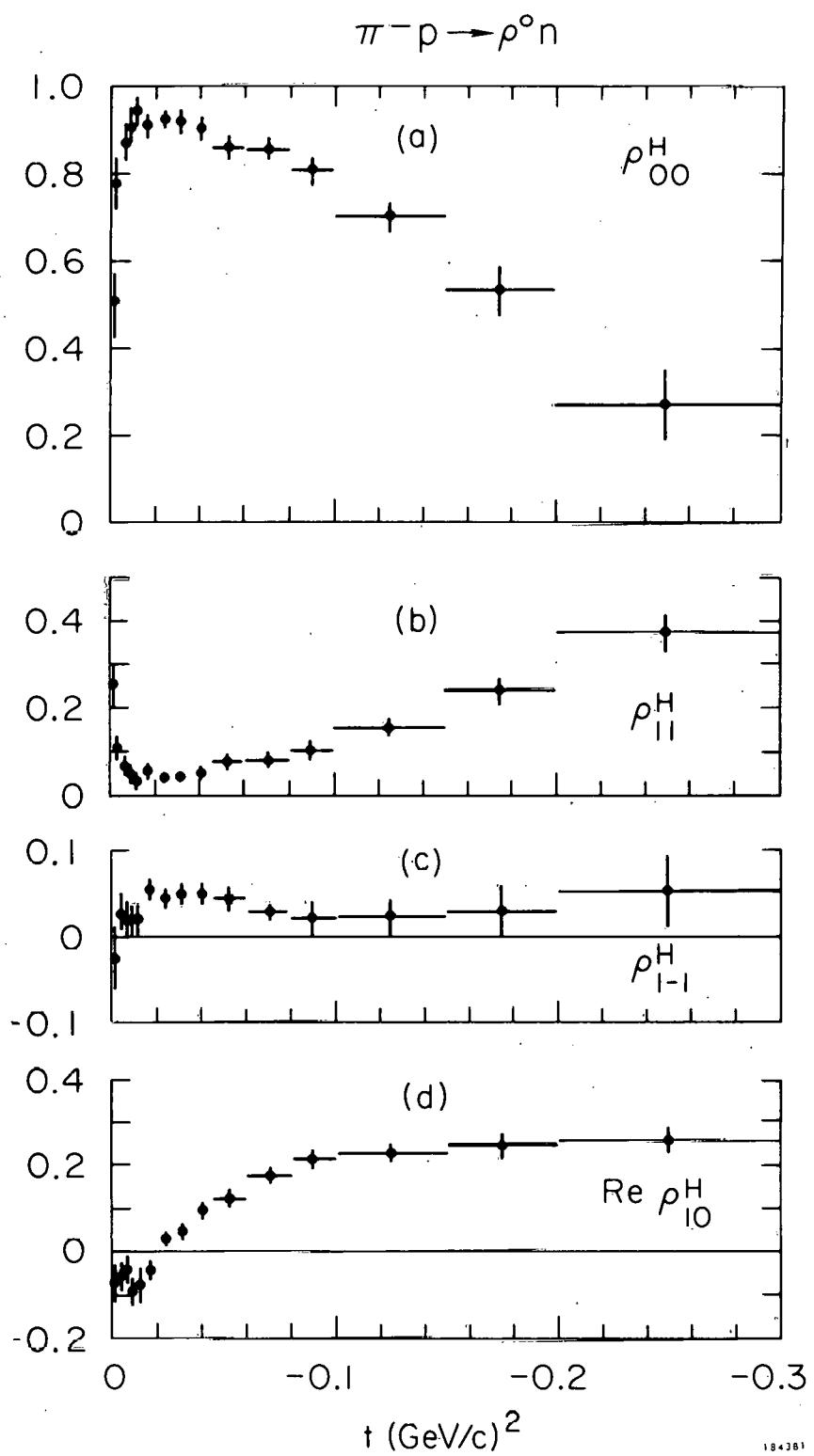
FIG. 57--Density matrix elements for the rho meson, evaluated in the
helicity frame.
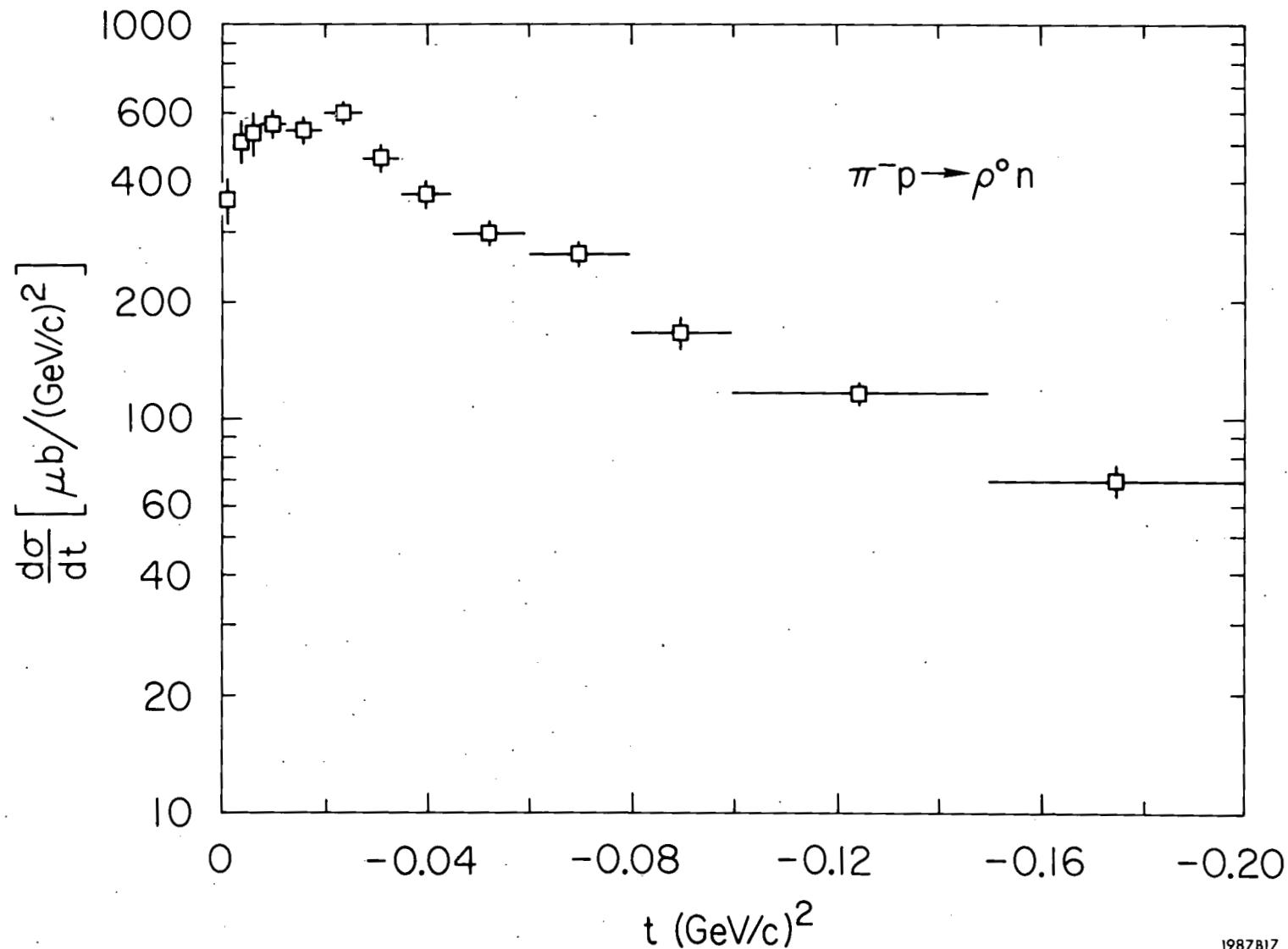
FIG. 58--Total differential cross section for $\pi^-p \to \rho^0 n$.

1987817

assuming that $d\sigma/dt$ extrapolates to larger momentum transfers as a simple

exponential,* agrees reasonably well with the other available measurements,

as is shown in Fig. 59.

B. Predictions of OPEA

As was mentioned in Chapter 1, OPEA has enjoyed considerable qualitative

success in describing various reactions which may be expected to be dominated

by one-pion-exchange at small momentum transfers. As more precise data

has become available recently, one has been provided with the opportunity to

make more quantitative tests of the predictions. Closely connected with this

point is the fact that although the physical motivations for absorption of some

kind are clear, there is no unique prescription for applying the absorption

corrections in a quantitative way. The model that is described below uses a

very simple prescription and yet describes the data rather well.

1. Formalism

One may write the amplitude for producing a dipion state of momentum

transfer t, which subsequently decays such that the direction of the decay

π^- (or π^+) in the helicity frame is described by the polar angles θ and φ in

the general form:[28, 31]

$$A_{\lambda\lambda'}(t, \theta, \varphi) = \sum_\mu (t_{min} - t)^{n/2} \sum_\ell M^\mu_{\lambda\lambda'\ell}(t) \, Y^\mu_\ell (\theta, \varphi) \qquad (6.1)$$

---

*It was assumed that at large t, $\frac{d\sigma}{dt} \propto e^{2.6t}$ as was observed by the Toronto-Wisconsin experiment[68] at 7 GeV/c.
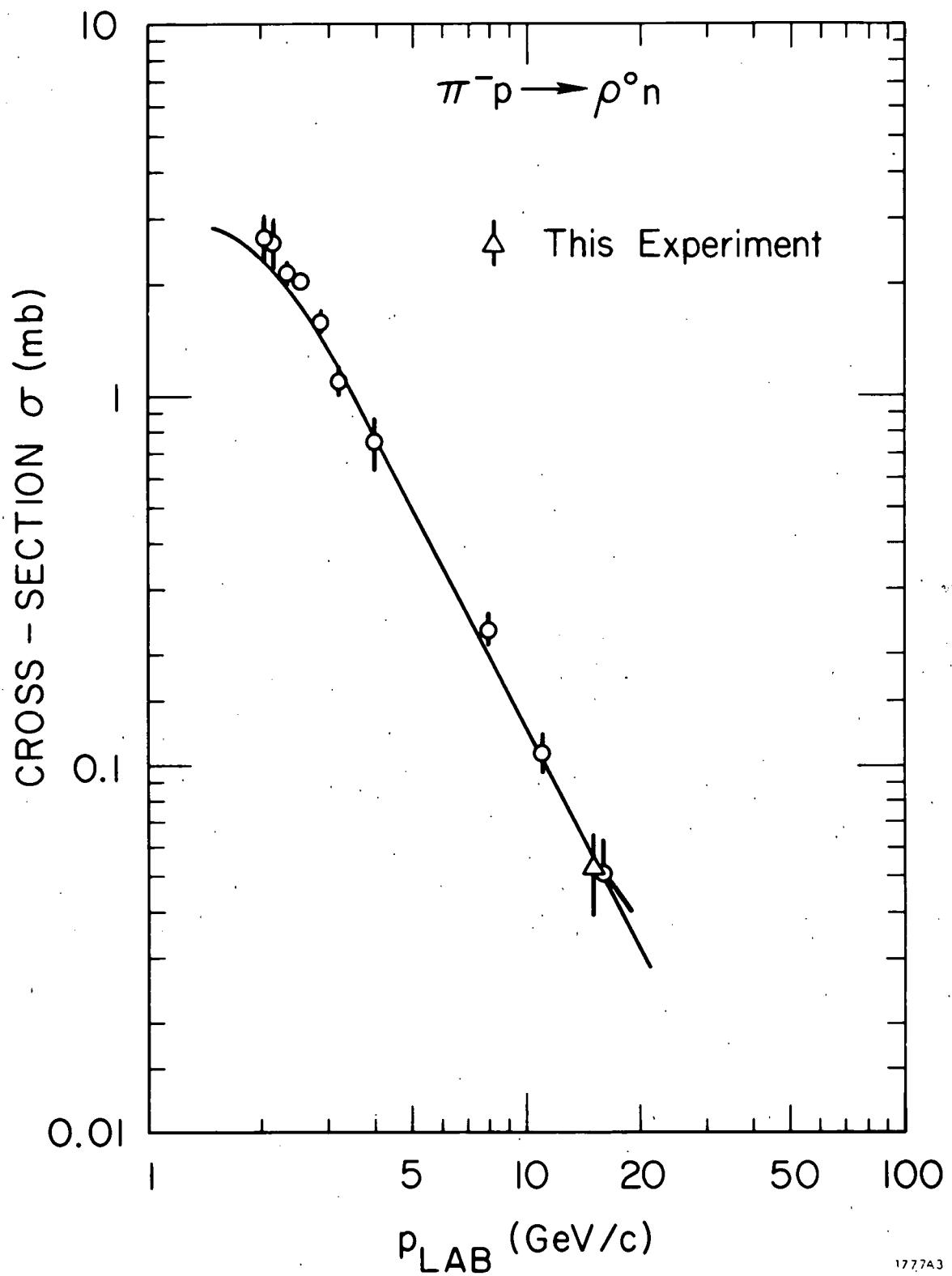
FIG. 59--Comparison of the total rho cross section measured in this experiment with previous measurements. The error bar shown includes a 20% systematic error due to uncertainty in the rho line shape.

- 163 -

where

λ and λ' are the initial and final nucleon helicities

ℓ is the relative angular momentum of the dipion state

μ is the dipion helicity

and $n \equiv \lambda + \mu - \lambda'$ is the net helicity change in the reaction.

The factor $(t_{min} - t)^{n/2}$ is the minimal t-dependence that is required by angular momentum conservation.

If one assumes that the nucleon helicity flip amplitude dominates, as is expected from OPE, and that the differential cross section should be proportional to the pion propagator-squared and s^{-2} (where $\sqrt{s}$ is the total c.m. energy), one may then write

$$\frac{d^3\sigma}{dt\,dm^2_{\pi\pi}\,d\Omega} = \frac{1}{s^2(t-\mu^2)^2} \frac{1}{2} \left\{ \left| A_{+-} \right|^2 + \left| A_{-+} \right|^2 \right\}$$

where (+) and (-) indicate + 1/2 and -1/2 respectively.

Substituting the expression (6.1) for $A_{\lambda\lambda'}$ and using the following parity relations for the $M^{\mu}_{\lambda\lambda'\ell}$

$$M^{\pm 1}_{\frac{1}{2}-\frac{1}{2}1} = -M^{\mp 1}_{-\frac{1}{2},\frac{1}{2}1} \qquad M^{0}_{\frac{1}{2}-\frac{1}{2}0} = M^{0}_{-\frac{1}{2}\frac{1}{2}0}$$

$$M^{0}_{\frac{1}{2}-\frac{1}{2}1} = M^{0}_{-\frac{1}{2}\frac{1}{2}1}$$

one obtains:

$$s^2(t-\mu^2)^2 \frac{d^3\sigma}{dt\,dm_{\pi\pi}^2\,d\Omega} = \frac{1}{2}\left| m_1^{-1}Y_1^{-1} + (-t')^{1/2}\left(m_1^0 Y_1^0 + m_0^0 Y_0^0\right) - t'\left(m_1^1 Y_1^1\right)\right|^2$$

$$+ \left| -m_1^{-1}Y_1^1 + (-t')^{1/2}\left(m_1^0 Y_1^0 + m_0^0 Y_0^0\right) + t'\left(m_1^1 Y_1^{-1}\right)\right|^2$$

$$= \frac{1}{4\pi}\left\{ -t'\left|m_0^0\right|^2 + 3\left(-t'\left|m_1^0\right|^2\right)\cos^2\theta \right.$$

$$+ 3/2\left(\left|m_1^{-1}\right|^2 + t'^2\left|m_1^1\right|^2\right)\sin^2\theta \qquad (6.2)$$

$$+ 3\sqrt{2}\,(-t')^{1/2}\,\frac{\mathrm{Re}\left(m_1^{-1}+t'm_1^1\right)^* m_1^0}{2}\,\sin 2\theta\cos\varphi$$

$$+ 2\sqrt{6}\,(-t')^{1/2}\,\frac{\mathrm{Re}\left(m_1^{-1}+t'm_1^1\right)^* m_0^0}{2}\,\sin\theta\cos\varphi$$

$$+ 3t'\,\mathrm{Re}\left(m_1^{-1*}m_1^1\right)\sin^2\theta\cos 2\varphi$$

$$\left. + 2\sqrt{3}\,(-t')\,\mathrm{Re}\left(m_1^{0*}m_0^0\right)\cos\theta\right\}$$

It has been assumed that only s- and p-waves contribute, and the following identifications have been made:

$$t' = t - t_{min}$$

$$m_\ell^\mu \equiv M_{\frac{1}{2} - \frac{1}{2}\ell}^\mu$$

- 165 -

A comparison of Eqs. (5.3) and (6.2) yields the following expressions for the density matrix elements:

$$\rho_{ss} = -t' \left| m_0^0 \right|^2 / N \qquad\qquad (6.3.a)$$

$$\rho_{00} = -t' \left| m_1^0 \right|^2 / N \qquad\qquad (b)$$

$$\rho_{11} = \left(\left| m_1^{-1} \right|^2 + t'^2 \left| m_1^1 \right|^2 \right) / 2N \qquad\qquad (c)$$

$$\mathrm{Re}\,\rho_{0s} = -t' \,\mathrm{Re}\left(m_1^{0*} m_0^0 \right) / N \qquad\qquad (d)$$

$$\mathrm{Re}\,\rho_{01} = -(-t')^{1/2} \mathrm{Re} \left(m_1^{-1} + t' m_1^1 \right)^* m_1^0 / 2N \qquad\qquad (e)$$

$$\mathrm{Re}\,\rho_{s1} = -(-t')^{1/2} \mathrm{Re} \left(m_1^{-1} + t' m_1^1 \right)^* m_0^0 / 2N \qquad\qquad (f)$$

$$\rho_{1-1} = -t' \,\mathrm{Re}\left(m_1^{-1*} m_1^1 \right) / N \qquad\qquad (g)$$

where $N = \left| m_1^{-1} \right|^2 + (-t') \left(\left| m_1^0 \right|^2 + \left| m_0^0 \right|^2 \right) + (-t')^2 \left| m_1^1 \right|^2 = s^2 (t-\mu^2)^2 \dfrac{d^2\sigma}{dt\,dm_{\pi\pi}^2}$

The expression for N follows from the normalization condition

$$\rho_{00} + 2\rho_{11} + \rho_{ss} = 1$$

Two other expressions of interest are those for $\rho_{11} + \rho_{1-1}$ and $\rho_{11} - \rho_{1-1}$ which give, respectively, the contributions of natural-and unnatural-parity

exchange in the t-channel to the helicity ± 1 states of the dipion system:

$$\rho_{11} + \rho_{1-1} = \left| m_1^{-1} - t' \, m_1^{1} \right|^2 \qquad \text{(6.4.a)}$$

$$\rho_{11} - \rho_{1-1} = \left| m_1^{-1} + t' \, m_1^{1} \right|^2 \qquad \text{(6.4.b)}$$

Except for the assumption that only the nucleon-helicity-flip amplitude contributes, the expressions above for the density matrix elements are completely general; the m_ℓ^μ's may, in principle, be complicated functions of t. The specific physical assumptions which comprise a particular model are concerned with prescribing the t-dependence and relative magnitudes and phases of these amplitudes.

2. The Pion Pole and Absorption

If the scattering amplitude for the reaction of interest, in this case $\pi^- p \rightarrow \pi^+ \pi^- n$, does in fact contain a pion pole, it is possible to relate the magnitudes of the m_ℓ^μ's <u>at the pole</u> by fairly general arguments. It is the variation of these amplitudes (both in phase and magnitude) as one goes away from the pole that is uncertain, and it is in this regard that absorptive effects are important.

Whatever non-OPE contributions to the scattering amplitude exist in the physical region -- absorption, exchange of heavier particles, or double-particle exchange -- these contributions are expected to vanish at the pion pole.

Then, in the Gottfried–Jackson frame, only $\rho_{00} \neq 0$ for $t = \mu^2$. The density

matrix elements in the helicity frame may be obtained by a rotation:

$$\rho_{11}^{H} = \rho_{11}^{GJ}\left(\frac{1+\cos^2\alpha}{2}\right) + \rho_{00}^{GJ}\left(\frac{\sin^2\alpha}{2}\right) + \frac{\text{Re}\rho_{10}^{GJ}}{\sqrt{2}}\sin2\alpha + \rho_{1-1}^{GJ}\frac{\sin^2\alpha}{2}$$

$$\rho_{00}^{H} = \rho_{11}^{GJ}\sin^2\alpha + \rho_{00}^{GJ}\cos^2\alpha - \rho_{1-1}^{GJ}\sin^2\alpha - \sqrt{2}\,\text{Re}\rho_{10}^{GJ}\sin2\alpha \qquad (6.5)$$

with the angle of rotation between the two frames being approximately given by

$$\cos\alpha \approx \frac{1+t/m_{\pi\pi}^2}{1-t/m_{\pi\pi}^2}\,; \qquad\qquad \sin\alpha \approx \frac{\frac{2}{m_{\pi\pi}}(-t)^{1/2}}{1-t/m_{\pi\pi}^2}$$

for small momentum transfers.

An evaluation of Eqs. (6.5) continued to the pion pole then yields

the result

$$\left.\frac{\rho_{00}^{H}}{2\rho_{11}^{H}}\right|_{t=\mu^2} = \left.\frac{\sigma_{\text{longitudinal}}}{\sigma_{\text{transverse}}}\right|_{t=\mu^2} = -\left(\frac{m_{\pi\pi}}{2\mu}\right)^2 \qquad (6.6)$$

Similarly, a constraint between the two transverse amplitudes may be

obtained by noting that at the pole there can be no natural-parity exchange. Thus,

$(\rho_{11}+\rho_{1-1})\big|_{t=\mu^2} = 0$ which implies by Eq. (6.4a),[*] that

$$\left[m_1^{-1} = \mu^2 m_1^1\right]_{t=\mu^2} \qquad (6.7)$$

---

[*] Since $t_{\text{min}} \ll m_\pi^2$ for this experiment, it is ignored in the following discussion.

The relative phases of m_1^{-1}, m_1^1, and m_1^0 at the pole are taken here to be those predicted by elementary OPE; namely, $\arg(m_1^{-1})=\arg(m_1^1)=\arg(m_1^0)$. The relative phase of m_1^{-1} and m_1^1 is, of course, fixed by Eq. (6.7) as well.

With the above assumptions, the only unknown quantities, at the pole, are the relative magnitude of the s-wave, the s-p phase, and the overall normalization of the amplitudes. There still remains, however, the question of the t-dependence of the amplitudes as one goes away from the pole.

According to elementary OPE, the m_ℓ^μ's may be quite rapid functions of t; for example, $m_1^{-1} \sim t$. Ross and Kane[28] have argued, however, that when absorption effects are included these amplitudes should be only weakly t-dependent; for small momentum transfers, viz., $-t \gtrsim 4\mu^2$, it is suggested that bilinear combinations of the m_ℓ^μ's may be approximated by a linear function of t.

In a similar vein, P. K. Williams[31] has suggested that aside from an overall helicity-independent collimating factor, $e^{A(t-\mu^2)}$, the m_ℓ^μ's may be considered independent of t (for $-t \gtrsim 10\,\mu^2$). The justifications of this assumption are discussed in considerable detail in the literature;[31,66] consequently, only a brief discussion is presented here.

Any one-pion-exchange amplitude may be written in the general form:

$$< \lambda_c \lambda_d |T| \lambda_a \lambda_b > = (\sin\tfrac{\theta}{2})^{|\lambda-\nu|} (\cos\tfrac{\theta}{2})^{|\lambda+\nu|} \frac{P(\lambda,\nu,t)}{t-\mu^2} \tag{6.8}$$

where $\lambda=\lambda_a-\lambda_b$, $\nu=\lambda_c-\lambda_d$, θ is the center-of-mass scattering angle, and $P(\lambda,\nu,t)$ is a polynomial in t. One may rewrite $\frac{P(\lambda\nu t)}{t-\mu^2}$ in the form

$$\frac{P(\lambda,\nu,t)}{t-\mu^2} = \frac{P(\lambda,\nu,\mu^2)}{t-\mu^2} + R(\lambda,\nu,t) \tag{6.9}$$

where $R(\lambda, \nu, t)$ is also a polynomial in t. Upon performing a partial wave

analysis of $< \lambda_c \lambda_d |T| \lambda_a \lambda_b >$, it is found that $R(\lambda, \nu, t)$ gives rise to anomalously

large, often unitarity-violating terms for low partial waves. At the very least,

these terms will be strongly reduced by absorption. It has furthermore been

suggested that since the contributions of the interaction to low partial waves

cannot be given correctly by OPE anyway, it is not unreasonable to drop these

terms altogether. It is evident from Eqs. (6.8) and (6.9) that this is equivalent

to dropping all t-dependence of the elementary OPE amplitudes other than

$(\sin \frac{\theta}{2})^{|\lambda-\nu|} (\cos \frac{\theta}{2})^{|\lambda+\nu|} \frac{1}{t-\mu^2}$. * It may then be assumed that the only other

effect of absorption is a helicity-independent collimation of the production

angular distribution which may be represented by a smooth function of t which is

normalized to 1 at $t=\mu^2$; one reasonable such function is $e^{A(t-\mu^2)}$.

Note that if one makes this assumption, viz., $m_\ell^\mu = \tilde{m}_\ell^\mu e^{A(t-\mu^2)}$ where $\tilde{m}_\ell^\mu$

is independent of t, the constraints between the p-wave amplitudes at the pole

are then valid for all values of t (within the region of validity of the model quoted

above). The behavior of the density matrix elements and the differential cross

section is then completely determined by only four parameters: the relative

magnitude of s- and p-wave, the relative s-p phase, the overall normalization,

and the parameter A which is related to the slope of the differential cross

section. The dependence of the density matrix elements and the differential

---

*Note that $(\sin \frac{\theta}{2})^{|\lambda-\nu|}$ is precisely the factor $(t_{min}-t)^{n/2}$ of Eq. (6.1) (within
factors independent of t). The term $(\cos \frac{\theta}{2})^{|\lambda+\nu|}$ could also have been
explicitly included in Eq. (6.1) but was suppressed since it is ≈ 1 for small t.

cross section on these four parameters may be explicitly illustrated by writing

$$\rho_{00} - \rho_{11} = \tfrac{1}{2} \cdot (X\delta - \delta^2 - 1) / \xi(t)$$

$$\rho_{1-1} = \delta / \xi(t)$$

$$\text{Re}\rho_{10} = \tfrac{1}{2}(\tfrac{1}{2}X\delta)^{\frac{1}{2}} \cdot (\delta - 1)/\xi(t) \qquad\qquad (6.10)$$

$$\text{Re}\rho_{0s} = \cos\varphi_{sp} \cdot \delta \cdot (\tfrac{1}{2}X\epsilon)^{\frac{1}{2}} / \xi(t)$$

$$\text{Re}\rho_{1s} = \tfrac{1}{2}\cos\varphi_{sp} \cdot (\delta - 1) \cdot (\delta\epsilon)^{\frac{1}{2}}/\xi(t)$$

$$\xi(t) = 1 + (X/2 + \epsilon) \cdot \delta + \delta^2$$

$$\frac{d^2\sigma}{dt\,dm_{\pi\pi}^2} = \frac{\gamma(m_{\pi\pi})}{s^2(t-\mu^2)^2} \cdot \xi(t) \cdot e^{2A(t-\mu^2)}$$

where $\delta = -t/\mu^2$,

φ_{sp} is the relative s-p phase

$\gamma(m_{\pi\pi})$ corresponds to the overall normalization

$$\frac{X}{2} = \frac{1}{2}\left(\frac{m_{\pi\pi}}{\mu}\right)^2 = \left|\frac{\rho_{00}}{\rho_{11}}\right|_{t=\mu^2}$$

and

$$\epsilon = \left|\frac{\rho_{ss}}{\rho_{11}}\right|_{t=\mu^2}$$

It is evident that $\rho_{00} - \rho_{11}$, ρ_{1-1}, and $\text{Re}\rho_{10}$ are parameter independent except for the dependence on ϵ via the normalization factor $\xi(t)$. This dependence is quite weak since $X \approx 30$ in the rho mass region whereas ϵ is empirically found to be ≈ 2.

Before discussing fits of the above parameterization to the density matrix

elements, it is interesting to note the following general features. The fact

that $m_1^{-1} = \mu^2 m_1^1$, together with Eqs. (6.3e-f) and (6.4b), requires that

$Re\rho_{10} = Re\rho_{1s} = (\rho_{11} - \rho_{1-1}) = 0$ at $t = -\mu^2$. It has already been pointed out in Section

5.B.4 that $Re\rho_{10}$ and $Re\rho_{1s}$ do cross zero at $t \approx -\mu^2$. The prediction that

$(\rho_{11} - \rho_{1-1})_{t=-\mu^2} = 0$ implies that the asymmetry between the natural-and

unnatural-parity-exchange contributions to the ± 1 helicity states, $\dfrac{\rho_{1-1}}{\rho_{11}} \equiv A$, must

be 1 at $t = -\mu^2$. Since ρ_{1-1} vanishes identically at $t = t_{min}$, the asymmetry A must

rise rapidly from 0 to 1 as $-t$ increases from t_{min} to μ^2. The measurements

of $\dfrac{\rho_{1-1}}{\rho_{11}}$, which are shown in Fig. 60, indicate good agreement with this

prediction. It should be noted that the analogous asymmetry for single-pion

photoproduction also exhibits just such a behavior, so that the prediction for this

reaction follows from VDM arguments as well.

Qualitative explanation of the other observed structure in the density matrix

elements and differential cross section (in the helicity frame) follows by obser-

vation from Eqs. (6.3): (1) The longitudinal cross section, $\rho_{00}\dfrac{d\sigma}{dt}$, must vanish

as $-t$ in the forward direction because of the net helicity change, $n=1$; (2) since

$\rho_{00}\dfrac{d\sigma}{dt} \gg 2\rho_{11}\dfrac{d\sigma}{dt}$ away from $t = t_{min}$, $(d\sigma/dt)_{TOTAL}$ also exhibits a forward

turnover; (3) although one of the transverse amplitudes vanishes at small t, the

other one is not required to ($n=0$); the transverse cross section is therefore

approximately proportional to $\dfrac{1}{(t-\mu^2)^2}$ for small t and exhibits a forward peak.

Each of these qualitative predictions (with the possible exception of

$Re\rho_{10} = Re\rho_{1s} = 0$) has been explicitly made prior to this experiment,[69] and each

is observed to be true. It is now interesting to see how well the above model

quantitatively fits our measurements.
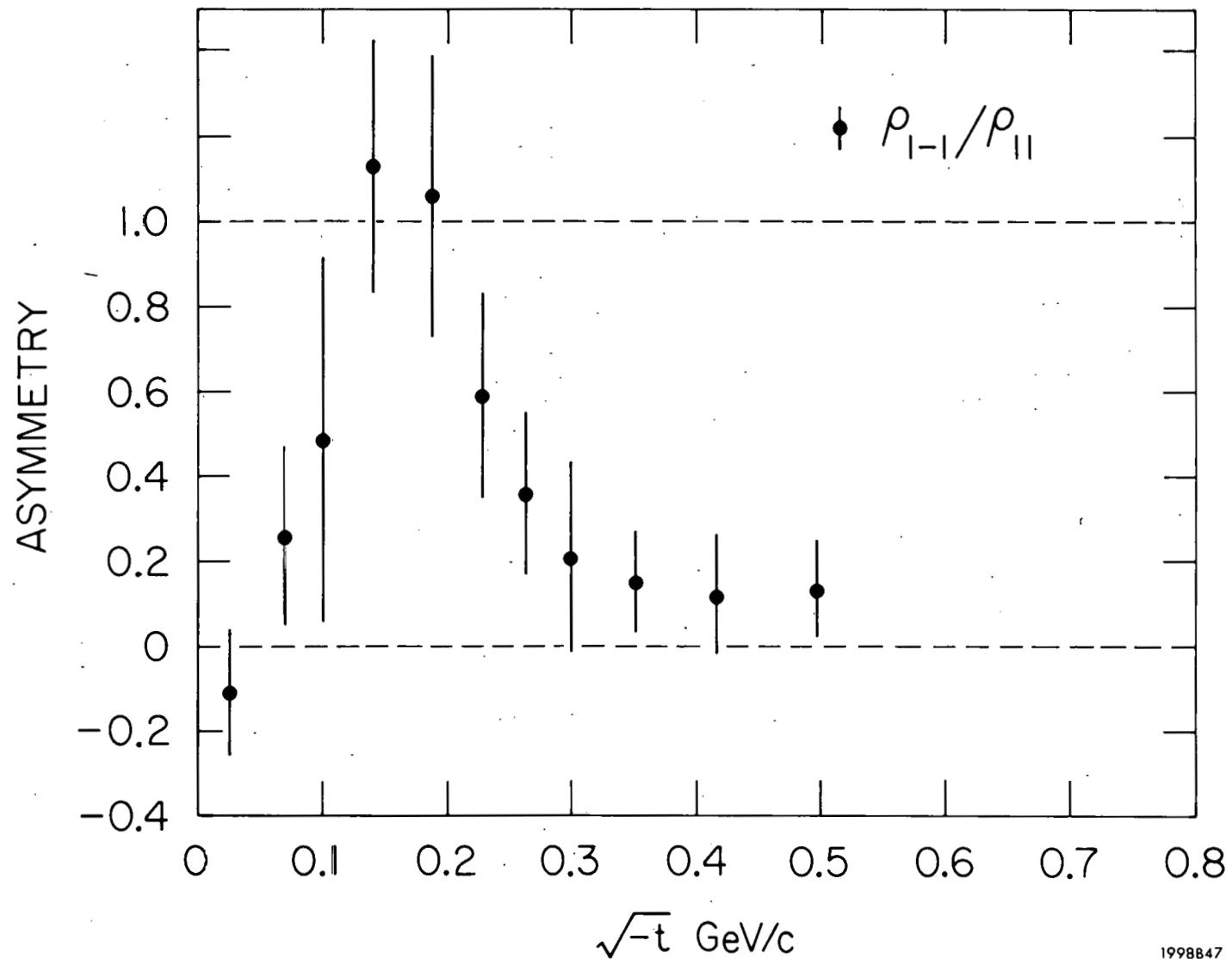
FIG. 60--The asymmetry, as a function of momentum transfer, between the natural- and unnatural-parity-exchange contributions to helicity ± 1 states (evaluated in the helicity frame).

3. OPEA Fits to the Density Matrix Elements and Differential Cross Section

The predictions of OPEA were quantitatively tested by fitting Eqs. (6.10) to the measured values of the density matrix elements and differential cross section for $-t < .15 (GeV/c)^2$; the model is not expected to be valid for larger $-t$.[*] The free parameters were ϵ, φ_{sp}, A, and $\bar{\gamma}$, where $\bar{\gamma}$ represents the average value of $\gamma(m_{\pi\pi})$ for our mass interval; a contribution from the non-flip amplitudes was also allowed. As noted in Chapter 5, there is a background of $\approx 6\% \pi^+\pi^-\Delta^0$ events in the "$\pi^+\pi^-$n" event sample from which the density matrix elements were obtained. The $\pi^+\pi^-\Delta^0$ cross section is expected from OPE to be dominated largely by the non-flip amplitude. In addition, although OPE predicts that the $\pi^+\pi^-$n channel is dominated by nucleon helicity-flip, there is no reason to expect that the non-flip contribution should be identically zero. The parameters describing the non-flip amplitude, φ_{sp}^{NF}, ϵ^{NF}, $\bar{\gamma}^{NF}$, and A^{NF} were obtained by fitting the parameterization analogous to Eqs. (6.10) for nucleon non-flip to the $\pi^+\pi^-\Delta^0$ data (selected by imposing the cuts $.665 < m_{\pi\pi} < .865$ GeV and $1.14 < MM < 1.34$ GeV). Only the <u>amount</u> of non-flip was a free parameter in the fit to the $\pi\pi$n data.

The resulting fit, which is indicated by the solid lines in Fig. 61 reproduces quite well all of the observed structure; a rather good fit is obtained with a χ^2 of 63 for 73 degrees of freedom. The parameters obtained for the flip amplitude were $\epsilon = 1.80 \pm .12$, $\varphi_{sp} = 0 \pm .19$, $\bar{\gamma} = 137 \pm 7$, and $A = 5.3 \pm .3$ (GeV/c)$^{-2}$. The amount of non-flip required, averaged over the interval $0 < -t < .15 (GeV/c)^2$

---

[*]Fits of a similar model to a large fraction of the world data existing prior to this experiment have also been made in an attempt to obtain information on the small momentum transfer behavior of the transverse cross section. See Ref. 70.

$\pi^- p \longrightarrow \pi^+ \pi^- n$ 15 GeV

$0.665 \leq m_{\pi\pi} \leq 0.865$ GeV

—— FIT TO ABSORPTION MODEL

(a)

$\frac{d\sigma}{dt} \left[mb/(GeV/c)^2 \right]$

(b) $\rho_{00}^H - \rho_{11}^H$

(c) ρ_{1-1}^H

(d)   Re ρ_{10}^H

(e)   Re ρ_{1S}^H

(f)   Re ρ_{0S}^H

t $(GeV/c)^2$

1868C15
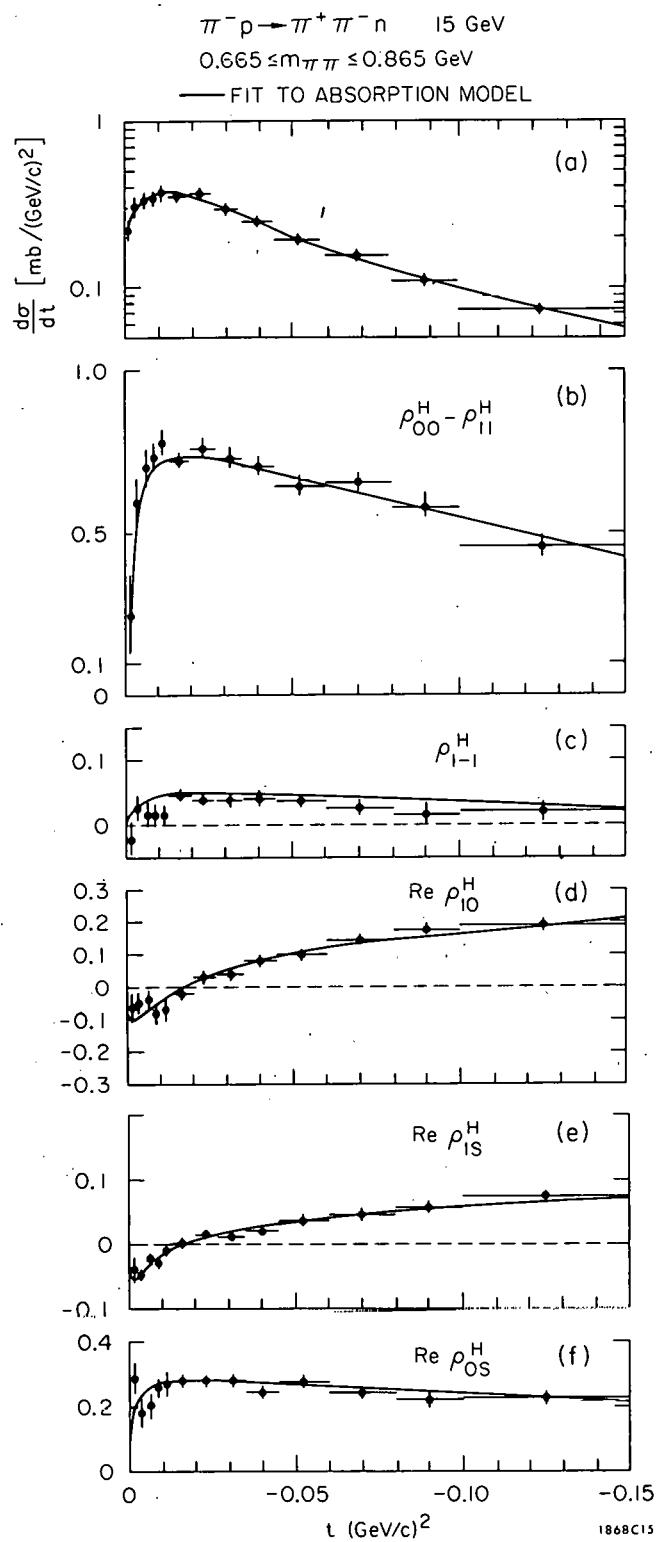
FIG. 61--A fit of OPEA to the measured density matrix
    elements and differential cross section.

- 175 -

was $16 \pm 2\%$.[*] This is in reasonable agreement with the known $\pi^+\pi^-\Delta^o$ background and the amount of non-flip contribution to $\pi^+\pi^-$n that may be expected. Fits were also performed with X a free parameter (Ref. Eqs. 6.10), and the value assumed agreed with the theoretical value, $m_{\pi\pi}^2/\mu^2$, within $\approx 10\%$.

C. Conclusion

In conclusion, the following is noted. The density matrix elements and the total $\pi\pi$ differential cross section measured in this experiment exhibit considerable structure in the forward direction. Particular examples are the turnover in $\rho_{00}-\rho_{11}$ and $d\sigma/dt$ for $-t < m_\pi^2$, and the fact that $\mathrm{Re}\rho_{10}^H$ and $\mathrm{Re}\rho_{1s}^H$ change sign for $-t=m_\pi^2$. Each of these qualitative features is predicted to occur if the reaction proceeds via absorptive one-pion-exchange.

The s-wave contribution to the $\pi\pi$ state was estimated from data on $\pi^-p \to \pi^o\pi^o n$ and from limits established by inequalities on the density matrix elements, thereby allowing extraction of the differential cross sections for transversely and longitudinally polarized rho mesons. The transverse cross section in the helicity frame rises sharply in the forward direction in agreement with the predictions of OPEA and VDM, but in contradiction to form-factor-modified OPE. Also in agreement with OPEA is the observed rapid rise in the asymmetry, ρ_{1-1}/ρ_{11}, as $-t$ increases from t_{min} to m_π^2. All of the qualitative features of the data therefore indicate that for small momentum transfers the reaction proceeds via one-pion-exchange with absorption.

---

[*] It was reported previously[32b] that a good fit to the data was obtained with the non-flip contribution fixed at 12%. At that time, a study of the Δ^{++} missing mass spectrum had not been made (Ref. Section 5.C.2), and it was assumed that all of the 12% background was due to $\pi^+\pi^-\Delta^o$. The results of this previous fit were almost identical with those presented above: the same values of the fitted parameters were obtained, within errors, and the χ^2 was 65/74 degrees of freedom.

Quantitative fits of OPEA to the density matrix elements and differential cross section reproduce the data quite well, but indicate that some small amount of non-flip amplitude may be present. The agreement of these fits with the data indicate that OPEA quantitatively describes the behavior of the reaction as a function of momentum transfer. In addition, the particular parameterization of absorption that was used is evidently a valid one, though perhaps somewhat phenomenological.

CHAPTER VII

$$\pi^- p \to K^+ K^- n, \; \bar{p}pn$$
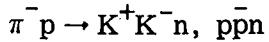
Information on the final state, K^+K^-n, was also obtained in this experi-
ment since the Čerenkov counter distinguished between π and K mesons. The
criteria that were used for isolating these events have been described in
detail in Chapter III. As noted there, contamination of the K^+K^- sample from
$\pi^+\pi^-$ events is negligible ($< .1\%$), while background from $K\pi$, πp and other
final states containing a single pion or lighter particle is estimated to be less
than 2%.

Since the pressure of the counter was set to distinguish pions from any
heavier particles, however, no information was available on $\bar{p}p$ final states.
In order to correct for this background and, in particular, to study the $\bar{p}p$
system, another set of runs (E67) were made with the pressure of the counter
increased so that it distinguished pions and kaons from protons (and anti-
protons). One of the more interesting things learned from these runs is that
the $\bar{p}pn$ cross section is comparable to that of K^+K^-n.* This is also verified
by the "K^+K^-" missing mass spectrum as shown below.**

A. <u>Mass and Missing Mass Distributions for "K^+K^-" and $\bar{p}p$ Events</u>

The missing mass distribution for the "K^+K^-" event sample is shown in
part (a) of Fig. 62. It is apparent that the peak corresponding to the neutron

---

* A study of $\pi^- p \to \bar{p}pn$ has also been made at 8 GeV in a bubble chamber
experiment. See Ref. 71.

** The notation "K^+K^-" is used to indicate an event sample that contains both
K^+K^- and $\bar{p}p$ events; absence of the quotation marks indicates that the $\bar{p}p$ back-
ground has been subtracted (statistically).
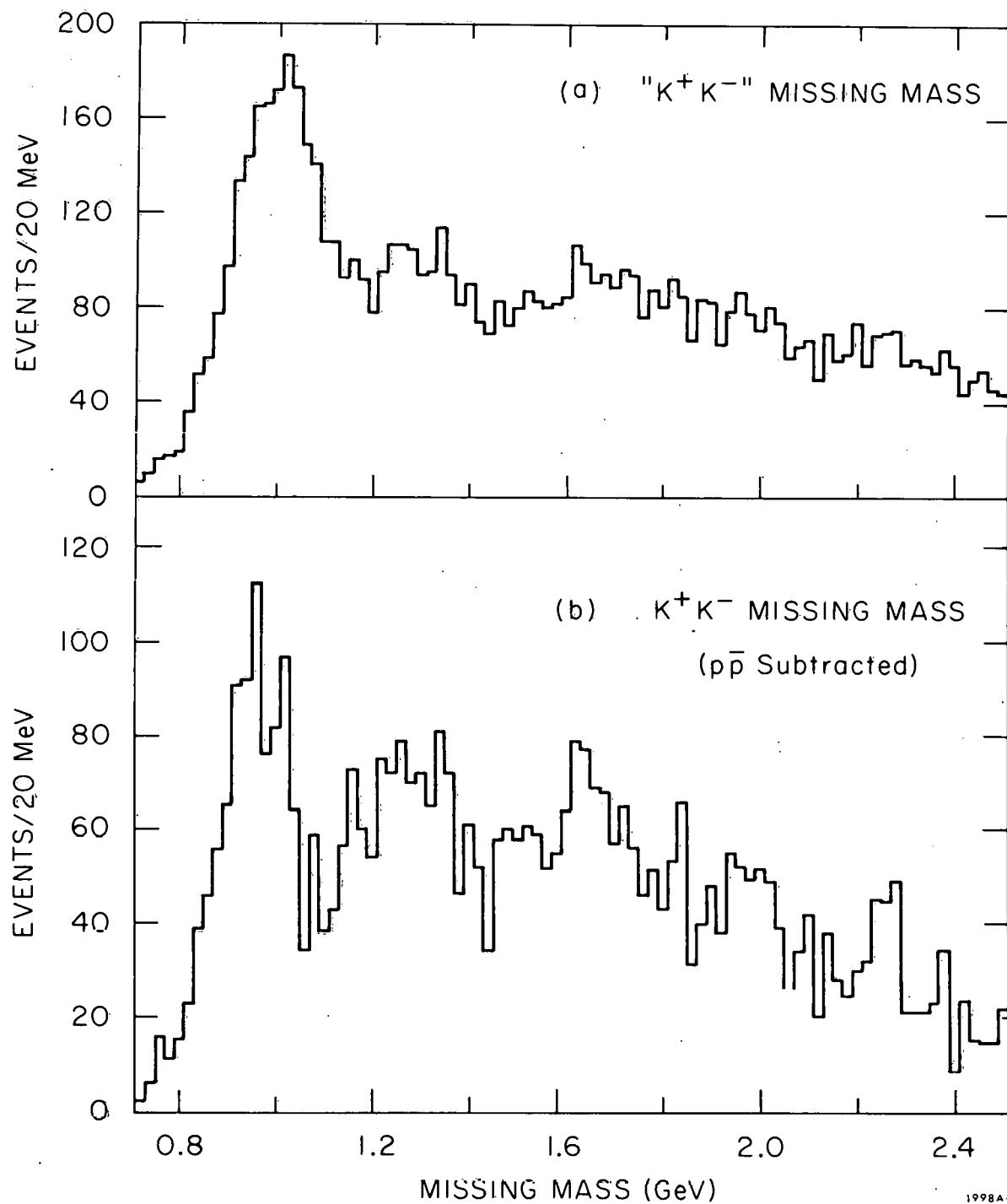
FIG. 62--Missing mass distribution for K^+K^- events in $\pi^-p \rightarrow K^+K^-X^0$. (a) Observed spectrum; (b) the spectrum obtained by subtracting, statistically, from part (a), the $p\bar{p}$ background.

is skewed and centered at ≈ 1.0 GeV, 60 MeV above the mass of the nucleon.
For $\bar{p}pn$ events, mistakenly identified as K^+K^-n, one would expect the neutron
peak to be centered at ≈ 1.03 GeV. It is therefore clear, solely from the
missing mass distribution, that a substantial number of $p\bar{p}$ events are con-
tained in the data sample. It was possible to correct the spectrum of Fig. 62a
by estimating the $p\bar{p}$ background from E67. Interpreting the proton anti-proton
events as K^+K^- and subtracting the resulting MM distribution, scaled by the
relative normalizations of the two experiments, from Fig. 62a, one obtains
the K^+K^- MM spectrum shown in Fig. 62b. It is evident that the neutron peak
is now reasonably well-centered at the nucleon mass. It is interesting to note
that the K^+K^- system apparently couples to many of the N* and Δ resonances
while the $p\bar{p}$ system couples only to the neutron as shown in Fig. 63.

The observed "K^+K^-" mass spectrum, obtained by imposing a MM cut of
.80 - 1.08 GeV on the sample of events in Fig. 62a is shown in Fig. 64a. The
dashed line indicates the acceptance of the apparatus for an isotropic K^+K^-
decay angular distribution and a momentum transfer distribution (to the
nucleon) of e^{10t}. No significant structure is observed except for a peak at
the mass of the ϕ. It should be noted, however, that the detection efficiency
is rather poor for K^+K^- masses above ≈ 1.2 GeV, particularly for high spin
resonances, and it is therefore difficult to conclude anything in this region.

The slope of the differential cross section for $\pi^-p \rightarrow \psi n$ has been measured
at 11 GeV/c (Ref. 40) to be 6.5 ± 3.5 $(GeV/c)^{-2}$. Since this falloff is signifi-
cantly slower than the $e^{10t} - e^{12t}$ observed in this experiment for the "K^+K^-"
distribution as a whole, one might expect that the ϕ signal would be enhanced
at larger momentum transfers. Figure 64b shows the mass spectrum for
$-t > .1$ $(GeV/c)^2$. The signal now stands quite clearly above the background
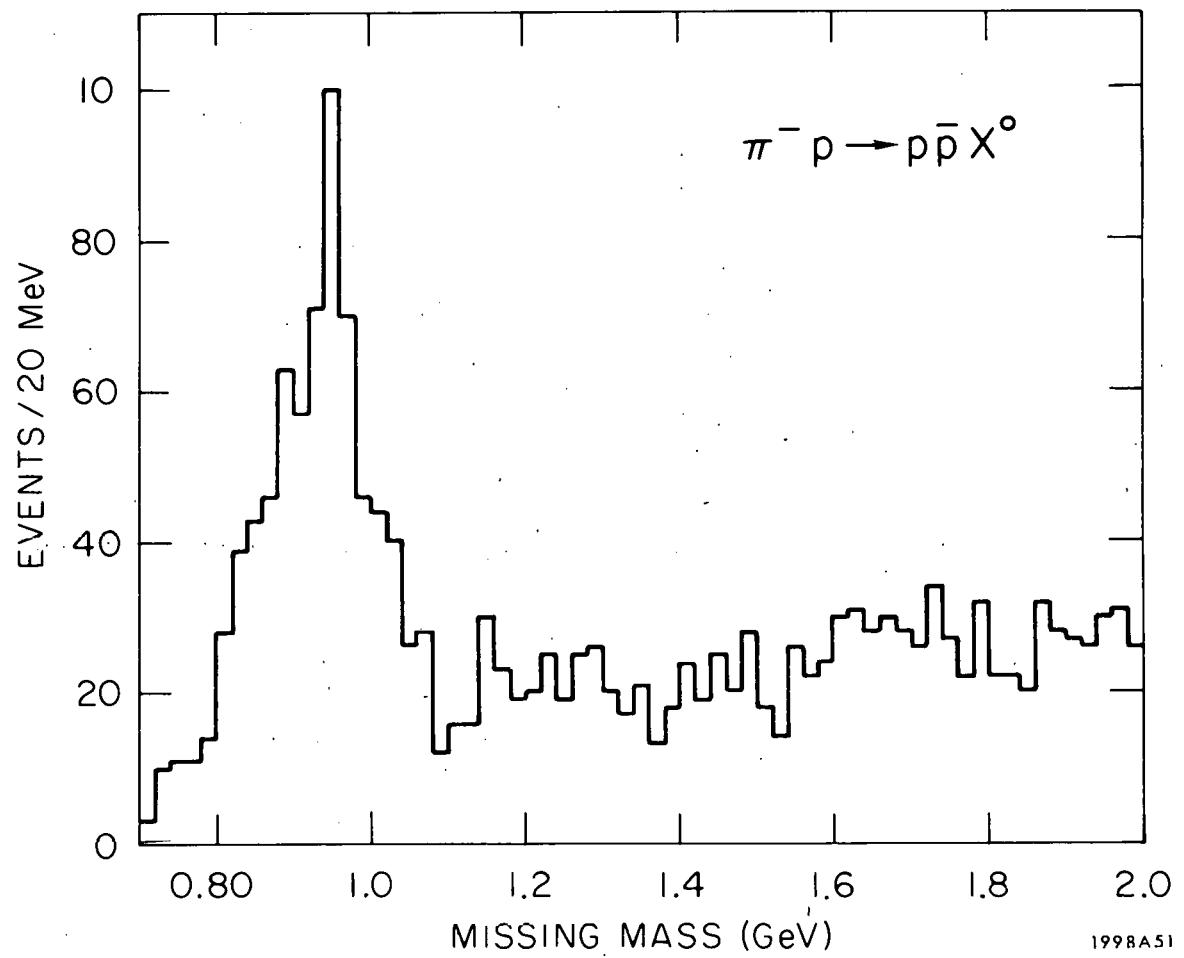
FIG. 63--Missing mass distribution for p$\bar{\text{p}}$ events.
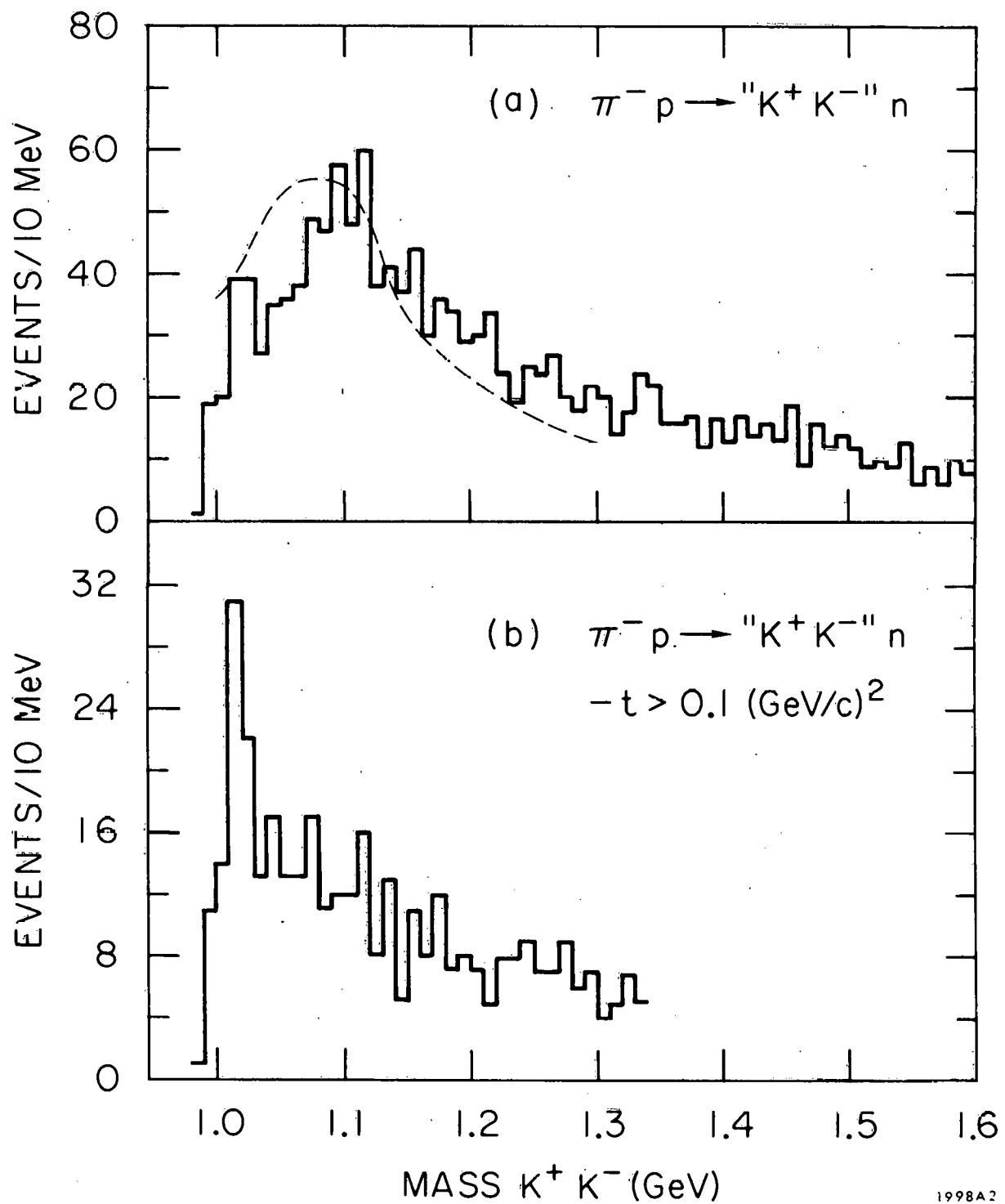
FIG. 64--Observed mass distribution for K⁺K⁻n events. (a) All events;
(b) events with -t > 0.1 (GeV/c)². The dashed line indicates
the variation in the detection efficiency, as a function of the
K⁺K⁻ mass, for an isotropic decay angular distribution and
differential cross section $\propto e^{10t}$.

and is approximately a 4 standard deviation effect. The production cross section is derived in the next section.

The raw mass distribution for the $p\bar{p}n$ events is shown in Fig. 65; the acceptance as a function of mass, for an isotropic angular distribution, is
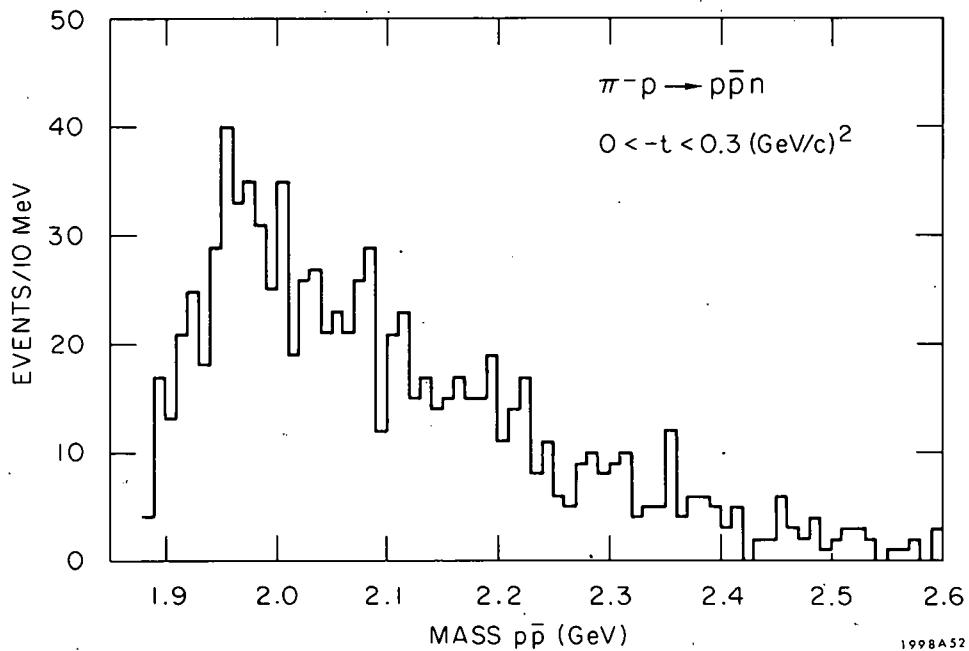
FIG. 65--Observed mass distribution for $p\bar{p}n$ events.

very similar to that shown in Fig. 64. Contrary to what might have been expected from the experiments discussed in Chapter 1, there is no evidence of any resonant structure. This supports the conclusions of Bricman et al.,[72] who also found no evidence of $N\bar{N}$ resonances in a study of $p\bar{p} \to n\bar{n}$ from 1 - 3 GeV/c.

The $p\bar{p}$ cross section rises rapidly at threshold, however, and is surprisingly large. As an example, the $K\bar{K}$ and $p\bar{p}$ cross sections are presented respectively, for the intervals 1.05 - 1.15 GeV and 1.94 - 2.04 GeV. A cut

has also been made on $0 < -t < .3$ $(\text{GeV/c})^2$:

$$\sigma(K^+K^-n;\ 1.05 - 1.15\ \text{GeV}) = 4.50 \pm 1.42\ \mu b/\text{GeV}$$

$$0 < -t < .3\ (\text{GeV/c})^2$$

$$\sigma(p\bar{p}n;\ 1.94 - 2.04\ \text{GeV}) = 5.43 \pm 1.23\ \mu b/\text{GeV}$$

The cross sections for these mass intervals are presented since they repre-
sent the same interval in Q, and the acceptance of the apparatus is optimal in
these regions. ($Q = M_{X\bar{X}} - M_X - M_{\bar{X}}$ where X and $\bar{X}$ represent the particle and
anti-particle.)

The density matrix elements for the "K^+K^-"n event sample were obtained
for $-t < .2$ $(\text{GeV/c})^2$ and for several mass bins in the region 1.03 - 1.18 GeV,
using an identical procedure as for the $\pi^+\pi^-$n events (again assuming only s-
and p-waves contribute). The results obtained were roughly consistent with
the values obtained at 11 GeV/c by Hyams et al.;[40] in particular, the value
of $\rho_{00} - \rho_{11}$ in the region 1.05 - 1.15 GeV was found to be .1 - .2. Attempts
to obtain the K^+K^- matrix elements by statistically subtracting the proton-
anti-proton background and fitting the resulting angular distribution were not
completely successful, largely because of statistical limitations. It was
observed, however, that the value of $\rho_{00} - \rho_{11}$ decreased when the $p\bar{p}$ events
were subtracted. For the purpose of calculating the above cross sections,
it was assumed that the K^+K^- decay angular distribution was isotropic
($\rho_{00} - \rho_{11} = 0$) and that the momentum transfer distribution was e^{At} with
$A = 10$ $(\text{GeV/c})^{-2}$. Variations in $\rho_{00} - \rho_{11}$ of $\approx .2$ and in A of $\approx .2$ $(\text{GeV/c})^{-2}$
result in variations in the cross section presented above of $\approx 10\%$. This
uncertainty, together with an estimated 10% systematic error resulting from
uncertainty in the $p\bar{p}$ background subtraction have been included in the error

estimate quoted above. Similarly, the error quoted for the $\bar{p}p$ cross section also includes a 10% contribution resulting from uncertainties in the angular distribution and hence in the average efficiency.

B. Determination of the ϕ Cross Section

Since there is no structure in the $\bar{p}p$ system, it is possible to estimate the number of ϕ events directly from Fig. 64 despite the fact that the spectrum includes a background of $\bar{p}p$ events. The ϕ cross section was calculated separately from part (a) which includes all t, and also from part (b) which includes only -t > .1 for comparison -- in particular to obtain an idea of the systematic error made in estimating the background. The results agreed within 5%. It is clear, however, that a more accurate estimate can be made from the -t > .1 sample and consequently the cross section quoted was obtained from Fig. 64b. The number of ϕ events with -t > .1 was estimated to be 23 ± 9.1.

In order to determine the average detection efficiency, it was necessary to know the decay angular distribution and production differential cross section for the ϕ. Because of the background and relatively small number of events, it was not possible to determine this from our data sample. As noted above, however, the experiment of Hyams et al. observes the ϕ at 11 GeV/c. They find the decay angular distribution to be consistent with $\sin^2 \theta$ (as would be expected from ρ exchange) and the slope of $\frac{d\sigma}{dt}$ to be 6.5 ± 3.5 $(\text{GeV/c})^{-2}$. We have therefore assumed these values in calculating the average acceptance. As an estimate of the systematic error introduced by these assumptions, we note that if the angular distribution were isotropic, rather than $\sin^2 \theta$, or if the slope of $\frac{d\sigma}{dt}$ were 8 $(\text{GeV/c})^{-2}$ rather than 6.5 $(\text{GeV/c})^{-2}$, the calculated cross section would change by $\approx$ 20%.

The value of the cross section obtained is

$$\sigma(\pi^- p \to \phi n \to K^+ K^- n) = 65 \pm 26 \text{ nb}$$

where the error quoted is statistical only. A comparison of this measurement with existing data is shown in Fig. 66.

C. Calculation of ω-ϕ Mixing Angle

It has been suggested by Alexander, Lipkin, and Scheck[73] that a calculation of the ω-ϕ mixing angle and a test of the quark model may be made from the ratio of the amplitudes for $\pi^- p \to \phi n$ and $\pi^- p \to \omega n$.

From the assumption that a meson is a quark-antiquark pair, and that the meson-baryon scattering amplitude is expressible as the sum of the constituent quark-baryon and antiquark-baryon amplitudes, they obtain the selection rule

$$< \pi^- p | M_\lambda n > = 0 \qquad (7.1)$$

where M_λ is the particular linear combination of neutral meson states which contains only strange quarks. Thus M_λ is given by

$$M_\lambda = \frac{1}{\sqrt{3}} \left(\sqrt{2} \, M_8 - M_1 \right) \qquad (7.2)$$

where M_8 and M_1 are the unitary octet states. From the conventional definition of the mixing angle

$$\phi = \omega_8 \cos \alpha - \omega_1 \sin \alpha$$

$$\omega = \omega_8 \sin \alpha + \omega_1 \cos \alpha \qquad (7.3)$$
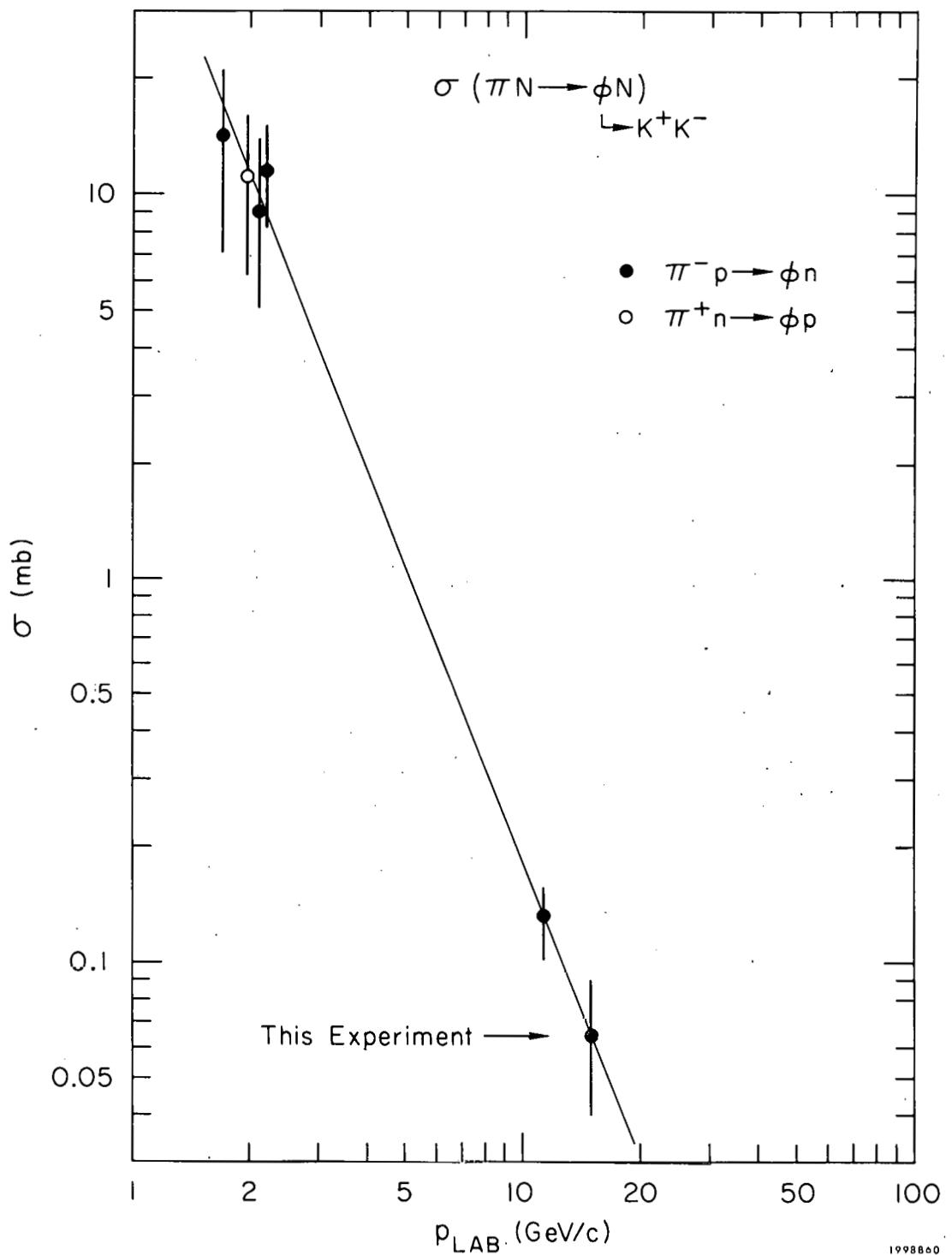
FIG. 66--Comparison of $\sigma(\pi^- p \rightarrow \phi n \rightarrow K^+ K^- n)$ measured in the experiment with previous measurements.

it follows that $M_\lambda \equiv \phi$ and $<\pi^- p | \phi n> = 0$ if $\sin \alpha = \dfrac{1}{\sqrt{3}}$ (=> $\alpha = 35.3^\circ$).

Substitution of Eqs. (7.3) and (7.2) in (7.1) yields the following prediction:

$$\frac{<\pi^- p | \phi n>}{<\pi^- p | \omega n>} = \frac{\cos \alpha - 2 \sin \alpha}{\sin \alpha + 2 \cos \alpha} \qquad (7.4)$$

Although a measurement of $\pi^- p \to \omega n$ at 15 GeV/c is not available, sufficiently good measurements of $\pi^+ n \to \omega p$ and $\pi^- p \to \omega n$ (largely the former) exist at lower energies that one can extrapolate the cross section with reasonable accuracy. By performing such an extrapolation and assuming by isospin invariance that the $\pi^- p \to \omega n$ and $\pi^+ n \to \omega p$ cross sections are the same, we obtain an estimated $\pi^- p \to \omega n$ cross section of 16 ± 4 μb at 15 GeV/c. This together with the above measurement of the ϕ cross section yields*

$$R = \left| \frac{<\pi^- p | \phi n>}{<\pi^- p | \omega n>} \right| = .092 \begin{smallmatrix} + .019 \\ - .026 \end{smallmatrix}$$

In principle, the comparison should be made at the same Q value for each reaction, and the difference in phase space factors taken into account, but at this large an energy the differences in these factors are negligible. Equation (7.4) may be rewritten in the form

$$\frac{<\pi^- p | \phi n>}{<\pi^- p | \omega n>} = - \tan (\gamma - \gamma_0) \qquad (7.5)$$

where $\gamma_0 = 35.3^\circ$. From the cross section measurements, it is only possible to determine the magnitude of $\gamma - \gamma_0$. If one assumes that $\gamma - \gamma_0 > 0$, then the value of R determined above yields

$$\gamma = 40.6 \begin{smallmatrix} + 1.1 \\ - 1.5 \end{smallmatrix} \text{ degrees}$$

---

* In calculating the total $\pi^- p \to \phi n$ cross section from our measurement of $\pi^- p \to \phi n \to K^+ K^- n$, the branching ratio $B = (\phi \to K^+ K^-)/(\phi \to \text{All})$ was taken to be $B = 0.48 \pm 0.04$.[74]

in excellent agreement with the value of 40.2^O which may be obtained from the Gell-Mann-Okubo quadratic mass formula. Similar values of 42.1 ± 1.8^O and 43.8 ± 1.5^O have been obtained at lower energies from the data of Boyd et al.[39] and Hess et al.,[38] respectively.

In conclusion, both the K^+K^-n and $\bar{p}pn$ final states appear to be dominated by a smooth effective mass distribution in the particle anti-particle pair, rather than by resonant structure. It is difficult to draw definite conclusions about the K^+K^- spectrum, however, because of the large $p\bar{p}$ background and the fact that the detection efficiency is poor for K^+K^- masses $\gtrsim 1.2$ GeV. The $\bar{p}pn$ cross section is found to be comparable to that for K^+K^-n; in particular, $\sigma(K^+K^-n; 1.05 < m_{K^+K^-} < 1.15 \text{ GeV}) = 4.50 \pm 1.42 \ \mu b/\text{GeV}$ and $\sigma(p\bar{p}n; 1.94 < m_{p\bar{p}} < 2.04 \text{ GeV}) = 5.43 \pm 1.23 \ \mu b/\text{GeV}$ for $-t < .3 \ (\text{GeV/c})^2$.

The cross section for the reaction $\pi^- p \to \phi n \to K^+K^-n$ is measured to be $65 \pm 26 \ \mu b$. This value, together with available data on $\pi N \to \omega N$ and a quark model prediction, allow a calculation of the $\omega - \phi$ mixing angle. The mixing angle is found to be $40.6^{+1.1}_{-1.5}$ degrees in good agreement with the value 40.2^O which may be obtained from the Gell-Mann-Okubo quadratic mass formula.

REFERENCES

1. L. M. Eisberg, W. B. Fowler, R. M. Lea, W. D. Shephard, R. P. Shutt, A. M. Thorndike, and W. L. Whittemore, Phys. Rev. 97, 797 (1955); W. D. Walker, Phys. Rev. 108, 872 (1957); G. Maenchen, W. B. Fowler, W. M. Powell, and R. W. Wright, Phys. Rev. 108, 850 (1957).

2. C. Goebel, Phys. Rev. Letters 1, 337 (1958).

3. G. F. Chew and F. E. Low, Phys. Rev. 113, 1640 (1959).

4. S. D. Drell, Phys. Rev. Letters 5, 342 (1960); Rev. Mod. Phys. 33, 458 (1961); F. Salzman and G. Salzman, Phys. Rev. 120, 599 (1960); E. Ferrari and F. Selleri, Nuovo Cimento Suppl. 24, 453 (1962). The one-pion-exchange model is also discussed in standard textbooks on elementary particle physics such as H. Pilkuhn, The Interactions of Hadrons (John Wiley and Sons, Inc., New York, 1967); S. Gasiorowicz, Elementary Particle Physics (John Wiley and Sons, Inc., New York, 1966).

5. See for example, E. Ferrari and F. Selleri, Nuovo Cimento Suppl. 24, 453 (1962); U. Amaldi and F. Selleri, Nuovo Cimento 31, 360 (1964); J. D. Jackson and H. Pilkuhn, Nuovo Cimento 33, 906 (1964); and J. D. Jackson, Rev. Mod. Phys. 37, 484 (1965). The earlier literature may be easily traced from these references.

6. H. P. Dürr and H. Pilkuhn, Nuovo Cimento 40, 899 (1965).

7. J. Benecke and H. P. Dürr, Nuovo Cimento 56, 269 (1968).

8. G. Wolf, Phys. Rev. 182, 1538 (1969).

9. N. J. Sopkovich, Nuovo Cimento $\underline{26}$, 186 (1962).

10. A. Dar, M. Kugler, Y. Dothan, and S. Nussinov, Phys. Rev. Letters $\underline{12}$, 82 (1964);

   A. Dar and W. Tobocman, *ibid.* $\underline{12}$, 511 (1964);

   A. Dar, *ibid.* $\underline{13}$, 91 (1964).

11. L. Durand, III, and Y. T. Chiu, Phys. Rev. Letters $\underline{12}$, 399 (1964);

   $\underline{E13}$, 45 (1964);

   L. Durand, III, and Y. T. Chiu, Phys. Rev. $\underline{137}$, B1530 (1965);

   L. Durand, III, and Y. T. Chiu, Phys. Rev. $\underline{139}$, B646 (1965).

12. M. H. Ross and G. L. Shaw, Phys. Rev. Letters $\underline{12}$, 627 (1964).

13. (a) K. Gottfried and J. D. Jackson, Nuovo Cimento $\underline{34}$, 735 (1964);

   (b) J. D. Jackson, Rev. Mod Phys. $\underline{37}$, 484 (1965);

   (c) J. D. Jackson, J. T. Donohue, K. Gottfried, R. Keyser, and
   B. E. Y. Svensson, Phys. Rev. $\underline{139}$, B428 (1965).

14. P. B. Johnson, J. A. Poirier, N. N. Biswas, N. M. Cason, T. H. Groves, V. P. Kenney, J. T. McGahan, W. D. Shephard, L. J. Gutay, J. H. Campbell, R. L. Eisner, F. J. Loeffler, R. E. Peters, R. J. Sahni, W. L. Yen, I. Derado, and Z. G. T. Guiragossián, Phys. Rev. $\underline{176}$, 1651 (1968).

15. L. J. Gutay, F. T. Meire, D. D. Carmony, F. J. Loeffler, and P. L. Csonka, Nucl. Phys. $\underline{B12}$, 31 (1969).

16. J. A. Poirier, N. N. Biswas, N. M. Cason, I. Derado, V. P. Kenney, W. D. Shephard, E. H. Synn, H. Yuta, W. Selove, R. Ehrlich, and A. L. Baker, Phys. Rev. $\underline{163}$, 1462 (1967).

17. B. D. Hyams, W. Koch, D. C. Potter, J. D. Wilson, L. von Lindern, E. Lorenz, G. Lütjens, U. Stierlin, and P. Weilhammer, Nucl. Phys. $\underline{B7}$, 1 (1968).

18. E. Colton, P. E. Schlein, E. Gellert, and G. A. Smith, Phys. Rev. Letters **21**, 1548 (1968).

19. W. E. Ellis, R. R. Kinsey, T. W. Morris, and R. S. Panvini, Phys. Letters **32B**, 140 (1970).

20. E. Colton, P. E. Schlein, E. Gellert, and G. A. Smith, Phys. Rev. **D3**, 1063 (1971).

21. Z. Ming Ma, G. A. Smith, R. J. Sprafka, E. Colton, and P. E. Schlein, Phys. Rev. Letters **23**, 342 (1969).

22. For a more detailed discussion of the material in the several preceding paragraphs, the reader is referred also to the review article of Peter Schlein: "Review of Some Experimental Results on the $\pi\pi$ and $K\pi$ Interactions," CERN preprint and to be published in the Proceedings of the International School of Subnuclear Physics, Erice, Sicily, 1970. This article also contains many references.

23. G. Manning, A. G. Parham, J. D. Jafar, H. B. van der Raay, D. H. Reading, D. G. Ryan, B. D. Jones, J. Malos, and N. H. Lipman, Nuovo Cimento **41A**, 167 (1966).

24. A. M. Boyarski, F. Bulos, W. Busza, R. Diebold, S. D. Ecklund, G. E. Fischer, J. R. Rees, and B. Richter, Phys. Rev. Letters **20**, 300 (1968);

    A. M. Boyarski, R. Diebold, S. D. Ecklund, G. E. Fischer, Y. Murata, B. Richter, and W.S.C. Williams, Phys. Rev. Letters **21**, 1767 (1968); P. Heide, U. Kötz, R. A. Lewis, P. Schmüser, H. J. Skronn, and H. Wahl, Phys. Rev. Letters **21**, 248 (1968).

25. See, for example, G. L. Kane, Experimental Meson Spectroscopy, edited by C. Baltay and A. H. Rosenfeld (Columbia University Press, New York, 1970), p. 1; and also Ref. 13b.

26. W. Selove, F. Forman, and H. Yuta, Phys. Rev. Letters $\underline{21}$, 952 (1968).

27. There exists a relatively large literature on the vector dominance model and the relation, via VDM, of single-pion photoproduction and the reaction $\pi^- p \to \rho^0 n$. See, e.g., (a) F. Bulos, R. K. Carnegie, G. E. Fischer, E. E. Kluge, D.W.G.S. Leith, H. L. Lynch, B. Ratcliff, H. H. Williams, and S. H. Williams, Phys. Rev. Letters $\underline{26}$, 1457 (1971) and the references contained therein;

    (b) B. Ratcliff, Stanford University Doctoral Dissertation in Physics (1972), to be issued as Report No. SLAC-141.

28. G. L. Kane and M. Ross, Phys. Rev. $\underline{177}$, 2353 (1969).

29. F. Henyey, G. L. Kane, Jon Pumplin, and M. H. Ross, Phys. Rev. $\underline{182}$, 1579 (1969).

30. M. Ross, F. S. Henyey, and G. L. Kane, Nucl. Phys. $\underline{B23}$, 269 (1970).

31. P. K. Williams, Phys. Rev. $\underline{D1}$, 1312 (1970).

32. Many of the results of this experiment, and a comparison of these results with absorptive one-pion-exchange, have been previously published in:
    (a) F. Bulos, R. K. Carnegie, G. E. Fischer, E. E. Kluge, D.W.G.S. Leith, H. L. Lynch, B. Ratcliff, B. Richter, H. H. Williams, and S. H. Williams, Phys. Rev. Letters $\underline{26}$, 1453 (1971); also SLAC-PUB-884 (1971);

    (b) P. Baillon, F. Bulos, R. K. Carnegie, G. E. Fischer, E. E. Kluge, D.W.G.S. Leith, H. L. Lynch, B. Ratcliff, B. Richter, H. H. Williams, and S. H. Williams, Phys. Letters $\underline{35B}$, 453 (1971).

33. See, e.g., D. Cline, "High Mass-Low Spin Meson Resonance Spectroscopy Using $N\overline{N}$ Reactions," a talk given at the Argonne National Laboratory Workshop on Meson Spectroscopy, July 1971, and a University of Wisconsin preprint;

D. Cline, <u>Meson Spectroscopy</u>, edited by C. Baltay and A. H. Rosenfeld (W. A. Benjamin, Inc., New York, 1968), p. 391.

34. D. J. Crennell, G. R. Kalbfleisch, K. W. Lai, J. M. Scarr, T. G. Schumann, I. O. Skillicorn, and M. S. Webster, Phys. Rev. Letters <u>16</u>, 1025 (1966).

35. K. W. Lai, <u>Meson Spectroscopy</u>, edited by C. Baltay and A. H. Rosenfeld (W. A. Benjamin, Inc., New York, 1968), p. 303. This article and Refs. 36, 37 contain many references to the earlier work.

36. T. F. Hoang, D. P. Eartly, J. J. Phelan, A. Roberts, C. L. Sandler, S. Bernstein, S. Margulies, D. W. McLeod, T. H. Groves, N. N. Biswas, N. M. Cason, V. P. Kenney, J. M. Marraffino, J. T. McGahan, J. A. Poirier, and W. D. Shephard, Phys. Rev. <u>184</u>, 1363 (1969).

37. W. Beusch, W. E. Fischer, B. Gobbi, M. Pepin, E. Polgar, P. Astbury, G. Brautti, G. Finocchiaro, J. C. Lassalle, A. Michelini, K. M. Terwilliger, D. Webodalc, and C. H. West, Phys. Letters <u>25B</u>, 357 (1967); W. Beusch, <u>Experimental Meson Spectroscopy</u>, edited by C. Baltay and A. H. Rosenfeld (Columbia University Press, New York, 1970), p. 185.

38. O. I. Dahl, L. H. Hardy, R. I. Hess, J. Kirz, and D. H. Miller, Phys. Rev. <u>163</u>, 1377 (1967); R. I. Hess, O. I. Dahl, L. M. Hardy, J. Kirz, and D. H. Miller, Phys. Rev. Letters <u>17</u>, 1109 (1966).

39. J. H. Boyd, A. R. Erwin, W. D. Walker, and E. West, Phys. Rev. <u>166</u>, 1458 (1968).

40. B. D. Hyams, W. Koch, D. C. Potter, L. von Lindern, E. Lorenz, G. Lütjens, U. Stierlin, and P. Weilhammer, Nucl. Phys. <u>B22</u>, 189 (1970).

41. R. J. Abrams, R. L. Cool, G. Giacomelli, T. F. Kycia, B. A. Leontić, K. K. Li, and D. N. Michael, Phys. Rev. Letters 18, 1209 (1967).

42. G. Chikovani, L. Dubal, M. N. Focacci, W. Kienzle, B. Levrat, B. C. Maglić, M. Martin, C. Nef, P. Schübelin, and J. Séguinot, Phys. Letters 22, 233 (1966).

43. D. Cline, J. English, D. D. Reeder, R. Terrell, and J. Twitty, Phys. Rev. Letters 21, 1268 (1968).

44. J. W. Chapman, F. Hess, J. Lys, C. T. Murphy, and J. C. Vander Velde, Phys. Rev. Letters 21, 1718 (1968);
G. Kalbfleisch, R. Strand, and V. Vanderburg, Phys. Letters 29B, 259 (1969).

45. R. Baud, H. Benz, B. Bošnjaković, D. R. Botterill, G. Damgaard, M. N. Focacci, W. Kienzle, R. Klanner, C. Lechanoine, M. Martin, C. Nef, P. Schübelin, and A. Weitsch, Phys. Letters 30B, 129 (1969).

46. For a more detailed discussion of the beam, the reader is referred to the SLAC Group C Internal Report by G. E. Fischer.

47. M. Gan, F. Bulos, and H. L. Lynch, Report No. SLAC-TN-71-20 (1971);
F. Bulos and H. L. Lynch, "Design and Performance of High Repetition Rate Wire Spark Chamber System with Magnetostrictive Readout," SLAC Group C Internal Report (1971).

48. For a discussion of magnetostrictive readout, see V. Perez-Mendez and J. M. Pfab, Nucl. Instr. and Methods 33, 141 (1965);
L. Kaufman, V. Perez-Mendez, and J. M. Pfab, IEEE Trans. Nucl. Sci. NS13, 578 (1966);
R. L. Grove, V. Perez-Mendez, and R. Van Tuyl, Nucl. Instr. and Methods 70, 306 (1969).

49. For the basic design of these horns see H. Hinterberger and R. Winston, Rev. Sci. Instr. **37**, 1094 (1966).

50. E. L. Garwin and A. Roder, Nucl. Instr. and Methods **93**, 593 (1971).

51. N. Barash-Schmidt, A. Barbaro-Galtieri, C. Bricman, T. Lasinski, A. Rittenberg, M. Roos, A. H. Rosenfeld, P. Söding, T. G. Trippe, and C. G. Wohl (Particle Data Group), Rev. Mod. Phys. **43**, S1 (1971).

52. K. Gottfried and J. D. Jackson, Nuovo Cimento **33**, 309 (1964);

    J. D. Jackson, Nuovo Cimento **34**, 1644 (1964);

    R. L. Eisner, P. B. Johnson, P. R. Klein, R. E. Peters, R. J. Sahni, W. L. Yen, and G. W. Tautfest, Phys. Rev. **164**, 1699 (1967).

53. For a general discussion of helicity amplitudes, $f_{\lambda_c \lambda_d; \lambda_a \lambda_b}$, see M. Jacob and G. C. Wick, Ann. Phys. **7**, 404 (1959).

54. B. Y. Oh, A. F. Garfinkel, R. Morse, W. D. Walker, J. D. Prentice, E. C. West, and T. S. Yoon, Phys. Rev. **D1**, 2494 (1970).

55. N. N. Biswas, N. M. Cason, P. B. Johnson, V. P. Kenney, J. A. Poirier, and W. D. Shephard, Phys. Rev. **D1**, 2705 (1970).

56. E. Malamud and P. E. Schlein, Phys. Rev. Letters **19**, 1056 (1967).

57. See Ref. 27b for a discussion of the elastic scattering measurements.

58. K. J. Foley, R. S. Jones, S. J. Lindenbaum, W. A. Love, S. Ozaki, E. D. Platner, C. A. Quarles, and E. H. Willen, Phys. Rev. **181**, 1775 (1969); Phys. Rev. Letters **19**, 330 (1967);

    K. J. Foley, S. J. Lindenbaum, W. A. Love, S. Ozaki, J. J. Russell, and L. C. L. Yuan, Phys. Rev. Letters **11**, 425 (1963).

59. J. Pišút and M. Roos, Nucl. Phys. **B6**, 325 (1968).

60. P. Sonderegger and P. Bonamy, Saclay preprint submitted to the <u>Fifth International Conference on Elementary Particles, Lund, Sweden, 25 June - 1 July 1969</u> (Abstract 372).

61. E. I. Shibata, D. H. Frisch and M. A. Wahlig, Phys. Rev. Letters <u>25</u>, 1227 (1970).

62. M. Alston-Garnjost, A. Barbaro-Galtieri, S. M. Flatté, J. H. Friedman, G. R. Lynch, S. D. Protopopescu, M. S. Rabin, and F. T. Solmitz, Phys. Letters <u>36B</u>, 152 (1971).

63. There exists quite a large literature on the s-wave $\pi\pi$ phase shift. Some of the more recent papers, which contain references to earlier work are: E. Colton and E. Malamud, Phys. Rev. <u>D3</u>, 2033 (1971); J. P. Baton, G. Laurens, and J. Reignier, Phys. Letters <u>33B</u>, 528 (1970); B. Y. Oh, A. F. Garfinkel, R. Morse, W. D. Walker, J. D. Prentice, E. C. West, and T. S. Yoon, Phys. Rev. <u>D1</u>, 2494 (1970); J. H. Scharenguivel, L. J. Gutay, D. H. Miller, L. D. Jacobs, R. Keyser, D. Huwe, E. Marquit, F. Oppenheimer, W. Schultz, S. Marateck, J. D. Prentice, and E. West, Phys. Rev. <u>186</u>, 1387 (1969). See also Refs. 14, 15, and 22.

64. W. Deinet, A. Menzione, H. Müller, and H. M. Staudenmaier, Phys. Letters <u>30B</u>, 359 (1969).

65. M. Bander and G. L. Shaw, Phys. Rev. <u>139</u>, B956 (1965).

66. P. K. Williams, Phys. Rev. <u>181</u>, 1963 (1969).

67. Y. Avni and H. Harari, Phys. Rev. Letters <u>23</u>, 262 (1969).

68. J.A.J. Matthews, J. D. Prentice, T. S. Yoon, J. T. Carroll, M. W. Firebaugh, and W. D. Walker, Nucl. Phys. <u>B32</u>, 366 (1971).

69. These qualitative features are implicit in most versions of OPEA, but see in particular Ref. 30.

70. J. H. Scharenguivel, L. J. Gutay, D. H. Miller, R. L. McIlwain, F. T. Meiere, D. Morgan, L. D. Jacobs, S. Marateck, C. D. Froggatt, D. Huwe, and E. Marquit, Phys. Rev. Letters 24, 332 (1970).

71. J. W. Andrews, N. N. Biswas, N. M. Cason, I. Derado, V. P. Kenney, J. A. Poirier, and W. D. Shephard, Phys. Rev. 163, 1502 (1967).

72. C. Bricman, M. Ferro-Luzzi, J. M. Perreau, J. K. Walker, G. Bizard, Y. Déclais, J. Duchon, J. Séquinot, and G. Valladas, Phys. Letters 29B, 451 (1969).

73. G. Alexander, H. J. Lipkin, and F. Scheck, Phys. Rev. Letters 17, 412 (1966).

74. J. S. Lindsey and G. A. Smith, Phys. Rev. 147, 913 (1966).